Chemo-mechanical couplings in inelastic solids : analytical solutions and application to oxidation

Svetlana Petrenko

INSTITUT POLYTECHNIQUE DE PARIS

NNT : 2021IPPAX069

Thèse de doctorat

Chemo-mechanical couplings in inelastic solids: analytical solutions and application to oxidation

Thèse de doctorat de l'Institut Polytechnique de Paris
préparée à l'École polytechnique

École doctorale n°626 École Doctorale de l'Institut Polytechnique de Paris (ED IP Paris)
Spécialité de doctorat : Mécanique des fluides et des solides, acoustique

Thèse présentée et soutenue à Palaiseau, le 14 septembre 2021, par

SVETLANA PETRENKO

Composition du Jury :

Olivier Hubert Professeur des Universités, CNRS - ENS Paris-Saclay	Président
Xavier Feaugas Professeur des Universités, CNRS - Université de La Rochelle, LaSIE	Rapporteur
Michael Peigney Professeur, CNRS - l'École des Ponts ParisTech	Rapporteur
Cécile Davoine Ingénieur de Recherche ONERA, Onera (centre francais de recherche aéronautique spatiale) Châtillon	Examinateur
Alexander Lion Professor, Institut für Mechanik Universität der Bundeswehr München	Examinateur
Eric Charkaluk Directeur de Recherche, CNRS - l'École Polytechnique, LMS	Directeur de thèse
Habibou Maitournam Professeur, CNRS - ENSTA Paris, IMSIA	Co-directeur de thèse
Alexander Freidin Professor, Peter the Great St.Petersburg Polytechnic University	Invité

Acknowledgments

First of all, I would like to thank my jury for the recognition they have given to this work done in my doctoral dissertation. I thank each member of jury for their ability to take a particular enthusiastic look at this work, for their very interesting questions, discussion and for all the interest they have shown me during this session. I would like to address special thanks to Xavier Feaugas and Michael Peigney for their roles as rapporteurs and their precise and relevant feedback.

In fact, the word 'thanks' is far from strong enough to express what I owe to my supervisors. It is therefore a very warm recognition that I address to Eric Charkaluk and Habibou Maitournam for their invaluable advice, support and supervision towards me. I thank them for these 4 stimulating years during which I matured and progressed alongside them. Eric and Habibou both made me grow and encouraged me by their kindness, their experience and their precision. I especially thank them for the trust they have always given me. Eric was able to help me give the best of myself and follow my ideas through his support, his enthusiasm and even our few confrontations. Eric gave me the opportunity to collaborate with Onera and to realise my idea to do the experiments. This work has, it seems to me, borne many fruits, but above all they have given me the possibility of maturing technically.

I especially thank Cecile Davoine for her support throughout this project, for the opportunity to work together, to exchange views with particular interest and to make the experiments in Onera Chatillon. It was great pleasure to work with you.

It is with great gratitude that I write these few lines to thank Simon Hallais and Alexandre Tanguy for their availability and their technical expertise. Thanks to you, I have been able to carry out high quality experiences.

I obviously thank all members of LMS with whom I was able to collaborate or simply share moments, especially Emilien, Filippo, Nicolas, Alexandra, Anna, Abdelfattah, Manas, Thien Nga and to many former PhD students. We were able to share an excellent moment in human and scientific terms.

I thank my parents and my sister for their unwavering support as well as all my close friends who will recognize themselves when they read this passage. Especially I want to thank my friend Leonid for his patience and his unfailing support.

To conclude on a lighter note, I would have a last word for Alexander Freidin who was the first to introduce me to mechanochemistry and perhaps laid the foundations for this adventure ...

Thank you all from the bottom of my heart.

Résumé

Au cours des dernières décennies, une attention particulière en mécanique des solides a été consacrée à l'étude des matériaux, dont la structure change en raison de transformations chimiques, ce qui induit des couplages forts entre la chimie, la mécanique et la physique. Ces réactions chimiques assistées par les contraintes sont observées dans diverses applications industrielles et médicales, et dans les technologies modernes telles que les cycles de charge/décharge des batteries introduisant des changements de volume et des fissurations dans les électrodes, les processus d'oxydation dans les MEMS ou les matériaux composites à base de métal, la thermo- ou photo-oxydation des polymères. Il est donc nécessaire de prendre en compte en détail l'influence de l'état de contrainte et de déformation sur la transformation chimique pour prédire le comportement des éléments structurels sous des chargements thermomécaniques et chimiques simultanés. De tels processus peuvent être décrits à l'aide du modèle de réaction à deux phases, dans lequel la réaction est localisée au niveau d'un front ou interface de réaction, et le réactif diffusant est transporté vers le front de réaction à travers le matériau transformé.Le travail présenté dans cette thèse de doctorat s'appuie sur le cadre de la mécanique des milieux continus et sur les couplages chemo-mécaniques appliqués à des géométries particulières et des lois de comportement inélastiques afin d'obtenir des solutions analytiques de référence qui sont comparées à des résultats expérimentaux. La propagation, sous contrainte, du front de réaction chimique dans un solide déformable inélastique (visqueux, plastique) a été considérée sur la base du concept du tenseur d'affinité chimique. Pour le cas d'un composant inélastique, la réaction chimique est obtenue et analysée par des solutions analytiques des problèmes aux limites les plus simples décrivant la propagation de fronts de réaction plans, cylindriques et sphériques. Il a été montré comment l'état de contrainte-déformation et la géométrie du solide affectent la cinétique de la réaction chimique. A partir de la notion de concentration d'équilibre, les effets de l'accélération sont étudiés, de même que le ralentissement et le blocage de la réaction par les sollicitations extérieures en fonction des paramètres des matériaux. Les contraintes et déformations, induites par les transformations chimiques, ont été déterminées. Leur impact sur les propriétés de déformation et de résistance des matériaux a été estimé. A partir du tenseur d'affinité chimique, une équation cinétique est formulée ; elle détermine la dépendance de la vitesse de propagation d'un front de réaction chimique dans les corps visco-élastiques et élasto-plastiques par rapport à l'état de contrainte-déformation. La propagation, sous contrainte, du front de réaction chimique dans un solide déformable dans le cas de fronts de réaction plan, sphérique et cylindrique a été ensuite considérée pour les corps élastiques. L'analyse mathématique précise de l'influence de divers paramètres sur le comportement du front de réaction est effectuée. Le front de réaction plan se propage uniquement selon une loi parabolique. Dans le cas du front de réaction sphérique, la cinétique peut être logarithmique et parabolique, selon les relations entre les combinaisons de modules d'élasticité des réactifs solides. Pour la réaction en configuration cylindrique une loi cinétique exponentielle a été observée ainsi qu'une loi parabolique. Ces différents résultats sont cohérents avec certaines données expérimentales issues de la littérature. Le troisième chapitre est consacré aux réactions chimiques sous contrainte en viscoélasticité et un modèle pour l'étude analytique de la relaxation de contrainte derrière le front de réaction est développé. Les résultats montrent que les déformations visqueuses n'affectent pas directement la cinétique du front dans le cas du modèle linéaire standard si la déformation externe agit dans le plan de l'interface, puisqu'elles n'ont pas le temps d'apparaître pour le moment de la transformation. Mais ils permettent la possibilité d'un phénomène de relaxation des contraintes derrière le front de réaction. Selon les paramètres visqueux et élastiques, cette relaxation peut être rapide, et la région des fortes contraintes est localisée dans une couche étroite adjacente au front de transformation. Notons également que d'autres chargements externes sont possibles, lors desquels la relaxation des contraintes peut réactiver le front de réaction initialement bloqué. Le changement de rhéologie d'un constituant solide dû à la réaction chimique localisée a été pris en compte à l'aide du Modèle Linéaire Standard (SLSM) et ses cas particuliers. Le modèle SLSM et Maxwell ont permis d'obtenir des solutions analytiques qui nous ont permis d'étudier les effets spécifiques des paramètres des

matériaux sur la relaxation des contraintes derrière le front de réaction. D'autre part, les matériaux visqueux purs et de Kelvin-Voigt peuvent difficilement être considérés comme des candidats appropriés pour modéliser les produits de réaction. Les effets de la plasticité sur la cinétique du front de réaction ont été étudiés au chapitre 4. La propagation sous contrainte du front de réaction chimique dans un solide déformable dans le cas d'un front de réaction plan, sphérique et cylindrique pour le matériau transformé élastique-parfaitement plastique a également été considérée. Dans ce cas, il est montré que la réaction chimique a un mécanisme différent des réactions en élasticité et en viscoélasticité. Ces mécanismes sont présentés et décrits. Il est montré que la prise en compte du seul phénomène de transformation chimique peut induire des déformations plastiques. L'influence de la condition aux limites pour l'initiation de la déformation plastique dans le matériau est étudiée. Pour le front de réaction plan, le choix de la condition aux limites conduit à deux situations différentes pour la phase élasto-plastique (si elle apparaît). On montre que pour le cas de déformations imposées, lorsque la limite d'élasticité est atteinte, le matériau élastique transformé devient entièrement plastique, tandis que pour des contraintes imposées, un front plastique apparaît. Dans le cas de la propagation du front de réaction sphérique et cylindrique, le front plastique apparaît dans le régime élasto-plastique. Deux fronts ont leurs propres vitesses et directions. La zone plastique s'étend dans deux directions. La relation entre le front de réaction et le front plastique est déterminée. Il est montré que la plastification du matériau accélère la réaction. En conséquence, les modèles proposés sont comparés entre eux dans le chapitre 5. Il est montré que la cinétique du front de réaction chimique est affectée par les lois de comportement, le type de chargement externe et les paramètres élastiques. L'influence de la géométrie des solides sur la cinétique de réaction est étudiée. Le front de réaction plan se propage plus vite que le front cylindrique et plus lentement que le front sphérique.

Enfin, des études expérimentales d'oxydation à haute température de fils et de billes de nickel pur ont été menées. Les données expérimentales pour l'évolution de l'épaisseur d'oxyde au cours du temps ont été obtenues et comparées aux modèles théoriques proposés. Il est montré que l'oxydation des fils de nickel démontre une cinétique parabolique, alors que pour les billes de nickel elle est plutôt logarithmique. La comparaison des résultats expérimentaux de l'oxydation des fils de nickel avec les modèles proposés montre que les expériences peuvent être décrites avec précision par le modèle de fronts de réaction cylindriques en élastoplasticité. Les billes de nickel étant de tailles différentes et contenant de nombreux défauts de surface, le modèle et l'expérience ne donnent qu'une concordance relative, qui reste à confirmer. En résumé, l'influence de la géométrie des solides, des lois de comportement, des conditions aux limites et des propriétés mécaniques sur la propagation du front de réaction a été analysée pour les lois de comportement inélastiques. Comme les géométries simples considérées correspondent à des applications industrielles, les résultats obtenus pourraient être utilisés pour les développements de la conception optimale de nano-anodes dans des batteries Li-ion à capacité spécifique, pour développer les bases théoriques du contrôle de la taille du matériau transformé (par exemple, oxyde, silicium lithié) et la géométrie de la nano-structure. Ces solutions analytiques pourraient également être utilisées pour vérifier les procédures numériques et pour l'estimation des impacts de la transformation et des déformations inélastiques sur l'épaississement lors de la propagation du front dans les expériences.

Contents

Introduction

...We went into science because it's fascinating and exciting, because we wanted to explore the Universe and find out the secrets it holds. We wanted to understand, to know, to comprehend, to write another chapter in the story of humanity's search for knowledge. We are part of a great tradition, using the work of those who went before to help us progress farther and yet farther across this amazing Universe in which we live. And to understand why we are here and how it all began. ... We bring enlightenment by sharing our knowledge. We don't keep it to ourselves. We explain, we teach, we seek...

Stephen and Lucy Hawking

The influence of stress-strain state on chemical reactions has been widely considered since the 70s of the last century. It is of primary importance in such fields as energy storage industry, nuclear power, medicine, aircraft industry, civil engineering and the list is far from being exhausted. The oxidation of silicon in nanowires [15], or in MEMS [99], reactions in ceramic composites with inclusions, i.e. [101], lithiation of silicon in Li-ion batteries, i.e. [93], are a few representative examples of the importance of establishing interconnections between chemical transformations and stress-strain states (see also, e.g., [54, 95, 153] and the references in [43]).

These and other similar processes can be described using a two-phase reaction model in which the reaction is localized at the sharp interface – a reaction front, and the diffusing reactant is transported to the reaction front through the solid transformed material. One of the first and most simple models that described such reactions was the model proposed by Deal and Grove [26] for a planar oxidation front. This model gave a general scenario of the problem statement but did not consider stress effects. However, previously mentioned chemical reactions are accompanied by volumetric expansion that produces internal stresses, which in turn may affect the chemical reaction (see, i.e. [7, 31, 74, 101]). An extension of the Deal-Grove model was proposed by considering a stress-dependent diffusion coefficient and a reaction rate parameter [59–61, 76, 120, 137]. Other alternatives to taking into account the influence of stresses on the diffusion and reaction are to introduce additional terms in the expression for the diffusion flux [71, 72, 141] or considering the influence through a scalar chemical potential [12, 13, 80, 89, 90].

In fact, stresses may affect the reaction via their influence on diffusion flux (diffusion-controlled reactions) or via direct influence on the reaction rate (reaction rate-controlled reactions), see, i.e., [22]. In the present work we focus on the second case, for which the reaction front propagation is controlled rather by the reaction rate than by the diffusion (see, i.e., [57, 159]). Modeling of the reaction front kinetics is based on the chemical affinity tensor derived initially for nonlinear elastic constituents [37], similar to how it was done for a propagating phase interface in [70]. Then it was derived from fundamental balance laws and the entropy inequality written down for an open system with a chemical reaction between diffusing and solid constituents of arbitrary rheology, and a kinetic equation in the form of the dependence of the reaction front velocity on the normal component of the affinity tensor was formulated [38, 40, 44]. This consideration is consistent with the approach of classical physical chemistry where reaction rate is determined by a scalar chemical affinity [119], and the notion of the chemical affinity arises to pioneering works by Gibbs [47] and de Donder [25].

In the case of solid constituents, tensorial nature of the chemical affinity follows from the consideration of a chemical reaction on the oriented area element of the reaction front (see a more detailed discussion in [43]), as well as the tensorial nature of the chemical potential followed from the fact that a phase equilibrium took place not just in a point but at oriented area elements of the phase interface passing through the point (see, i.e., [48]). It should be noted that the chemical affinity tensor was not postulated but derived in the spirit of irreversible thermodynamics with the use of the Clausius–Duhem inequality. The normal component of the tensor was conjugate to the reaction rate at the oriented area element in the expression of the energy dissipation due to the reaction front propagation, and this tensor was naturally called chemical affinity tensor. In a quasi-static case, the chemical affinity tensor is represented by the linear combination of the chemical potential tensors, which are the Eshelby stress tensors divided by the reference mass densities (see the next Section 1.2.2). This combination is the same as the combination of scalar chemical potentials which defines the classical chemical affinity.

Up to now, the approach based on the chemical affinity tensor has been applied to a number of boundary value problems with propagating reaction fronts in a formulation which assumed solid constituents to be linear elastic [41, 42, 44, 143]. Then the theory has been used to describe numerically two-phase lithiation of Si particles used in Li-ion batteries, where the constituent materials undergoing finite elasto-viscoplastic deformations were considered [116, 117]. However, inelastic constitutive laws have rarely been used to obtain analytic results and a systematic analysis of viscoelasticity or elastoplasticity influence on the chemical reaction front is clearly missing.

In the present work we come back to the case of small strains and develop a model for analytical studies of stress relaxation behind the reaction front and of plastic deformations due to the chemical transformation. Since one observes the total thickness of the transformed layer in simple experiments with planar reaction fronts, even simple models may be useful for estimation of the inputs to the thickness of the reaction front propagation due to a chemical reaction and the thickening due to inelastic deformations.

The thesis consists of five chapters. In the first chapter, a general formulation of the mechano-chemistry problem is given. The general thermodynamical approach is formulated and a short summary of the concept of the chemical affinity tensor is given firstly in Section 1.2.2, along with the formulation of a general quasi-static coupled problem involving mechanics, diffusion and chemistry.

The second chapter is devoted to the solution of the mechano-chemical problem with elastic reaction product. The kinetics equation is obtained for planar, spherical and cylindrical fronts. The influence of strains and material parameters on the kinetics of the front propagation was studied in detail with the use of the notion of the equilibrium concentration. Two types of the dependencies of the equilibrium concentration and, thus, front velocity on strain are demonstrated, depending on the relations between the combinations of elastic moduli of solid reactants.It is shown that reaction kinetics depends on the geometry of the structural element. It is demonstrated the possibility of logarithmic kinetics in the case of the spherical reaction front. For the reaction in cylindrical element the exponential law of the kinetics was observed.

The third chapter is devoted to the viscoelastic transformed material. The changing of the rheology of a solid constituent due to the localized chemical reaction was taken into account with the use of the Standard Linear Solid Model and its particular cases. The analytical solution is obtained. The influence of viscosity on the chemical reaction is studied in details. Analytical expressions of stress relaxation behind the reaction front are developed.

In the fourth chapter the influence of plastic strains on chemical reaction front propagation is studied. Theoretical analysis is conducted for the case of elastic-perfectly plastic transformed material. The equations for the reaction kinetics are obtained. The different mechanism of the chemical reaction front propagation in comparison with the cases of elastic and viscoelastic reaction product is studied. The importance of the type of the boundary condition for the initiation of the plastic deformation in the material is shown. The appearance of the second (plastic) front and its kinetics is analyzed.

The last fifth chapter is devoted to the experimental work and to the comparison between the theoretical results and experimental data. In the first part, in order to validate this approach, high-temperature oxidation experiments for pure nickel wires and balls are conducted. The evolution of the oxide surface morphology and internal microstructure of Ni and NiO is obtained. The oxide thickness is measured. The second part of the chapter is devoted to two types of comparisons: between models and experiments and between models. Such comparisons show how the rheological properties of materials and geometry of the considered body are important to predict the reaction front propagation.

Chapter 1

General formulation of the mechanochemistry problem

Thermodynamics is a funny subject. The first time you go through it, you don't understand it at all. The second time you go through it, you think you understand it, excepting for one or two small point. The third time you go through it, you know you don't understand it, but by that time you are so used to the subject, it doesn't bother you any more...

Arnold Johannes Wilhelm Sommerfeld

Contents

1.1 State of the art

In recent decades the study of the materials, whose structure changes due to chemical phase transformation under thermal and mechanical effects, has attracted extremely wide attention due to its interesting interdisciplinary. In such research the problems of physics, mechanics and chemistry are coupled. Moreover, stress-assisted chemical reactions are relevant in various industrial and biomedical applications and in modern technologies. Important examples of such reactions are: polymers degrading by hydrolysis in water (e.g. PLA, PCL), with emphasis on biomedical applications (bioresorbable implants, sutures, drug delivery) (see i.e. [27, 83, 134, 144]); oxidation of ceramic composites dispersed metal particles for the high temperature applications [56, 101, 102]; oxidation of nanowires [15, 65, 154], MEMS elements [98, 99] and chips; austenite-martensite phase transformation in polymers; formation of hydrides in hydrogen-storage materials [51, 64, 66, 135]; processes of charging/discharging of lithium-batteries [81, 91, 93, 129, 151]. It is thus necessary to take into account the influence of stress-strain state on chemical transformation in detail for predicting the lifetime and the behavior of structural elements under conditions of joint thermomechanical and chemical effects. All these and a lot of other processes can be described using the two-phase reaction model, it is thus important to be able to handle it efficiently. As applications are too numerous, in this state of the art, we will only focus on silicon as an example of such mechanochemistry problems.

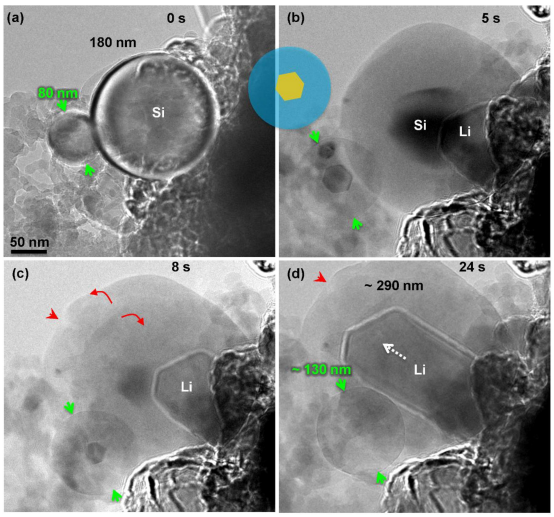

Figure 1.1: Chemical lithiation of two Si nanoparticles [87]

Silicon has all the required semiconducting properties, photoconductivity, high mechanical strength, excellent temperature characteristics, good chemical compatibility, formation of junction and it highest known specific capacity to store lithium, even higher than graphite electrodes. This is why silicon is a wide-used material in the industry, biomedicine, solar cells, batteries, microeletronics systems and in technological processes.

As previously mentioned, amorphous silicon has high theoretical specific capacity of $4200 mAhg^{-1}$ [17], while for graphite it is of $372 mAhg^{-1}$. Due to such high specific capacity, silicon is one of the most promising candidate for the anode material in Li-ion batteries (another one is Sn, for which the theoretical capacity of $873 mAhg^{-1}$). However, the insertion of such big amount of Li atoms into the silicon electrode during lithiation, leads to the enormous volume expansion up to 400% [93, 142] and large elastic-plastic deformations [104]. There are two aspects of negative affect of anode deformations: failure of anode particles and failure of solid electrolyte interface. Volume changes in anode, associated with insertion or remove of Li atoms, cause the huge stresses in the anode and in turn can lead to the fracture of the anode particle, initiation and further propagation of cracks and places the solid electrolyte interface under tensile stress (see Fig. 1.1). Therefore, it leads to degradation of battery performance and limits the lifetime of it [7].

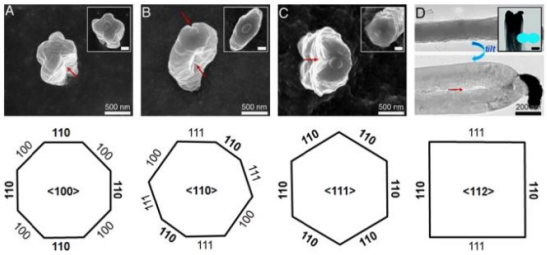

Figure 1.2: SEM and TEM images of anisotropic swelling and fracture in lithiated Si nanowires with four different axial orientations: (A) ⟨100⟩ , (B) ⟨110⟩, (C) ⟨111⟩, and (D) ⟨112⟩[152].

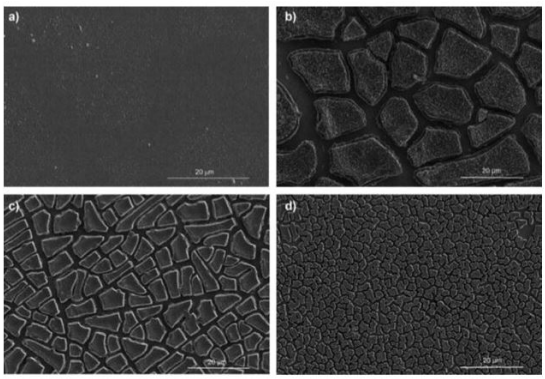

Figure 1.3: SEM images of crack patterns formed in a-Si thin films [81]

Various designs for anode structure have been developed in order to reduce the effect of large volume change, therefore, to obtain better capacity and prolongation of silicon anode life-time. The sharp interface is observed in the experiments and is correspond to the surface between the lithiated silicon and silicon, even in amorphous Si thin-film electrodes [85–87, 93, 100, 152]. Also it was reported that the interface has significant influence on the kinetics of charging and discharging processes and on the induced stresses due to the chemical transformation (lithiation/delithation) [21, 80, 155]. Experiments shows that the phase interface mobility is anisotropic and depends on its orientation [78, 86, 152] (see Fig. 1.2). It was also shown in [88, 127], that there is strong dependence between the particle size and fracture behavior during first lithiation, the critical size exists, below which the cracking does not occur. In nanostructured materials, the surface stresses via the induced internal stresses can change the capacity and diffusivity of the particle, which are strongly correlated with size, geometry of the particle. Hence, the detailed understanding and controlling of the stress-strain state on the lithiation/delithiation processes can be the major question for the life-time and performances of the batteries.

As outlined above, the huge volume change during cycles of lithition and delithiation leads to massive cracking of the electrodes, and subsequent loss in capacity. The swelling generates stress, which can cause fracture even after a few cycles of charge and discharge [99]. In order to reduce the effect of the volume expansion, the different designs of Si anodes were proposed, such as thin films, nanoparticles, nanowires or nanotubes, and more complex structure designs. To study the size-dependent fracture of silicon electrodes during lithiation and delithiation cycles the silicon thin films are considered. In [81] the cracks patterns, which appears during the elecrochemical cycling of Si thin film anode, were studied. It was shown that the crack density increases with decreasing of silicon film thickness (Fig. 1.3). Moreover, in [81, 138] it was obtained that a critical thickness of the silicon film exists, below which a continuous film no longer cracks even under repeated cycling [81, 138]. These results show that through the film thickness pattering of silicon islands on a substrate it can be possible to control the electrode damage, therefore, the mechanical degradation and capacity loss. From the experimental observations it follows that the curvature-

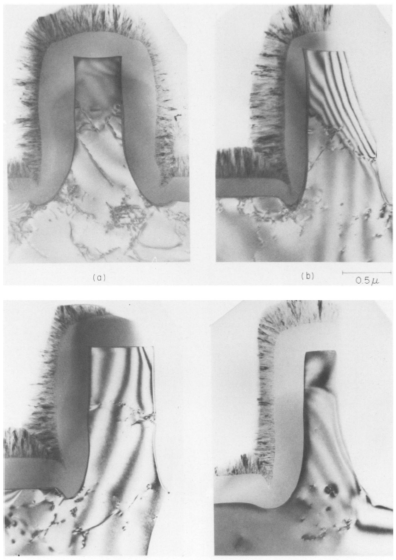

Figure 1.4: TEM images of cross section of silicon samples oxidized in wet O_2 at various temperatures [92].

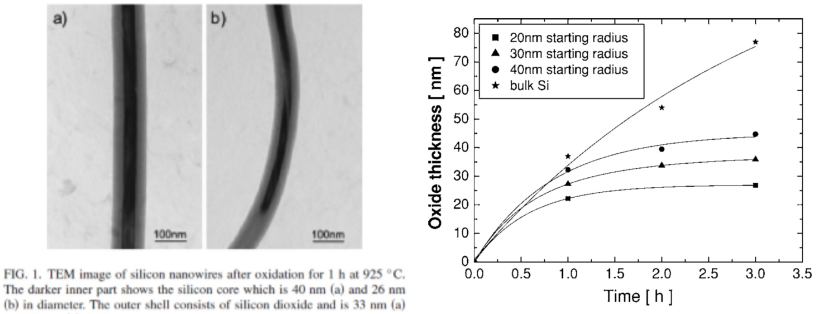

FIG. 1. TEM image of silicon nanowires after oxidation for 1 h at 925 °C. The darker inner part shows the silicon core which is 40 nm (a) and 26 nm (b) in diameter. The outer shell consists of silicon dioxide and is 33 nm (a) and 26 nm (b) thick.

(a) (b)

Figure 1.5: (a) TEM images of silicon nanowires after oxidation for 1h at 925°C; (b) dependency of the oxide thickness from the oxidation time for different nanowire starting radii [15].

induced average stress of the silicon film is always in compression during lithiation and in tension during delithiation [130].

Other examples of mechanochemistry problem are taken from microelectronics and MEMS. Silicon dioxide is used in microelectronics to isolate one device from another, to act as a structured mask against the insertion of the additive atoms as well as gate oxide in metal–oxide–silicon structures. The transformation of silicon substrates into SiO_2 is realized by the thermal oxidation, which is a complex process including the diffusion of the oxidants, chemical reaction and volume change due to the chemical transformation. The oxide is susceptible to viscoelastic deformation at the oxidation temperature [30, 31]. Due to the oxidation, the volume increases, which in turn causes large residual stresses, especially when oxide forms on the surface subjected to the large curvatures. The residual stresses affect the mechanical behaviour of the oxide, may modify the reaction rate, cause the plastic deformations, especially near corners and change the electrical characteristics. In [92] it was shown that the oxidation kinetics at the edges of monocrystalline silicon and the interface between oxide and polycrystalline silicon substrate after oxidation depend on the stresses in oxide (Fig. 1.4). The influence of external stresses was examined in [54, 69, 92, 95]. It was shown that external tensile stresses enhanced the oxidation rate, and compressive stresses retarded it [54]. The effect of external stress on oxidation of silicon wafers was studied in [153]. It was shown that the tensile stress strongly enhances the oxidation rate.

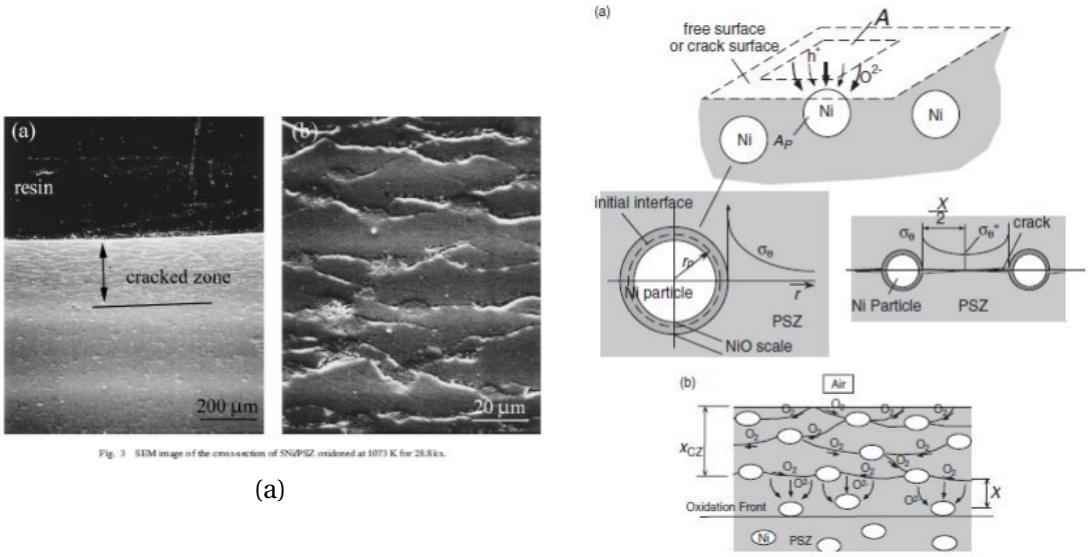

Figure 1.6: (a) SEM image of the cross-section of 5Ni/PSZ oxidized at 1073K; (b) schematic illustration of high temperature oxidation Ni/PSZ composite [102].

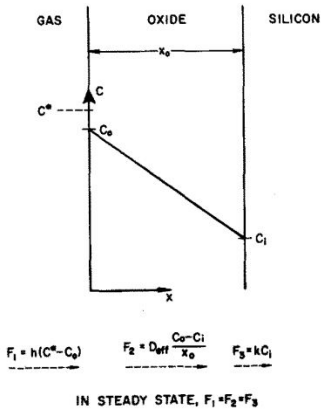

Figure 1.7: Deal-Grove model for the oxidation of silicon [26].

The retarded or self-limited oxidation in silicon nanostructures is a phenomena used in technology in order to manipulate the size, geometry, distribution, mechanical properties of structures [15, 76] (see Fig. 1.5). Another experimental tests were done in [95] for silicon strips in four-point bending in oxidizing environment. The results of this set of experiments indicated that applied compressive stress had a retarding effect upon the growth of the oxide layer, while the effect of tensile stress was ambiguous. In [92] the retarded oxide growth was observed at both convex and concave corners of trenches in polycrystalline silicon. Therefore, the kinetics of oxide film grown on non-planar substrates differs from oxide on planar substrates. The set of the cylindrical silicon oxidation was performed in [59, 60]. It was demonstrated that the oxidation of curved silicon surfaces is retarded at sharp curvatures, and that the retardation is more severe on concave than convex structures. From these facts it has been inferred that internal stresses generated during the oxidation process affect the oxidation.

The life-time of polysilicon parts in MEMS is determined by the oxidation processes interconnected with crack growth in polycrystalline silicon microscale parts. The 'reaction-layer fatigue' mechanism is only significant in thin films where the critical crack size for catastrophic failure can be reached by a crack growing within the oxide layer [58, 98, 99]. The silicon oxidation was also

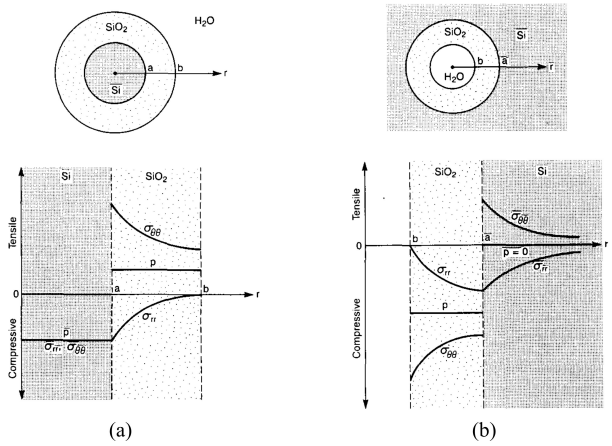

Figure 1.8: Stress components in (a) convex and (b) concave silicon structures during oxidation [61].

studied in the problem of the oxidation of inclusions of different types in ceramic composites for the high temperature applications [50, 56, 101, 102]. For example, in [56, 101, 102] the metallic inclusions in the ceramic composites being heated up and oxidized, expand and induce internal strain to the matrix, which affects the life-time of the composite (see Fig. 1.6).

All these examples show how geometry, dimensions, temperature, loading modify mechanochemistry phenomena.

Despite the experimental possibilities and a large number of works devoted to the mechanochemistry problems the key issues of describing the couplings between chemical reaction and stresses, which include the formulation of conditions on the moving front of chemical transformations in solids and the influence of internal and external stresses on the kinetics of the reaction, remain rather on the empirical lever than on the theoretical level.

Hence, silicon oxidation and silicon lithiation/delithiation need detailed modelling of the interconnection between chemical reaction and stress-strain state, the influence of the stresses induced by the chemical transformation and external one on the reaction kinetics, the effect of the size and geometry of the silicon construction on the reaction propagation. Silicon oxidation and silicon lithiation are sustained by the diffusion of the diffusive constituent (oxidant or Li, correspondingly, which is consumed at the reaction front) through the transformed material, and accompanying by the large transformation deformations, which in turn cause the internal stresses. These two reactions take place at the sharp interface – a reaction front that divides two solid constituents, and their reaction front kinetics is limited by the reaction rate and less by the diffusion of the movable constituent [57]. Such processes can be described using the two-phase reaction model, it is thus important to be able to handle it efficiently. The model however relies heavily on the rheological properties of the involved materials, which are in general to be defined.

One of the first and more significant models describing such reactions was suggested by Deal and Grove [26]. This model is one-dimensional, stress free and applied for films growth on plane substrates (see Fig. 1.7). This model gave a general scenario of the problem statement but did not consider stress effects (see also [41, 43] where this model is described in the context of introducing a chemical affinity tensor). However, chemical reactions can be accompanied by volumetric expansion that produces internal stresses, which in turn may affect the kinetics of the chemical reaction. In order to explain microscopic oxidation behavior a big amount of models have been developed by extending the Deal-Grove model to two-dimensional stress-dependant models. In these models the effect of stress on chemical reaction was associated with the stress-dependent oxidation parameters: surface reaction rate, oxidation diffusivity, and oxide viscosity [19, 61, 121]. Based on the notion of the activation volume, the stress characteristics (the first invariant, the normal stress, or the intensity of shear stresses) were chosen [61, 120, 137]. In these models, via the boundary condition in the diffusion problem, the reaction constants are determined by the

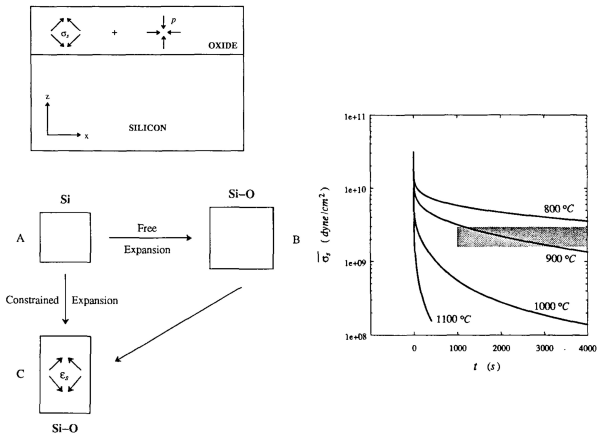

Figure 1.9: Scheme of volume expansion during silicon oxidation and average shear stress in the oxide [137].

consumption rate of the diffusive component at the reaction front. Simultaneously the model parameters (reaction constant and diffusion coefficient) depend on the stresses heuristically. The choice of the parameters was made intuitively based on the confirmation of the model results with experimental data.

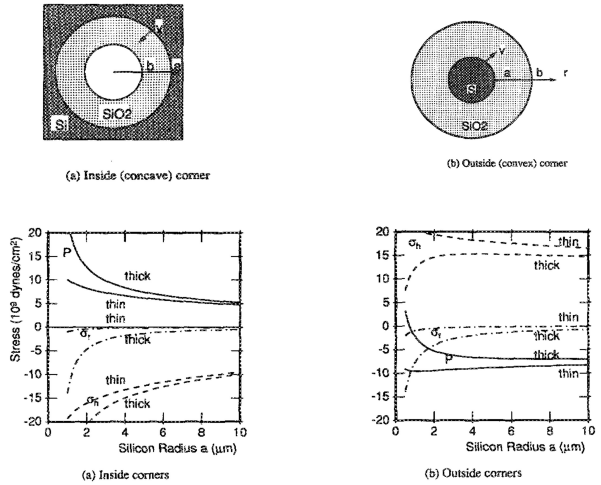

Figure 1.10: Stress at the silicon/oxide interface as a function of radius of curvature at 800°C [120].

The first models assumed that the oxidation parameters are affected mostly by hydrostatic and normal stresses at the reaction front (see i.e.[61]). Further, the models were established with shear stress-dependent viscosity [120, 137]. In [61], the oxidation of concave and convex cylindrical silicon studied (see Fig. 1.8). In this work the viscous stress associated with the nonuniform deformation of the oxide is identified as the fundamental force of retardation, and the oxide viscosity is chosen pressure-dependent. The extension of this work by the replacement of pressure-dependent oxide viscosity model with the shear-stress-dependent oxide viscosity model was done in [137] (the stress distribution for this model is shown in Fig. 1.9). In [120] it was mentioned that models in i.e.[59–61, 137] predict stresses much larger than that threshold at low temperature, it is reasonable to assume that plastic flow does indeed occur during. Like in many studies, the plastic flow were studied considering non-linear viscoelastic (Maxwell) model and critical stress depending on Eyring's viscosity model. Then, the stress distribution was obtained Fig. 1.10. However, the reaction kinetics was not studied in [120]. The problem of such viscosity-based approach not considering the yield stress is to minimize the effect of plastic strain and residual stresses.

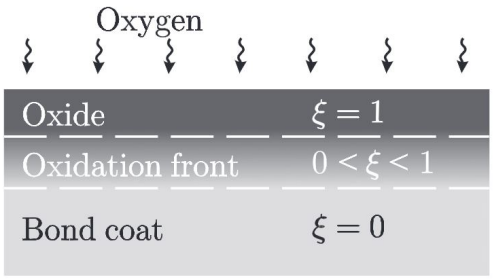

Figure 1.11: Schematic of the oxidation process. The scalar $\xi \in [0,1]$ denotes the volume fraction of oxide [90].

In another group of models, a concentration-dependent volumetric expansion was introduced, which led to the total stress-diffusion coupling, e.g. [121, 122]. In [157], the reaction is considered pressure-dependent, and the reaction-controlled diffusion model for the lithiation process of a spherical Si particle and numerical solution was obtained.

Other alternatives to take into account the influence of stresses on the diffusion and the reaction are to introduce additional terms in the expression of the diffusion flux, e.g. [71, 72, 141], or to consider the influence through a scalar chemical potential, which depends on the concentration and the stresses, and gradient of which governs the flux of the reactant, e.g. [3, 9–14, 21, 23, 28, 80, 80, 81, 89, 90, 103, 109]. In [71] the diffusion model for a medium with a nonuniform internal structure is developed. The kinetic model proposed in [13] couples both mechanical and chemical driving forces affects the rates of inelastic deviatoric strains and concentration. This model was applied to analyze the mechanochemical yield condition, flow rule and ratcheting by generalizing von Mises theory of plastic potential. In [89] the chemo-thermo-mechanically coupled theory that accounts for elastic-viscoplastic deformation is formulated. Stress-diffusion model in which the isotropic volumetric expansion depends linearly on the concentration of Li, while the diffusion is driven by the spatial gradient of the chemical potential, is proposed in [23]. In this model the chemical potential is considered as the function of the concentration and the pressure. Another stress-diffusion model with stress-dependent chemical potential is developed for the case of the lithiation of spherical silicon particle [21]. This model was extended in [22] to the problem with a chemical reaction as a kinetics governing process.

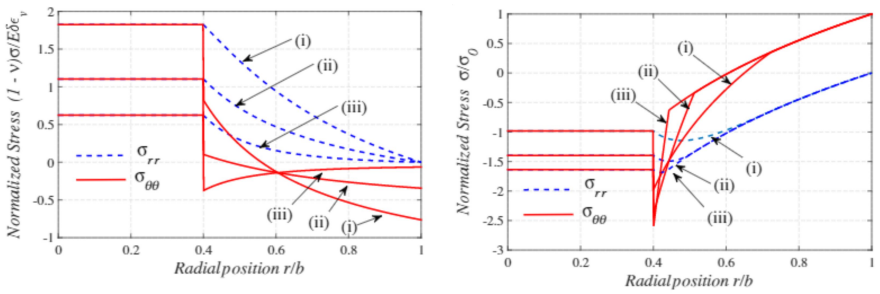

Figure 1.12: (a) The influence of Li insertion rate and elasticity on stress distributions in an electrode particle. (b) Stress distributions for particles that exceed yield only at the phase boundary [10].

In order to describe the additional physical effects, such as failure of silicon particles during the silicon lithiation, the coupled stress-diffusion-reaction models were also developed. The approach of [157] was extended in [156], and the effective damage field was introduced. The studies of crack growth during lithiation process were made using a coupled stress-diffusion model in [67, 68].

The phase field method is widely used for such problems. In [89, 90] the model with a region of oxidation front instead of the sharp interface was proposed and approved numerically for the alu-

minium oxidation of flat plates. In this approach the region of the reaction front is described as a mixture of the oxide with the based material (see Fig. 1.11). In this approach the term proportional to the concentration gradient is included in the free energy.

As it was mentioned before, the chemical reaction is accompanied by plastic deformations and viscous strains as well: the chemical transformation induces the volumetric expansion, which in turn causes the internal stresses. The internal stresses produce plastic deformations and affect the reaction kinetics. Moreover, the chemical transformation generates the growth stresses in the transformed material and accompanying stress relaxation. Therefore, from the mechanical perspective, there has been an extensive research focus on modelling of stresses produced by the chemical transformation and the impact of the inelastic strains on the propagation of the chemical reaction, e.g. [14, 29, 89, 90, 120, 137]. But the influence of stresses on the lithiation kinetics still remains unclear and must be captured to model the reaction propagation accurately. The plastic deformations were numerically studied e.g. in [3, 14, 28, 90, 103, 109]. For the extended Deal-Grove model the plastic model as the viscosity dependent on the maximum resolved shear stress was proposed in [76, 120]. The viscous deformations due to the chemical reaction were included in the models in e.g. [3, 61, 89, 90, 103, 107, 137]. The disadvantages of such governing equations that they can be solved only numerically [3, 13, 14, 71, 109, 156], what makes difficult to isolate the effects of different parameters and inelastic strains on the reaction. Some analytical solution for stresses for elastic-plastic spherical electrode particle is obtained in [10] (Fig. 1.12) and for viscoelastic stresses in oxide film in [53].

Stresses may affect the front propagation via the direct influence on the reaction rate (see, e.g., [22]). This corresponds to the case of reaction rate-controlled reactions for which the reaction front propagation is controlled rather by the reaction rate than by the diffusion, and lithiation is an example of such a reaction (see, e.g., [57, 159]). Note, that the diffusion is also affected by stresses in this case but not via the constitutive equation of the diffusion but via the boundary conditions at the reaction front. In this work we focus on such type of the models.

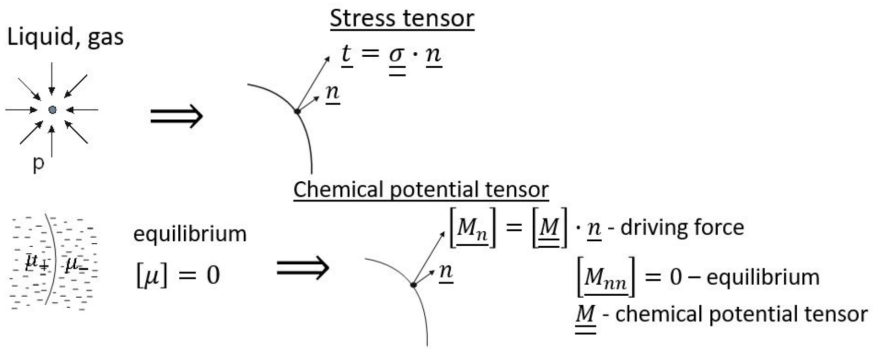

Figure 1.13: About tensorial nature of chemical potential.

An approach to describe stresses effects based on the ideas of classical physical chemistry, according to which the reaction rate is determined by the chemical affinity is used in this work. The notion of the chemical affinity was introduced by Gibbs [47] and de Donder [25] and laid the foundation of thermodynamical theory of phase transformations and chemical reactions [119]. The chemical affinity as a thermodynamic force is a factor outside the reaction rate. Then, a kinetic equation was formulated that determined the reaction rate as a function of the chemical affinity. An additional constitutive equation is obtained as dependence between the reaction rate and the affinity. In the case of gaseous or liquid constituents chemical potentials and affinity are scalar. In the case of solid constituents the tensorial nature of the chemical affinity follows from the consideration of a chemical reaction on the oriented area element of the reaction front (see a more detailed discussion in [43]), as well as the tensorial nature of the chemical potential followed from the fact that a phase equilibrium took place not just in a point but at oriented area elements of

the phase interface passing trough the point Fig. 1.13 (see, e.g. [2, 48]). The tensorial nature of the chemical affinity was also pointed out in [125, 126]. In a quasi-static case, the chemical affinity tensor is represented by the linear combination of the chemical potential tensors, which are the Eshelby stress tensors divided by the reference mass densities. This combination is the same as the combination of scalar chemical potentials which defines the classical chemical affinity.

Modeling of the reaction front kinetics is based on the chemical affinity tensor derived from fundamental balance laws and the entropy inequality written down for an open system with a chemical reaction between diffusing and solid constituents of arbitrary rheology in the case of finite strains (see [38, 40, 44] and a review [43]). It was shown that the normal component of this tensor acts as a configurational force conjugated to the reaction rate in the expression of the energy dissipation due to the front propagation, and a kinetic equation in the form of the dependence of the reaction front velocity on the normal component of the affinity tensor was formulated.

The approach based on the chemical affinity tensor has been applied to the statement and solution of a number of boundary value problems with propagating reaction fronts in formulations which assumed solid constituents to be linear elastic [41, 42, 44, 143]. Then the theory has been used to describe numerically two-phase lithiation of Si particles used in Li-ion batteries, where the constituent materials undergoing finite elasto-viscoplastic deformations were considered [116, 117].

Following this framework, in the present work new problems related to the description of chemical reactions between solid and diffusing components will be solved. It will be explored how the stress-strain state and the geometry of the body affect the kinetics of the chemical reactions. We will extend the previously developed models to describe the propagation of the front of chemical reactions between deformable solids and gaseous components under conditions of thermomechanical effects for reactions of inelastic (viscous, plastic) bodies. The concept of the chemical affinity tensor will be applied for the first time to the chemical reactions in inelastic solids and a theoretical basis for predicting the distribution of the chemical reaction front in elastic and inelastic materials under different conditions of mechanical loading will be developed. For the case of an inelastic component the chemical reaction will be received and investigated by analytical solutions of the simplest boundary value problems describing the propagation of plane, cylindrical, and spherical fronts of reaction. The relationships of chemical reactions and processes of stress relaxation and plastic deformations will be investigated, induced by the large deformations due to chemical transformations. The effects of acceleration will be studied, as well as the slowing down and blocking of the reaction by mechanical loading and parameters.

The stresses and deformations, induced by chemical transformations, will be determined. Their impact on the deformation and strength properties of the materials will be predicted. Resulting from the chemical affinity tensor a kinetic equation will be formulated, which determines the dependence of the rate of a chemical reaction front propagation in visco-elastic and elastic-plastic bodies from the stress-strain state. The impact of parameters on the kinetics of the chemical reaction and on the mechanical properties of the components of the reaction will be studied. The analytical solutions will be obtained in order to be used to numerical procedures in future.

High-temperature oxidation experiments for pure nickel wires and balls are conducted in order to validate the model assumption, to precise the limits of the presented models and to compare the experimental data with different proposed models.

1.2 General framework

The objective of this section is to give the general framework for the modeling of thermo-chemo-mechanical couplings and to establish the jump conditions imposed on the discontinuity surface due to the chemical transformation.

The main difficulties of such framework are:

– to write the mass balance, as we have the diffusion of the material from 'outside' of the body. Therefore, the system is 'open'. The similar problem you can find for combustion reaction prob-

lems. Despite the diffusion flux, locally, at the reaction interface, there is a mass conservation.

– to choose the relevant state variables and derive the state equations;

– to express the dissipation and Clausius-Duhem inequality, taking into account the impact of chemical reaction, diffusion flux and heat flux.

1.2.1 Balances laws with discontinuity surface. Chemo-mechanical couplings

We consider a deformable body of a material B_- occupying a domain Ω_-. The guest atoms of diffusive material B_* come to the surface of the solid, start to react with it and transform into a new transformed material B_+ occupying a domain Ω_+. The chemical reaction between solid and diffusing constituents of the following type is written as:

$$n_- B_- + n_* B_* \longrightarrow n_+ B_+$$

where B_-, B_* and B_+ are the chemical formulae of an initial solid constituent, a diffusing constituent and a transformed solid constituent, respectively, n_-, n_* and n_+ are the stoichiometric coefficients. Further sub- and superscripts refer values to materials B_-, B_* and B_+.

The reaction is localized at the reaction front Γ that divides the solid constituents B_- and B_+, and it is sustained by the diffusion of B_* through the transformed material B_+ (Fig. 1.14). The reaction front Γ moves due to the consumption of the diffusive reactant B_*, which diffuses through the transformed material B_+ from the outer surface of Ω_+ to the reaction front Γ. For simplicity we assume that the host atoms do not diffuse, but may to re-arrange to accommodate the guest atoms. This problem comes from the classical problems of moving discontinuity surface [118, 128] by adding a two-phase state and a chemical reaction as the governing equation for the velocity of the interface.

Recall. Derivative of a volume integral in the case of a body with moving discontinuity surface. Consider the quantity $\mathscr{J}(\Omega,t)=\int_\Omega b(\boldsymbol{x},t)d\Omega$ *which is the integral of the volume density* $b(\boldsymbol{x},t)$ *over the actual configuration* Ω. Γ *is a discontinuity surface in* Ω*; each point of* Γ *is moving with a velocity* $\boldsymbol{V}$. $\boldsymbol{x}$ *is the position vector in the current configuration,* $\boldsymbol{v}$ *the current velocity.*

$$\frac{d\mathscr{J}}{dt}=\int_\Omega \frac{\partial b}{\partial t}d\Omega+\int_{\partial\Omega}(b\otimes\boldsymbol{v})\cdot\boldsymbol{n}da+\int_\Gamma [\![b]\!]\boldsymbol{V}\cdot\boldsymbol{n}d\Gamma=\int_\Omega(\frac{\partial b}{\partial t}+\mathrm{div}(b\otimes\boldsymbol{v}))d\Omega-\int_\Gamma [\![b\otimes(\boldsymbol{v}-\boldsymbol{V})]\!]\cdot\boldsymbol{n}d\Gamma$$

where $\mathbf{n}$ *is the normal vector of* Γ *oriented toward* $'+'$. *Only in this section,* $[\![a]\!]=a_- - a_+$*; while in the following parts,* $[\![a]\!]=a_+ - a_-$*;* $(b\otimes\mathbf{v})$ *is the tensor product of* b *and* $\mathbf{v}$. *Recall that, if* b *is a scalar,* $(b\otimes\mathbf{v})$ *is just the product* $b\mathbf{v}$.

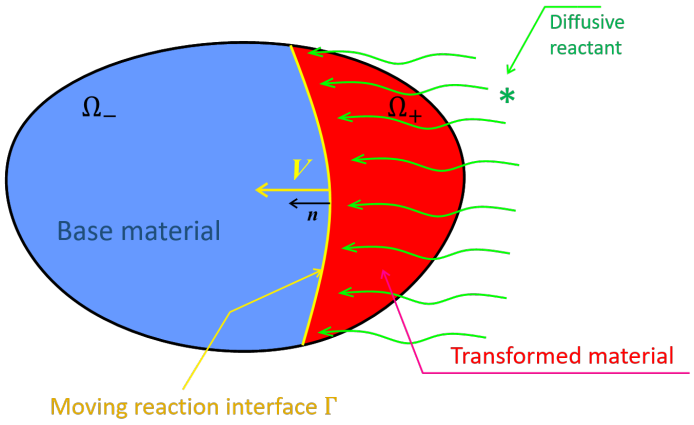

Figure 1.14: Chemical reaction between solid and diffusive constituents.

If Ω is a control volume whose boundary moves with a velocity $\boldsymbol{U}$, the balance equation relative to a continuous quantity b, which internal rate production R_i and surface rate production $\boldsymbol{R_s}\cdot\boldsymbol{n}$, is written as:

$$\frac{d\mathscr{J}}{dt} = \int_\Omega \mathrm{R}_i\, d\Omega + \int_{\partial\Omega} \boldsymbol{R_s}\cdot\boldsymbol{n}\, da$$

with

$$\begin{aligned}\frac{d\mathscr{J}}{dt} &= \int_\Omega \left(\frac{db}{dt} + b\,\mathrm{div}(\boldsymbol{U})\right) d\Omega + \int_{\partial\Omega} (b\otimes(\boldsymbol{v}-\boldsymbol{U}))\cdot\boldsymbol{n}\, da \\ &= \int_\Omega \left(\frac{db}{dt} + b\,\mathrm{div}(\boldsymbol{U}) + \mathrm{div}(b\otimes(\boldsymbol{v}-\boldsymbol{U}))\right) d\Omega\end{aligned}$$

In the case of the presence of the discontinuity surface Γ is in Ω, the previous balance in written for the two domains Ω_- and Ω_+ and then added to obtain:

$$\begin{aligned}\frac{d\mathscr{J}}{dt} &= \int_\Omega \left(\frac{db}{dt} + b\,\mathrm{div}(\boldsymbol{U})\right) d\Omega + \int_{\partial\Omega} (b\otimes(\boldsymbol{v}-\boldsymbol{U}))\cdot\boldsymbol{n}\, da + \int_\Gamma [\![b(\boldsymbol{v}-\boldsymbol{V})]\!]\cdot\boldsymbol{n}\, d\Gamma \\ &= \int_\Omega \left(\frac{db}{dt} + b\,\mathrm{div}(\boldsymbol{U}) + \mathrm{div}(b\otimes(\boldsymbol{v}-\boldsymbol{U}))\right) d\Omega + \int_\Gamma [\![b(\boldsymbol{U}-\boldsymbol{V})]\!]\cdot\boldsymbol{n}\, d\Gamma\end{aligned}$$

The local equation derived for any point in Ω, is:

$$\frac{db}{dt} + b\,\mathrm{div}(\boldsymbol{U}) + \mathrm{div}(b\otimes(\boldsymbol{v}-\boldsymbol{U}) = \mathrm{R}_i + \mathrm{div}\boldsymbol{R_s}$$

For any point of the interface Γ,

$$[\![b\otimes(\boldsymbol{U}-\boldsymbol{V})]\!]\cdot\boldsymbol{n} = 0$$

The situation considered in this thesis is illustrated in figure 1.14. We denote b^s the property b associated with the materials $'+'$ (namely b^+) or $'-'$ (b^-), and b^* the one associated with the material $'*'$. The substance $'*'$ is assumed to occupied the same domain as $'+'$, so that all the densities considered are relative densities (densities weighted by the phase proportions which are assumed fixed).

$$\begin{aligned}\frac{d}{dt}\int_\Omega b(\boldsymbol{x},t)\,d\Omega &= \frac{d}{dt}\int_\Omega b^s(\boldsymbol{x},t)\,d\Omega + \frac{d}{dt}\int_\Omega b^*(\boldsymbol{x},t)\,d\Omega \\ &= \int_\Omega \left(\frac{db^s}{dt} + b^s\,\mathrm{div}(\boldsymbol{v})\right) d\Omega + \int_\Gamma [\![b^s(\boldsymbol{v}-\boldsymbol{V})]\!]\cdot\boldsymbol{n}\, d\Gamma + \\ &\quad \int_{\Omega_+} \left(\frac{db^*}{dt} + b\,\mathrm{div}(\boldsymbol{v}) + \mathrm{div}(b\otimes(\boldsymbol{v}^*-\boldsymbol{v}))\right) d\Omega + \int_\Gamma b^*(\boldsymbol{v}-\boldsymbol{V})\cdot\boldsymbol{n}\, d\Gamma\end{aligned}$$

Balance of mass

In order to write the mass balance, we consider the following contributions for the mass change:

– diffusion flux of the guest diffusive material '*' through the layer of the transformed material and its leak at the reaction front;

– consumption of the base material '-' at Γ;

– production of the new transformed material at the reaction front.

Therefore, the global form of the mass balance of the open "deformable body-diffusive component" system at the time t is calculated for $b = \rho$ is obtained as follows:

$$\begin{aligned}&\int_{\Omega_+}\left(\frac{\partial\rho^+}{\partial t} + \frac{\partial\rho^*}{\partial t}\right) d\Omega + \int_{\Omega_-}\left(\frac{\partial\rho^-}{\partial t}\right) d\Omega + \int_{\partial\Omega_+\setminus\Gamma}\rho^+\mathbf{v}^+\cdot\mathbf{n}\, da + \int_{\partial\Omega_-\setminus\Gamma}\rho^-\mathbf{v}^-\cdot\mathbf{n}\, da + \\ &\qquad + \int_{\partial\Omega_+\setminus\Gamma}\rho^*\left(\mathbf{v}^*-\mathbf{v}^+\right)\cdot\mathbf{n}\, da - \int_\Gamma \left([\![\rho]\!]-\rho^*\right)\mathbf{V}\cdot\mathbf{n}\, da = 0 \qquad (1.1)\end{aligned}$$

where ρ^+ and ρ^- are the densities of the materials B_+ and B_-, respectively, ρ^* is the density of the diffusing constituent; $\mathbf{v}^+$ and $\mathbf{v}^-$ are the velocities of points of the transformed and initial

materials, $\mathbf{v}^*$ is the velocities of the diffusive reactant's particles, then the relative velocity $(\mathbf{v}^* - \mathbf{v}^+)$ is the diffusion rate of diffusive constituent, $\mathbf{V}$ is the front velocity. In local form the mass balance can be written as:

$$\text{initial material, in } \Omega_- : \quad \dot{\rho}^- + \rho^- \operatorname{div}(\mathbf{v}^-) = 0 \tag{1.2}$$

$$\text{transformed material, in } \Omega_+ : \quad \dot{\rho}^+ + \rho^+ \operatorname{div}\left(\mathbf{v}^+\right) = 0 \tag{1.3}$$

$$\text{diffusive component, in } \Omega_+ : \quad \dot{\rho}^* + \rho^* \operatorname{div}\left(\mathbf{v}^* - \mathbf{v}^+\right) = 0 \tag{1.4}$$

$$\text{reaction front } \Gamma : \quad [\![\rho(\mathbf{v} - \mathbf{V})]\!] \cdot \mathbf{n} = \rho^* \left(\left(\mathbf{v}^* - \mathbf{v}^+\right) - \mathbf{V}\right) \cdot \mathbf{n} \tag{1.5}$$

Let's make the following notation

$$\rho(\mathbf{v} - \mathbf{V}) \cdot \mathbf{n} = -m_f \tag{1.6}$$

Then our formulae (1.5) of the mass balance at the reaction front takes the following form:

$$[\![m_f]\!] = -\rho^* \left(\left(\mathbf{v}^* - \mathbf{v}^+\right) - \mathbf{V}\right) \cdot \mathbf{n} \tag{1.7}$$

Balance of momentum

The friction between the guest diffusive component and the solid constituent and volumetric forces are neglected for simplicity. Hence, the different contributions in the linear momentum balance are:

– supply of the momentum by the diffusive '*' constituent;

– forces acting on the outer surface $\partial\Omega$;

– external pressure p_* acting on the diffusive component.

Therefore, the global form of balance of momentum (it is calculated for $b = \rho\mathbf{v}$) can be written as:

$$\begin{aligned}
&\int_{\Omega_+} \frac{\partial}{\partial t}\left(\rho^+\mathbf{v}^+ + \rho^*\mathbf{v}^*\right) d\Omega + \int_{\Omega_-} \frac{\partial}{\partial t}\left(\rho^-\mathbf{v}^-\right) d\Omega + \int_{\partial\Omega_+\setminus\Gamma} \left(\rho^+\mathbf{v}^+ \otimes \mathbf{v}^+\right) \cdot \mathbf{n} da + \\
&+ \int_{\partial\Omega_-\setminus\Gamma} \left(\rho^-\mathbf{v}^- \otimes \mathbf{v}^-\right) \cdot \mathbf{n} da + \int_{\partial\Omega_+\setminus\Gamma} \left(\rho^*\mathbf{v}^* \otimes \left(\mathbf{v}^* - \mathbf{v}^+\right)\right) \cdot \mathbf{n} da - \int_{\partial\Omega_+\setminus\Gamma} \mathbf{S}^+ \cdot \mathbf{n} da - \\
&- \int_{\partial\Omega_-\setminus\Gamma} \mathbf{S}^- \cdot \mathbf{n} da - \int_{\partial\Omega_+\setminus\Gamma} \mathbf{S}^* \cdot \mathbf{n} da - \int_\Gamma \left([\![\rho\mathbf{v}]\!] - \rho^*\mathbf{v}^*\right) \mathbf{V} \cdot \mathbf{n} da = 0
\end{aligned} \tag{1.8}$$

where $\mathbf{S}^\pm = (\det\mathbf{F}_\pm)\,\sigma_\pm \cdot \mathbf{F}_\pm^{-\mathrm{T}}$ and $\mathbf{S}^* = -p_*\,(\det\mathbf{F}_+)\,\mathbf{F}_+^{-\mathrm{T}}$ are the Piola-Kirchhoff stress tensors; $\mathbf{F}_\pm = \nabla\mathbf{x}_\pm^{\mathrm{T}}$ are the strain gradients and $\sigma_\pm$ are the Cauchy stress tensors.

Then using (1.2) and (1.3), in the local form the balance of momentum can be written as follows:

$$\text{initial material, in } \Omega_- : \quad \rho^-\dot{\mathbf{v}}^- - \operatorname{div}(\mathbf{S}^-) = 0 \tag{1.9}$$

$$\text{transformed material, in } \Omega_+ : \quad \rho^+\dot{\mathbf{v}}^+ - \operatorname{div}\left(\mathbf{S}^+\right) = 0 \tag{1.10}$$

$$\text{diffusive component, in } \Omega_+ : \quad \rho^*\dot{\mathbf{v}}^* - \operatorname{div}\left(\mathbf{S}^*\right) = 0 \tag{1.11}$$

$$\text{reaction front } \Gamma : \quad [\![\mathbf{S} - \mathbf{S}^*]\!] \cdot \mathbf{n} = -[\![\rho\mathbf{v}]\!]\mathbf{V} \cdot \mathbf{n} - \rho^*\mathbf{v}^* \left(\left(\mathbf{v}^* - \mathbf{v}^+\right) - \mathbf{V}\right) \cdot \mathbf{n} \tag{1.12}$$

Using the formulae (1.6), rewrite the balance of momentum (1.12) at the reaction front:

$$[\![\mathbf{S} - \mathbf{S}^*]\!] \cdot \mathbf{n} = -[\![m_f\left(\mathbf{v} - \mathbf{v}^*\right)]\!] \tag{1.13}$$

Introducing $\mathbf{T} = \mathbf{S} \cdot \mathbf{n}$, we obtain

$$[\![\mathbf{T} - \mathbf{T}^*]\!] = -[\![m_f\left(\mathbf{v} - \mathbf{v}^*\right)]\!]$$

Balance of energy

For the variations in the balance of energy there are following sources:

– variations of the kinetic and internal energies of the solid and diffusive constituents;

– power of the external forces acting on the outer surface and deforming the solid;

– power of the external pressure acting on the diffusive component;

– power of the thermal energy supply (taking into account the energy supply due to the chemical transformation as well).

Hence, the balance of energy in the global form (calculated for $b = \rho\left(u + \frac{1}{2}v^2\right)$) is written as:

$$\begin{aligned}
&\int_{\Omega_+} \frac{\partial}{\partial t}\left(\rho^+\left(u^+ + \frac{1}{2}v^{+2}\right) + \rho^*\left(u^* + \frac{1}{2}v^{*2}\right)\right)d\Omega + \int_{\Omega_-} \frac{\partial}{\partial t}\left(\rho^-\left(u^- + \frac{1}{2}v^{-2}\right)\right)d\Omega + \\
&+ \int_{\partial\Omega_+\setminus\Gamma}\left(\rho^+\left(u^+ + \frac{1}{2}v^{+2}\right)\mathbf{v}^+\right)\cdot\mathbf{n}da + \int_{\partial\Omega_-\setminus\Gamma}\left(\rho^-\left(u^- + \frac{1}{2}v^{-2}\right)\mathbf{v}^-\right)\cdot\mathbf{n}da + \\
&+ \int_{\partial\Omega_+\setminus\Gamma}\left(\rho^*\left(u^* + \frac{1}{2}v^{*2}\right)\left(\mathbf{v}^* - \mathbf{v}^+\right)\right)\cdot\mathbf{n}da - \int_\Gamma\left(\left[\!\left[\rho\left(u + \frac{1}{2}v^2\right)\right]\!\right] - \rho^*\left(u^* + \frac{1}{2}v^{*2}\right)\right)\mathbf{V}\cdot\mathbf{n}da = \\
&= \int_{\partial\Omega_+\setminus\Gamma}\left(\mathbf{v}^+\cdot\mathbf{S}^+\cdot\mathbf{n} + \mathbf{v}^*\cdot\mathbf{S}^*\cdot\mathbf{n}\right)da + \int_{\partial\Omega_-\setminus\Gamma}\mathbf{v}^-\cdot\mathbf{S}^-\cdot\mathbf{n}da + \int_{\Omega_+}\left(\rho^+\mathbf{r}^+ + \rho^*\mathbf{r}^*\right)d\Omega + \int_{\Omega_-}\rho^-\mathbf{r}^-d\Omega + \\
&+ \int_\Gamma q_\Gamma da - \int_{\partial\Omega_+\setminus\Gamma}\mathbf{h}^+\cdot\mathbf{n}da - \int_{\partial\Omega_-\setminus\Gamma}\mathbf{h}^-\cdot\mathbf{n}da
\end{aligned} \tag{1.14}$$

where $u^\pm$ and u^* are the mass densities of the internal energy of solid and gaseous components, correspondingly; $v^2 = \mathbf{v}\cdot\mathbf{v}$; $\mathbf{h}^\pm$ are the heat flux vectors; $\mathbf{r}^\pm$ and $\mathbf{r}^*$ are the mass densities of the bulk energy supply, and q_Γ is the surface density of the energy supply due to the chemical reaction at the reaction front Γ (this is the thermal effect of the reaction).

Therefore, using (1.3) and (1.4), the energy balance in the local form can be obtained as:

$$\text{initial material, in } \Omega_-: \quad \rho^-\left(\dot{u}^- + \mathbf{v}^-\cdot\dot{\mathbf{v}}^-\right) = \operatorname{div}\left(\mathbf{v}^-\cdot\mathbf{S}^-\right) + \rho^-\mathbf{r}^- - \operatorname{div}\left(\mathbf{h}^-\right) \tag{1.15}$$

$$\text{transformed material, in } \Omega_+: \quad \rho^+\left(\dot{u}^+ + \mathbf{v}^+\cdot\dot{\mathbf{v}}^+\right) = \operatorname{div}\left(\mathbf{v}^+\cdot\mathbf{S}^+\right) + \rho^+\mathbf{r}^+ - \operatorname{div}\left(\mathbf{h}^+\right) \tag{1.16}$$

$$\text{diffusive component, in } \Omega_+ \quad \rho^*\left(\dot{u}^* + \mathbf{v}^*\cdot\dot{\mathbf{v}}^*\right) = \operatorname{div}\left(\mathbf{v}^*\cdot\mathbf{S}^*\right) + \rho^*\mathbf{r}^* \tag{1.17}$$

$$\begin{aligned}
\text{reaction front } \Gamma: \quad &\left[\!\left[\rho\left(u + \frac{1}{2}v^2\right)(\mathbf{v} - \mathbf{V})\right]\!\right]\cdot\mathbf{n} - \rho^*\left(u^* + \frac{1}{2}v^{*2}\right)\left(\left(\mathbf{v}^* - \mathbf{v}^+\right) - \mathbf{V}\right)\cdot\mathbf{n} = \\
&= \left([\![\mathbf{v}\cdot\mathbf{S}]\!] - \mathbf{v}^*\cdot\mathbf{S}^*\right)\cdot\mathbf{n} + q_\Gamma - [\![\mathbf{h}]\!]\cdot\mathbf{n}
\end{aligned} \tag{1.18}$$

Using Eq.(1.6) and (1.7), the balance of energy at the reaction front (1.18) can be rewritten as follows:

$$-\left[\!\left[m_f\left(\left(u - u^*\right) + \frac{1}{2}\left(v^2 - v^{*2}\right)\right)\right]\!\right] = [\![\mathbf{v}\cdot\mathbf{S} - \mathbf{v}^*\cdot\mathbf{S}^*]\!]\cdot\mathbf{n} + q_\Gamma - [\![\mathbf{h}\cdot\mathbf{n}]\!] \tag{1.19}$$

Entropy balance

We introduce entropy as:

$$\mathrm{S} = \int_{\Omega_+}\left(\rho^+ s^+ + \rho^* s^*\right)d\Omega + \int_{\Omega_-}\rho^- s^- d\Omega$$

where $s^\pm$ and s^* are the mass densities of the entropy of the solid and diffusive components.

The rate of change of entropy:

$$\Psi\left[\mathrm{S}\right] = -\int_{\partial\Omega_-\setminus\Gamma}\frac{\mathbf{h}^-}{\mathrm{T}}\cdot\mathbf{n}da - \int_{\partial\Omega_+\setminus\Gamma}\frac{\mathbf{h}^+}{\mathrm{T}}\cdot\mathbf{n}da + \int_\Gamma\alpha\frac{q_\Gamma}{\mathrm{T}}da + \int_{\Omega_+}\frac{\rho^+\mathbf{r}^+ + \rho^*\mathbf{r}^*}{\mathrm{T}}d\Omega + \int_{\Omega_-}\frac{\rho^-\mathbf{r}^-}{\mathrm{T}}d\Omega$$

where T is the temperature, $0 < \alpha \leq 1$ is the coefficient determining the part of the reaction thermal effect which is transformed into the entropy flow, and $\alpha \neq 1$ means that, on the reaction front, there is an additional source of entropy related to the reaction thermal effect.

The global form for the entropy balance (calculated for $b = \rho s$) takes the following form:

$$\int_{\Omega_+} \frac{\partial}{\partial t}\left(\rho^+ s^+ + \rho^* s^*\right) d\Omega + \int_{\Omega_-} \frac{\partial}{\partial t}\left(\rho^- s^-\right) d\Omega + \int_{\partial\Omega_+\setminus\Gamma} \rho^+ s^+ \mathbf{v}^+ \cdot \mathbf{n} da + \int_{\partial\Omega_-\setminus\Gamma} \rho^- s^- \mathbf{v}^- \cdot \mathbf{n} da +$$
$$+ \int_{\partial\Omega_+\setminus\Gamma} \rho^* s^* \left(\mathbf{v}^* - \mathbf{v}^+\right) \cdot \mathbf{n} da - \int_\Gamma \left([\![\rho s]\!] - \rho^* s^*\right) \mathbf{V} \cdot \mathbf{n} da - \left(- \int_{\partial\Omega_-\setminus\Gamma} \frac{\mathbf{h}^-}{\mathrm{T}} \cdot \mathbf{n} da - \int_{\partial\Omega_+\setminus\Gamma} \frac{\mathbf{h}^+}{\mathrm{T}} \cdot \mathbf{n} da + \right.$$
$$\left. + \int_\Gamma \alpha \frac{q_\Gamma}{\mathrm{T}} da + \int_{\Omega_+} \frac{\rho^+ \mathbf{r}^+ + \rho^* \mathbf{r}^*}{\mathrm{T}} d\Omega + \int_{\Omega_-} \frac{\rho^- \mathbf{r}^-}{\mathrm{T}} d\Omega \right) \geq 0 \tag{1.20}$$

Then, taking into account (1.2), (1.3), (1.4), (1.6) and (1.7) in the local for the balance of entropy can be written as:

$$\text{initial material, in } \Omega_- : \quad \rho^- \dot{s}^- + \operatorname{div}\left(\frac{\mathbf{h}^-}{\mathrm{T}}\right) - \frac{\rho^- \mathbf{r}^-}{\mathrm{T}} \geq 0 \tag{1.21}$$

$$\text{transformed material, in } \Omega_+ : \quad \rho^+ \dot{s}^+ + \operatorname{div}\left(\frac{\mathbf{h}^+}{\mathrm{T}}\right) - \frac{\rho^+ \mathbf{r}^+}{\mathrm{T}} \geq 0 \tag{1.22}$$

$$\text{diffusive component, in } \Omega_+ \quad \rho^* \dot{s}^* - \frac{\rho^* \mathbf{r}^*}{\mathrm{T}} \geq 0 \tag{1.23}$$

$$\text{reaction front } \Gamma : - [\![m_f \left(s - s^*\right)]\!] + \frac{[\![\mathbf{h}]\!]}{\mathrm{T}} \cdot \mathbf{n} - \alpha \frac{q_\Gamma}{\mathrm{T}} \geq 0 \tag{1.24}$$

Dissipation

To obtain the dissipation equation we have to combine two equations of the first and second principle of thermodynamics.

For the transformed material we substitute the energy balance (1.16) in entropy inequality (1.22)

$$\rho^+ \dot{s}^+ \geq \frac{1}{\mathrm{T}}\left(\rho^+ \left(\dot{u}^+ + \mathbf{v}^+ \cdot \dot{\mathbf{v}}^+\right) - \operatorname{div}\left(\mathbf{v}^+ \cdot \mathbf{S}^+\right)\right) - \frac{1}{\mathrm{T}^2} \mathbf{h}^+ \cdot \nabla \mathrm{T}$$

Analogically for the initial material after substitution (1.15) in (1.21) we obtain:

$$\rho^- \dot{s}^- \geq \frac{1}{\mathrm{T}}\left(\rho^- \left(\dot{u}^- + \mathbf{v}^- \cdot \dot{\mathbf{v}}^-\right) - \operatorname{div}\left(\mathbf{v}^- \cdot \mathbf{S}^-\right)\right) - \frac{1}{\mathrm{T}^2} \mathbf{h}^- \cdot \nabla \mathrm{T}$$

For gaseous component we are doing the same procedure, substitute (1.17) into (1.23):

$$\rho^* \dot{s}^* \geq \frac{1}{\mathrm{T}}\left(\rho^* \left(\dot{u}^* + \mathbf{v}^* \cdot \dot{\mathbf{v}}^*\right) - \operatorname{div}\left(\mathbf{v}^* \cdot \mathbf{S}^*\right)\right)$$

And at the reaction front Γ we substitute (1.19) into (1.24):

$$- [\![m_f \left(s - s^*\right)]\!] + \frac{1}{\mathrm{T}} \left([\![\mathbf{v} \cdot \mathbf{S} - \mathbf{v}^* \cdot \mathbf{S}^*]\!] \cdot \mathbf{n} + q_\Gamma + \left[\!\!\left[m_f \left(\left(u - u^*\right) + \frac{1}{2}\left(v^2 - v^{*2}\right) \right) \right]\!\!\right] \right) - \alpha \frac{q_\Gamma}{\mathrm{T}} \geq 0$$

We introduce Helmholtz free energy for each component of the reaction as: $f^{\pm,*} = u^{\pm,*} - \mathrm{T} s^{\pm,*}$. Then $\dot{f}^{\pm,*} = \dot{u}^{\pm,*} - \mathrm{T}\dot{s}^{\pm,*} - \dot{\mathrm{T}} s^{\pm,*}$. We will rewrite our inequalities using the Helmholtz free energy

Using The balances of momentum (1.10), (1.9) and (1.11) for each component, respectively, and (1.12) for the reaction front, we obtain:

$$\text{initial material, in } \Omega_- : \quad -\rho^- \left(\dot{f}^- + \dot{\mathrm{T}} s^-\right) + \mathbf{S}^- : \nabla \mathbf{v}^- + \frac{1}{\mathrm{T}} \mathbf{h}^- \cdot \nabla \mathrm{T} \geq 0$$

$$\text{transformed material, in } \Omega_+ : \quad -\rho^+ \left(\dot{f}^+ + \dot{\mathrm{T}} s^+\right) + \mathbf{S}^+ : \nabla \mathbf{v}^+ + \frac{1}{\mathrm{T}} \mathbf{h}^+ \cdot \nabla \mathrm{T} \geq 0$$

$$\text{diffusive component, in } \Omega_+ : \quad -\rho^* \left(\dot{f}^* + \dot{\mathrm{T}} s^*\right) + \mathbf{S}^* : \nabla \mathbf{v}^* \geq 0$$

$$\text{reaction front } \Gamma : \quad \left[\!\left[m_f \left(f - f^*\right) \right]\!\right] + \left[\!\left[\frac{m_f}{2} \left(v^2 - v^{*2}\right) \right]\!\right] + \left[\!\left[\mathbf{v} \cdot \mathbf{S} - \mathbf{v}^* \cdot \mathbf{S}^* \right]\!\right] \cdot \mathbf{n} + (1 - \alpha)\, q_\Gamma \geq 0 \quad (1.25)$$

Note, that as we obtained the coupled system of the equations, it is now necessary to choose state variables and constitutive laws. In the present, case the state variables are: ε, ε^{in}, T, c, $\mathbf{V}$.

ε^{in} represents the non reversible deformation due for instance to plasticity, viscosity or chemical transformation.

c is the concentration of the diffusive reactant, which is non reversible or not dependent on the other variables of the problem.

$\mathbf{V}$ is the velocity of the reaction front, directly related the reaction rate; it can be reversible or not. For instance, in the oxidation problem it is not reversible, which not the case for the problem of charging and discharging of batteries.

The constitutive laws are now described by two sets of equations:

– reversible part: through a thermodynamic potential which can be the Helmholtz free energy;

– dissipated part, usually through a dissipation potential.

The specific free energy $f(\varepsilon, \varepsilon^{in}, \mathrm{T}, c, \boldsymbol{V})$ defines the reversible thermodynamic forces:

$$\boldsymbol{\sigma} = \rho \frac{\partial f}{\partial \varepsilon}$$

$$-\boldsymbol{\sigma}^{in} = \rho \frac{\partial f}{\partial \varepsilon^{in}}$$

$$s = -\frac{\partial f}{\partial \mathrm{T}}$$

$$\mu = \frac{\partial f}{\partial c}$$

$$\boldsymbol{A} = \frac{\partial f}{\partial \boldsymbol{V}}$$

where μ is chemical potential; c is concentration; $\boldsymbol{A}$ is chemical affinity and $\boldsymbol{V}$ is reaction front velocity.

Adding Fourier and Fick's laws and dissipated parts, this system becomes fully coupled and can be solved numerically. However, the chemical potential in such 'state relation' is scalar, since it was mentioned in the 'state of the art' it has to be tensor.

Taking into account tensorial nature of the chemical potential, we go to the approach proposed in [40]. In this article, the chemical potentials are equal to the Eshelby energy-momentum tensors, divided by the reference mass densities. Therefore, from (1.25) the equation for the chemical affinity tensor has to be derived. The equations we will use in the thesis are presented in the next section.

1.2.2 Chemical affinity tensor. Kinetic equation

In the previous section, the fully thermo-mechano-chemical coupled problem is defined.

In this section, a brief summary of the concept of chemical affinity tensor, that is used in the present work, is given below. More detailed explanations are given in [38, 40, 43, 44].

A chemical reaction between solid and diffusing constituents of the following type is considered:

$$n_- \mathrm{B}_- + n_* \mathrm{B}_* \longrightarrow n_+ \mathrm{B}_+$$

where B_-, B_* and B_+ are the chemical formulae of an initial solid constituent, a diffusing constituent and a transformed solid constituent, respectively, n_-, n_* and n_+ are the stoichiometric coefficients.

The reaction is localized at the reaction front Γ that divides the solid constituents B_- and B_+, and it is sustained by the diffusion of B_* through the transformed material B_+ (Fig. 1.14). Following [38, 40, 44], we consider the solid component B_+ as a solid skeleton for the diffusing constituent B_*, neglecting the deformations which could be produced in the transformed material by the diffusion. The thermal effects of the chemical reaction are also neglected and the temperature T is assumed to be a given parameter.

To describe the chemical reaction front kinetics we use an approach based on the concept of chemical affinity tensor developed in [38, 40, 44] (see also [43] and references therein). The normal component of the chemical affinity tensor appeared as a multiplier conjugate to the reaction rate in the expression of the energy dissipation due to the reaction front propagation and acts as a configurational force driving the reaction front. Initially it was derived for the case of a chemical reaction between diffusing and nonlinear elastic constituents [37] similar to how it was done for propagating phase interface [70]. Then as a result of the analysis of the mass, linear momentum and energy balance equations and the entropy inequality it was written down for a chemical reaction between diffusing and solid constituents of arbitrary rheology in the case of finite strains[38].

In order to understand how the chemical affinity tensor equation was derived, we consider the kinetic equation from classical chemical thermodynamics [119]:

$$\omega = k_* c \left(1 - \exp\left(-\frac{\mathrm{A}}{\mathrm{R}_g \mathrm{T}}\right)\right) \tag{1.26}$$

where k_* is the kinetic constant, R_g is the universal gas constant, c is the molar concentration of the diffusive constituent per unit volume. Note that the value $k_* c$ represents the partial rate of a direct reaction between diffusing and solid constituents. $\mathrm{A} = -\sum n_k \mathscr{M}_k \mu_k$ is the scalar chemical affinity and μ_k are scalar chemical potentials, $\mathscr{M}_{\pm,*}$ are the molar masses of $\mathrm{B}_{\pm,*}$, respectively. The scalar nature of chemical potential and chemical affinity does not contradict the ideas of classical chemical thermodynamics, which deals with ideal gases and liquids. But as it was mentioned at the end of 'state of the art' in the beginning of this chapter, that since 60^{th} [8, 48, 126] it was shown that chemical potential has to be a tensor. Therefore, its associate quantity, chemical affinity, has to be tensor as well.

In [40] the chemical affinity tensor equation was obtained from Clausius-Duhem inequality by recombining the terms in it, based on the following aspects:

– chemical affinity has to act as thermodynamical driving force;

– chemical affinity has tensorial nature;

– chemical potentials are tensors.

It was shown that the chemical affinity tensor in a quasi-static approach is given by

$$\mathbf{A} = n_- \mathscr{M}_- \mathbf{M}_- + n_* \mathscr{M}_* \mu_* \mathbf{I} - n_+ \mathscr{M}_+ \mathbf{M}_+$$

where μ_* is the chemical potential of the diffusing constituent; $\mathbf{I}$ is the second-rank identity tensor, $\mathbf{M}_-$ and $\mathbf{M}_+$ are the chemical potential tensors which are equal to the Eshelby energy-momentum tensors, divided by the reference mass densities ρ_- and ρ_+

$$\mathbf{M}_- = f_- \mathbf{I} - \frac{\mathbf{F}_-^{\mathrm{T}} \mathbf{S}_-}{\rho_-}, \quad \mathbf{M}_+ = f_+ \mathbf{I} - \frac{\mathbf{F}_+^{\mathrm{T}} \mathbf{S}_+}{\rho_+} \tag{1.27}$$

The stresses and strains affect the reaction front propagation as they are present in the configurational force. It follows from the comparison of formulas of scalar chemical affinity and its tensorial

expression (1.27) that the formulas have the similar form and $\mathbf{A}$ in (1.27) can be called the chemical affinity tensor.

Lets consider a surface element with normal $\mathbf{N}$ at the reaction front Γ (see Figure 1.14). The substitution of the normal component $A_{NN} = \mathbf{N}\cdot\mathbf{A}\cdot\mathbf{N}$ of the chemical affinity tensor into a known formula for the reaction rate (1.26) instead of a scalar chemical potential gives the following formula for the reaction rate ω_N at this reaction front surface element [38]:

$$\omega_N = k_* c\left(1-\exp\left(-\frac{A_{NN}}{R_g T}\right)\right)$$

Then, since the normal component V_N of the reaction front velocity is related with the reaction rate as

$$V_N = \frac{n_-\mathscr{M}_-}{\rho_-}\omega_N$$

where ρ_- is the mass density of the initial material B_-, we accept the following dependence of the normal component of the reaction front velocity on the normal component of the affinity tensor [38, 44]:

$$V_N = \frac{n_-\mathscr{M}_-}{\rho_-} k_* c\left(1-\exp\left(-\frac{A_{NN}}{R_g T}\right)\right)$$

It can be shown that in the case of small strains, with a chemical potential of the diffusing constituent taken as

$$\mathscr{M}_*\mu_* = f_* + R_g T\ln\frac{c}{c_*} \tag{1.28}$$

where f_* and c_* are the referential chemical energy and volume concentration of the diffusing constituent, the normal component of the chemical affinity tensor takes the form [40, 41, 44]:

$$A_{NN} = \frac{n_-\mathscr{M}_-}{\rho_-}(\gamma + w_- - w_+ + \boldsymbol{\sigma}_\pm : [[\varepsilon]]) + n_* R_g T\ln\frac{c}{c_*} \tag{1.29}$$

which can be rewritten as

$$A_{NN} = \frac{n_-\mathscr{M}_-}{\rho_-}(\gamma - \chi) + n_* R_g T\ln\frac{c}{c_*} \tag{1.30}$$

where

$$\gamma = f_0^- - f_0^+ + \frac{\rho_-}{n_-\mathscr{M}_-} f_*$$

is the temperature-dependent chemical energy parameter equal to the combination of the chemical energies f_0^-, f_0^+ of the solid constituents and the energy f_* of the diffusing constituent, γ is taken as a parameter at given temperature; $w_\pm$ are the strain energies of the solid constituents per unit volume, $[[\varepsilon]] = \varepsilon_+ - \varepsilon_-$ where $\varepsilon_\pm$ are the strains at the reaction front,

$$\chi = w_+ - w_- - \boldsymbol{\sigma}_\pm : [[\varepsilon]] \tag{1.31}$$

characterizes the input of stresses and strains. Note that we neglect the input of the pressure produced by the diffusing constituent into the stresses, and from the displacement and traction continuity it follows that the stresses $\boldsymbol{\sigma}_\pm$ on any side of the front can be substituted into Eq. (1.29).

The equilibrium concentration c_{eq} can be introduced such that [38, 44]

$$A_{NN}(c = c_{eq}) = 0 \tag{1.32}$$

Then the normal component of the affinity tensor can be expressed via the equilibrium concentration c_{eq} and chemical potential of the diffusing constituent calculated at the current concentration $c(\Gamma)$ and the equilibrium concentration c_{eq} found from (1.32) for stresses and strains at the reaction front as

$$A_{NN} = n_*\mathscr{M}_*\left(\mu_*(c(\Gamma)) - \mu_*(c_{eq})\right)$$

In a solid skeleton approach χ does not depend on the concentration. Then from (1.30) and (1.32) it follows that

$$\frac{c_{eq}}{c_*} = \exp\left\{-\frac{n_-\mathscr{M}_-}{\rho_-}\frac{(\gamma-\chi)}{n_* R_g T}\right\} \tag{1.33}$$

During further analysis the stoichiometric coefficients are normalized by n_*: $n_- \to n_-/n_*$, $n_+ \to n_+/n_*$ and $n_* \to 1$. Then, if the chemical potential of the diffusing constituent is given by Eq. (1.28), the reaction rate and the reaction front velocity become

$$\omega_N = k_*\left(c(\Gamma) - c_{eq}\right), \quad V_N = \frac{n_-\mathscr{M}_-}{\rho_-}k_*\left(c(\Gamma) - c_{eq}\right). \tag{1.34}$$

In such a representation from (1.33) and (1.31) one can observe that equilibrium concentration c_{eq} is dependent on the stress-strain state in base and transformed materials. From (1.34) it follows that the kinetics of the reaction depend on c_{eq}. Hence, stresses and strains affect the reaction rate via the equilibrium concentration, and one can see (1.34) that the front may propagate only if at the front $c > c_{eq}$.

1.2.3 Problem statement

To find the reaction front velocity one has to find stresses and strains at the reaction front, to solve the diffusion problem and to calculate A_{NN} (or find c_{eq} corresponding to stresses and strains at the front). Note the chemo-mechanical coupling: the front velocity depend of stress-strain state and the concentration while stress-state and the concentration depend on the front kinetics and position.

To find the stresses in quasistatic case, in the absence of body forces, one has to solve the equilibrium equation

$$\nabla\cdot\boldsymbol{\sigma} = 0 \tag{1.35}$$

where $\boldsymbol{\sigma}$ is the Cauchy stress tensor. The equation Eq. (1.35) is to be solved within domains υ_- and υ_+, which are occupied by materials B_- and B_+, respectively, with boundary conditions at the outer surface of the body (i.e. forces and/or displacements), and with displacement and traction continuity conditions at the reaction front.

To find the gas concentration c at the reaction front we assume that the gas diffusion flux $\mathbf{j}_*$ is given by Fick's Law

$$\mathbf{j}_* = -D\nabla c$$

where D is the diffusion coefficient of the reactant B_* through B_+. Further we assume that D is a constant, the diffusion process happening on much faster time scale than the chemical reaction. We neglect the initial stage of the diffusion prior to the start of the reaction at the outer boundary of the body. Considering reaction rate controlled front propagation, we also assume that the diffusion process is fast enough to consider a steady-state diffusion. Under such assumptions, The diffusion problem is described by the Laplace equation

$$\Delta c = 0$$

with the boundary conditions

$$D\frac{\partial c}{\partial N}\bigg|_{\partial\Omega_+} - \alpha\left(c_* - c(\partial\Omega)\right) = 0, \qquad D\frac{\partial c}{\partial N}\bigg|_{\Gamma} + \omega_N = 0$$

where Ω_+ is the part of the outer surface of the body corresponding to the transformed material (see Fig. 1.14), c_* is the solubility of B_* in the material B_+, α is the mass transfer coefficient, ω_N is the reaction rate at the surface element of the reaction front with the normal $\mathbf{N}$. Without loss of generality, we may take c_* also as the referential volume density in Eq. (1.28),

The first boundary condition states that the diffusion flux through the outer boundary of the body becomes zero if the saturation c_* is reached. The second condition means that all the diffusing reactant is fully consumed at the reaction front and with the use of Eq. $(1.34)_1$ can be rewritten as

$$\mathrm{D}\frac{\partial c}{\partial \mathrm{N}}\bigg|_{\Gamma} + k_* \left(c(\Gamma) - c_{eq}\right) = 0$$

Finally we come to the coupled problems for a solid with internal unknown propagating interfaces which velocity depends on mechanical stresses and the concentration of a diffusing matter, while the stresses and concentration depend on the position of the interface. All the equations are summarized in the following Box. Note that this set of equations can be used for any constitutive models of the constituents.

Equilibrium equation:

$$\nabla \cdot \boldsymbol{\sigma} = 0; \quad [[\boldsymbol{\sigma}]]|_{\Gamma} \cdot \mathbf{N} = 0, \; [[\mathbf{u}]]|_{\Gamma} = 0 \quad + \quad \text{B.C.}$$

Constitutive models *(some examples)*:

$$\begin{aligned}
&\textit{Elasticity} && \boldsymbol{\sigma} = \mathbb{C} : \varepsilon; \\
&\textit{Plasticity} && \boldsymbol{\sigma} = \mathbb{C} : (\varepsilon - \varepsilon^p), \quad \dot{\varepsilon}^p = \dot{\lambda}\frac{\partial f}{\partial \boldsymbol{s}}, \quad f \le 0, \quad \lambda \ge 0, \quad \lambda f = 0; \\
&\textit{Visco-elasticity} && \boldsymbol{\sigma} = \mathbb{C} : \varepsilon + \eta\dot{\varepsilon}; \\
&\textit{Thermoelasticity} && \boldsymbol{\sigma} = \mathbb{C} : \varepsilon + \kappa \Delta \mathrm{T} \boldsymbol{I}; \quad \ldots
\end{aligned}$$

Diffusion problem:

$$\begin{gathered}
\Delta c = 0, \\
\mathrm{D}\frac{\partial c}{\partial \mathrm{N}}\bigg|_{\partial\Omega} - \alpha \left(c_* - c(\partial\Omega)\right) = 0, \\
\mathrm{D}\frac{\partial c}{\partial \mathrm{N}}\bigg|_{\Gamma} + k_* \left(c(\Gamma) - c_{eq}\right) = 0
\end{gathered}$$

Chemical reaction front kinetics:

$$\mathrm{V_N} = \frac{n_- \mathscr{M}_-}{\rho_-} k_* \left(c(\Gamma) - c_{eq}\right) = 0$$

$$c_{eq}: \; \mathrm{A_{NN}}|_{c=c_{eq}} = 0, \quad \mathrm{A_{NN}} = \frac{n_- \mathscr{M}_-}{\rho_-}(\gamma + w_- - w_+ + \boldsymbol{\sigma}_{\pm} : [[\varepsilon]])$$

The general framework is independent of the constitutive equations. In the following chapters we will use different geometries, boundary conditions and constitutive models to demonstrate its effect on the chemical reaction front propagation.

1.3 Conclusions

In this chapter we defined the thermodynamical framework for the analysis of thermo-chemo-mechanical problem. We use the general balance equations for mass, momentum, energy and entropy to establish the local equations and jump conditions governing the problem. After choosing the state variables, the general form of the constitutive laws based on the free energy is given.

Then the thermodynamical framework based on the concept of the chemical affinity tensor is presented. The concept of affinity tensor was introduced and finally, the general equations of the mechanochemistry problem have been defined. This group of equations and boundary conditions is independent of the constitutive laws which will be defined and studied in the next chapters.

Chapter 2

Geometry precision. Elastic reaction product

Contents

The general framework is independent of the constitutive equations. This PhD thesis is concerned to study the effect of inelastic material behaviour on the reaction front propagation. In this chapter we assume the transformed material to be elastic with different elastic modulus from the initial material. The objective of this chapter is to show how the given framework works, to obtain an elastic reference solutions and to demonstrate the influence of the body's geometry (plane, spherical and cylindrical). The obtained results will be used in the following chapters with the aim of comparison and demonstration of the inelastic behaviour features.

Despite there are already some results in elasticity [38, 42, 44], in this chapter will be new results even for elastic transformed material. The solution for the planar reaction front was obtained in [44]. In this work, another boundary conditions for the diffusion problem, which affects the form of the kinetic equation, are given. The spherically-symmetric problem was solved in [42] and parabolic kinetics was shown. Here, for the chemical reaction in sphere, the logarithmic kinetics and for which conditions it can be observed are studied. The problem of cylindrical reaction front was considered in [38] for the case of incompressible material. In this work, the material is considered compressible, the given problem is solved for another boundary conditions in the diffusion problem, the kinetic equation is obtained and given, the exponential and parabolic kinetics and for which conditions they are achieved are studied. For all considered problems the accurate mathematical analysis of influence of various parameters on the reaction front behavior is conducted, and these are also new results.

In this chapter we formulate the problem for initially elastic plate, sphere and cylinder, solve the diffusion problem for each case, present the equations for reaction front velocity, and then derive and solve the kinetic equation.

2.1 Reaction front kinetics

To demonstrate the reaction front kinetics in the case of elastic reaction product, we consider, in this section, the simple plane, spherically- symmetric and axially-symmetric problems, respectively.

The behaviors of the initial and transformed materials are represented by rheological models formulated as relationships between deviatoric parts of stress and strain tensors. Then we use the following decompositions

$$\boldsymbol{\sigma} = \sigma\mathbf{I} + \mathbf{s}, \qquad \varepsilon = \frac{\vartheta}{3}\mathbf{I} + \mathbf{e} \tag{2.1}$$

where $\sigma = \frac{1}{3}\mathrm{tr}\boldsymbol{\sigma}$ and $\vartheta = \mathrm{tr}\varepsilon$ denote the hydrostatic parts of the stress tensor and volume strain; $\mathbf{s}$ and $\mathbf{e}$ are the deviatoric stress and strain, respectively.

We assume that the transformation strain is spherical: $\varepsilon^{tr} = (\vartheta^{tr}/3)\mathbf{I}$. Then the hydrostatic parts of the stress tensor and volume strain are related in constituent "+" as

$$\sigma^{+} = k_{+}(\vartheta^{+} - \vartheta^{tr}) \tag{2.2}$$

To show the geometry effect, in this section we suppose that the solid constituents are isotropic elastic. Then the elasticity tensors are defined as

$$\mathbb{C}_{\pm} = k_{\pm}\mathbf{I}\otimes\mathbf{I} + 2\mu_{\pm}\left(\mathbb{I} - \frac{1}{3}\mathbf{I}\otimes\mathbf{I}\right) \tag{2.3}$$

where $k_{\pm}$ and $\mu_{\pm}$ are bulk and shear modulus; $\mathbb{I}$ is symmetric forth rank unit tensor. We consider that initial and transformed materials are compressible.

2.1.1 Plane front propagation

We consider in this section the simple plane strain problem for a chemical reaction in a plane layer of thickness H and length L >> H with a planar reaction front (Fig. 4.2). The reaction starts at the outer surface $y = 0$ of an initially elastic layer. The planar reaction front propagates in the y-direction, a transformed material forms a plane layer of the material of the thickness h. The lower $y = 0$ and upper $y = \mathrm{H}$ faces of the layer are traction free. Displacement u_0 at the edges $x = \pm\mathrm{L}$ prescribes the strain $\varepsilon_0 = u_0/\mathrm{L}$ in x-direction. Therefore, the strains have to satisfy the following conditions:

$$\varepsilon_z = \varepsilon_{xz} = \varepsilon_{yz} = 0, \quad \varepsilon_x = \varepsilon_0$$

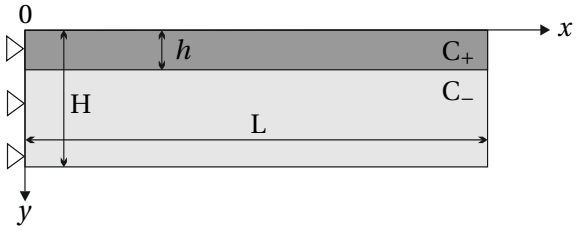

Figure 2.1: The planar reaction front.

The diffusion problem is reduced to the diffusion equation

$$\frac{d^2c}{dy^2} = 0, \quad y \in [0, h]$$

with boundary conditions

$$\mathrm{D}\left.\frac{dc}{dy}\right|_{y=0} = \alpha(c(0) - c_*), \quad \mathrm{D}\left.\frac{dc}{dy}\right|_{y=h} = -k_*(c(h) - c_{eq})$$

From the solution of diffusion problem it follows that the concentration of the diffusing constituent B_* at the reaction front is equal to

$$c(h) = \frac{c_* + k_*\left(\dfrac{h}{\mathrm{D}} + \dfrac{1}{\alpha}\right)c_{eq}}{1 + k_*\left(\dfrac{h}{\mathrm{D}} + \dfrac{1}{\alpha}\right)}$$

Then, by Eq. (1.34), the reaction front velocity can be calculated as

$$\mathrm{V_N} = \frac{n_-\mathscr{M}_-}{\rho_-}\frac{c_* - c_{eq}}{\dfrac{1}{k_*} + \left(\dfrac{h}{\mathrm{D}} + \dfrac{1}{\alpha}\right)} \tag{2.4}$$

where the equilibrium concentration c_{eq}, defined by Eq. (1.32), depends on stresses and strains at the reaction front. Formula (4.3) can be rewritten as

$$\dot{\xi} = \frac{n_-\mathrm{M}_-}{\rho_-}\frac{c_* - c_{eq}}{\mathrm{T}_{ch} + \mathrm{T_D}\xi},$$

where $\xi = \dfrac{h}{\mathrm{H}}$, the dot denotes the time derivative, the characteristic times of diffusion and chemical reaction, $\mathrm{T_D}$ and T_{ch}, are defined by formulae

$$\mathrm{T_D} = \frac{\mathrm{H}^2}{\mathrm{D}}, \quad \mathrm{T}_{ch} = \mathrm{H}\left(\frac{1}{k_*} + \frac{1}{\alpha}\right). \tag{2.5}$$

In the mechanical problem, the equilibrium equations and boundary conditions are satisfied if we take

$$\sigma_y = 0, \qquad \sigma_{xy} = 0 \tag{2.6}$$

From the continuity of the displacement it follows that, at the reaction front

$$[[\varepsilon_x]] = 0$$

Then, from Eq. (2.6) and plane strains conditions it follows that $\boldsymbol{\sigma}_- : [[\boldsymbol{\varepsilon}]] = 0$ in the expression of the normal component of the chemical affinity tensor Eq. (1.29).

From (2.3) and due to the plane strains conditions, using Hooke's law, non-zero stresses in the elastic layer $y \in [h, \mathrm{H}]$ are the stresses

$$\sigma_x^- = \frac{4\mu_-\left(3k_- + \mu_-\right)}{3k_- + 4\mu_-}\varepsilon_0, \quad \sigma_z^- = \frac{2\mu_-\left(3k_- - 2\mu_-\right)}{3k_- + 4\mu_-}\varepsilon_0 \tag{2.7}$$

Then the strain energy density of the material B_- is

$$w_- = \frac{2\mu_-\left(3k_- + \mu_-\right)}{3k_- + 4\mu_-}\varepsilon_0^2 \tag{2.8}$$

To find the strain energy w_+ at the reaction front there is no need to solve the elastic problem. We know that

$$\boldsymbol{\sigma}^+ = k_+\left(\vartheta^+ - \vartheta^{tr}\right)\mathbf{I} + 2\mu_+\mathbf{e}^+ \tag{2.9}$$

Then

$$w_+ = \frac{1}{2}k_+(\vartheta^+ - \vartheta^{tr})^2 + \mu_+\mathbf{e}^+ : \mathbf{e}^+$$

Since, due to the plane strain restriction, $\varepsilon_y^+ = \vartheta^+ - \varepsilon_0$,

$$\mathbf{e}^+ : \mathbf{e}^+ = \boldsymbol{\varepsilon}^+ : \boldsymbol{\varepsilon}^+ - \frac{(\vartheta^+)^2}{3} = 2\left(\varepsilon_0^2 - \varepsilon_0\vartheta^+ + \frac{(\vartheta^+)^2}{3}\right) \tag{2.10}$$

From the relationships

$$\sigma_y^+ = k_+(\vartheta^+ - \vartheta^{tr}) + 2\mu_+ e_y^+ = 0$$
$$e_x^+ = \varepsilon_0 - \frac{\vartheta^+}{3}, \quad e_z^+ = -\frac{\vartheta^+}{3}, \quad e_y^+ = -(e_x^+ + e_z^+) = \frac{2\vartheta^+}{3} - \varepsilon_0$$

we deduce that

$$\vartheta^+ = \frac{3(2\mu_+\varepsilon_0 + k_+\vartheta^{tr})}{3k_+ + 4\mu_+} \tag{2.11}$$

$$e_x^+ = \frac{(3k_+ + 2\mu_+)\varepsilon_0 - k_+\vartheta^{tr}}{3k_+ + 4\mu_+}, \quad e_y^+ = \frac{k_+(2\vartheta^{tr} - 3\varepsilon_0)}{3k_+ + 4\mu_+}, \quad e_z^+ = -\frac{2\mu_+\varepsilon_0 + k_+\vartheta^{tr}}{3k_+ + 4\mu_+} \tag{2.12}$$

Then the strain energy of the strain constituent is found to be

$$w_+ = \frac{2\mu_+\left(\left(3k_+ + \mu_+\right)\varepsilon_0^2 - 3k_+\vartheta^{tr}\varepsilon_0 + k_+\vartheta^{tr2}\right)}{3k_+ + 4\mu_+} \tag{2.13}$$

With the use of (2.10) and (2.11), the strain energy w_+ becomes a function of the external deformation ε_0 and material parameters. Then the substitution of (2.8) for w_- and obtained expressions

of w_+ and ϑ^+ into (1.31) gives χ as the quadratic function of external and transformation strains (ε_0 and ε^{tr}, respectively) and elastic moduli of the constituents:

$$\chi(\varepsilon_0) = 2(G_+ - G_-)\varepsilon_0^2 - 3S\vartheta^{tr}\varepsilon_0 + S_+(\vartheta^{tr})^2 \tag{2.14}$$

where

$$G_\pm = \frac{\mu_\pm(3k_\pm + \mu_\pm)}{3k_\pm + 4\mu_\pm} = \frac{E_\pm}{2(1-\nu_\pm^2)}, \quad S_+ = \frac{2k_+\mu_+}{3k_+ + 4\mu_+} = \frac{E_+}{9(1-\nu_+)}$$

$E_\pm$ and $\nu_\pm$ are the Young moduli and Poisson's ratios. Substitution of (2.14) into Eq. (1.30) leads to the explicit dependencies of A_{NN} and c_{eq} at the reaction front on external and transformation strains, elastic modulus of the constituents and chemical energies. Particularly,

$$\frac{c_{eq}}{c_*} = \exp\left\{-\frac{n_-\mathscr{M}_-}{\rho_-}\frac{(\gamma - \chi(\varepsilon_0))}{R_gT}\right\} \tag{2.15}$$

Note that at given ε_0 the equilibrium concentration does not depend on the front position. Then the integration of the Eq.(2.4) leads to the *kinetic equation* in the form of the parabolic law:

$$\xi^2 + L\xi = Qt \tag{2.16}$$

where $\xi = \dfrac{h}{H}$, $L = \dfrac{2D}{H}\left(\dfrac{1}{k_*} + \dfrac{1}{\alpha}\right)$, $Q = \dfrac{n_-\mathscr{M}_-}{\rho_-}\dfrac{2D}{H^2}c_*(1-\phi)$, $\phi = \exp\left\{-\dfrac{n_-\mathscr{M}_-}{\rho_-}\dfrac{(\gamma - \chi(\varepsilon_0))}{R_gT}\right\}$.

The new variable ξ, which is introduced above, has a meaning of a relative thickness or a degree of the chemical transformation. Since $\xi \in [0,1]$, the situation of $\xi = 0$ corresponds to $h = 0$, which refers to the beginning of the chemical transformation; and $\xi = 1$ is associated with the case, when $h = H$ and the plate is completely transformed into a new material.

2.1.2 Spherical front propagation

In this section we consider a sphere of radius R that is subjected to the reaction from the outer surface under external stress $\boldsymbol{\sigma}_0$. The spherical reaction front propagates in the direction of the center of the sphere. Transformed materials forms a spherical layer of thickness h (Fig. 2.2). The chemical reaction is localized on spherical reaction front of the radius $(R-h)$ and divides the sphere onto regions occupied by the initial and new materials.

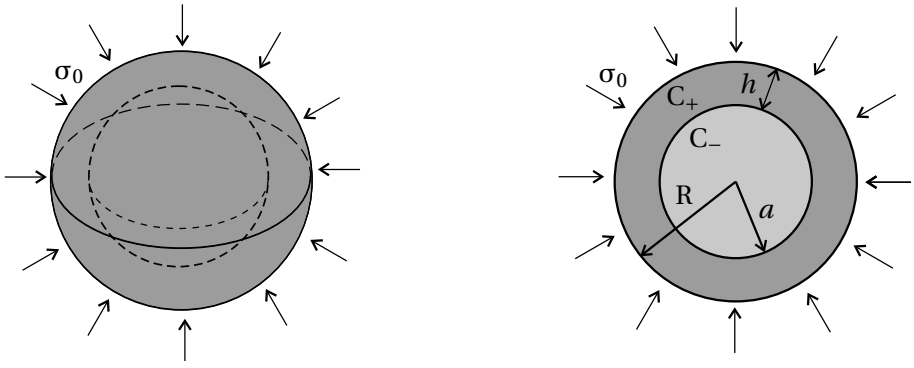

Figure 2.2: The spherical reaction front.

The Laplace diffusion equation reduce to the following one

$$\frac{\partial^2 c}{\partial r^2} + \frac{2}{r}\frac{\partial c}{\partial r} = 0, \qquad r \in [0, R]$$

with boundary conditions

$$\mathrm{D}\frac{\partial c}{\partial r}\bigg|_{r=\mathrm{R}} = \alpha(c_* - c(\mathrm{R})), \qquad \mathrm{D}\frac{\partial c}{\partial r}\bigg|_{r=a} = -k_*(c(a) - c_{eq})$$

From the solution it follows that the concentration of the diffusing constituent B_* at the reaction front is equal to

$$c(a) = \frac{c_* + k_*\left(\dfrac{1-\xi}{\alpha} + \dfrac{\xi}{\mathrm{D}_0}\right)(1-\xi)c_{eq}}{1 + k_*\left(\dfrac{1-\xi}{\alpha} + \dfrac{\xi}{\mathrm{D}_0}\right)(1-\xi)}, \qquad h = \mathrm{R} - a, \qquad \xi = \frac{h}{\mathrm{R}}, \qquad \mathrm{D}_0 = \frac{\mathrm{D}}{\mathrm{R}}$$

Then, by eq.(1.34), the reaction front velocity can be calculated as

$$\mathrm{V_N} = \frac{n_- \mathscr{M}_-}{\rho_-} \frac{k_*}{1 + k_*\left(\dfrac{1-\xi}{\alpha} + \dfrac{\xi}{\mathrm{D}_0}\right)(1-\xi)}\left(c_* - c_{eq}\right) \tag{2.17}$$

Note, that the variable ξ, which is introduced above, has the same meaning as described for the plate: it is the relative thickness or the degree of the chemical transformation. Since the body's geometry is spherical symmetric and since the material is isotropic, the equilibrium and kinematic boundary conditions can be expressed as

$$\frac{d\sigma_r}{dr} + 2\frac{\sigma_r - \sigma_\varphi}{r} = 0$$
$$\varepsilon_r = \frac{du}{dr}, \qquad \varepsilon_\varphi = \varepsilon_\vartheta = \frac{u}{r}$$

where u is the radial displacement. Then the radial displacements in initial and transformed materials are given by Lame formulae

$$u_- = \mathfrak{A}_- r, \qquad u_+ = \mathfrak{A}_+ r + \frac{\mathfrak{B}_+}{r^2} \tag{2.18}$$

where $\mathfrak{A}_\pm$ and $\mathfrak{B}_+$ are found from the boundary conditions and the displacement and stress continuity at the reaction front:

$$u_-(a) = u_+(a), \qquad \sigma_r^-(a) = \sigma_r^+(a), \qquad \sigma_r^+(\mathrm{R}) = \sigma_0$$

The integration constants are obtained as follows

$$\mathfrak{B}_+ = -\frac{\left(k_- k_+ \vartheta^{tr} - \sigma_0\,(k_+ - k_-)\right)\mathrm{R}^3(1-\xi)^3}{k_+\left(3k_- + 4\mu_+\right) - 4\mu_+\,(k_+ - k_-)\,(1-\xi)^3}$$
$$\mathfrak{A}_+ = \frac{\sigma_0(3k_- + 4\mu_+) + k_+\vartheta^{tr}\left(3k_- + 4\mu_+\left(1 - (1-\xi)^3\right)\right)}{3\left(k_+(3k_- + 4\mu_+) - 4\mu_+(k_+ - k_-)(1-\xi)^3\right)}$$
$$\mathfrak{A}_- = \frac{\sigma_0(3k_+ + 4\mu_+) + 4k_+\mu_+\vartheta^{tr}\left(1 - (1-\xi)^3\right)}{3\left(k_+(3k_- + 4\mu_+) - 4\mu_+(k_+ - k_-)(1-\xi)^3\right)}$$

Then the strain and stresses in the initial and transformed materials are determined by the following equations:

$$\varepsilon^- = \mathfrak{A}_-\mathbf{I}, \quad \boldsymbol{\sigma}^- = 3k_-\mathfrak{A}_-\mathbf{I}$$
$$\varepsilon^+ = \left(\mathfrak{A}_+ - 2\frac{\mathfrak{B}_+}{r^3}\right)\mathbf{e_r}\mathbf{e_r} + \left(\mathfrak{A}_+ + \frac{\mathfrak{B}_+}{r^3}\right)(\mathbf{I} - \mathbf{e_r}\mathbf{e_r})$$
$$\boldsymbol{\sigma}^+ = \left(k_+\left(3\mathfrak{A}_+ - \vartheta^{tr}\right) - 4\mu_+\frac{\mathfrak{B}_+}{r^3}\right)\mathbf{e_r}\mathbf{e_r} + \left(k_+\left(3\mathfrak{A}_+ - \vartheta^{tr}\right) + 2\mu_+\frac{\mathfrak{B}_+}{r^3}\right)(\mathbf{I} - \mathbf{e_r}\mathbf{e_r})$$

where $\mathbf{e}_r$ is a unit radial vector.

Then the strain energy density of the initial material "-" is

$$w^- = \frac{9}{2} k_- \mathfrak{A}_-^2 \tag{2.19}$$

in the transformed material it can be found as

$$w^+ = \frac{1}{2} k_+ (3\mathfrak{A}_+ - \vartheta^{tr})^2 + 6\mu_+ \left(\frac{\mathfrak{B}_+}{r^3} \right)^2 \tag{2.20}$$

and

$$\boldsymbol{\sigma}^- : [\![\boldsymbol{\varepsilon}]\!] = 9 k_- \mathfrak{A}_- (\mathfrak{A}_+ - \mathfrak{A}_-) \tag{2.21}$$

Then, we substitute (2.19), (2.20) and (2.21) into Eq. (1.29), (1.31) and (1.33). This results in the explicit dependencies of A_{NN} and c_{eq} at the reaction front on external stress and transformation strain, elastic modulus of the constituents and the chemical energies, specifically

$$\frac{c_{eq}}{c_*} = \exp\left\{ -\frac{n_- \mathscr{M}_-}{\rho_- R_g T} \left(\gamma + 9 k_- \mathfrak{A}_- \left(\mathfrak{A}_+ - \frac{1}{2}\mathfrak{A}_- \right) - \frac{1}{2} k_+ (3\mathfrak{A}_+ - \vartheta^{tr})^2 - 6\mu_+ \frac{\mathfrak{B}_+^2}{R^6 (1-\xi)^6} \right) \right\}$$

Hence, χ is given as the quadratic function of external stress and transformation strain, front position and elastic modulus of the constituents:

$$\chi(\sigma_0, \xi) = \mathfrak{P}(k_+ - k_-)\sigma_0^2 - 2\mathfrak{P} k_+ k_- \sigma_0 \vartheta^{tr} - \mathfrak{K}(\vartheta^{tr})^2 \tag{2.22}$$

where

$$\mathfrak{P} = \frac{1}{\beta}\left(3k_+(3k_- - 4\mu_+) + 4\mu_+(9k_- + 4\mu_+)\right), \qquad \beta = 2\left(k_+(3k_- + 4\mu_+) - 4\mu_+(k_+ - k_-)(1-\xi)^3\right)^2$$

$$\mathfrak{K} = \frac{4\mu_+ k_- k_+}{\beta}\left(k_+(9k_- + 4\mu_+) - 2k_+(3k_- + 4\mu_+)(1-\xi)^3 + 4\mu_+(k_+ - k_-)(1-\xi)^6\right)$$

Therefore, substitution of (2.22) into Eq. (1.33) leads to the following form of c_{eq}

$$\frac{c_{eq}}{c_*} = \exp\left\{ -\frac{n_- \mathscr{M}_-}{\rho_-} \frac{(\gamma - \chi(\sigma_0, \xi))}{R_g T} \right\} \tag{2.23}$$

Consequently, the *kinetic equation* will take form:

$$\dot{\xi} = \frac{n_- \mathscr{M}_-}{\rho_-} \frac{k_*}{1 + k_* \left(\frac{1-\xi}{\alpha} + \frac{\xi}{D_0} \right)(1-\xi)} \left(1 - \exp\left\{ -\frac{n_- \mathscr{M}_-}{\rho_-} \frac{(\gamma - \chi(\sigma_0, \xi))}{R_g T} \right\} \right) \tag{2.24}$$

Note, that due to the spherical geometry, the kinetic equation takes a more complex form than it was in the planar case as it depends on the relative reaction front position ξ as well, and it is not possible to obtain the explicit form of the resulting formulae.

2.1.3 Cylindrical front propagation

In this subsection we consider the chemical reaction for an axially-symmetric problem. As an example we consider a linear-elastic cylinder of radius R and length L subjected to an external stress σ_0. Assume L >> R. The displacement in a radial direction is a function on r alone and does not depend on upon z. Therefore, $\varepsilon_z = 0$, as we assume that tube material is compressible, then from (3.1) we have non zero $\boldsymbol{e}_z$. The diffusive material surrounds the cylinder. We suppose

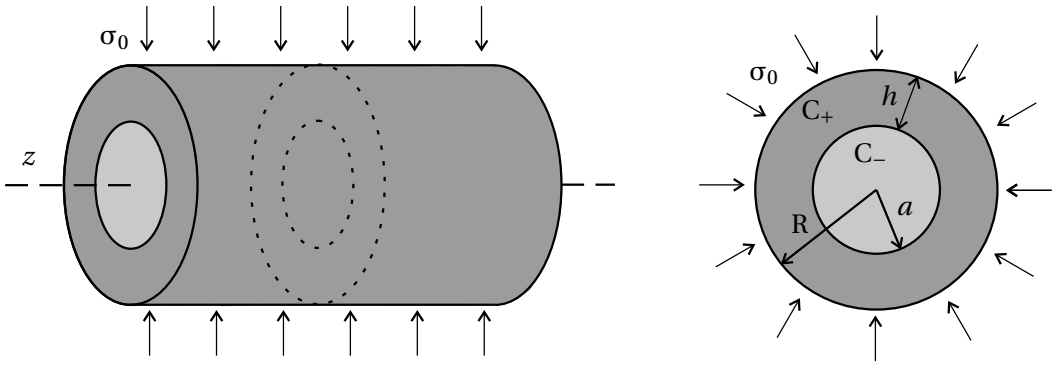

Figure 2.3: The cylindrical reaction front.

that reaction starts from the outer surface and transformed material forms a cylindrical layer of a thickness h from the body surface (Fig. 2.3).

The diffusion equation in cylindrical coordinates takes the following form

$$\frac{\partial^2 c}{\partial r^2}+\frac{1}{r}\frac{\partial c}{\partial r}=0$$

with boundary conditions

$$\mathrm{D}\frac{\partial c}{\partial r}\bigg|_{r=\mathrm{R}}=\alpha(c_*-c(\mathrm{R})),\qquad \mathrm{D}\frac{\partial c}{\partial r}\bigg|_{r=a}=-k_*(c(a)-c_{eq})$$

Therefore, the concentration of the diffusing constituent B_* at the reaction front is equal to

$$c(a)=\frac{c_*\dfrac{\mathrm{D}_0}{k_*(1-\xi)}+c_{eq}\left(\ln(1-\xi)-\dfrac{\mathrm{D}_0}{\alpha}\right)}{\dfrac{\mathrm{D}_0}{k_*(1-\xi)}-\dfrac{\mathrm{D}_0}{\alpha}+\ln(1-\xi)},\qquad \mathrm{D}_0=\frac{\mathrm{D}}{\mathrm{R}},\qquad h=\mathrm{R}-a,\qquad \xi=\frac{h}{\mathrm{R}} \tag{2.25}$$

Hence, by (1.34), the velocity at the reaction front can be calculated as

$$\mathrm{V_N}=\frac{n_-\mathscr{M}_-}{\rho_-}\frac{c_*-c_{eq}}{\dfrac{1}{k_*}-\dfrac{1-\xi}{\alpha}+\dfrac{\ln(1-\xi)}{\mathrm{D}_0}(1-\xi)} \tag{2.26}$$

In cylindrical coordinates (r,φ,z) the radial displacements in the base and transformed material are given by Lame formula:

$$u^{\pm}=\mathscr{A}_{\pm}r+\frac{\mathscr{B}_{\pm}}{r} \tag{2.27}$$

where $\mathscr{A}_{\pm}$, $\mathscr{B}_{\pm}$ are found from the boundary conditions and displacement and traction continuity at the reaction front:

$$\mathscr{B}_+=\frac{3\mathrm{R}^2}{\mathscr{G}}(1-\xi)^2\left(k_+\vartheta^{tr}(3k_-+\mu_-)-\sigma_0\left(3(k_+-k_-)+(\mu_+-\mu_-)\right)\right)$$

$$\mathscr{A}_+=\frac{3}{\mathscr{G}}\left(3\mu_+(k_+\vartheta^{tr}(\xi^2-2\xi)-\sigma_0)-(3k_-+\mu_-)(k_+\vartheta^{tr}+\sigma_0)\right)$$

$$\mathscr{A}_-=\frac{3}{\mathscr{G}}\left(3k_+\mu_+\vartheta^{tr}(\xi^2-2\xi)-(3k_++4\mu_+)\sigma_0\right)$$

where $\mathscr{G} = 6\mu_+(\xi^2-2\xi)\left(3(k_+-k_-)+(\mu_+-\mu_-)\right)-2(3k_-+\mu_-)(3k_++4\mu_+)$

In the case of the cylinder u is to be finite at $r=0$, therefore $\mathscr{B}_-=0$.

Therefore strains and stresses in initial and transformed materials are given by

$$\boldsymbol{\varepsilon}^- = \mathscr{A}_-\mathbf{I}, \qquad \boldsymbol{\sigma}^- = 2\left(k_- + \frac{\mu_-}{3}\right)\mathscr{A}_-\mathbf{I}$$

$$\varepsilon_r^+ = \mathscr{A}_+ - \frac{\mathscr{B}_+}{r^2}, \qquad \varepsilon_\varphi^+ = \mathscr{A}_+ + \frac{\mathscr{B}_+}{r^2}, \qquad \varepsilon_z^+ = 0$$

$$\sigma_r^+ = 2\left(k_+ + \frac{\mu_+}{3}\right)\mathscr{A}_+ - 2\mu_+\frac{\mathscr{B}_+}{r^2} - k_+\vartheta^{tr}, \qquad \sigma_\varphi^+ = 2\left(k_+ + \frac{\mu_+}{3}\right)\mathscr{A}_+ + 2\mu_+\frac{\mathscr{B}_+}{r^2} - k_+\vartheta^{tr}$$

$$\sigma_z^+ = 2\left(k_+ - \frac{\mu_+}{3}\right)\mathscr{A}^+ - k_+\vartheta^{tr}$$

In the initial material the strain is

$$w^- = 2\left(k_- + \frac{\mu_+}{3}\right)\mathscr{A}_-^2 \tag{2.28}$$

The strain energy of the transformed material can be obtained as

$$w^+ = \frac{1}{2}k_+\left(2\mathscr{A}^+ - \vartheta^{tr}\right)^2 + 2\mu_+\left(\frac{\mathscr{A}_+^2}{3} + \frac{\mathscr{B}_+^2}{r^4}\right) \tag{2.29}$$

and the jump condition at the reaction front can be written as follows

$$\boldsymbol{\sigma}^- : [\![\boldsymbol{\varepsilon}]\!] = 4\left(k_- + \frac{\mu_-}{3}\right)\mathscr{A}_-(\mathscr{A}_+ - \mathscr{A}_-) \tag{2.30}$$

Substitution of (4.56), (2.29) and (2.30) into Eq. (1.29) and (1.33) causes the explicit dependencies of A_{NN} and c_{eq} at the reaction front on external stress and transformation strain, elastic modulus of the constituents and the chemical energies. In particularly,

$$\frac{c_{eq}}{c_*} = \exp\left\{-\frac{n_-\mathscr{M}_-}{\rho_- R_g T}\left(\gamma + 2\left(k_- + \frac{\mu_-}{3}\right)\mathscr{A}_-(2\mathscr{A}_+ - \mathscr{A}_-) - \frac{k_+}{2}\left(2\mathscr{A}^+ - \vartheta^{tr}\right)^2 - 2\mu_+\left(\frac{\mathscr{A}_+^2}{3} + \frac{\mathscr{B}_+^2}{R^4(1-\xi)^4}\right)\right)\right\}$$

It gives χ as the quadratic function of external stress and transformation strain, front position and elastic modulus of the constituents:

$$\chi(\sigma_0,\xi) = \frac{1}{\mathscr{U}}\left((\mathscr{K}_+ - \mathscr{K}_-)\mathscr{P}\sigma_0^2 - 2\mathscr{K}_- k_+ \mathscr{P}\vartheta^{tr}\sigma_0 - \mu_+ k_+ \mathscr{Q}(\vartheta^{tr})^2\right) \tag{2.31}$$

where

$$\mathscr{P} = 3(3k_+ + 4\mu_+)(\mathscr{K}_- + 3\mu_+), \quad \mathscr{U} = 2\left(3\mu_+(\mathscr{K}_+ - \mathscr{K}_-)\xi(\xi-2) - (3k_+ + 4\mu_+)\mathscr{K}_-\right)^2, \quad \mathscr{K}_\pm = 3k_\pm + \mu_\pm$$

$$\mathscr{Q} = 9\mu_+(\mathscr{K}_+ - \mathscr{K}_-)(\mathscr{K}_- - \mu_+)\xi^2(\xi^2 - 4\xi + 4) - 2(3k_+ + 4\mu_+)\mathscr{K}_-\left(3(\mathscr{K}_- - \mu_+)\xi(\xi-2) - 2\mathscr{K}_-\right)$$

Substituting (2.31) into Eq. (2.31) leads to the following form of c_{eq}

$$\frac{c_{eq}}{c_*} = \exp\left\{-\frac{n_-\mathscr{M}_-}{\rho_-}\frac{(\gamma - \chi(\sigma_0,\xi))}{R_g T}\right\} \tag{2.32}$$

Then the *kinetic equation* takes form:

$$\dot{\xi} = \frac{n_-\mathscr{M}_-}{\rho_-}\frac{1}{\frac{1}{k_*} + \frac{1-\xi}{\alpha} - \frac{\ln(1-\xi)}{D_0}(1-\xi)}\left(1 - \exp\left\{-\frac{n_-\mathscr{M}_-}{\rho_-}\frac{(\gamma - \chi(\sigma_0,\xi))}{R_g T}\right\}\right) \tag{2.33}$$

Similarly to the spherical problem, the kinetic equation takes more complex form in cylindrical geometry in comparison with the planar case. The explicit form of the solution for Eq.(2.33) cannot be obtained.

In sammary, we have formulated and solved the problems for a planar, spherical and cylindrical reaction fronts propagation in the case of the elastic reaction product. We dispose now on the reference elastic solutions, that will be used further in order to study features of inelastic transformed material. As explicit form of kinetic equation is not possible for the reaction in sphere and cylinder, numerical solutions here have to be determined using the Runge-Kutta method.

2.2 Equilibrium concentration, kinetics of the reaction front and blocking effect

2.2.1 Planar reaction front

In this Section, the dependencies of the reaction front position on time and of the reaction front velocity on the front position, which are deduced from (2.4), will be presented finally at various values of the external strain ε_0, energy parameter γ and elastic moduli. Since, by (2.4), the reaction front velocity increases if c_{eq}/c_* decreases and, respectively, the velocity decreases if c_{eq}/c_* increases, the influence of various parameters on the reaction front behavior can be predicted qualitatively if one knows how the parameters affect the equilibrium concentration. So, we start with such predictions.

By (2.4), the reaction front can propagate only if the stress-strain state at the front and the energy parameter are such that $c_{eq} < c_*$. We study further how the condition $c_{eq} < c_*$ is affected by the parameters. By (2.15), this is possible only if the transformation strain, external strains, elasticity parameters and the energy parameter are such that $\chi < \gamma$ [38, 44]. By (2.14), in the considered case this condition takes the form

$$\chi(\varepsilon_0) - \gamma = 2(G_+ - G_-)\varepsilon_0^2 - 3S_+\vartheta^{tr}\varepsilon_0 - \left(\gamma - \gamma_0\right) < 0,$$

where

$$\gamma_0 = S_+(\vartheta^{tr})^2 \tag{2.34}$$

is the critical value of the parameter γ in the sense that the reaction front may propagate at the external strain $\varepsilon_0 = 0$ only if

$$\gamma > \gamma_0.$$

Formula (2.34) for the critical value of γ for the plane transformation strain with slightly different S_+ was presented in [41, 44] for the case of elastic reaction constituents. The same formula appears here because of the pure elastic behavior of both constituents at the front at the transformation moment t_y.

The dependencies of c_{eq}/c_* on external strain ε_0 for the planar front are schematically shown in Fig. 2.4. The extrema is reached at $\varepsilon_0 = \varepsilon_0^*$ with $c_{eq}/c_* = c_{eq}^*/c_*$:

$$\varepsilon_0^* = \frac{3S_+\vartheta^{tr}}{4(G_+ - G_-)}, \quad \frac{c_{eq}^*}{c_*} = \exp\left\{\frac{n_-M_-}{\rho_-}\frac{(\chi(\varepsilon_0^*) - \gamma)}{R_gT}\right\}, \quad \chi(\varepsilon_0^*) = \left(1 - \frac{9S_+}{8(G_+ - G_-)}\right)\gamma_0 \equiv \gamma_*. \tag{2.35}$$

Note that $\varepsilon_0^* \neq 0$, since k_+ and μ_+ are positive values. The character of the dependence of c_{eq}/c_* on ε_0 and the signs of ε_0^* and $\chi(\varepsilon_0^*)$ depend on the relation between G_+, G_- and S_+ and the sign of the transformation strain ϑ^{tr}. Without loss of generality, we assume further that $\vartheta^{tr} > 0$. As for the elastic modulus, the following three cases can be listed.

(i) If

$$8(G_+ - G_-) - 9S_+ > 0, \tag{2.36}$$

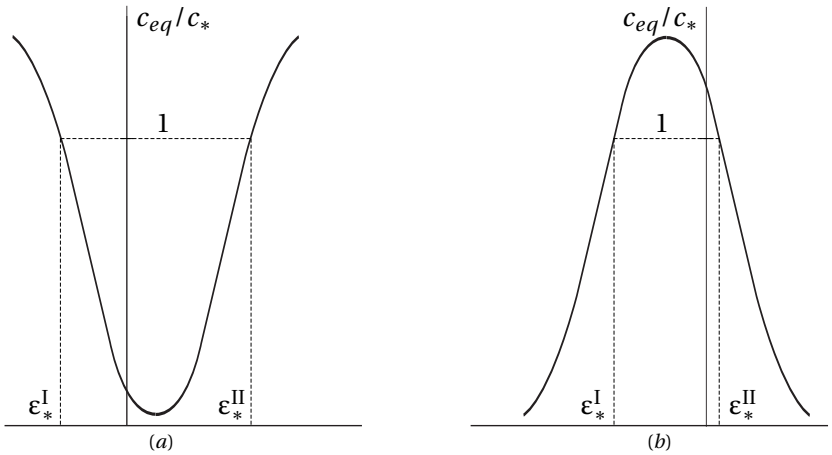

Figure 2.4: Dependencies of the equilibrium concentration on the external strain: (a) $G_+ > G_-, \gamma > \gamma_*$, (b) $G_+ < G_-, \gamma > \gamma_*$.

then $G_+ > G_-$ and, therefore, $\chi(\varepsilon_0^*) > 0$ and $\varepsilon_0^* > 0$ correspond to the minimal value of $\chi(\varepsilon_0)$ as it is shown in Fig. 2.4*a*. Note that the inequality (2.36) can be rewritten through elastic moduli as

$$\mu_+ > \frac{4\mu_-(3k_- + \mu_-)}{3k_- + 4\mu_-} \iff \frac{E_+}{1+\nu_+} > \frac{2E_-}{1-\nu_-^2}.$$

The front can propagate only if the energy parameter, elastic moduli of the solid constituents and transformation strain are such that $\gamma > \gamma_*$ and only at strains $\varepsilon_0 \in [\varepsilon^{\mathrm{I}}, \varepsilon^{\mathrm{II}}]$ where $\varepsilon^{\mathrm{I}}, \varepsilon^{\mathrm{II}}$ are the roots of the quadratic equation $\chi(\varepsilon_0) - \gamma = 0$. Both roots are positive if $\gamma_* < \gamma < \gamma_0$, and the front cannot propagate without applied tensile strain $\varepsilon_0 > \varepsilon^{\mathrm{I}} > 0$.

If the front can propagate at $\varepsilon_0 = 0$ then $\gamma > \gamma_0$ and the roots have different signs, $\varepsilon^{\mathrm{I}} < 0$, $\varepsilon^{\mathrm{II}} > 0$. The front cannot propagate at $\varepsilon_0 > \varepsilon^{\mathrm{II}}$ and at $\varepsilon_0 < \varepsilon^{\mathrm{I}}$, i.e. the propagation is blocked starting from some strains in both tension and compression.

If the energy parameter is such that $\gamma < \gamma_*$ then $c_{eq}/c_* > 1$ at all ε_0, and the planar front cannot propagate in y-direction. To avoid misunderstanding, note that this does not mean that the reaction cannot occur at all. In a general case, χ depends on the geometry of the front since the stress-strain state at the reaction front depends on the geometry. It may happen that other configurations of the reaction front than a configuration with a planar reaction front may develop. On the other hand, a forbidden zone can be constructed in a strain space, formed by the strains at which the reaction front cannot propagate whatever the local normals to the front are [39, 41]. Also, strictly speaking, even if the considered solution with a planar propagating front is allowed by kinetic equation at given ε_0, an additional stability analysis would be appropriate [96]. Consideration of these aspects is beyond the scope of this work. Note only that the use of the semi-inverse approach may give a mathematically consistent solution but other solutions that do not follow a priori assumptions about the geometry of the front may also be of interest.

(ii) If the elastic moduli satisfy the inequalities

$$G_+ > G_- \quad \text{but} \quad 8(G_+ - G_-) - 9S_+ < 0,$$

which can be rewritten as

$$\mu_+ < \frac{4\mu_-(3k_- + \mu_-)}{3k_- + 4\mu_-} < \frac{4\mu_+\left(3k_+ + \mu_+\right)}{3k_+ + 4\mu_+} \iff \frac{E_+}{2(1+\nu_+)} < \frac{E_-}{1-\nu_-^2} < \frac{E_+}{1-\nu_+^2},$$

then $\varepsilon_0^* > 0$ as in the case (i), but the minimal value of χ is negative, $\chi(\varepsilon_0^*) < 0$. The front may propagate even at negative jump of the chemical energies, $\gamma < 0$, but such that $\gamma > -|\gamma_*|$, and at strains ε_0 such that $\chi(\varepsilon_0^*) < \chi(\varepsilon_0) < \gamma < 0$. This would be impossible without accounting for strain energy effects.

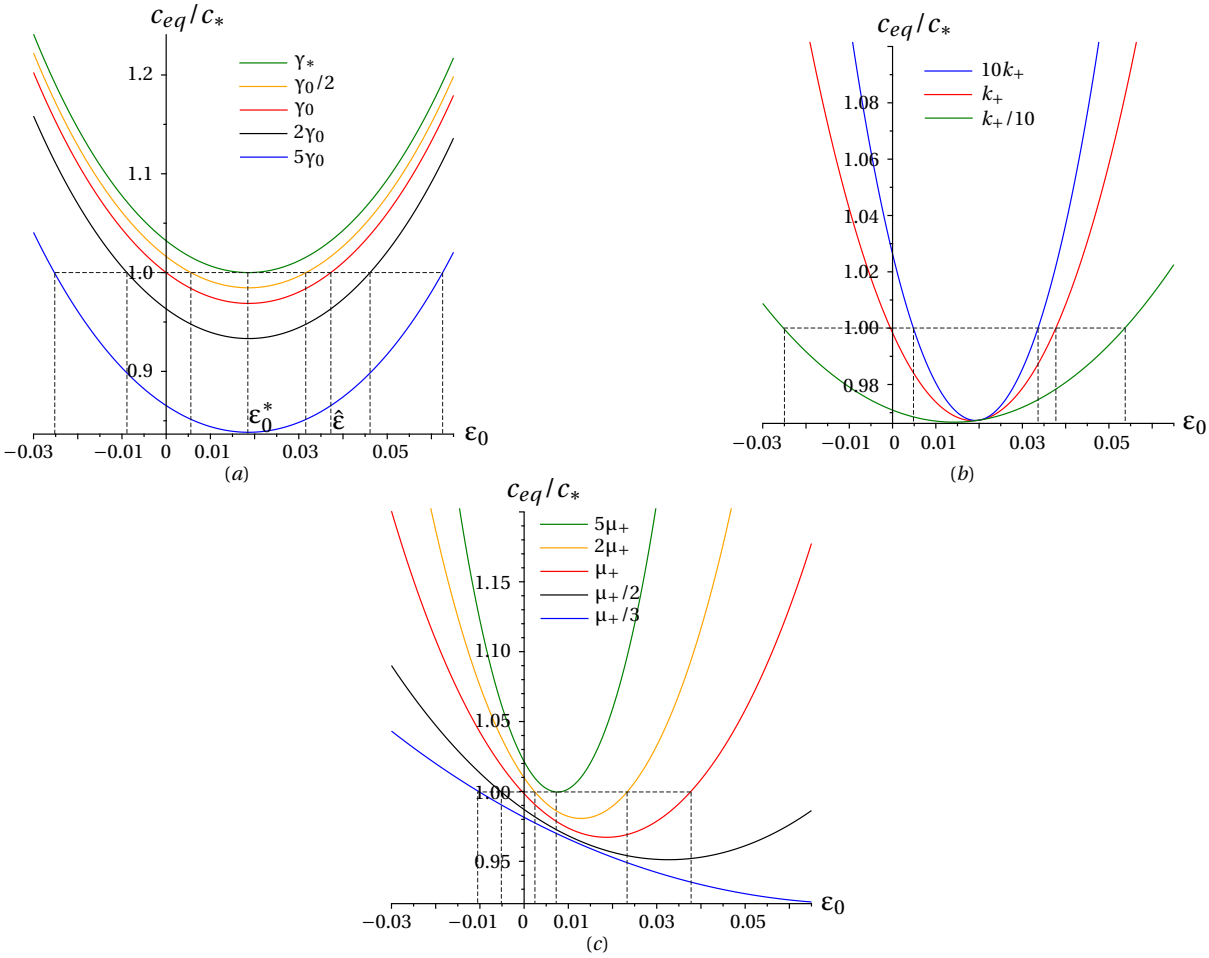

Figure 2.5: Planar reaction front: dependencies of the equilibrium concentration on external strain ε_0 for the case $G_+ > G_-$: (*a*) for different values of the energy parameter γ; (*b*) for different values of bulk modulus k_+; (*c*) different values of μ_+.

Since $\varepsilon_0^* > 0$ at $G_+ > G_-$, the increase of the tensile strain from $\varepsilon_0 = 0$ until ε_0^* accelerates the reaction front in both cases (i) and (ii). Further increase of ε_0 retards the front until blocking at ε^{II}. On the whole, if $|\varepsilon_0 - \varepsilon_0^*|$ increases then the front velocity decreases until zero.

(iii) If $G_+ < G_-$ then $\gamma_0 < \gamma_*$, $\varepsilon_0^* < 0$, and $\chi(\varepsilon_0^*) > 0$ corresponds to the maximal value on the dependence $\chi(\varepsilon_0)$ (Fig. 2.4*b*). Such a case was also discussed for an elastic case with plane transformation strain in [44]. If $\gamma > \gamma_*$ then the front may propagate at any ε_0. If $\gamma < \gamma_*$ then the propagation of the front is blocked at $\varepsilon_0 \in [\varepsilon^{\text{I}}, \varepsilon^{\text{II}}]$ but may start to propagate at proper tension $\varepsilon_0 > \varepsilon^{\text{II}}$ or compression $\varepsilon_0 < \varepsilon^{\text{I}}$. Thus, in this case, in contrast to the previous ones, the front can propagate at any γ at some external strains.

By (2.35), the bulk and shear elastic modules, $k_\pm$ and $\mu_\pm$, affect the dependence $\chi(\varepsilon_0)$ and, thus, the dependencies of c_{eq}/c_* and the reaction front velocity on ε_0 via parameters $(G_+ - G_-)$ and S_+, and the strain ε_0^* is determined by the dimensionless parameter $S_+/(G_+ - G_-)$. For example, it is easy to see that ε_0^* decreases if μ_+ increases and other moduli are fixed. As another example, one can examine how k_+ affects the dependence $\chi(\varepsilon_0)$ and the extrema values $\chi(\varepsilon_0^*)$ and ε_0^*. From (3.13) it follows that

$$\frac{\partial \chi(\varepsilon_0)}{\partial k_+} = \frac{2\mu_+^2 (3\varepsilon_0 - 2\vartheta^{tr})^2}{(3k_+ + 4\mu_+)^2} \geq 0.$$

Then, if the front propagates at a given set of parameters, further increase of k_+ increases $\chi(\varepsilon_0)$ and, therefore, decreases the front velocity. Note also that increase of k_+ leads to increasing the extrema value $\chi(\varepsilon_0^*)$ for both cases $G_+ > G_-$ and $G_+ < G_-$.

The dependence of extrema strain ε_0^* on bulk module k_+ is defined by relations between elastic

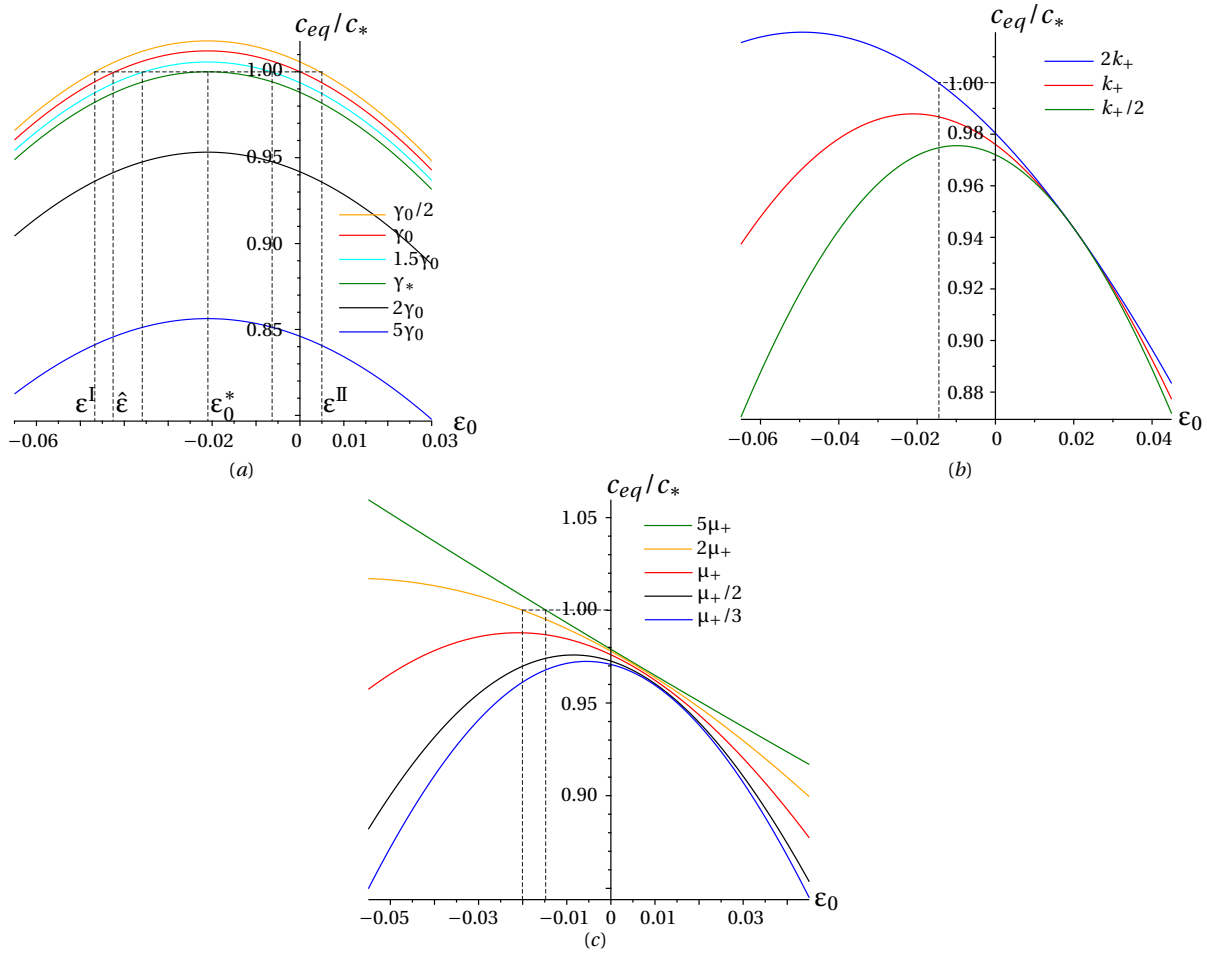

Figure 2.6: Planar reaction front: dependencies of the equilibrium concentration on external strain ε_0 for the case $G_+ < G_-$: (*a*) for different values of the energy parameter γ; (*b*) for different values of bulk modulus k_+; (*c*) different values of μ_+.

moduli. Since, by (2.35),

$$\frac{\partial \varepsilon_0^*}{\partial k_+} = \frac{3\mu_+^2 \vartheta^{tr}}{(3k_+ + 4\mu_+)^2} \frac{8(G_+ - G_-) - 9S_+}{4(G_+ - G_-)^2}$$

one can see that if $8(G_+ - G_-) - 9S_+ > 0$ (the case (i)) then the point ε_0^* in Fig. 2.4*a* is shifted to the right if k_+ increases, and is shifted to the left leaving ε_0^* positive if k_+ decreases, respectively.

If $G_+ > G_-$ but $8(G_+ - G_-) - 9S_+ < 0$ (the case (ii)) or $G_+ < G_-$ (the case (iii)), then the extrema point ε_0^* in Fig. 2.4*a* is shifted to the left or right if k_+ increases or decreases, respectively.

More detailed quantitative analysis is presented in Fig. 2.5 and Fig. 2.6, where the dependencies of the relative equilibrium concentration c_{eq}^*/c_* on the external stain ε_0 at various values of the energy parameter γ and the bulk and shear modules k_+, μ_+ of the transformed material are shown for the cases $G_+ > G_-$ and $G_+ < G_-$, respectively. The reference values of the parameters for the cases $G_+ > G_-$ and $G_+ < G_-$ and corresponding values of γ_0 and γ_* are given in Tables 2.1 and 2.2,

Table 2.1: Material parameters used in the simulations for the case $G_+ > G_-$

Parameter	k_-[GPa]	μ_-[GPa]	η_0[GPa·s]	D[m^2/s]	$\mathscr{M}_-$[g/mol]	T[K]	σ_{yd}[GPa]	n_-	R[m]
Value	27.3	25.9	15.9	$8\cdot10^{-10}$	28.1	920	1.65	1	10^{-3}
Parameter	k_+[GPa]	μ_+[GPa]	ρ_-[g/cm^3]	α[m/s]	k_*[m/s]	ε^{tr}	H[m]	c_*	
Value	90.9	67.7	2.2	$2.3\cdot10^{-7}$	$1.27\cdot10^{-6}$	0.01	10^{-3}	1	

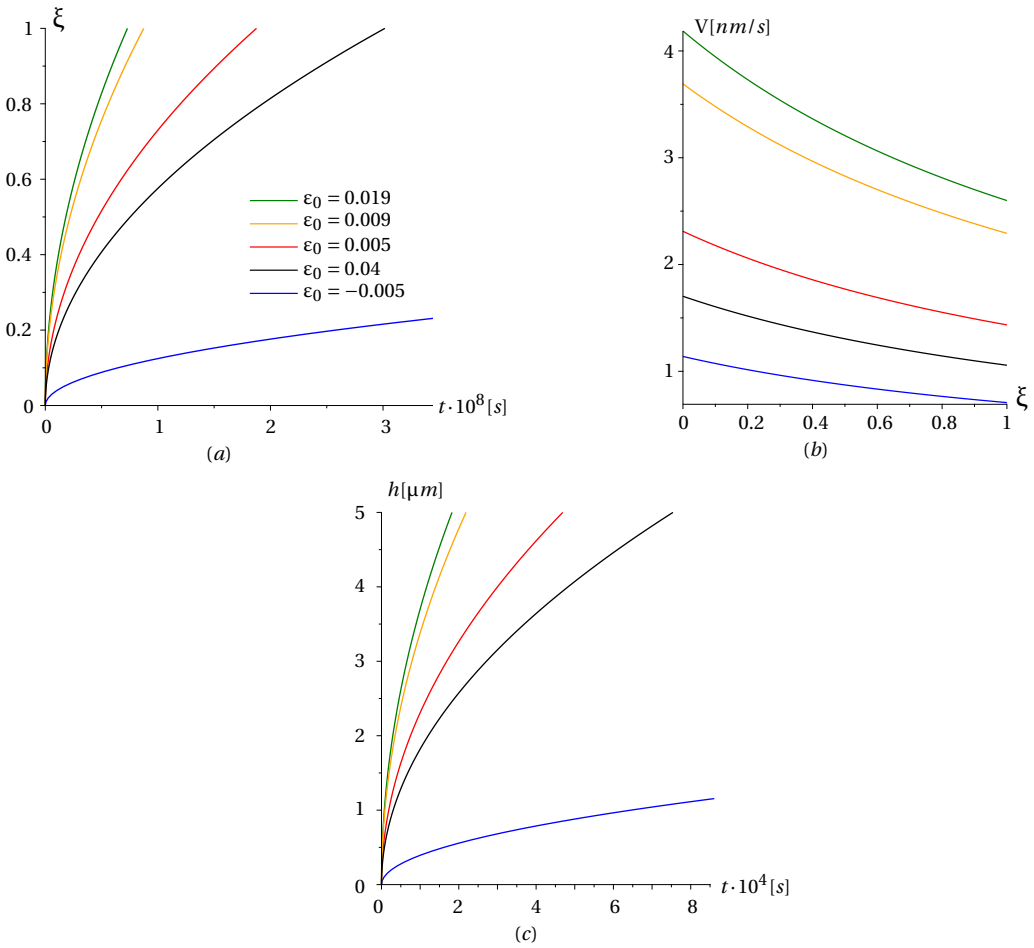

Figure 2.7: Planar reaction front: dependencies of the dimensionless front position on time (*a*), and the front velocity on the front position (b) at various values of external tension ε_0 for the case $G_+ > G_-$; (c) – the front position versus time at the initial stage of the front propagation

respectively. Only the parameters differ in two cases are shown in Table 2.2.

The choice of the values was made according to the reasons of the consistency with a small strain approach and better visualisation of the parameters influence. To demonstrate the variety of the reaction front behaviours and to examine quantitatively how the parameters affect the front behaviour two sets of bulk and shear moduli, $k_\pm$ and $\mu_\pm$, are taken which correspond to the cases $G_+ > G_-$ and $G_+ < G_-$. The data for quantitative analysis were taken from [41, 42, 97], where they were examined for such type of the problems.

Fig. 2.5*a* and Fig. 2.6*a* reflect the competition between strain and chemical energies at $G_+ > G_-$ and $G_+ < G_-$, respectively. If $\gamma = \gamma_0$ then the dependence of c_{eq}/c_* on ε_0 passes through the point $\varepsilon_0 = 0$, $c_{eq}/c_* = 1$. If $G_+ > G_-$ and $\gamma = \gamma_0$ then the front may propagate only at tension restricted by the strain $\hat{\varepsilon} = 3S\vartheta^{tr}/[2(G_+ - G_-)]$, i.e. at strains $0 < \varepsilon_0 < \hat{\varepsilon}$ ($\hat{\varepsilon} = 0.037$ in Fig. 2.5*a*). One can see how increasing γ results in enlarging the interval of allowed strains ε_0 (see the curves for $\gamma = 2\gamma_0$ and $\gamma = 5\gamma_0$) and how the decrease of γ shortens and shifts the interval of the strains at $\gamma_* < \gamma < \gamma_0$.

Table 2.2: Material parameters used in the simulations for the case $G_+ < G_-$

Parameter	k_-[GPa]	μ_-[GPa]	k_+[GPa]	μ_+[GPa]
Value	62.3	33.9	27.3	25.9

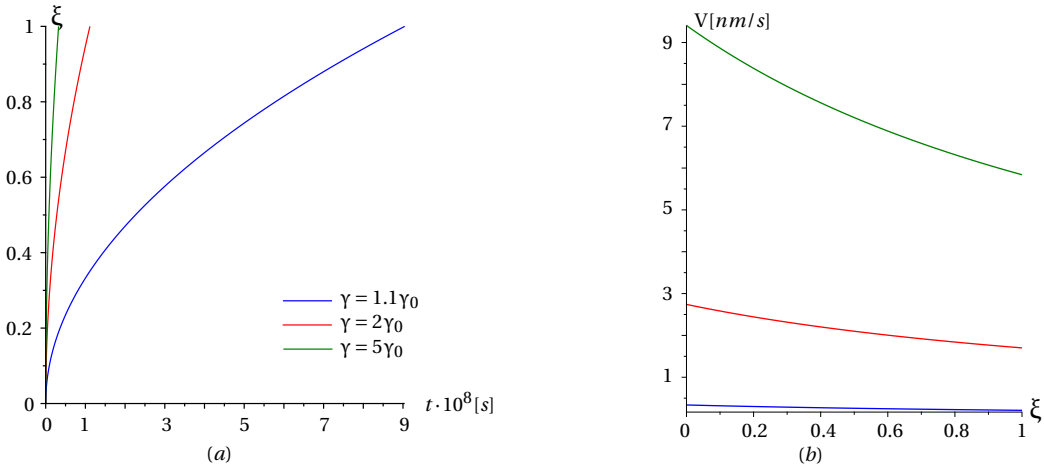

Figure 2.8: Planar reaction front: dependencies of the front position on time (*a*) and the front velocity on the front position (*b*) at various values of energy parameter γ

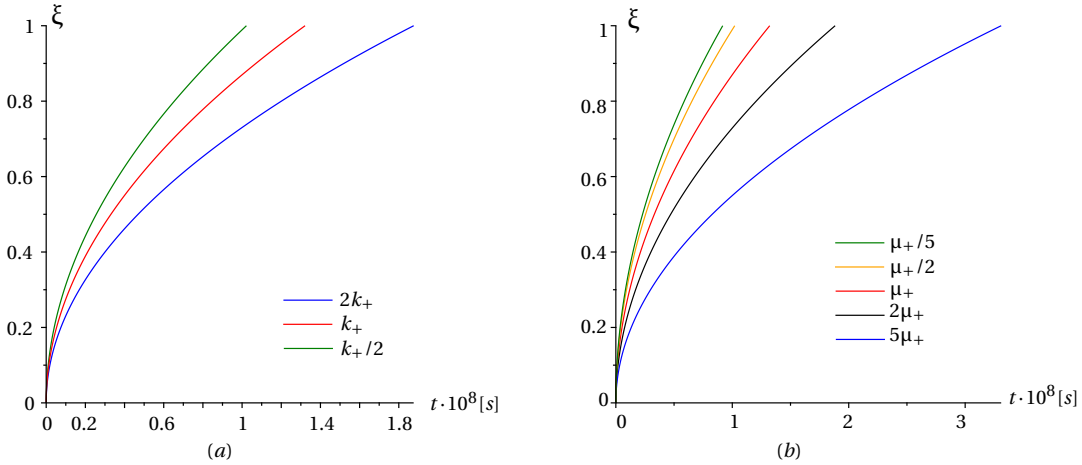

Figure 2.9: Planar reaction front: dependencies of the front position on time at various values of bulk modulus k_+ (a) and at various values of shear modulus μ_+ (b)

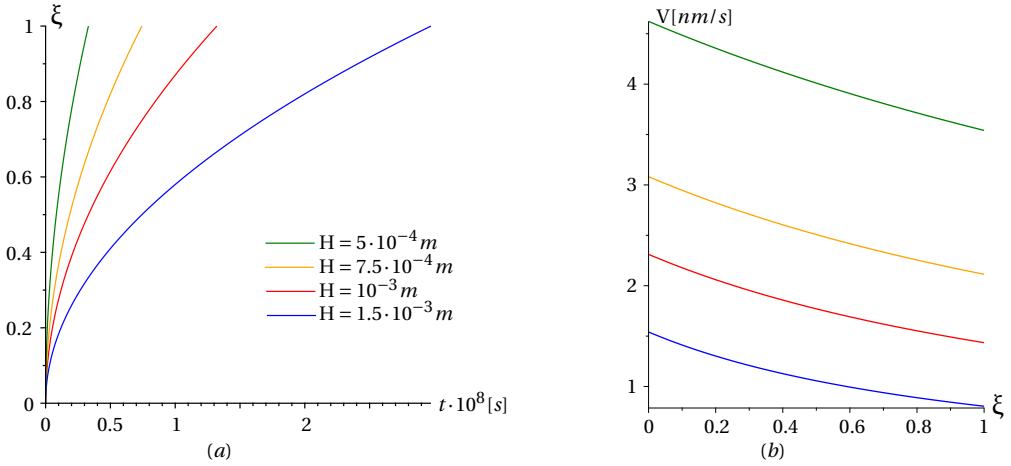

Figure 2.10: Planar reaction front: dependencies of the front position on time (*a*) and the front velocity on the front position (b) at various initial thickness H of the plate

If $G_+ < G_-$ and $\gamma = \gamma_0$ then the front may propagate only at tension $\varepsilon_0 > 0$ or compression $\varepsilon_0 < \hat{\varepsilon} = -0.042$ (Fig. 2.6*a*). If $\gamma < \gamma_0$, for example, $\gamma = \gamma_0/2$, then the front can propagate only

if additional tension $\varepsilon_0 > \varepsilon^{II} > 0$ or compression $\varepsilon_0 < \varepsilon^{I} < 0$ is applied. The case $\gamma_0 < \gamma < \gamma_*$ is presented by $\gamma = 1.5\gamma_0$, and the front propagation is blocked at $\varepsilon_0 \in [-0.036, -0.006]$. If $\gamma > \gamma_*$ ($\gamma = 2\gamma_0$ and $\gamma = 5\gamma_0$ in Fig. 2.6*a* then the front may propagate at any ε_0.

One can also see in Fig. 2.4*b*, Fig. 2.6*a* that if, at $G_+ < G_-$, the front can propagate at some ε_0 then further increasing of the absolute value $|\varepsilon_0|$ decreases c^*_{eq}/c_* and, thus, increases the front velocity.

Fig. 2.5*b*,*c* and Fig. 2.6*b*,*c* characterize quantitatively the role of volume and shear strain energies via the influence of the bulk module k_+ and shear module μ_+ on the dependencies of c^*_{eq}/c_* on ε_0. Since G_+ decreases if μ_+ decreases and G_+ increases if μ_+ increases, one can observe in Fig. 2.5*c* and Fig. 2.6*c* how the dependencies change if $G_+ \to G_-$ due to decreasing μ_+ at $G_+ > G_-$ and increasing μ_+ at $G_+ < G_-$.

Corresponding dependencies of the front position on time and the front velocity on the front position for the case $G_+ > G_-$ are shown in Fig. 2.7. The parameters are given in Table 2.1; if the parameters are varying then the values are indicated in figures. One can see how the strains retard or accelerate the reaction front. The maximal front velocity is observed at tensile strain $\varepsilon_0 = \varepsilon^*_0 = 0.019$. The velocity decreases at both additional tension (as at $\varepsilon_0 = 0.04$) and at compression relatively to ε^*_0 (as at $\varepsilon_0 = 0.005, 0.009, -0.005$), as it has to be in accordance with the increasing c_{eq}/c_* in Fig. 2.5*a*.

Fig. 2.8 and 2.9 demonstrate how increasing of the energy parameter accelerates the front, and how the values of elastic moduli affect the front kinetics. These dependencies are consistent with the dependencies of c_{eq}/c_* shown in Fig. 2.5.

The initial thickness of the plate also has an effect on the front kinetics (Fig. 2.10) through characteristic times T_D and T_{ch} of the diffusion supply and chemical reaction (see Eq. (2.5)). Increasing the plate thickness increases the characteristic times and therefore decreases the relative front velocity.

2.2.2 Spherical reaction front

In this section, in the same way as it was done for the planar reaction front, the dependencies of the reaction position on time and of the reaction front velocity on the front position in a sphere will be presented finally for various values of the external stresses σ_0, energy parameter γ and elastic moduli. Since, by (2.17), the reaction front velocity increases if c_{eq}/c_* decreases and, respectively, the velocity decreases if c_{eq}/c_* increases, the influence of various parameters on the reaction front behavior can be predicted qualitatively if one knows how the parameters affect the equilibrium concentration.

By (2.24) and (2.23), the main difference between spherical and plane reaction front is that the kinetic equation and equilibrium concentration depend on the reaction front position as well for the spherical reaction front propagation.

We study further how the condition $c_{eq} < c_*$ is affected by the parameters for the purpose of analysis the propagation of the reaction front. By (2.23), this is possible only if the transformation strain, external stress, elasticity parameters and the energy parameter are such that $\chi < \gamma$. By (2.22), in the considered case this condition takes the form

$$\chi(\sigma_0, \xi) - \gamma = \mathfrak{P}(k_+ - k_-)\sigma_0^2 - 2\mathfrak{P}k_+k_-\sigma_0\vartheta^{tr} - (\gamma - \gamma_0) < 0$$

where

$$\gamma_0 = \mathfrak{K}(\vartheta^{tr})^2$$

is the critical value of the parameter γ in the sense that the reaction front can start from the outer surface at $\sigma_0 = 0$ only if

$$\gamma > \gamma_0$$

The dependencies of c_{eq}/c_* on external stress σ_0 for the spherical front are schematically shown in Fig. 2.4. The extrema is reached at $\sigma_0 = \sigma_0^*$ with $c_{eq}/c_* = c_{eq}^*/c_*$:

$$\sigma_0^* = \frac{k_+ k_- \vartheta^{tr}}{k_+ - k_-}, \qquad \frac{c_{eq}^*}{c_*} = \exp\left\{\frac{n_- \mathscr{M}_-}{\rho_-}\frac{\left(\chi(\sigma_0^*,\xi) - \gamma\right)}{R_g T}\right\}, \qquad \chi(\sigma_0^*,\xi) = \frac{k_+ k_- \left(\vartheta^{tr}\right)^2}{2(k_+ - k_-)} \equiv \gamma_* \tag{2.37}$$

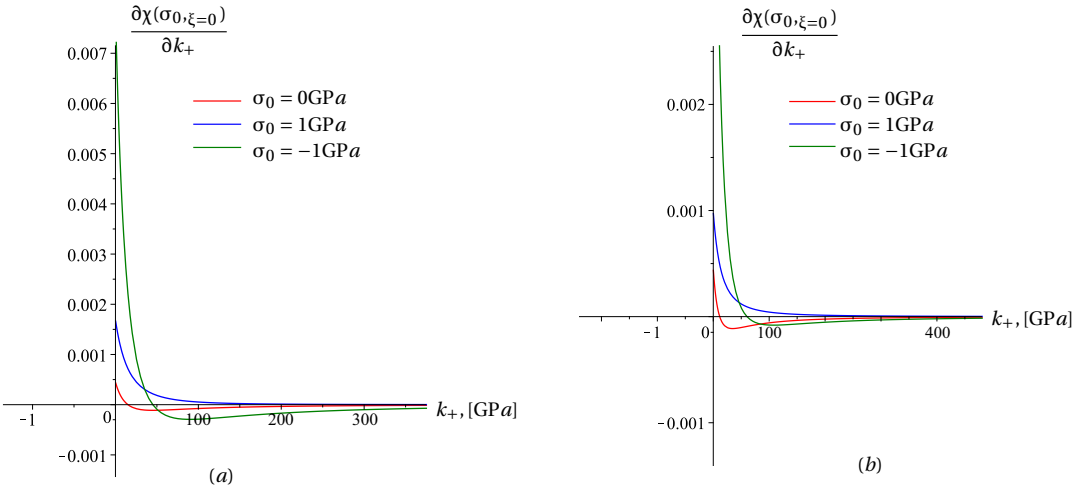

Figure 2.11: Spherical reaction front: behavior of $\frac{\partial\chi(\sigma_0,\xi=0)}{\partial k_+}$ at different intensity of the external loading σ_0 a) $k_+ > k_-$ and b) $k_+ < k_-$ front

The character of the dependence of c_{eq}/c_* on σ_0 and ξ and the sign of σ_0^* and $\chi(\sigma_0^*)$ depend on the relation between $\mathfrak{P}$ and $\mathfrak{K}$ and the sign of $(k_+ - k_-)$ as well as ϑ^{tr}. Note that to study the sign of $\chi(\sigma_0,\xi)$ we have to consider the sign of $(k_+ - k_-)$ and the discriminant of the quadratic equation (2.22). It means that we have to study the sign of $\mathfrak{P}\left((k_+ k_-)^2\mathfrak{P} + (k_+ - k_-)\mathfrak{K}\right)$, where the expression in bracket is always positive for any positive elastic moduli and thickness of transformed layer ξ. As for elastic modulus, the following three cases can be listed.

(i) If

$$k_+ > k_- \qquad \text{and} \qquad \mathfrak{P} < 0, \tag{2.38}$$

therefore, $\chi(\sigma_0^*,\xi) > 0$ and $\sigma_0^* > 0$ correspond to the maximal value of $\chi(\sigma_0,\xi)$ as it is shown in Fig. 2.4a. Note that inequalities (2.38) can be rewritten through elastic moduli as

$$k_- < \frac{4\mu_+(3k_+ - 4\mu_+)}{9(4\mu_+ + 3k_+)}$$

The front can propagate only if the energy parameter, elastic moduli of the solid constituents and transformation strain are such that $\gamma > \gamma_*$ and only at stresses $\sigma \in [\sigma^{\mathrm{I}}, \sigma^{\mathrm{II}}]$, where σ^{I} and σ^{II} are the roots of the quadratic equation $\chi(\sigma_0) - \gamma = 0$. Both roots are positive if $\gamma_* < \gamma < \gamma_0$, and the front cannot propagate without applied tension $\sigma_0 > \sigma^{\mathrm{I}} > 0$. If the front can propagate at $\sigma_0 = 0$ then $\gamma > \gamma_0$ and the roots have different signs, $\sigma^{\mathrm{I}} < 0$, $\sigma^{\mathrm{II}} > 0$. The front cannot propagate at $\sigma_0 > \sigma^{\mathrm{II}}$ and $\sigma_0 < \sigma^{\mathrm{I}}$, i.e. the propagation is blocked starting from some stress in both compression and tension.

(ii) If the elastic moduli satisfied the inequalities

$$k_+ > k_- \qquad \text{and} \qquad \mathfrak{P} > 0,$$

which can be rewritten as follows

$$k_+ > k_- > \frac{4\mu_+(3k_+ - 4\mu_+)}{9(4\mu_+ + 3k_+)}$$

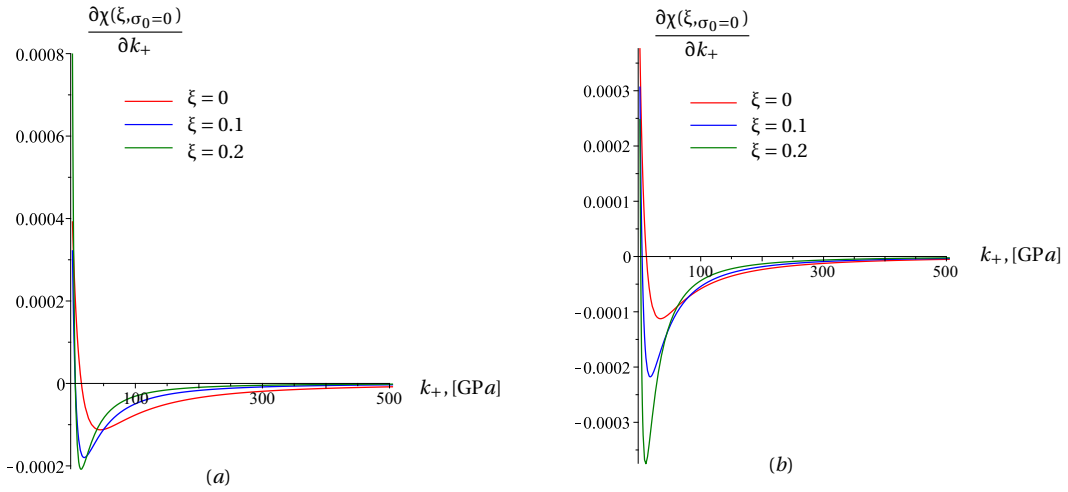

Figure 2.12: Spherical reaction front: behavior of $\frac{\partial\chi(\xi,\sigma_0=0)}{\partial k_+}$ at different position of the reaction front for the cases a) $k_+ > k_-$ and b) $k_+ < k_-$ front

then $\sigma_0^* > 0$ as in the case (i), but the minimal value of χ is negative, $\chi(\sigma_0^*) < 0$. Then front may propagate even at negative jump of the chemical energies, $\gamma < 0$, but such that $\gamma > -|\gamma_*|$, and at stresses σ_0 such that $\chi(\sigma_0^*) < \chi(\sigma_0) < \gamma < 0$.

Since $\sigma_0^* > 0$ at $k_+ > k_-$, the increase of tensile stress from $\sigma_0 = 0$ until σ_0^* accelerates the reaction front in both cases (i) and (ii). Further increase of σ_0 retards the front until blocking at σ^{II}. On the whole, if $|\sigma_0 - \sigma_0^*|$ increases then the front velocity decreases until zero.

(iii) If $k_+ < k_-$ then $\gamma_0 < \gamma_*$, $\sigma_0^* < 0$, and $\chi(\sigma_0^*) > 0$ corresponds to the maximal value on the dependence $\chi(\sigma_0)$. If $\gamma < \gamma_*$ then the front may propagate at any σ_0. If $\gamma_0 < \gamma < \gamma_*$ then the propagation of the front is blocked at $\sigma_0 \in [\sigma^I, \sigma^{II}]$, in contrast to the case $k_+ > k_-$. On the other hand, the spherical reaction front may start propagate at proper tension $\sigma_0 > \sigma^{II}$ or compression $\sigma_0 < \sigma^I$ even if it is blocked in the underformed state σ_0. In this case the front can propagate at any γ at some external loading.

By (2.22) and (2.37), the bulk and shear elastic modules, k_+ and μ_+, affect the dependence $\chi(\sigma_0)$ and, thus, the dependence of c_{eq}/c_* and the reaction front velocity on σ_0 via parameters $(k_+ - k_-)$, $\mathfrak{P}$ and $\mathfrak{K}$, and the stress σ_0^* is determined by the $k_+k_-\vartheta^{tr}/(k_+ - k_-)$. One can examine how k_+ affects the dependence $\chi(\sigma_0)$ and the extrema values $\chi(\sigma_0^*)$ and σ_0^*. Note, that from the form of the function $\chi(\sigma_0, \xi)$ (see eq.(2.22)), we can study separately the influence of σ_0 and ξ, since the terms containing σ_0 do not contain ξ, and vice versa. From (2.23) at $\xi = 0$ it follows that

$$\frac{\partial\chi(\sigma_0,\xi=0)}{\partial k_+} = \frac{(\sigma_0(3k_- + 4\mu_+) - 4k_-\mu_+\vartheta^{tr})}{2k_-^2(3k_+ + 4\mu_+)^3}\Big(\sigma_0\left(4\mu_+(4\mu_+ + 15k_-) + 9k_+(k_- - 4\mu_+)\right) + \\ + k_-\mu_+\vartheta^{tr}\left(9k_+ - 4\mu_+\right)\Big) \le 0$$

so that

$$\frac{\partial\chi(\sigma_0,\xi=0)}{\partial k_+} \ge 0 \quad \text{if} \quad k_+ > k_- \quad \text{and} \quad \begin{cases} (3k_- + 4\mu_+)\sigma_0 > 4k_-\mu_+\vartheta^{tr} \\ 12\mu_+k_+k_-\vartheta^{tr} + k_-(3k_+ + 4\mu_+)\sigma_0 > 12\mu_+(k_+ - k_-)\sigma_0 \end{cases}$$

$$\text{or} \quad \begin{cases} (3k_- + 4\mu_+)\sigma_0 < 4k_-\mu_+\vartheta^{tr} \\ 12\mu_+k_+k_-\vartheta^{tr} + k_-(3k_+ + 4\mu_+)\sigma_0 < 12\mu_+(k_+ - k_-)\sigma_0 \end{cases}$$

$$\text{if} \quad k_+ < k_- \quad \text{and} \quad (3k_- + 4\mu_+)\sigma_0 > 4k_-\mu_+\vartheta^{tr}$$

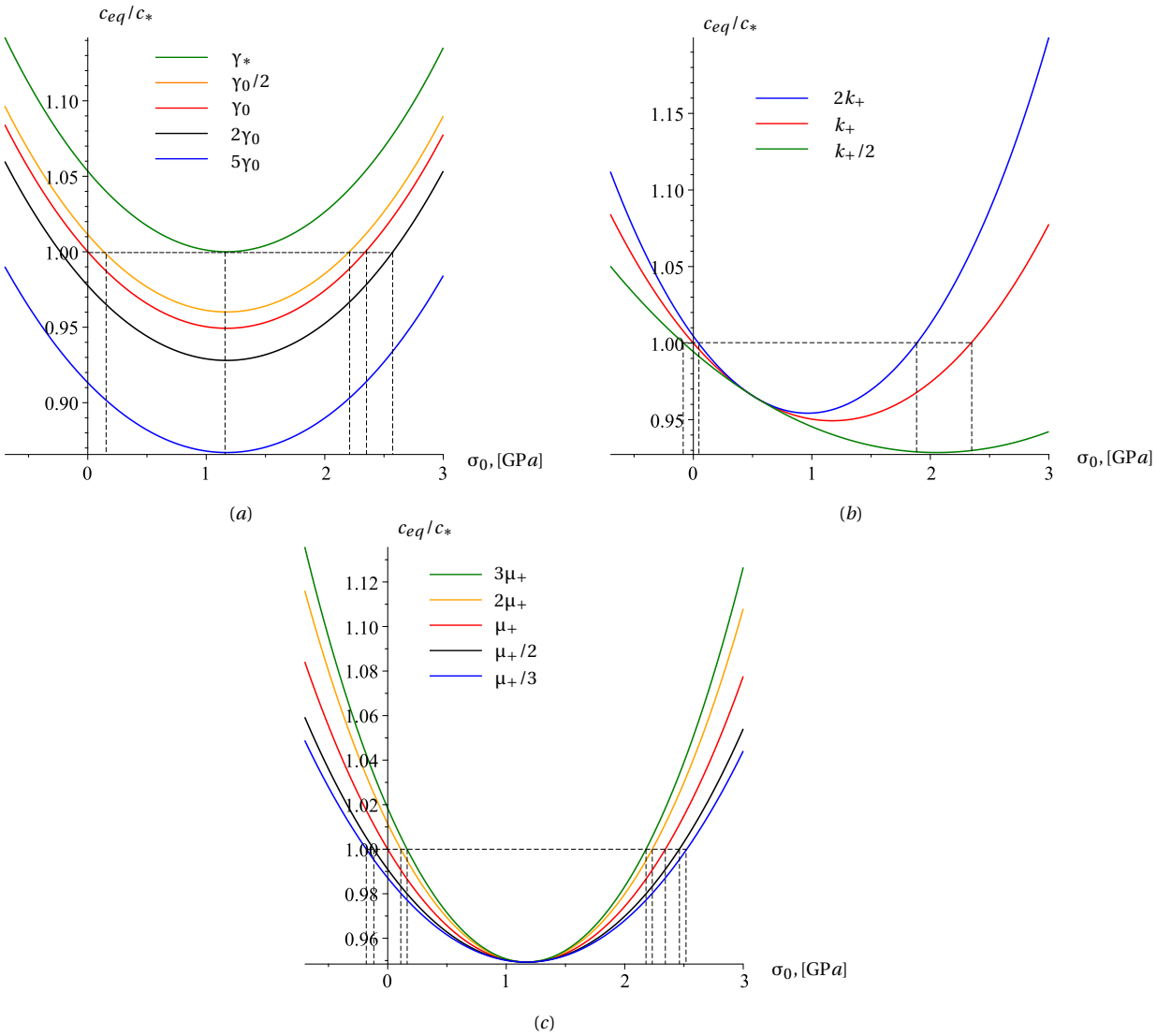

Figure 2.13: Spherical reaction front: dependencies of the equilibrium concentration on external stress σ_0 for the case $k_+ > k_-$: (*a*) for different values of the energy parameter γ; (*b*) for different values of bulk modulus k_+; (*c*) different values of μ_+.

$$\frac{\partial\chi(\sigma_0,\xi=0)}{\partial k_+}\le 0 \quad \text{if} \quad k_+ > k_- \quad \text{and} \quad \begin{cases} (3k_- + 4\mu_+)\sigma_0 > 4k_-\mu_+\vartheta^{tr} \\ 12\mu_+k_+k_-\vartheta^{tr} + k_-(3k_+ + 4\mu_+)\sigma_0 < 12\mu_+(k_+ - k_-)\sigma_0 \end{cases}$$

$$\text{or} \quad \begin{cases} (3k_- + 4\mu_+)\sigma_0 < 4k_-\mu_+\vartheta^{tr} \\ 12\mu_+k_+k_-\vartheta^{tr} + k_-(3k_+ + 4\mu_+)\sigma_0 > 12\mu_+(k_+ - k_-)\sigma_0 \end{cases}$$

$$\text{if} \quad k_+ < k_- \quad \text{and} \quad (3k_- + 4\mu_+)\sigma_0 < 4k_-\mu_+\vartheta^{tr}$$

Such non-monotonic behaviour of $\dfrac{\partial\chi(\sigma_0,\xi=0)}{\partial k_+}$ is presented on Fig. 2.11 at various σ_0. It shows how k_+ affects the dependence $\chi(\sigma_0)$ at initial position of the reaction front, $\xi = 0$.

To study the influence of k_+ on $\chi(\sigma_0,\xi)$ for propagating reaction front, let $\sigma_0 = 0$. Then for various ξ, we have:

$$\frac{\partial\chi(\xi,\sigma_0=0)}{\partial k_+} = \frac{\left(2\mu_+k_-\vartheta^{tr}\right)^2\mathfrak{z}\left(k_+(\mathfrak{z}-2)(4\mu_+(\mathfrak{z}-1)-9k_-)-4\mu_+k_-\mathfrak{z}^2\right)}{\left(k_+(\mu_+(\mathfrak{z}-1)-3k_-)-4\mu_+k_-\mathfrak{z}\right)^3}, \qquad \mathfrak{z} = (1-\xi)^3, \quad \mathfrak{z}\in[0,1]$$

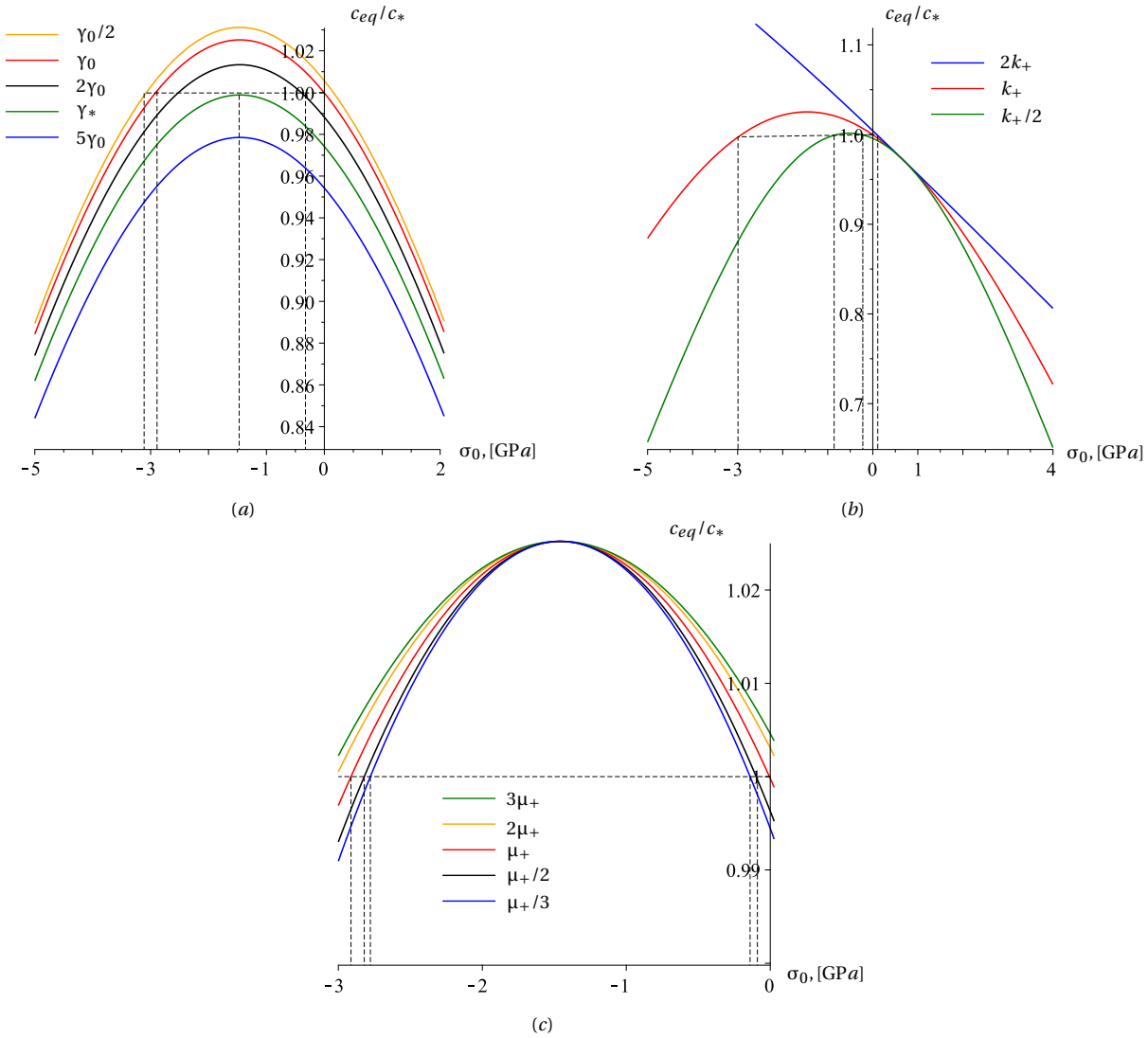

Figure 2.14: Spherical reaction front: dependencies of the equilibrium concentration on external stress σ_0 for the case $k_+ < k_-$: (*a*) for different values of the energy parameter γ; (*b*) for different values of bulk modulus k_+; (*c*) different values of μ_+.

so that

$$\frac{\partial\chi(\xi,\sigma_0=0)}{\partial k_+}\geq 0 \quad \text{if} \quad k_+ > k_- \quad \text{and} \quad \begin{cases} k_+(3k_- + 4\mu_+) < 4\mu_+(k_+ - k_-)\mathfrak{z} \\ 9(3k_- + 4\mu_+)\mathfrak{z} < 8\mu_+ k_+^2(9k_- + 4\mu_+) \end{cases}$$

$$\text{or} \quad \begin{cases} k_+(3k_- + 4\mu_+) > 4\mu_+(k_+ - k_-)\mathfrak{z} \\ 9(3k_- + 4\mu_+)\mathfrak{z} > 8\mu_+ k_+^2(9k_- + 4\mu_+) \end{cases}$$

$$\text{if} \quad k_+ < k_- \quad \text{and} \quad k_+(3k_- + 4\mu_+) < 4\mu_+(k_+ - k_-)\mathfrak{z}$$

$$\frac{\partial\chi(\xi,\sigma_0=0)}{\partial k_+}\leq 0 \quad \text{if} \quad k_+ > k_- \quad \text{and} \quad 16\frac{\mu_+^2}{k_+^2}(k_+ - k_-)^2\mathfrak{z}^2 < (3k_- + 4\mu_+)^2 < \frac{32}{9}\mu_+^2 k_+(k_+ - k_-)(9k_- + 4\mu_+)$$

$$\text{or} \quad 16\frac{\mu_+^2}{k_+^2}(k_+ - k_-)^2\mathfrak{z}^2 > (3k_- + 4\mu_+)^2 > \frac{32}{9}\mu_+^2 k_+(k_+ - k_-)(9k_- + 4\mu_+)$$

such function is shown on Fig. 2.12 for different position of the reaction front.

Then, if the front propagates at a given set of parameters, further increase of k_+ firstly decreases $\chi(\sigma_0,\xi)$, but following increase of bulk modulus of the transformed material as well as front propagation increases $\chi(\sigma_0,\xi)$ accelerates the reaction.

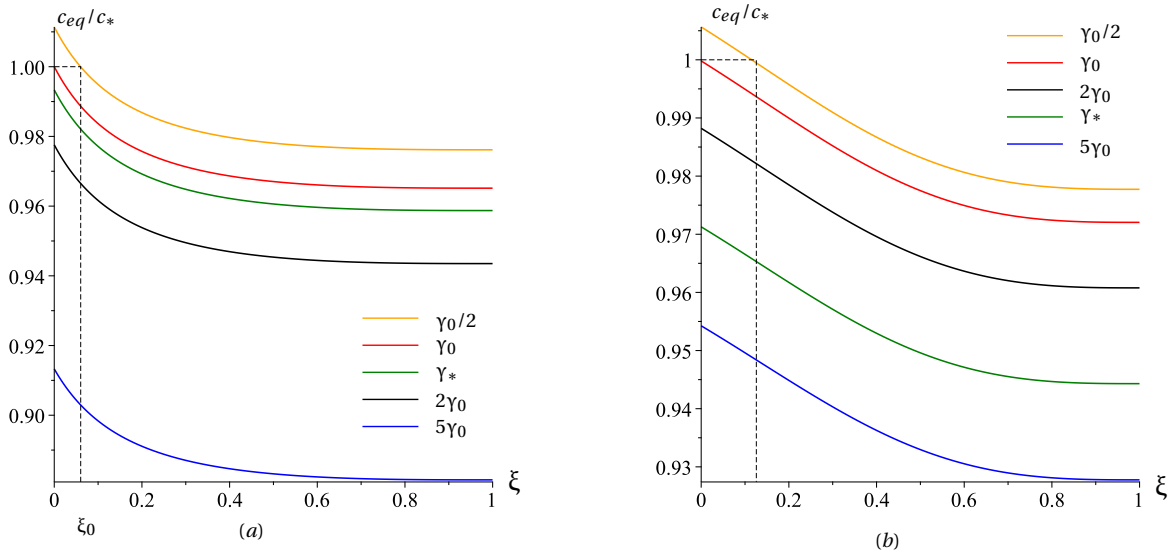

Figure 2.15: Spherical reaction front: Dependencies of equilibrium concentration on the reaction front relative position $\xi = h/R$ at $\sigma_0 = 0$ and various values of energy parameter γ for the case: *a*) $k_+ > k_-$ and *b*) $k_+ < k_-$

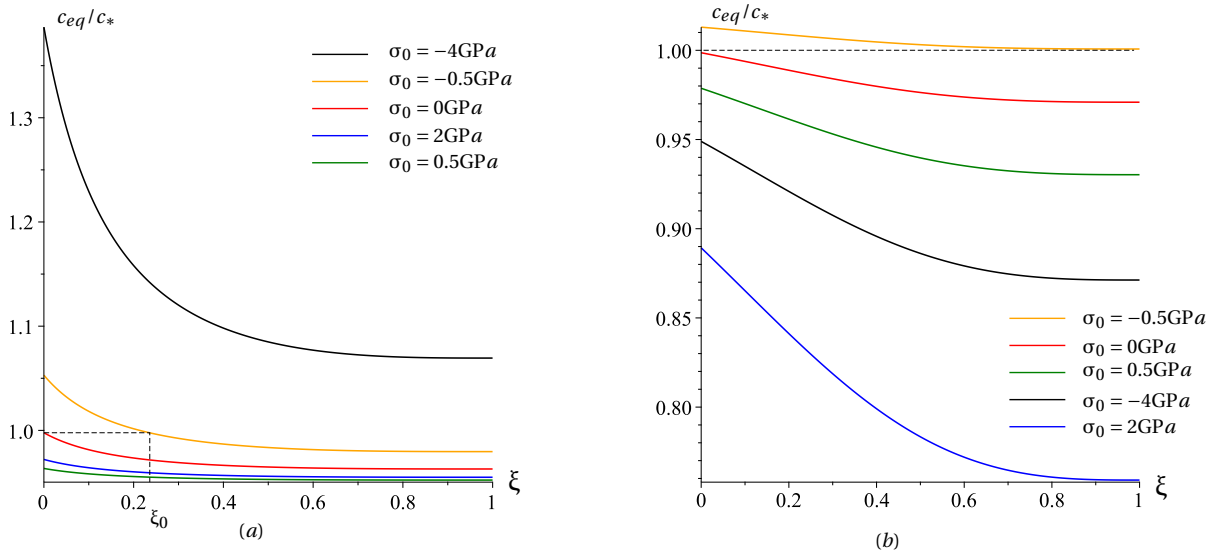

Figure 2.16: Spherical reaction front: Dependencies of equilibrium concentration on the reaction front relative position $\xi = h/R$ at $\gamma = 1.1\gamma_0$ and various values of σ_0 for the case: *a*) $k_+ > k_-$ and *b*) $k_+ < k_-$

The dependence of extrema stress σ_0^* on bulk module k_+ is defined by relations between elastic moduli. Since, by (2.22)

$$\frac{\partial \sigma_0^*}{\partial k_+} = -\frac{k_-^2 \vartheta^{tr}}{(k_+ - k_-)^2}$$

one can see that if $k_+ < k_-$ then the extrema point σ_0^* in Fig. 2.4*b* is shifted to the left/right if k_+ increases/decreases. If $k_+ > k_-$, then the extrema point σ_0^* in Fig. 2.4*a* is also shifted to the left/right if k_+ increases/decreases.

More detailed quantitative analysis is presented in Fig. 2.13 and Fig. 2.14, where the dependencies of the relative equilibrium concentration c_{eq}^*/c_* on the external stress σ_0 for initial position of the reaction front, $\xi = 0$, at various values of the energy parameter γ and the bulk and shear modules k_+, μ_+ of the transformed material are shown for the cases $k_+ > k_-$ and $k_+ < k_-$, respectively. The reference values of the parameters for the cases $k_+ > k_-$ and $k_+ < k_-$ are given

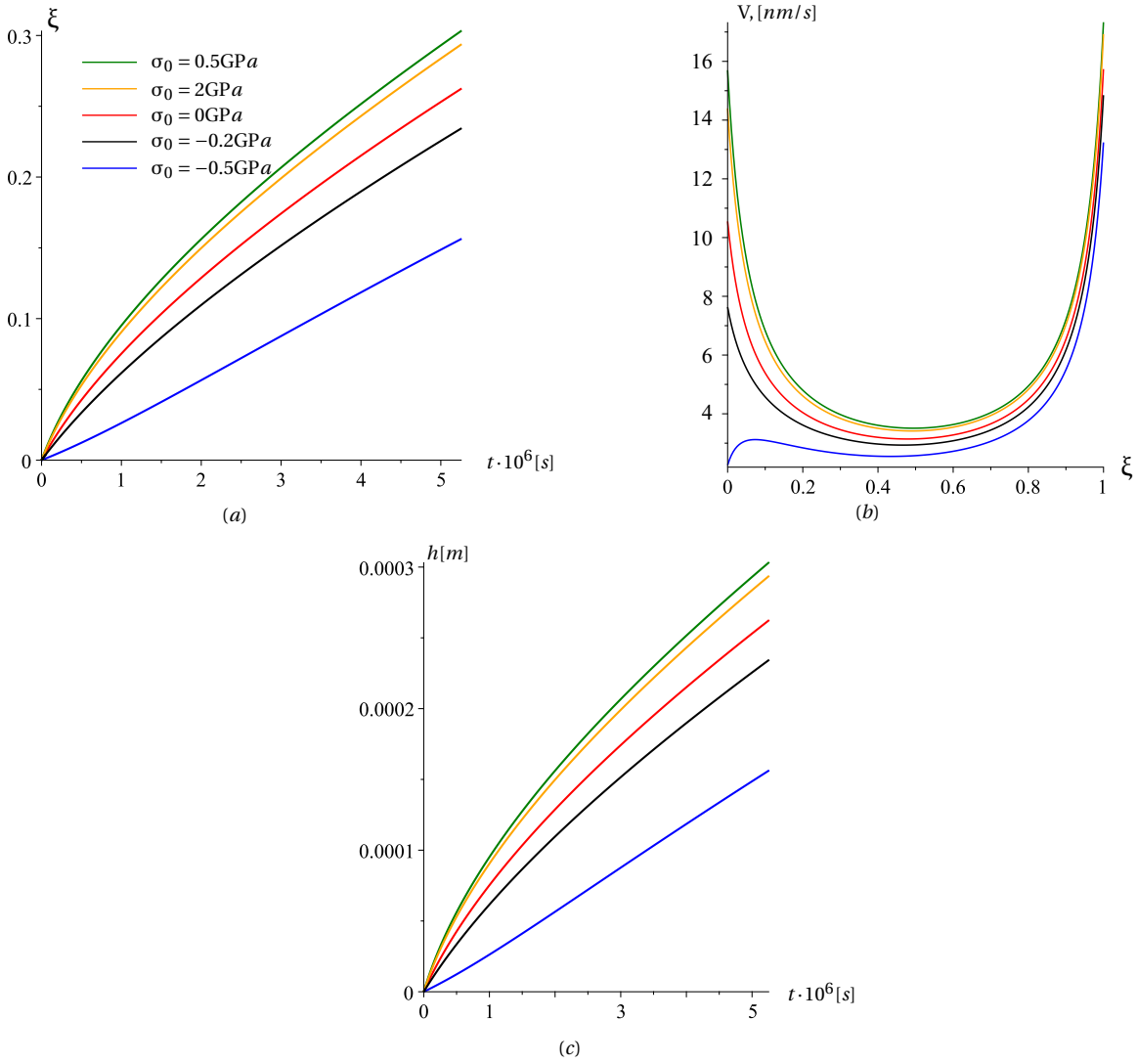

Figure 2.17: Spherical reaction front: kinetics of the reaction front at various values of external loading σ_0 for the case $k_+ > k_-$. Dependencies of the dimensionless front position on time (a), and the front velocity on the front position (b); (c) – the front position versus time at the initial stage of the front propagation

in Tables 2.1 and 2.2, respectively. Only the parameters which differ in two cases are shown in Table 2.2.

Fig. 2.13a and Fig. 2.14a reflect the competition between strain and chemical energies at $k_+ > k_-$ and $k_+ < k_-$, respectively. If $\gamma = \gamma_0$ then the dependence of c_{eq}/c_* on σ_0 passes through the point $\sigma_0 = 0$, $c_{eq}/c_* = 1$. If $k_+ > k_-$ and $\gamma = \gamma_0$ then the front may propagate only at tension restricted by $\hat{\sigma} = 2k_+k_-\vartheta^{tr}/(k_+ - k_-)$ (Fig. 2.13a). One can see how increasing γ results in enlarging the interval of allowed stresses σ_0 (see the curves for $\gamma = 2\gamma_0$ and $\gamma = 5\gamma_0$) and how the decrease of γ shortens and shifts the interval of the stresses at $\gamma_* < \gamma < \gamma_0$.

If $k_+ < k_-$ and $\gamma = \gamma_0$ then the front may propagate only at tension $\sigma_0 > 0$ or compression $\sigma_0 < \hat{\sigma} = 2k_+k_-\vartheta^{tr}/(k_+ - k_-)$ (Fig. 2.14a). If $\gamma < \gamma_0$, for example, $\gamma = \gamma_0/2$, then the front can propagate only if additional tension $\sigma_0 > \sigma^{II} > 0$ or compression $\sigma_0 < \sigma^{I} < 0$ is applied. If $\gamma > \gamma_*$ (e.g., $\gamma = 5\gamma_0$ in Fig. 2.14a) then the front may propagate at any σ_0.

One can also see in Fig. 2.4b, Fig. 2.14a that if, at $k_+ < k_-$, the front can propagate at some σ_0 then further increasing of the absolute value $|\sigma_0|$ decreases c^*_{eq}/c_* and, thus, increases the front velocity.

Fig. 2.13b,c and Fig. 2.14b,c characterize quantitatively the role of volume and shear strain energies via the influence of the bulk module k_+ and shear module μ_+ on the dependencies of

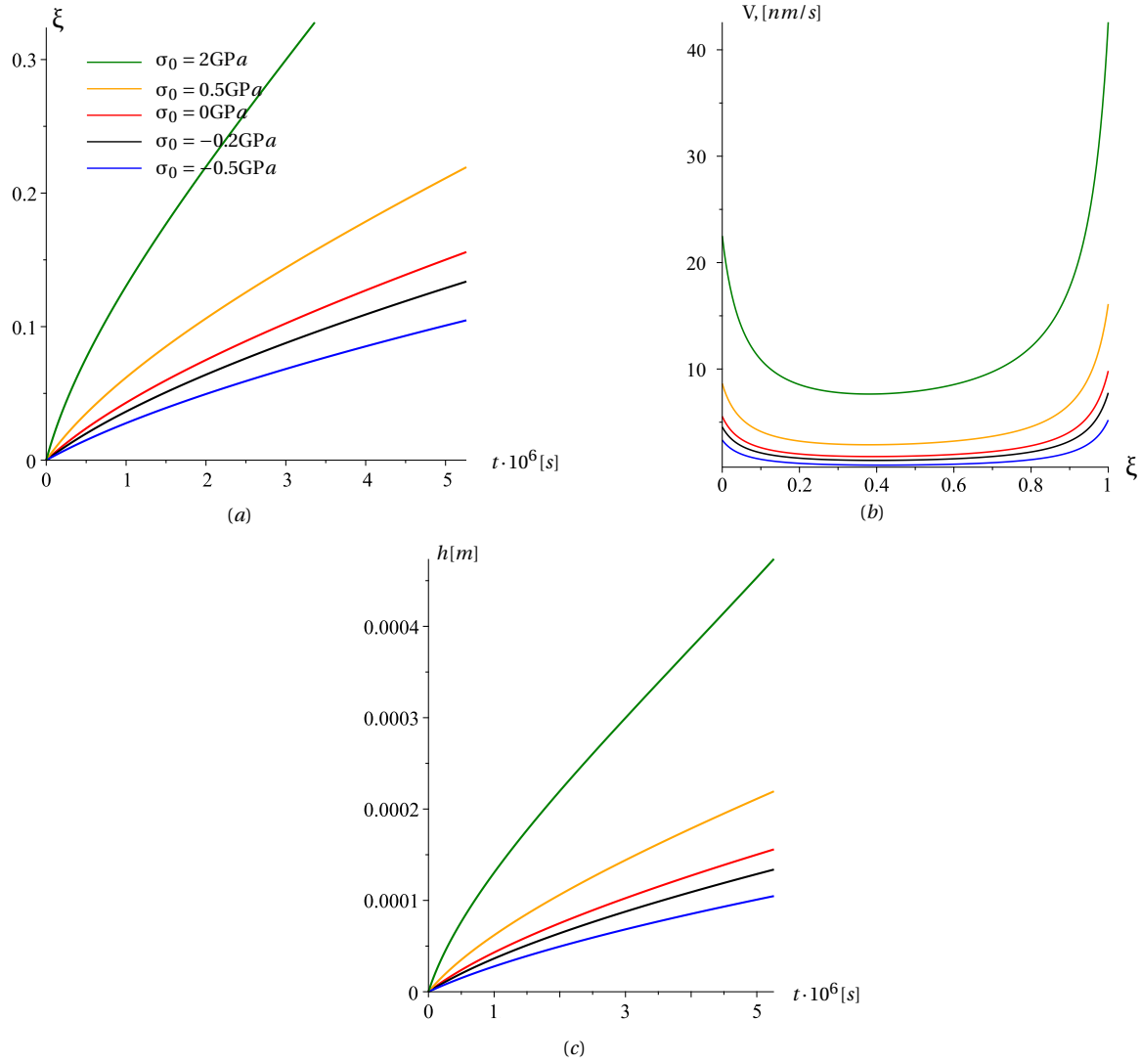

Figure 2.18: Spherical reaction front: kinetics of the reaction front at various values of external loading σ_0 for the case $k_+ < k_-$. Dependencies of the dimensionless front position on time (*a*), and the front velocity on the front position (b); (c) – the front position versus time at the initial stage of the front propagation

c^*_{eq}/c_* on σ_0 at initial position of the reaction front, $\xi = 0$. We can see from Fig. 2.13*c* and Fig. 2.14 that shear module does not affect on extrema of χ (it comes from (2.37)), when in the case of planar front propagation it affects. In the spherical geometry, the increasing of shear module of the transformed material decreases the range of allowable loading for chemical reaction propagation, as well as decelerates the reaction velocity.

If the reaction front moves then stresses at the front changes and, thus, the equilibrium concentration changes. Let us consider how $\chi(\sigma_0,\xi)$ changes if the reaction front propagates. Let the stress σ_0 be given. If the front propagates, then $\chi(\sigma_0,\xi)$ changes according to (2.22) so that

$$\frac{\partial\chi(\sigma_0)}{\partial\xi} = -\frac{12\mu_+\left(k_+k_-\vartheta^{tr}(1-\xi)\right)^2\left(16\mu_+^2+12\mu_+(3k_- - k_+)+9k_+k_-\right)}{\left(4\mu_+\left(k_-(1-\xi)^3+k_+\xi(\xi^2-3\xi+3)\right)+3k_+k_-\right)^3} \le 0$$

Then from above relationships it follows that increase of relative thickness of the transformed layer ξ increases $\chi(\sigma_0)$ and decreases equilibrium concentration c_{eq}. Thus, the equilibrium concentration at the reaction front decreases as the front propagates if the external stress is given as a boundary condition.

If the external stress σ_0 and energy parameter γ are such that $c_{eq}(\xi = 0|\sigma_0,\gamma) \ge c_*$ then the reaction can not start from the external surface of the sphere, but can start if an initial layer of a new

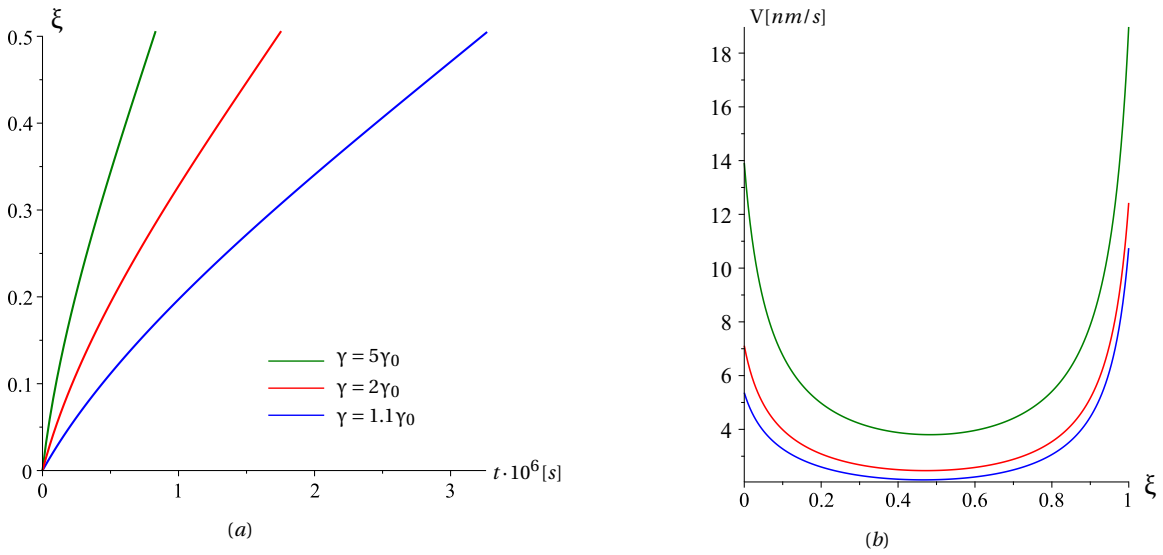

Figure 2.19: Spherical reaction front: dependencies of the front position on time (*a*), and the front velocity on the front position (*b*) at various values of energy parameter γ for the case $k_+ > k_-$

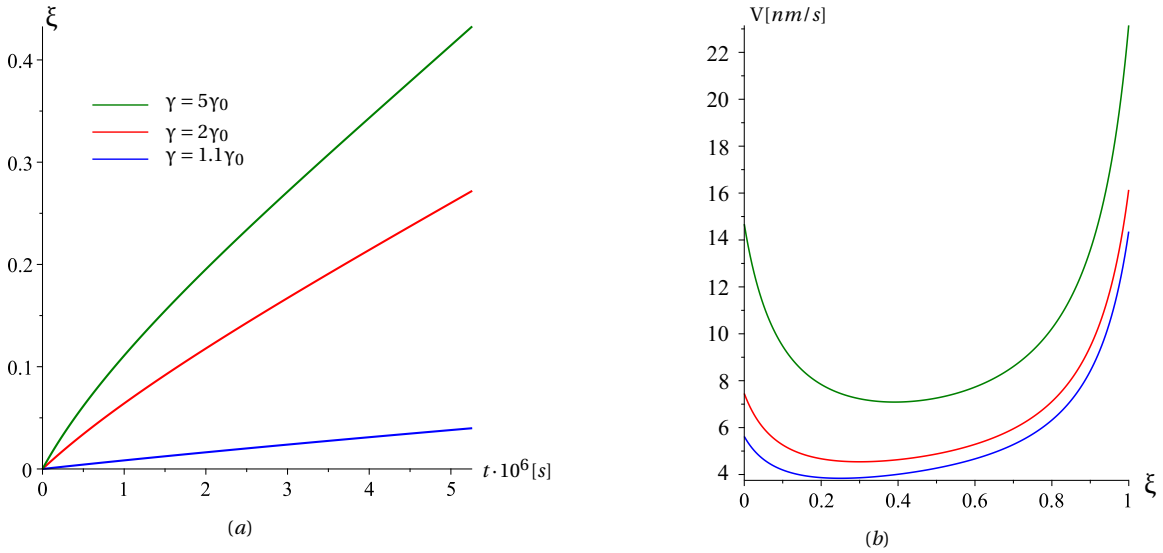

Figure 2.20: Spherical reaction front: dependencies of the front position on time (*a*), and the front velocity on the front position (*b*) at various values of energy parameter γ fro the case $k_+ < k_-$

material already exists of thickness $\xi_0 : c(\xi_0|\sigma_0, \gamma) \geq c_*$ (Fig. 2.15). Fig. 2.16 shows the dependencies of the equilibrium concentration on the thickness of transformed material at various external stresses. In the case of the sphere, the equilibrium concentration decreases with propagation of the reaction front, and this in turn accelerates the reaction.

Fig. 2.15 shows the dependence of the equilibrium concentration on the reaction front position at fixed stress at the sphere surface. If the stress σ_0 is given then the layer growth decreases the equilibrium concentration and enhances the reaction (Fig. 2.15). The yellow curves in Fig. 2.15 demonstrates that a thin layer of a new material can act as a protective layer if the value of the equilibrium concentration exceeds the gas solubility. External tension decreases the equilibrium concentration while compression increases it. Note also that at different values of the energy parameter the curves are similar but pass lower at larger values of γ or higher at smaller one. This means that the temperature change can initiate the reaction or, conversely, block it.

The dependencies of the front position on time and the front velocity on the front position for various values of external stress σ_0, energy parameter γ, bulk and shear moduli k_+ and μ_+ are

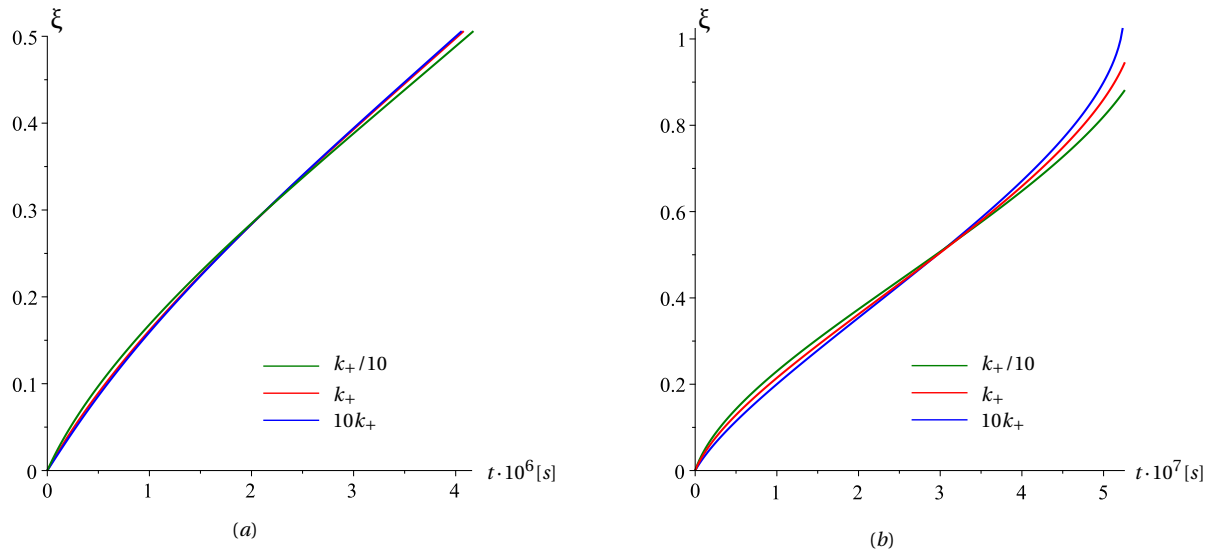

Figure 2.21: Spherical reaction front: dependencies of the front position on time at various values of bulk modulus k_+ for the case (*a*) $k_+ > k_-$ and (*b*) $k_+ < k_-$ energy parameter γ

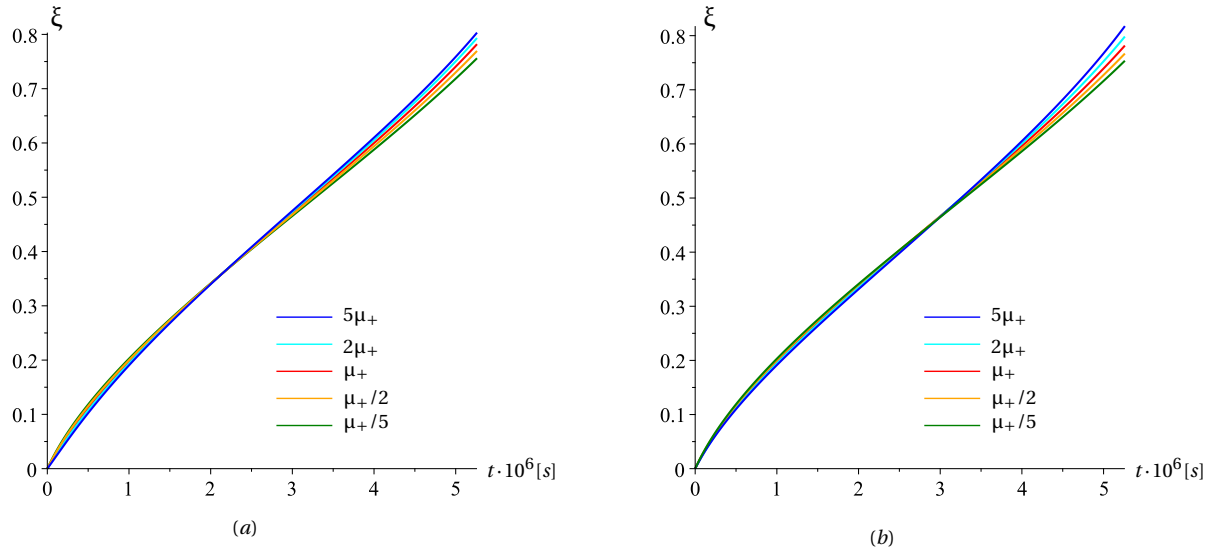

Figure 2.22: Spherical reaction front: dependencies of the front position on time at various values of shear modulus μ_+ for the case (*a*) $k_+ > k_-$ and (*b*) $k_+ < k_-$

shown in Fig. 2.17 – Fig. 2.23. One can see how the strains can retard or accelerate the reaction front, how the increase of the energy parameter accelerates the front, how elastic moduli affect the front kinetics.

Note, that in the case of the spherical reaction front the reaction can propagate not only with parabolic law: logarithmic law is observed in the case $k_+ < k_-$ (see e.g. Fig. 2.21*b* and Fig. 2.22*b*). The behaviour of kinetic depends on the mechanical properties of the initial and transformed materials and of geometry of the structure element (body's geometry affect the diffusion equation, which defines the form of the kinetic equation (1.34), while the stress-strain state has influence on the reaction velocity through the equilibrium concentration c_{eq} (1.33), (1.34)). The front velocity is shown in Fig. 2.17*b*, Fig. 2.18*b* at various values of external loading σ_0 and in Fig. 2.19*b* and Fig. 2.20*b* at various γ. From these plots we can conclude, that initially the reaction front velocity decelerates along the front propagation and from some position it increases. Such kinetics was described by Cabrera-Mott model and this behavior was observed in the experiments (see i.e., [6, 33, 34, 46, 77, 79, 150, 160]). Depending of the material properties and structure geometry,

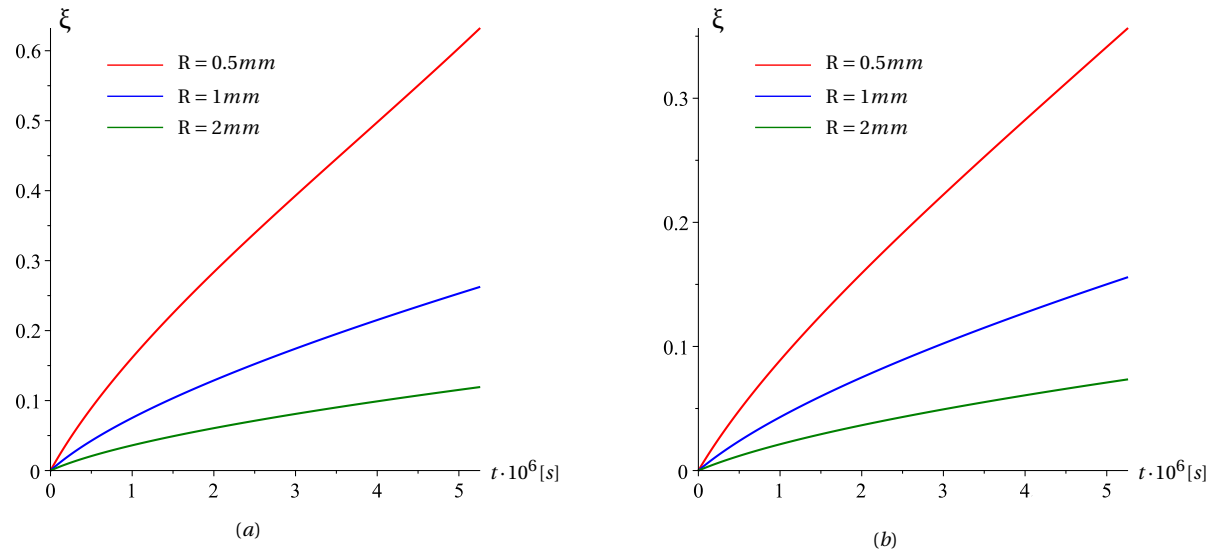

Figure 2.23: Spherical reaction front: dependencies of the front position on time at various initial radius R of the sphere fro the case (*a*) $k_+ > k_-$ and (*b*) $k_+ < k_-$

non-parabolic kinetics can be reached or not.

The influence of the elastic modulus k_+ and μ_+ of transformed material is shown in Fig. 2.21 and Fig. 2.22. Initially, increase of k_+ decelerates the reaction, but with front propagation we see that the effect become inverse, and from some moment as bigger k_+ as faster the reaction kinetics (Fig. 2.21). Similarly, shear modulus μ_+ affects the reaction velocity: firstly, up to some moment, as smaller the value of μ_+ as faster the reaction goes, but at some position of the reaction front the dependence changes, and increasing of μ_+ accelerates the reaction at the end.

2.2.3 Cylindrical reaction front

In this last section, similar to how it was done for the chemical reaction in the plane and sphere, the dependencies of the reaction position on time and of the reaction front velocity on the front position in a cylinder will be presented for various values of the external stresses σ_0, energy parameter γ and elastic moduli. Given that, by (2.26), the kinetics of the reaction front accelerates if c_{eq}/c_* decreases and, respectively, the reaction kinetics slows down if c_{eq}/c_* increases, knowing how the parameters affect the equilibrium concentration the influence of various parameters on the reaction front behavior can be predicted qualitatively.

By (2.33), the reaction front can propagate only if the stress-strain state at the front and the energy parameter are such that $c_{eq} < c_*$. We study further how the condition $c_{eq} < c_*$ is affected by the parameters. By (2.32), this is possible only if the transformation strain, external stress, elasticity parameters and the energy parameter are such that $\chi < \gamma$. By (2.31), in the considered case this condition takes the form

$$\chi(\sigma_0) - \gamma = \frac{1}{\mathscr{U}}\left((\mathscr{K}_+ - \mathscr{K}_-)\mathscr{P}\sigma_0^2 - 2\mathscr{K}_- k_+ \mathscr{P}\vartheta^{tr}\sigma_0\right) - (\gamma - \gamma_0) < 0$$

where

$$\gamma_0 = \frac{\mu_+ k_+ \mathscr{Q}(\vartheta^{tr})^2}{\mathscr{U}}$$

is the critical value of the parameter γ in the sense that the reaction front may propagate at the external stress $\sigma_0 = 0$ only if

$$\gamma > \gamma_0$$

The dependencies of c_{eq}/c_* on external stress σ_0 for the spherical front are schematically shown in Fig. 2.4. The extrema is reached at $\sigma_0 = \sigma_0^*$ with $c_{eq}/c_* = c_{eq}^*/c_*$:

$$\sigma_0^* = \frac{k_+\mathscr{K}_-\vartheta^{tr}}{\mathscr{K}_+ - \mathscr{K}_-}, \qquad \frac{c_{eq}^*}{c_*} = \exp\left\{\frac{n_-\mathscr{M}_-}{\rho_-}\frac{\left(\chi(\sigma_0^*) - \gamma\right)}{R_gT}\right\}, \qquad \chi(\sigma_0^*) = \frac{-k_+(\vartheta^{tr})^2}{\mathscr{U}}\left(\mu_+\mathscr{Q} + \frac{\mathscr{P}k_+\mathscr{K}_-^2}{\mathscr{K}_+ - \mathscr{K}_-}\right) \equiv \gamma_* \tag{2.39}$$

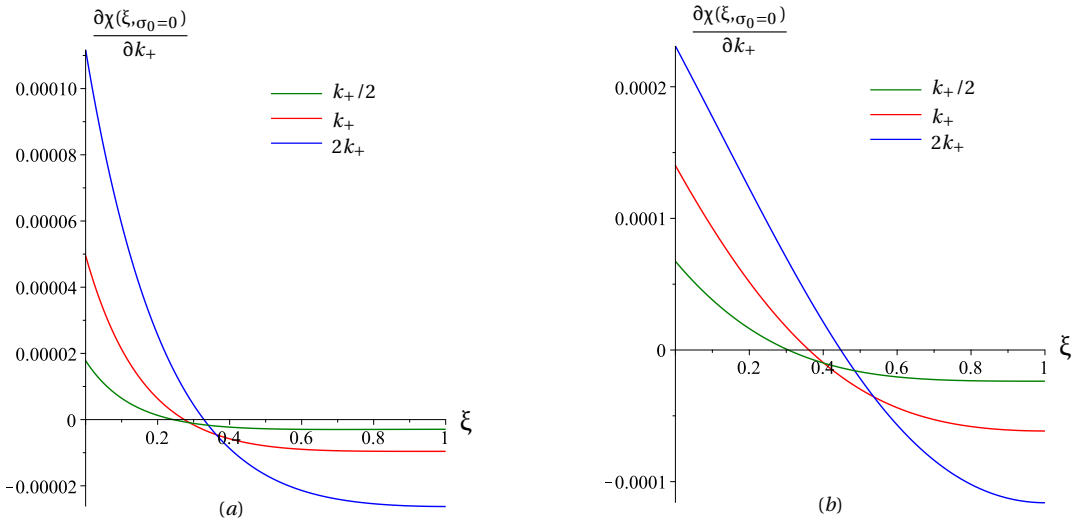

Figure 2.24: Cylindrical reaction front: behavior of $\frac{\partial\chi(\xi,\sigma_0=0)}{\partial k_+}$ at different position of the reaction front for the cases a) $\mathscr{K}_+ > \mathscr{K}_-$ and b) $\mathscr{K}_+ < \mathscr{K}_-$ front

The character of the dependence of c_{eq}/c_* on σ_0 and the sign of σ_0^* and $\chi(\sigma_0^*)$ are determined by the sign of $(\mathscr{K}_+ - \mathscr{K}_-)$ and the sign of $(\mathscr{P}k_+\mathscr{K}_-^+ + \mu_+\mathscr{Q}(\mathscr{K}_+ - \mathscr{K}_-))$. The following cases can be listed:

(i) if

$$\mathscr{K}_+ > \mathscr{K}_- \quad \text{and} \quad 0 > \mathscr{Q} > \frac{\mathscr{P}k_+\mathscr{K}_-^2}{\mathscr{K}_- - \mathscr{K}_+}$$

therefore $\chi(\sigma_0^*, \xi) > 0$ and $\sigma_0^* > 0$ corresponds to the maximal value of $\chi(\sigma_0, \xi)$. Note that $\mathscr{Q}$ depends on the relative thickness of the transformed layer, and has a complex form. It can change the sign along with the front propagation.

(ii) If the elastic moduli and position of the reaction front satisfy the inequalities

$$\mathscr{K}_+ > \mathscr{K}_- \quad \text{and} \quad \left[\begin{array}{l} \mathscr{Q} > 0 \\ \mathscr{Q} < \dfrac{\mathscr{P}k_+\mathscr{K}_-^2}{\mathscr{K}_- - \mathscr{K}_+} \end{array}\right.$$

then $\sigma_0^* > 0$ as in the case (i), but the minimal value of χ is negative, $\chi(\sigma_0^*, \xi) < 0$. Then front may propagate even at negative jump of the chemical energies, $\gamma < 0$, but such that $\gamma > -|\gamma_*|$, and at stresses σ_0 such that $\chi(\sigma_0^*) < \chi(\sigma_0) < \gamma < 0$.

(iii) if

$$\mathscr{K}_+ < \mathscr{K}_- \quad \text{and} \quad \mathscr{Q} > \frac{\mathscr{P}k_+\mathscr{K}_-^2}{\mathscr{K}_- - \mathscr{K}_+}$$

then $\gamma_0 < \gamma_*$, $\sigma_0^* < 0$, and $\chi(\sigma_0^*) > 0$ corresponds to the maximal value on the dependence $\chi(\sigma_0)$. If $\gamma < \gamma_*$ then the front may propagate at any σ_0. If $\gamma_0 < \gamma < \gamma_*$ then the propagation of the front is blocked at $\sigma_0 \in [\sigma^{\mathrm{I}}, \sigma^{\mathrm{II}}]$, in contrast to the case $k_+ > k_-$. On the other hand, the spherical reaction

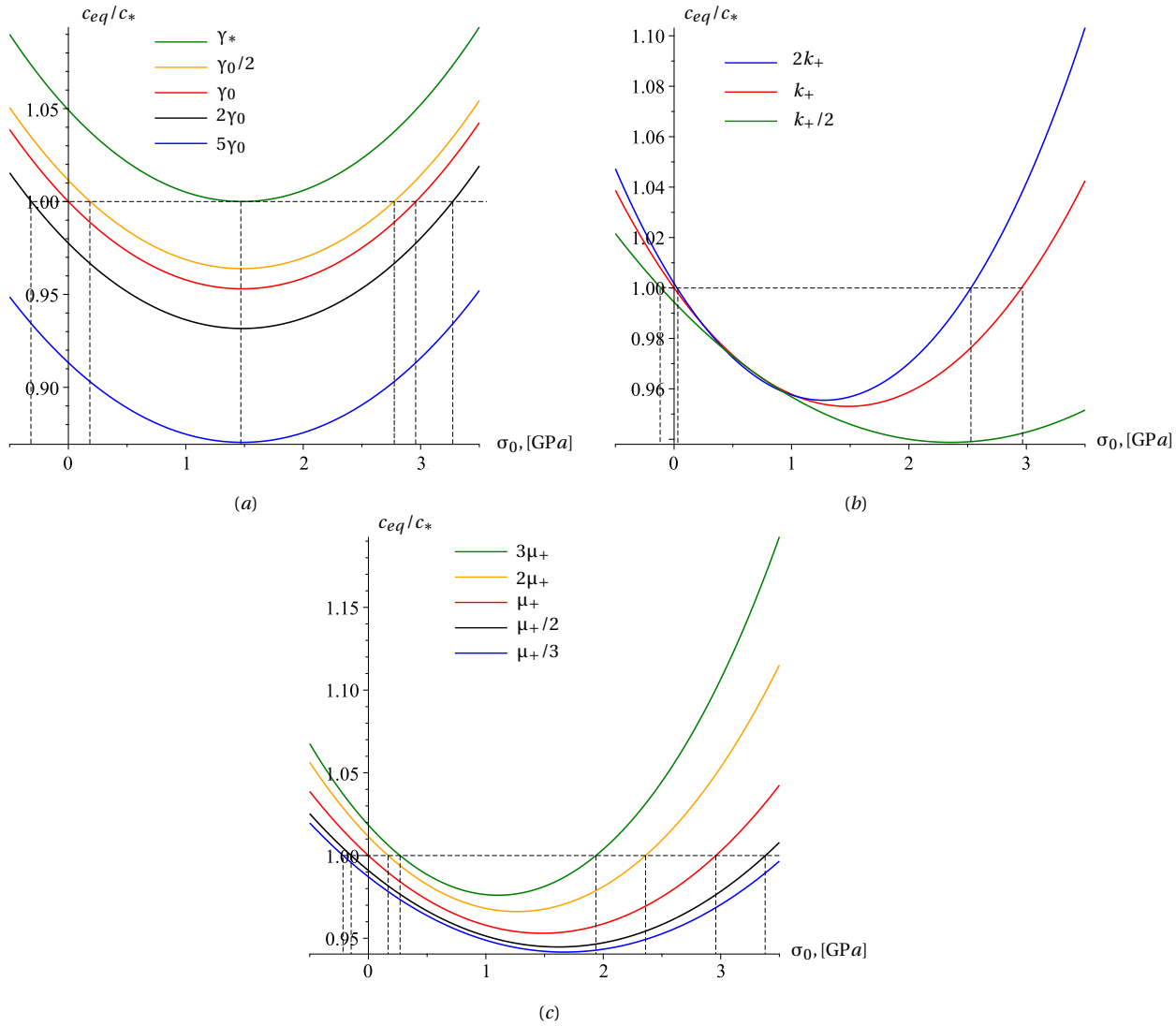

Figure 2.25: Cylindrical reaction front: dependencies of the equilibrium concentration on external strain ε_0 for the case $\mathscr{K}_+ > \mathscr{K}_-$: (*a*) for different values of the energy parameter γ; (*b*) for different values of bulk modulus k_+; (*c*) different values of μ_+.

front may start propagating at proper tension $\sigma_0 > \sigma^{\mathrm{II}}$ or compression $\sigma_0 < \sigma^{\mathrm{I}}$ even if it is blocked in the underformed state σ_0. In this case the front can propagate at any γ at some external loading.

By (2.31) and (2.39), the bulk ans shear elastic modules, k_+ and μ_+, affect the dependence $\chi(\sigma_0,\xi)$ and, thus, the dependence of c_{eq}/c_* and the reaction front velocity on σ_0 via parameters $(\mathscr{K}_+ - \mathscr{K}_-)$, $\mathscr{P}$ and $\mathscr{Q}$. One can examine how k_+ affects the dependence $\chi(\sigma_0)$ and the extrema values $\chi(\sigma_0^*)$ and σ_0^*. Note, that from the form of the function $\chi(\sigma_0,\xi)$ we can study separately the influence of σ_0 and ξ, since the terms containing σ_0 do not contain ξ, and vice versa. From (2.32) at $\xi = 0$ it follows that

$$\frac{\partial\chi(\sigma_0,\xi=0)}{\partial k_+} = \frac{\left(4\mu_+\mathscr{K}_-\vartheta^{tr} - 3\sigma_0(\mathscr{K}_- + \mu_+)\right)^2}{2\mathscr{K}_-^2(3k_+ + 4\mu_+)^2} \geq 0$$

and for $\sigma_0 = 0$ at various ξ, we have:

$$\frac{\partial\chi(\xi,\sigma_0=0)}{\partial k_+} = \frac{3\left(\mu_+\vartheta^{tr}\right)^2\left(3(\mathscr{K}_- - \mu_+)\xi(\xi-2) + \mathscr{K}_+ + 3\mu_+\right)}{2\left(3\mu_+(\mathscr{K}_+ - \mathscr{K}_-)(\xi^2-2\xi) - \mathscr{K}_-(\mathscr{K}_+ + 3\mu_+)\right)^3}\Big(3\mu_+(\mathscr{K}_- - \mu_+)(\mathscr{K}_+ - \mathscr{K}_-)\xi^2(\xi^2-4\xi+4) -$$
$$- \mathscr{K}_-\left(\left(9k_+\mathscr{K}_- + \mu_+(8\mathscr{K}_- + \mathscr{K}_+ - 9\mu_+)\right)\xi(\xi-2) + 4(\mathscr{K}_+ + 3\mu_+)\mathscr{K}_-\right)\Big)$$

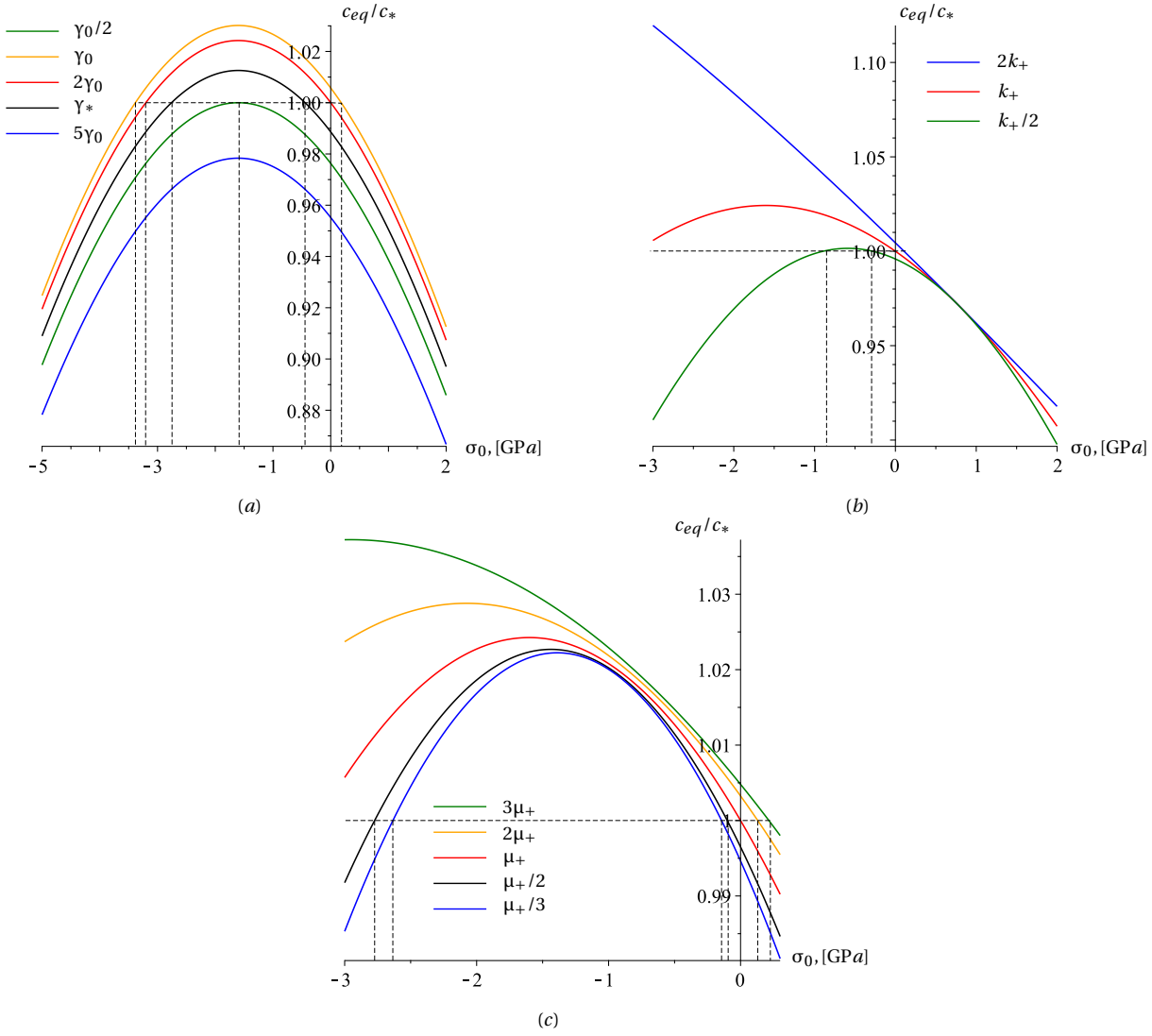

Figure 2.26: Cylindrical reaction front: dependencies of the equilibrium concentration on external strain ε_0 for the case $\mathscr{K}_+ < \mathscr{K}_-$: ($a$) for different values of the energy parameter γ; (b) for different values of bulk modulus k_+; (c) different values of μ_+.

In this case the behavior of derivative is non-monotonic, and it is shown on the Fig. 2.24.

More detailed quantitative analysis is presented in Fig. 2.25 and Fig. 2.26, where the dependencies of the relative equilibrium concentration c^*_{eq}/c_* on the external stress σ_0 for initial position of the reaction front, $\xi = 0$, at various values of the energy parameter γ and the bulk and shear modules k_+, μ_+ of the transformed material are shown for the cases $\mathscr{K}_+ > \mathscr{K}_-$ and $\mathscr{K}_+ < \mathscr{K}_-$, respectively. The reference values of the parameters for the cases $\mathscr{K}_+ > \mathscr{K}_-$ and $\mathscr{K}_+ < \mathscr{K}_-$ are given in Tables 2.1 and 2.2, respectively. Only the parameters differ in two cases are shown in Table 2.2.

Fig. 2.25a and Fig. 2.26a reflect the competition between strain and chemical energies at $\mathscr{K}_+ > \mathscr{K}_-$ and $\mathscr{K}_+ < \mathscr{K}_-$, respectively. If $\gamma = \gamma_0$ then the dependence of c_{eq}/c_* on σ_0 passes through the point $\sigma_0 = 0$, $c_{eq}/c_* = 1$. If $\mathscr{K}_+ > \mathscr{K}_-$ and $\gamma = \gamma_0$ then the front may propagate only at tension restricted by $\hat{\sigma} = 2k_+\mathscr{K}_-\vartheta^{tr}/(\mathscr{K}_+ - \mathscr{K}_-)$ (Fig. 2.25a). One can see how increasing γ results in enlarging the interval of allowed stresses σ_0 (see the curves for $\gamma = 2\gamma_0$ and $\gamma = 5\gamma_0$) and how the decrease of γ shortens and shifts the interval of the stresses at $\gamma_* < \gamma < \gamma_0$.

If $\mathscr{K}_+ < \mathscr{K}_-$ and $\gamma = \gamma_0$ then the front may propagate only at tension $\sigma_0 > 0$ or compression $\hat{\sigma} = 2k_+\mathscr{K}_-\vartheta^{tr}/(\mathscr{K}_+ - \mathscr{K}_-)$ (Fig. 2.26a). If $\gamma < \gamma_0$, for example, $\gamma = \gamma_0/2$, then the front can propagate only if additional tension $\sigma_0 > \sigma^{\mathrm{II}} > 0$ or compression $\sigma_0 < \sigma^{\mathrm{I}} < 0$ is applied. If $\gamma > \gamma_*$ (corresponds to $\gamma = 5\gamma_0$ in Fig. 2.26a), then the front may propagate at any σ_0.

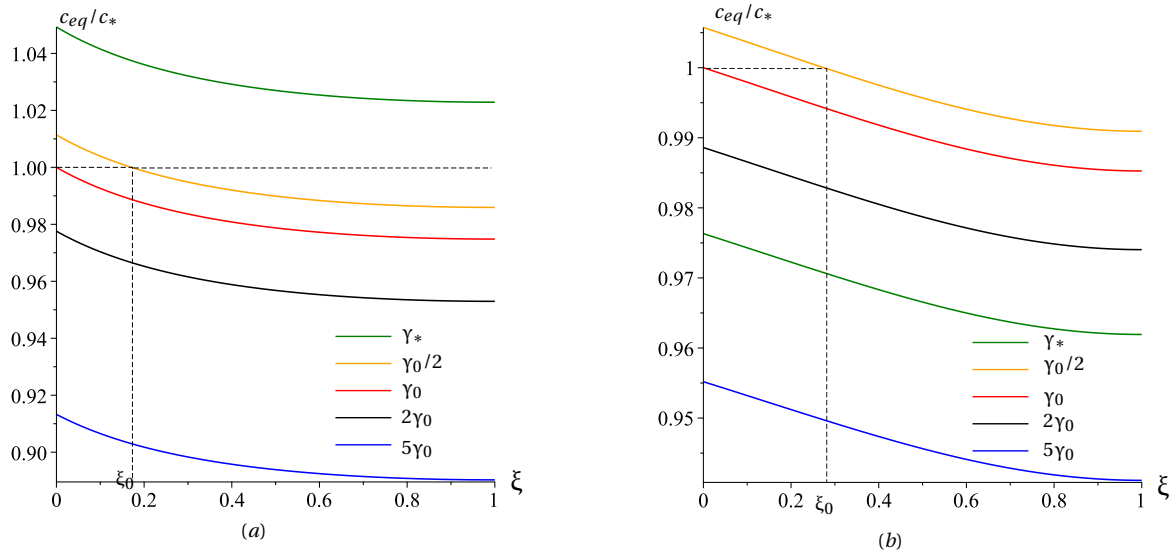

Figure 2.27: Cylindrical reaction front: dependencies of equilibrium concentration on the reaction front relative position $\xi = h/R$ at $\sigma_0 = 0$ and various values of energy parameter γ for the case: *a*) $\mathscr{K}_+ > \mathscr{K}_-$ and *b*) $\mathscr{K}_+ < \mathscr{K}_-$

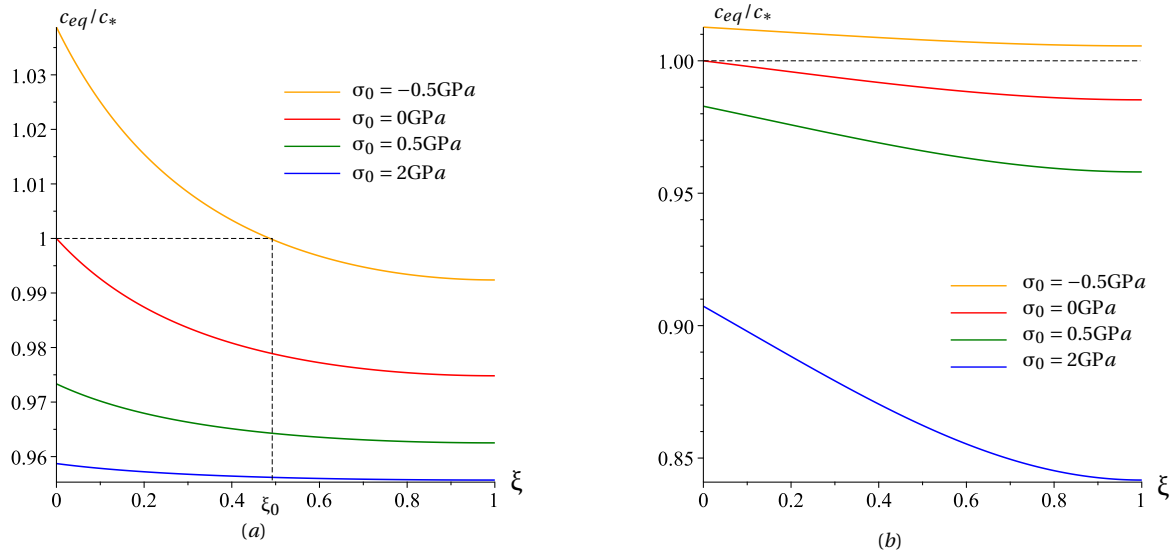

Figure 2.28: Cylindrical reaction front: dependencies of equilibrium concentration on the reaction front relative position $\xi = h/R$ at $\gamma = 1.1\gamma_0$ and various values of σ_0 for the case: *a*) $\mathscr{K}_+ > \mathscr{K}_-$ and *b*) $\mathscr{K}_+ < \mathscr{K}_-$

One can also see in Fig. 2.4*b*, Fig. 2.26*a* that if, at $\mathscr{K}_+ < \mathscr{K}_-$, the front can propagate at some σ_0 then further increasing of the absolute value $|\sigma_0|$ decreases c^*_{eq}/c_* and, thus, increases the front velocity.

Fig. 2.25*b*,*c* and Fig. 2.26*b*,*c* characterize quantitatively the role of volume and shear strain energies via the influence of the bulk module k_+ and shear module μ_+ on the dependencies of c^*_{eq}/c_* on σ_0 at initial position of the reaction front, $\xi = 0$. We can see from Fig. 2.25*c* and Fig. 2.26 that shear module affects on extrema of χ (it comes from (2.39)).

If the reaction front moves then stresses at the front changes and, thus, the equilibrium concentration changes. As $\chi(\sigma_0, \xi)$ depends on the position front ξ as well, therefore consider how it changes if the reaction front propagates. Let the stress σ_0 be given. If the front propagates, then

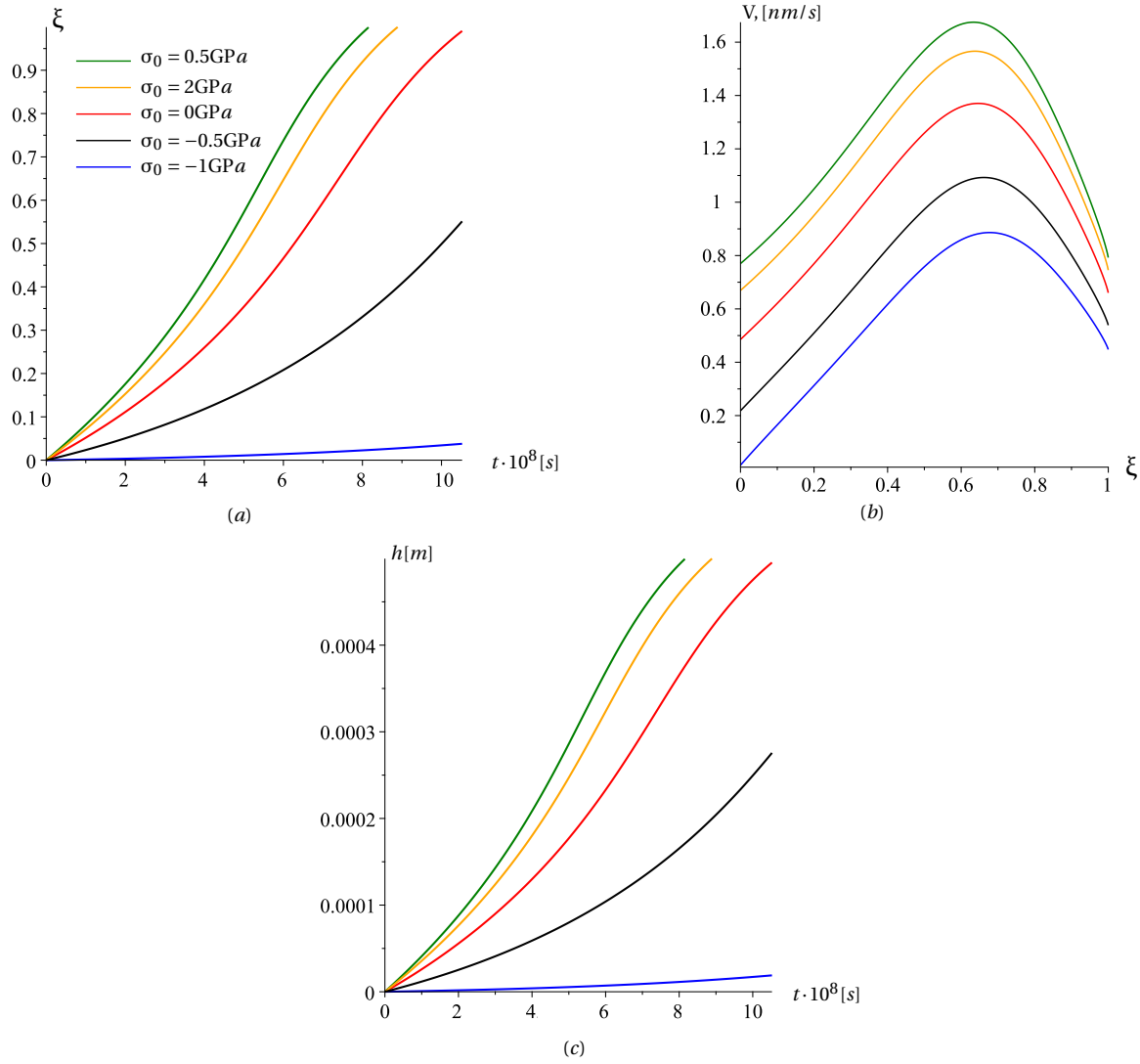

Figure 2.29: Cylindrical reaction front: kinetics of the reaction front at various values of external loading σ_0 for the case $\mathscr{K}_+ > \mathscr{K}_-$. Dependencies of the dimensionless front position on time (a), and the front velocity on the front position (b); (c) – the front position versus time at the initial stage of the front propagation

$\chi(\sigma_0, \xi)$ changes according to (2.31) so that

$$\frac{\partial \chi(\xi, \sigma_0=0)}{\partial \xi} = \frac{k_+ \mu_+ \vartheta^{tr\,2}}{\left(\mu_+^2 \xi^2 - \mu_+(\mathscr{K}_+ - \mathscr{K}_- + \mu_+)\xi - \dfrac{\mathscr{K}_-(\mathscr{K}_+ + 3\mu_+)}{3}\right)^3} \Big(\xi^2 \mu_+ (\mathscr{K}_- - \mu_+)(3k_+ - \mathscr{K}_-)\big(\mu_+(\mathscr{K}_+ -$$

$$- \mathscr{K}_-)\xi(\xi+2) + 2\mathscr{K}_-(\mathscr{K}_+ + 3\mu_+)(\xi - 1)\big) - 2\mathscr{K}_-(\mathscr{K}_+ + 3\mu_+)\left(\left(\frac{\xi}{3} - \mathscr{K}_-\right)\big(\mathscr{K}_-\mathscr{K}_+ + \mu_+(3k_+ - \mathscr{K}_-)\big) + 3\mu_+^2 \mathscr{K}_-\right)\Big) \le 0$$

Then from above relationships it follows that increase of relative thickness of the transformed layer ξ increases $\chi(\sigma_0)$ and decreases equilibrium concentration c_{eq}. Thus, the equilibrium concentration at the reaction front decreases as the front propagates if the external stress is given as a boundary condition.

If the external stress σ_0 and energy parameter γ are such that $c_{eq}(\xi = 0|\sigma_0, \gamma) \ge c_*$ then the reaction can not start from the external surface of the cylinder, but can start if an initial layer of a new material already exists of the thickness $\xi_0 : c(\xi_0|\sigma_0, \gamma) \ge c_*$ (Fig. 2.27). Fig. 2.28 shows the dependencies of the equilibrium concentration on the thickness of transformed material at various external stresses. In the case of the cylinder, similarly as it was in the case of the sphere,

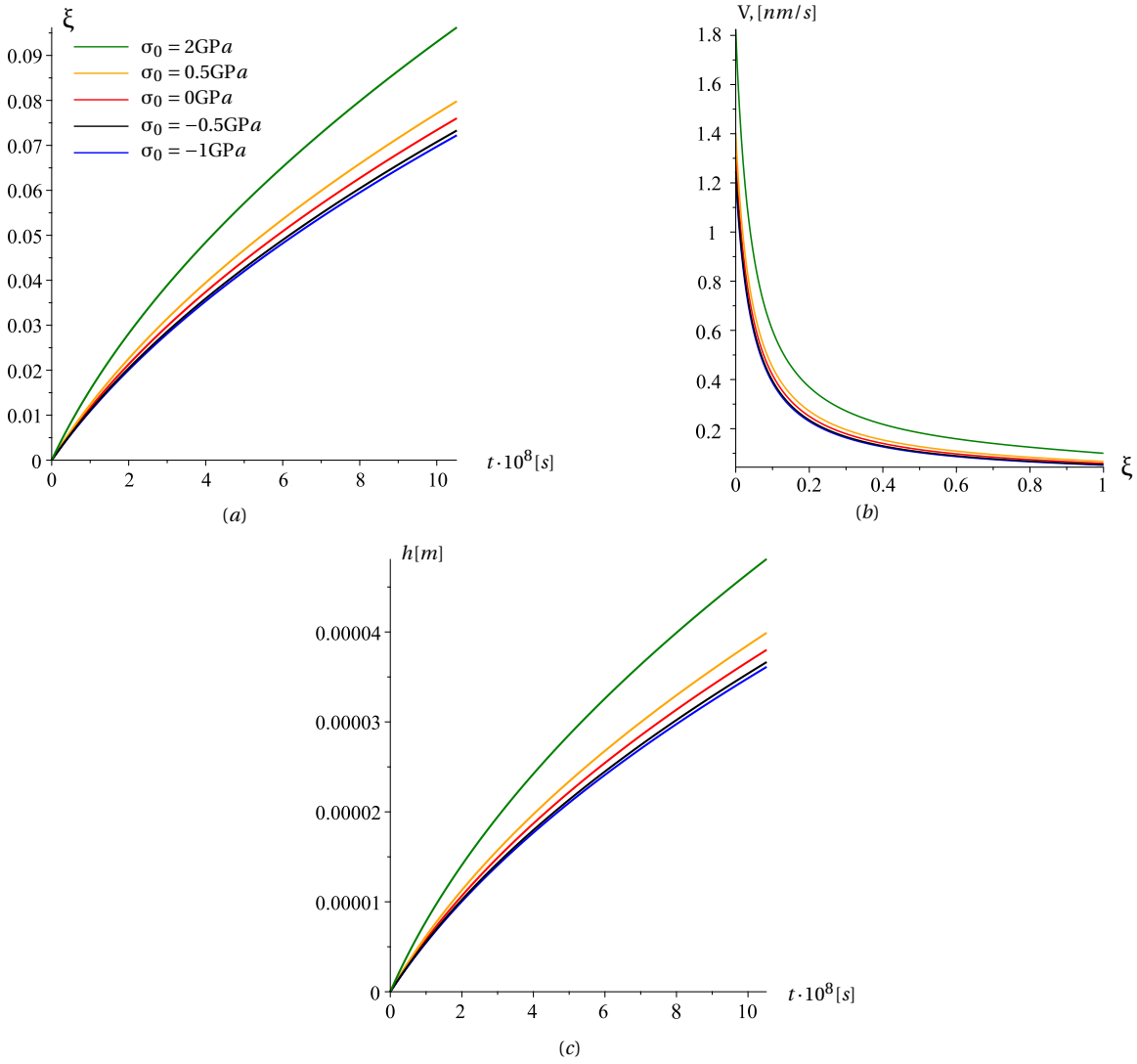

Figure 2.30: Cylindrical reaction front: kinetics of the reaction front at various values of external loading σ_0 for the case $\mathscr{K}_+ < \mathscr{K}_-$. Dependencies of the dimensionless front position on time (*a*), and the front velocity on the front position (b); (c) – the front position versus time at the initial stage of the front propagation

the equilibrium concentration decreases with propagation of the reaction front, and this in turn accelerates the reaction.

If the stress σ_0 is given then the layer growth decreases the equilibrium concentration and enhances the reaction (Fig. 2.27). The orange curves in Fig. 2.27 demonstrates that a thin layer of a new material can act as a protective layer if the value of the equilibrium concentration exceeds the gas solubility. External tension decreases the equilibrium concentration while compression increases it. Note also that at different values of the energy parameter the curves are similar but pass lower at larger values of γ or higher at smaller one. This means that the temperature change can initiate the reaction or, conversely, block it.

The dependencies of the front position on time and the front velocity on the front position for various values of external stress σ_0, energy parameter γ, bulk and shear moduli k_+ and μ_+ are shown in Fig. 2.29 – Fig. 2.35. One can see how the strains can retard or accelerate the reaction front, how the increase of the energy parameter accelerates the front, and how elastic moduli affect the front kinetics.

We should point out, that in the case of the chemical reaction in cylinder, the reaction can propagate as well with parabolic law, as with exponential law (see i.e. Fig. 2.29 and Fig. 2.31). As it was mention for spherical reaction front, the behaviour of kinetic depends on the mechan-

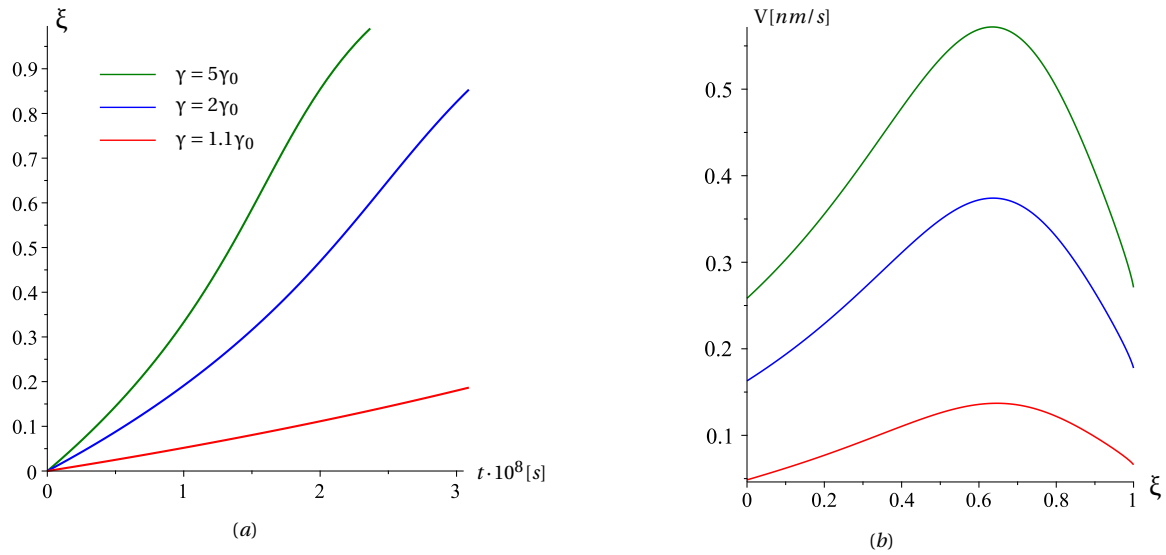

Figure 2.31: Cylindrical reaction front: dependencies of the front position on time (*a*), and the front velocity on the front position (*b*) at various values of energy parameter γ for the case $\mathscr{K}_+ > \mathscr{K}_-$

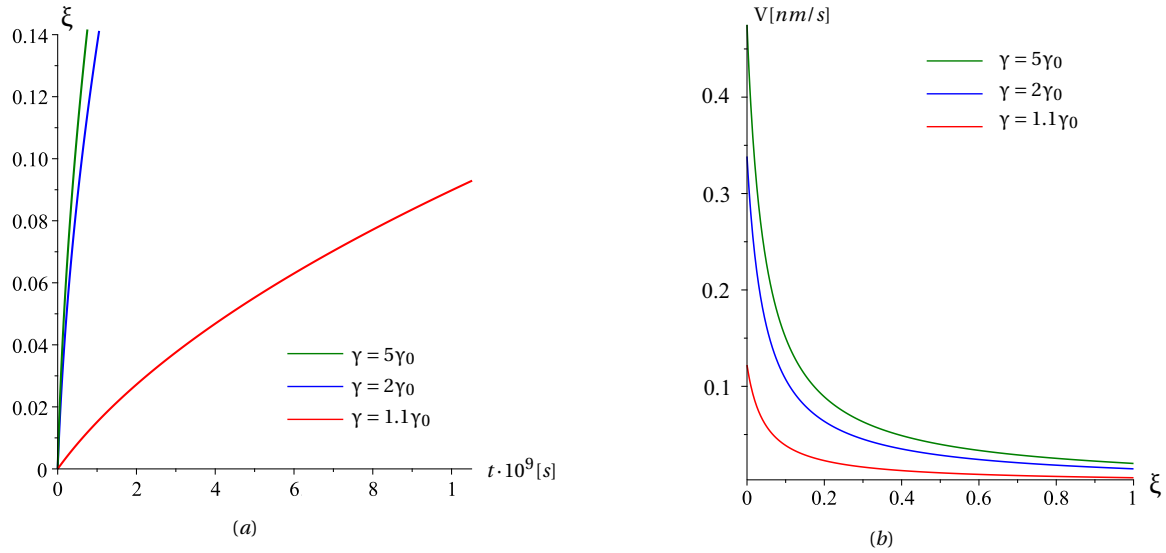

Figure 2.32: Cylindrical reaction front: dependencies of the front position on time (*a*), and the front velocity on the front position (*b*) at various values of energy parameter γ fro the case $\mathscr{K}_+ < \mathscr{K}_-$

ical properties initial and transformed materials and the geometry of the structure element (see Eq.(1.33) and (1.34)). Comparing Fig. 2.29-Fig. 2.35, it is worth mentioning that case for $\mathscr{K}_+ > \mathscr{K}_-$ demonstrates non-parabolic (exponential law) behavior that is different from the behavior in the case of the reaction in sphere, while the case for $\mathscr{K}_+ < \mathscr{K}_-$ shows the parabolic law.

Let $\mathscr{K}_+ > \mathscr{K}_-$. The front velocity is plotted in Fig. 2.29*b* at various values of external loading σ_0 and Fig. 2.31*b* at various γ. From these plots we can conclude, that initially the reaction front velocity increases along the front propagation and from some position it decelerates. Such behavior is inverse to the velocity behaviour in the spherical case. Such kinetics was described by Cabrera-Mott model and this behavior was observed in the experiments (see i.e., [6, 32, 34, 46, 77, 160]). Depending of the material properties and structure geometry, non-parabolic kinetics can be reached or not.

The influence of the elastic modulus k_+ and μ_+ of transformed material is shown in Fig. 2.33 and Fig. 2.34.

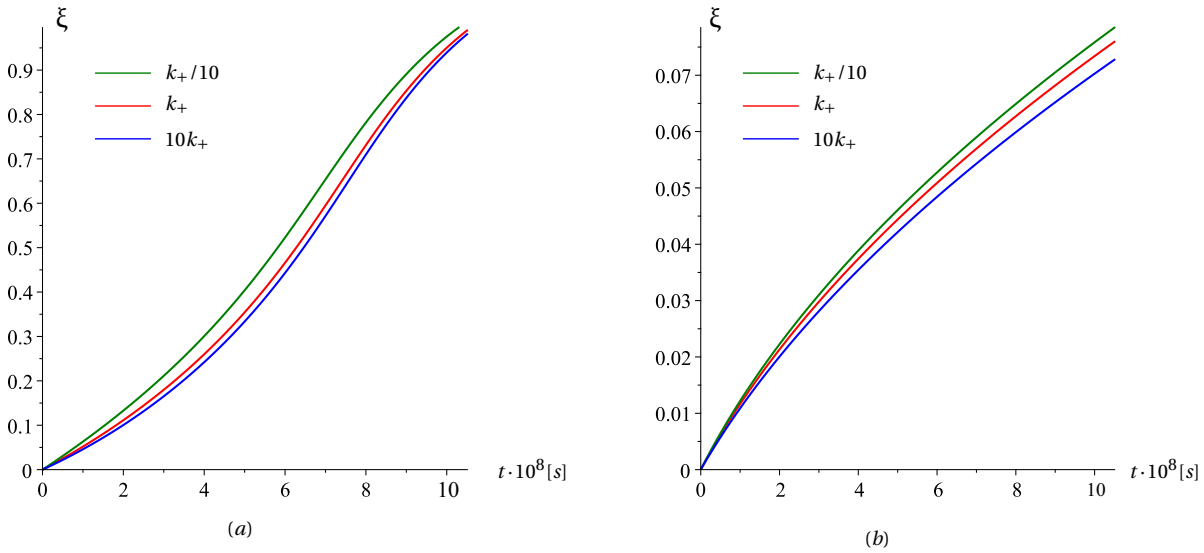

Figure 2.33: Cylindrical reaction front: dependencies of the front position on time at various values of bulk modulus k_+ for the case (*a*) $\mathscr{K}_+ > \mathscr{K}_-$ and (*b*) $\mathscr{K}_+ < \mathscr{K}_-$ energy parameter γ

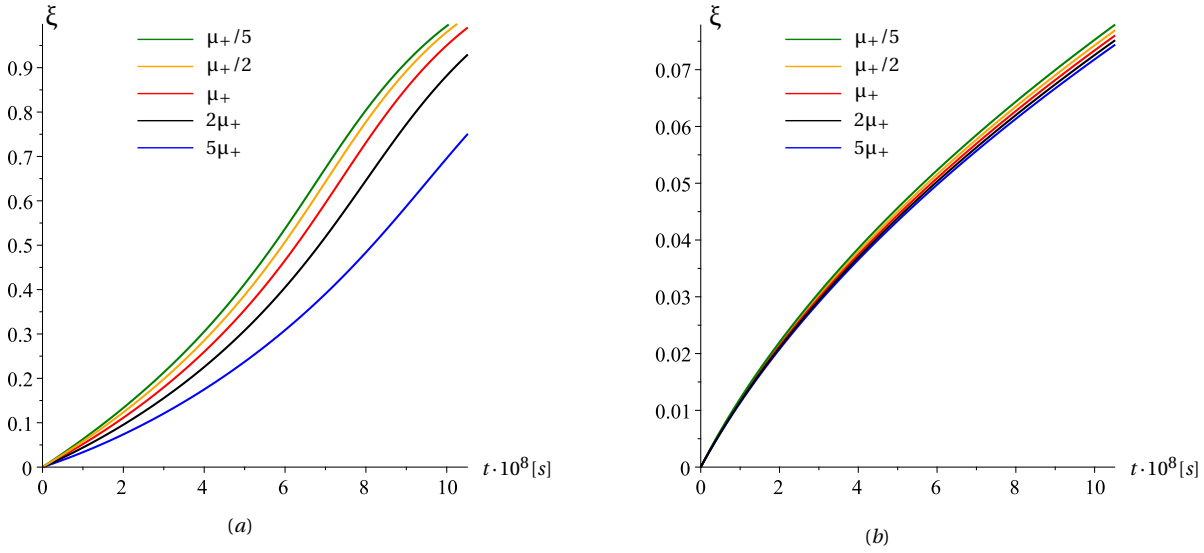

Figure 2.34: Cylindrical reaction front: dependencies of the front position on time at various values of shear modulus μ_+ for the case (*a*) $\mathscr{K}_+ > \mathscr{K}_-$ and (*b*) $\mathscr{K}_+ < \mathscr{K}_-$

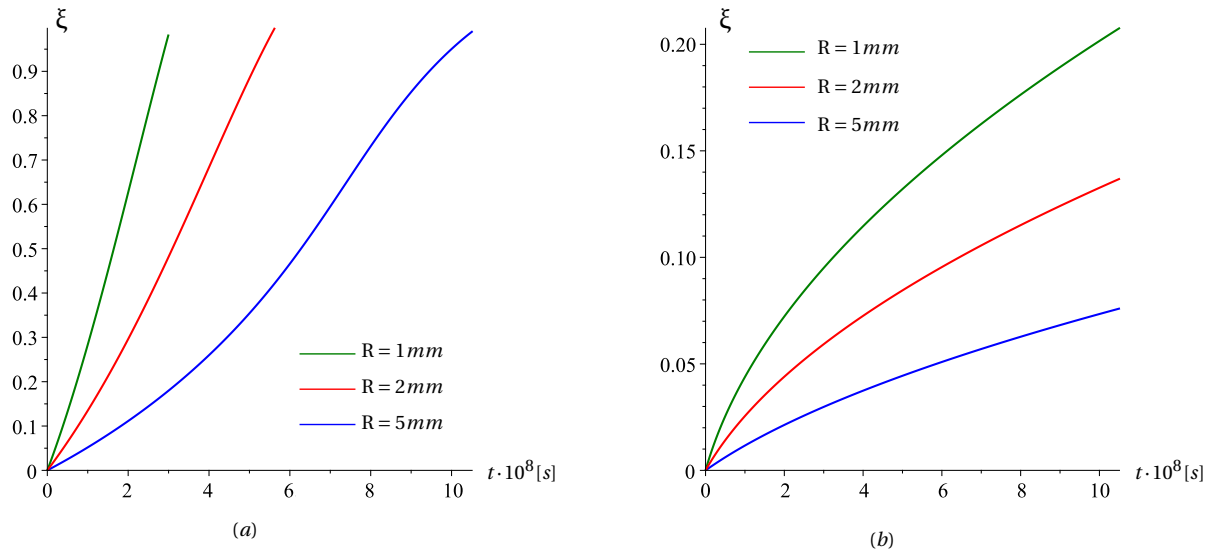

Figure 2.35: Cylindrical reaction front: dependencies of the front position on time at various initial radius R of the sphere fro the case (*a*) $\mathscr{K}_+ > \mathscr{K}_-$ and (*b*) $\mathscr{K}_+ < \mathscr{K}_-$

2.3 Conclusions

In this chapter the thermodynamical framework based on the concept of the chemical affinity tensor is presented. The stress-affected chemical reaction front propagation in deformable solid in the cases of a planar, spherical and cylindrical reaction fronts has been considered for elastic bodies. The reaction kinetics is studied. The influence of strains and material parameters on the kinetics of the front propagation was studied in detail with the use of the notion of the equilibrium concentration. Two types of the dependencies of the equilibrium concentration and, thus, front velocity on strain are demonstrated, depending on the relations between the combinations of elastic moduli of solid reactants. In the first case the front can propagate only if strains belong to some interval, and it cannot propagate at all if the energy parameter is less than the critical value defined by the elastic moduli and transformation strain. In the second case the front can propagate at any energy parameter at proper strains which are outside of a corresponding interval. Different cases also correspond to different effects of strains on the front acceleration or retardation. It is shown that reaction kinetics depends on the geometry of the structural element. It is demonstrated the possibility of logarithmic kinetics in the case of the spherical reaction front. For the reaction in cylindrical element the exponential law of the kinetics was observed. These different results are consistent with some experimental data coming from literature.

Chapter 3

Viscoelastic product of chemical reaction

Contents

In the present chapter we develop a model for analytical studies of stress relaxation behind the reaction front. Considered chemical reactions are accompanied by transformation strains which may generate huge stresses, and reaction products often demonstrate more viscous than elastic behaviours, e.g., [23,24]. This motivates the relevance of stress relaxation studies. In addition, since the total thickness of the transformed layer is observed in experiments, even simple models may be useful for the estimation of the impacts of the transformation and inelastic (viscous) strains on the thickening during the front propagation.

The difference of molar volumes of initial material and transformed material is a source of volume expansion due to chemical reaction. Kinematic compatibility, i.e. displacement continuity at the reaction front, restricts the transformation strain and produces stresses which can be huge in the case of an elastic behavior of the reaction product. Viscoelastic assumption allows the strain in the transformed layer to be partly accommodated by the viscous deformation, making it possible that the volume increases due to the increase of the thickness of the transformed layer leading to the stress relaxation (see, e.g., [20, 30, 31, 73, 74]).

To study how the viscosity and the specified choice of the viscoelastic rheology of the transformed material affects the reaction front propagation, we take at first the standard linear solid model (SLSM) that was refered as the Poynting-Thomson viscoelastic material.

The results obtained in the case of planar front are part of the article S.Petrenko, A.Freidin and E.Charkaluk "Chemical reaction planar fronts with a viscoelastic reaction product" (in revision).

3.1 Reaction front kinetics

For the inelastic material "+" we assume that volumetric strains are elastic, and inelastic behaviors are represented by rheological models formulated as relationships between deviatoric parts of stress and strain tensors. Then we use the following decompositions

$$\boldsymbol{\sigma} = \sigma\mathbf{I} + \mathbf{s}, \qquad \boldsymbol{\varepsilon} = \frac{\vartheta}{3}\mathbf{I} + \mathbf{e} \tag{3.1}$$

where $\sigma = \frac{1}{3}\mathrm{tr}\boldsymbol{\sigma}$ and $\vartheta = \mathrm{tr}\boldsymbol{\varepsilon}$ denote the hydrostatic parts of the stress tensor and volume strain, and $\mathbf{s}$ and $\mathbf{e}$ are the deviatoric stress and strain, respectively.

We assume that the transformation strain is spherical: $\boldsymbol{\varepsilon}^{tr} = (\vartheta^{tr}/3)\mathbf{I}$. Then the hydrostatic parts of the stress tensor and volume strain are related in constituent "+" as

$$\sigma^+ = k_+(\vartheta^+ - \vartheta^{tr}) \tag{3.2}$$

To study how the viscosity and the specified choice of the viscoelastic rheology of the transformed material affect the reaction front propagation, we take at first the standard linear solid model (SLSM) (Fig. 3.2*a*) that was also referred as the Poynting-Thomson viscoelastic material [124] (see also [106]).

The constitutive equation which relates the deviatoric tensors $\mathbf{s}^+$ and $\mathbf{e}^+$ in the material "+" is derived from the following relationships (see Fig. 3.2):

$$\begin{gathered}
\mathbf{s}^+ = \mathbf{s}_1 + \mathbf{s}_2, \quad \mathbf{e}^+ = \mathbf{e}_1 = \mathbf{e}_2 \\
\mathbf{s}_1 = \mathbf{s}_1^e = \mathbf{s}^\eta, \quad \mathbf{e}_1 = \mathbf{e}_1^e + \mathbf{e}^\eta \\
\mathbf{s}_1^e = \mathbf{s}_1 = 2\mu_1\mathbf{e}_1^e, \quad \mathbf{s}^\eta = \mathbf{s}_1 = 2\eta\dot{\mathbf{e}}^\eta, \quad \mathbf{s}_2 = 2\mu_2\mathbf{e}_2 = 2\mu_2\mathbf{e}^+
\end{gathered} \tag{3.3}$$

where μ_1 and μ_2 are the shear moduli of the elastic elements, η is the viscosity, $\mathbf{e}$ and $\mathbf{s}$ with various indices denote deviatoric strains and stresses in corresponding rheological elements. Finally, the constitutive equation takes the known form

$$\left(1 + \frac{\mu_2}{\mu_1}\right)\dot{\mathbf{e}}^+ + \frac{\mu_2}{\eta}\mathbf{e}^+ = \frac{1}{2\mu_1}\dot{\mathbf{s}}^+ + \frac{1}{2\eta}\mathbf{s}^+ \tag{3.4}$$

The strain energy of the constituents "+" is defined as

$$w_+ = \frac{1}{2}k_+(\vartheta^+ - \vartheta^{tr})^2 + \mu_1 \mathbf{e}_1^e : \mathbf{e}_1^e + \mu_2 \mathbf{e}^+ : \mathbf{e}^+ \tag{3.5}$$

where it is taken into account that $\mathbf{e}_2 = \mathbf{e}^+$.

3.1.1 Planar front

To demonstrate the influence of the viscosity on the reaction front kinetics, we consider in this section the simple plane strain problem for a chemical reaction in a plane layer of thickness H and length L >> H with a planar reaction front (Fig. 4.2). The reaction starts at the outer surface $y = 0$ of an initially elastic layer. The planar reaction front propagates in the y-direction, the reaction front position is given by $y = h$. The lower $y = 0$ and upper $y = \mathrm{H}$ faces of the layer are traction free. Displacement u_0 at the edges $x = \pm\mathrm{L}$ prescribes the strain $\varepsilon_0 = u_0/\mathrm{L}$ in x-direction. Therefore, the strains have to satisfy the following conditions:

$$\varepsilon_z = \varepsilon_{xz} = \varepsilon_{yz} = 0, \quad \varepsilon_x = \varepsilon_0$$

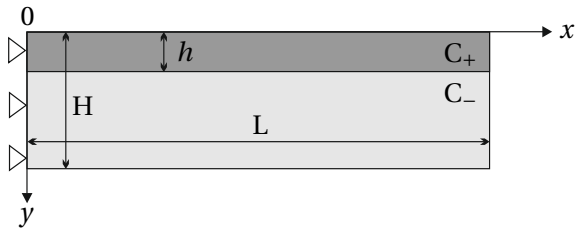

Figure 3.1: The planar reaction front.

The 3D diffusion problem is reduced to 1D the diffusion equation

$$\frac{d^2c}{dy^2} = 0, \quad y \in [0, h]$$

with boundary conditions

$$\mathrm{D}\left.\frac{dc}{dy}\right|_{y=0} = \alpha(c(0) - c_*), \quad \mathrm{D}\left.\frac{dc}{dy}\right|_{y=h} = -k_*(c(h) - c_{eq})$$

From the solution it follows that the concentration of the diffusing constituent B_* at the reaction front is equal to

$$c(h) = \frac{c_* + k_*\left(\dfrac{h}{\mathrm{D}} + \dfrac{1}{\alpha}\right)c_{eq}}{1 + k_*\left(\dfrac{h}{\mathrm{D}} + \dfrac{1}{\alpha}\right)}$$

Then, by Eq. (1.34), the reaction front velocity can be calculated as

$$\mathrm{V_N} = \frac{n_-\mathscr{M}_-}{\rho_-}\frac{c_* - c_{eq}}{\dfrac{1}{k_*} + \left(\dfrac{h}{\mathrm{D}} + \dfrac{1}{\alpha}\right)} \tag{3.6}$$

where the equilibrium concentration c_{eq}, defined by Eq. (1.32), depends on stresses and strains at the reaction front.

In the stress problem, the equilibrium equations and boundary conditions are satisfied if we take

$$\sigma_y = 0, \qquad \sigma_{xy} = 0 \tag{3.7}$$

From the continuity of the displacement it follows that, at the reaction front

$$[[\varepsilon_x]] = 0$$

Then, from Eq. (3.7) and plane strains conditions it follows that $\boldsymbol{\sigma}_- : [[\boldsymbol{\varepsilon}]] = 0$ in the expression of the normal component of the chemical affinity tensor Eq. (1.29).

We assume that the initial material "$-$" is isotropic linear elastic. Then due to the plane strains conditions, by using Hooke's law, non-zero stresses in the elastic layer $y \in [h, \mathrm{H}]$ are the stresses

$$\sigma_x^- = \frac{4\mu_-\left(3k_- + \mu_-\right)}{3k_- + 4\mu_-}\varepsilon_0, \quad \sigma_z^- = \frac{2\mu_-\left(3k_- - 2\mu_-\right)}{3k_- + 4\mu_-}\varepsilon_0$$

where k_- and μ_- are the bulk and shear modules of the material B_-. Then the strain energy density of the material B_- is

$$w_- = \frac{2\mu_-\left(3k_- + \mu_-\right)}{3k_- + 4\mu_-}\varepsilon_0^2 \tag{3.8}$$

To find strain energy w_+ at the reaction front there is no need to solve complete viscoelastic problem. Indeed, the viscous strains cannot occur instantaneously at a point when the front passes through this point, while the transformation and elastic strains appear instantaneously. Therefore, the viscous strain

$$\mathbf{e}^{\eta}(y, t_y) = 0 \tag{3.9}$$

where t_y is the time at which the reaction front passed through the position $y \in [0, h]$. The dependence $t_y = t_y(y)$ is determined by the kinetics of the front propagation:

$$\int_0^{t_y} \mathrm{V_N}(t)\,dt = y$$

The condition (3.9) will serve as initial condition in the stress relaxation analysis, but now it is enough to know that at the reaction front $\mathbf{e}_1^e = \mathbf{e}^+$ and

$$\boldsymbol{\sigma}^+ = k_+\left(\vartheta^+ - \vartheta^{tr}\right)\mathbf{I} + 2\mu_+\mathbf{e}^+$$
$$w_+ = \frac{1}{2}k_+(\vartheta^+ - \vartheta^{tr})^2 + \mu_+\mathbf{e}^+ : \mathbf{e}^+$$

where deviatoric strain $\mathbf{e}^+$ is taken at the reaction front.

Since, due to the plane strain restriction, $\varepsilon_y^+ = \vartheta^+ - \varepsilon_0$,

$$\mathbf{e}^+ : \mathbf{e}^+ = \boldsymbol{\varepsilon}^+ : \boldsymbol{\varepsilon}^+ - \frac{(\vartheta^+)^2}{3} = 2\left(\varepsilon_0^2 - \varepsilon_0\vartheta^+ + \frac{(\vartheta^+)^2}{3}\right) \tag{3.10}$$

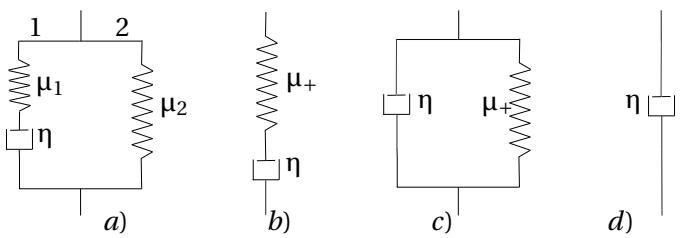

Figure 3.2: Rheological viscoelastic models: *a*) standard linear solid model, *b*) Maxwell model, *c*) Kelvin-Voigt model, *d*) linear viscous model.

Thus to calculate the strain energy w_+ at the reaction front it is enough to find the volume strain ϑ^+. From the relationships

$$\sigma_y^+ = k_+(\vartheta^+ - \vartheta^{tr}) + 2\mu_+ e_y^+ = 0$$
$$e_x^+ = \varepsilon_0 - \frac{\vartheta^+}{3}, \quad e_z^+ = -\frac{\vartheta^+}{3}, \quad e_y^+ = -(e_x^+ + e_z^+) = \frac{2\vartheta^+}{3} - \varepsilon_0$$

it immediately follows that at the reaction front

$$\vartheta^+ = \frac{3(2\mu_+\varepsilon_0 + k_+\vartheta^{tr})}{3k_+ + 4\mu_+} \tag{3.11}$$

$$e_x^+ = \frac{(3k_+ + 2\mu_+)\varepsilon_0 - k_+\vartheta^{tr}}{3k_+ + 4\mu_+}, \quad e_y^+ = \frac{k_+(2\vartheta^{tr} - 3\varepsilon_0)}{3k_+ + 4\mu_+}, \quad e_z^+ = -\frac{2\mu_+\varepsilon_0 + k_+\vartheta^{tr}}{3k_+ + 4\mu_+} \tag{3.12}$$

Then the strain energy of the strain constituent can be found as

$$w_+ = \frac{2\mu_+\left(\left(3k_+ + \mu_+\right)\varepsilon_0^2 - 3k_+\vartheta^{tr}\varepsilon_0 + k_+\vartheta^{tr2}\right)}{3k_+ + 4\mu_+}$$

The relationships (3.12) will be also used further in the stress relaxation analysis.

With the use of (3.11) and (3.10), the strain energy w_+ becomes a function of ε_0 and material parameters. Then the substitution of (3.8) for w_- and obtained expressions of w_+ and ϑ^+ into (1.31) gives χ as the quadratic function of external and transformation strains and elastic moduli of the constituents:

$$\chi(\varepsilon_0) = 2(G_+ - G_-)\varepsilon_0^2 - 3S\vartheta^{tr}\varepsilon_0 + S(\vartheta^{tr})^2 \tag{3.13}$$

where

$$G_\pm = \frac{\mu_\pm\left(3k_\pm + \mu_\pm\right)}{3k_\pm + 4\mu_\pm} = \frac{E_\pm}{2(1-\nu_\pm^2)}, \quad H = \frac{2k_+\mu_+}{3k_+ + 4\mu_+} = \frac{E_+}{9(1-\nu_+)}$$

$E_\pm$ and $\nu_\pm$ are the Young moduli and Poisson's ratios. Substitution of (3.13) into Eq. (1.30) and (1.33) leads to the explicit dependencies of A_{NN} and c_{eq} at the reaction front on external and transformation strains, elastic modules of the constituents and the chemical energies. In particularly,

$$\frac{c_{eq}}{c_*} = \exp\left\{-\frac{n_-\mathscr{M}_-}{\rho_-}\frac{(\gamma - \chi(\varepsilon_0))}{R_gT}\right\}$$

Note that at given ε_0 the equilibrium concentration does not depend on the front position. Then the integration of the equation (4.3) leads to the kinetic equation in the form of the parabolic law:

$$\xi^2 + L\xi = Qt \tag{3.14}$$

where $\xi = \frac{h}{H}$, $L = \frac{2D}{H}\left(\frac{1}{k_*} + \frac{1}{\alpha}\right)$, $Q = \frac{n_-M_-}{\rho_-}\frac{2D}{H^2}c_*(1-\phi)$, $\phi = \exp\left\{-\frac{n_-\mathscr{M}_-}{\rho_-}\frac{(\gamma - \chi(\varepsilon_0))}{R_gT}\right\}$ (cf. with [97]).

The dependence (3.10) for $t_y(y)$ can be presented in the explicit form:

$$t_y = \frac{1}{Q}\left(\frac{y}{H}\right)^2 + \frac{L}{Q}\left(\frac{y}{H}\right) \tag{3.15}$$

3.1.2 Spherical front propagation

In this section, a sphere of radius R that is subjected to the reaction from the outer surface is now considered. We solve the problem in the same statement as it was in the Section 1.4.2., taking into account that the transformed material is viscoelastic and described by standard linear solid model. Transformed material forms a spherical layer of thickness h (Fig. 3.3). The chemical reaction

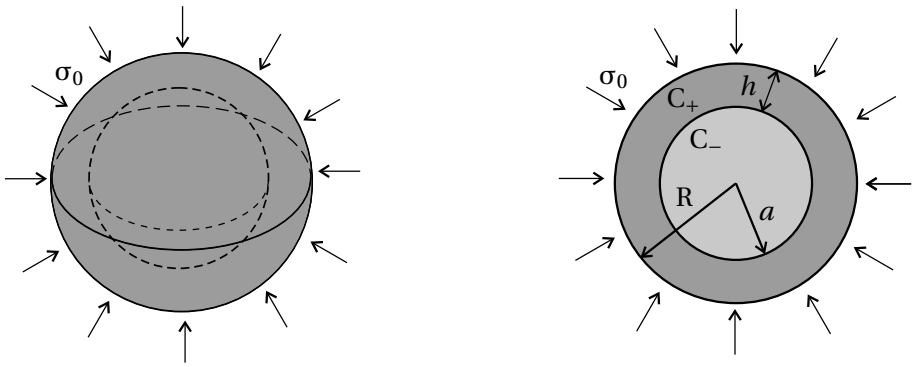

Figure 3.3: The spherical reaction front.

is localized on spherical reaction front of the radius $(\mathrm{R}-h)$ and divides the sphere onto regions occupied by the initial and new materials. The external stress $\boldsymbol{\sigma}_0$ is given as a boundary condition.

The solution of the diffusion problem for the spherical geometry was done in the Section 1.4.2. Here, we recall the resulting equations.The concentration of the diffusing constituent B_* at the reaction front is equal to

$$c(a)=\frac{c_*+n_*^2k_*\left(\dfrac{1-\xi}{\alpha}+\dfrac{\xi}{\mathrm{D}_0}\right)(1-\xi)c_{eq}}{1+n_*^2k_*\left(\dfrac{1-\xi}{\alpha}+\dfrac{\xi}{\mathrm{D}_0}\right)(1-\xi)},\qquad h=\mathrm{R}-a,\qquad \xi=\frac{h}{\mathrm{R}},\qquad \mathrm{D}_0=\frac{\mathrm{D}}{\mathrm{R}}$$

The reaction front velocity can be calculated as

$$\mathrm{V_N}=\frac{n_-\mathscr{M}_-}{\rho_-}\frac{k_*n_*}{1+n_*^2k_*\left(\dfrac{1-\xi}{\alpha}+\dfrac{\xi}{\mathrm{D}_0}\right)(1-\xi)}\left(c_*-c_{eq}\right) \tag{3.16}$$

Since the body's geometry (spherical symmetry) and since the material is isotropic, the equilibrium and kinematic boundary conditions can be expressed as

$$\begin{gathered}\frac{d\sigma_r}{dr}+2\frac{\sigma_r-\sigma_\varphi}{r}=0\\ \varepsilon_r=\frac{du_r}{dr},\qquad \varepsilon_\varphi=\varepsilon_\vartheta=\frac{u_r}{r}\end{gathered} \tag{3.17}$$

where u_r is the radial displacement.

If the solution for the displacement field can be obtained from the stress field using the constitutive equations, and if this field is compatible with the kinematic boundary conditions, the solution is unique.

Due to the spherical symmetry condition, the only non zero component of displacement is radial. As viscosity does not produce any volume change, the volume variation is due to the elastic strain only

$$\varepsilon_r^+ + 2\varepsilon_\varphi^+ - \vartheta^{tr}=\frac{\sigma_r^+ + 2\sigma_\varphi^+}{3k_+} \tag{3.18}$$

As the transformed material is described by the standard linear solid model, then we obtain:

$$\boldsymbol{\sigma}^+=k_+\left(\vartheta^+-\vartheta^{tr}\right)\mathbf{I}+2\mu_1\mathbf{e}_1^e+2\mu_2\mathbf{e}^+=k_+\left(\vartheta^+-\vartheta^{tr}\right)\mathbf{I}+2\mu_1\left(\boldsymbol{\epsilon}-\frac{\vartheta^+}{3}\mathbf{I}-\mathbf{e}^\eta\right)+2\mu_2\left(\boldsymbol{\varepsilon}-\frac{\vartheta^+}{3}\mathbf{I}\right) \tag{3.19}$$

$$\boldsymbol{\sigma}^+=k_+\left(\vartheta^+-\vartheta^{tr}\right)\mathbf{I}+2\eta\dot{\boldsymbol{e}}^\eta+2\mu_2\mathbf{e}^+=k_+\left(\vartheta^+-\vartheta^{tr}\right)\mathbf{I}+2\eta\left(\dot{\boldsymbol{\varepsilon}}-\frac{\dot{\vartheta}^+}{3}\mathbf{I}-\dot{\boldsymbol{e}}_1^e\right)+2\mu_2\left(\boldsymbol{\varepsilon}-\frac{\vartheta^+}{3}\mathbf{I}\right) \tag{3.20}$$

where

$$\varepsilon_r^+ = \frac{du_r}{dr} = \frac{\vartheta^+}{3} + e_r^+ = \frac{\vartheta^+}{3} + e_{1r}^e + e_r^\eta$$
$$\varepsilon_\varphi^+ = \frac{u_r}{r} = \frac{\vartheta^+}{3} + e_\varphi^+ = \frac{\vartheta^+}{3} + e_{1\varphi}^e + e_\varphi^\eta$$

from (3.3) we have:

$$\mu_1 e_1^e = \eta \dot{e}^\eta \tag{3.21}$$

Then from it, using (3.21), we have the following set of equations:

$$\frac{\eta}{\mu_1}\dot{e}_r^\eta + e_r^\eta = \frac{2}{3}\left(u_r' - \frac{u_r}{r}\right), \qquad \frac{\eta}{\mu_1}\dot{e}_\varphi^\eta + e_\varphi^\eta = \frac{1}{3}\left(\frac{u_r}{r} - u_r'\right) \tag{3.22}$$

$$\dot{e}_{1r}^e + \frac{\mu_1}{\eta}e_{1r}^e = \frac{2}{3}\left(\dot{u}_r' - \frac{\dot{u}_r}{r}\right), \qquad \dot{e}_{1\varphi}^e + \frac{\mu_1}{\eta}e_{1\varphi}^e = \frac{1}{3}\left(\frac{\dot{u}_r}{r} - \dot{u}_r'\right) \tag{3.23}$$

where the dot means differentiation w.r.t time t, and the dash differentiation w.r.t. position r.

From condition (3.18), substituting (3.3) into (3.1), it follows:

$$e_{1r}^e + 2e_{1\varphi}^e = 0, \qquad \dot{e}_r^\eta + 2\dot{e}_{1\varphi}^\eta = 0 \tag{3.24}$$

The equilibrium equation (3.17), taking into account (3.20), can be written as:

$$\left(k_+ + \frac{4}{3}\mu_2\right)\left(u_r'' + \frac{2}{r}u_r' - 2\frac{u_r}{r^2}\right) + \frac{4}{3}\eta\left(\dot{u}_r'' + \frac{2}{r}\dot{u}_r' - 2\frac{\dot{u}_r}{r^2}\right) - 2\eta\left(\left(\dot{e}_{1r}^e\right)' + \frac{2}{r}\left(\dot{e}_{1r}^e - \dot{e}_{1\varphi}^e\right)\right) = 0 \tag{3.25}$$

We solve Partial Differential Equations (PDEs) (3.25) and (3.23) together, with condition (3.24). These PDEs must be solved in combination with boundary conditions and initial conditions:

$$u_r(r,0) = 0, \qquad u_r^+(a,t) = u_r^-(a,t), \qquad \sigma_r^+(a,t) = \sigma_r^-(a,t), \qquad \sigma_r^+(\mathrm{R},t) = \sigma_0 \tag{3.26}$$

the initial condition simply requires that there is no displacement in the beginning.

Usually such type of problem can be solved using the Laplace transformation (see Appendix A). This solution is convenient to the general problem, where we just have to describe the stress-strain state, using only the initial conditions. But in our case, we are interested in introducing the condition at the reaction front, which is not possible using the Laplace transformation. Therefore, we have to solve the given problem in a general way, and the solution will be more complex. The solution of the non-linear system of PDEs will takes the following form:

$$u^+(r,t) = e^{-z_1 t}\mathrm{F}_1(r) + \frac{e^{-z_1 t}}{\eta\left(3k_+ + 4\mu_+\right)}\left(r\int e^{z_1 t}\mathrm{F}_2(t)\,dt + \frac{1}{r^2}\int e^{z_1 t}\mathrm{F}_3(t)\,dt\right)$$

$$e_{1r}^e(r,t) = \frac{2e^{-z_2 t}}{r^3\eta(3k_+ + 4\mu_+)}\left(z_2\int e^{(z_2-z_1)t}\left(\int e^{z_1 t}\mathrm{F}_3(t)\,dt\right)dt - e^{-z_1 t}\int e^{z_1 t}\mathrm{F}_3(t)\,dt\right) +$$
$$+ \frac{3k_+ + 4\mu_2}{6\mu_1 r}e^{-z_1 t}\left(-r\mathrm{F}_1'(r) + \mathrm{F}_1(r)\right) - \frac{\mathfrak{C}_1}{r^3}e^{-z_2 t}$$

$$e_r^\eta(r,t) = \frac{e^{-z_2 t}}{r^3}\left(-\frac{2z_2}{\eta(3k_+ + 4\mu_+)}\int e^{(z_2-z_1)t}\left(\int e^{z_1 t}\mathrm{F}_3(t)\,dt\right)dt + \mathfrak{C}_1\right) + \frac{(3k_+ + 4\mu_+)e^{-z_1 t}}{6\mu_1 r}\left(r\mathrm{F}_1'(r) - \mathrm{F}_1(r)\right)$$

$$z_1 = \frac{\mu_1(3k_+ + 4\mu_2)}{\eta(3k_+ + 4\mu_+)}, \qquad z_2 = \frac{\mu_1}{\eta}, \qquad \mu_+ = \mu_1 + \mu_2$$

where $\mathrm{F}_1(r)$ is arbitrary function of r, what can be found from the initial conditions; $\mathrm{F}_2(t)$ and $\mathrm{F}_3(t)$ are arbitrary functions of t can be found from the boundary conditions; $\mathfrak{C}_1$ is an integration constant.

Introduce the following notations: $f_{2,3}(t) = \dfrac{e^{-z_1 t}}{\eta(3k_+ + 4\mu_+)} \int e^{z_1 t} \mathrm{F}_{2,3}(t)\,dt$, $\int e^{z_2 t} f_3(t)\,dt = \widetilde{f}_3(t)$, then it follows $f_3(t) = \dddot{\widetilde{f}}_3(t) e^{-z_2 t}$. Using such notation, we can rewrite our solution in more compact and simple form:

$$u^+(r,t) = e^{-z_1 t}\mathrm{F}_1(r) + r f_2(t) + \frac{1}{r^2}\ddot{\widetilde{f}}_3(t) e^{-z_2 t} \tag{3.27}$$

$$e^e_{1r}(r,t) = \frac{2}{r^3} e^{-z_2 t}\left(z_2 \widetilde{f}_3(t) - \dot{\widetilde{f}}_3(t)\right) + \frac{3k_+ + 4\mu_2}{6\mu_1 r} e^{-z_1 t}\left(-r\mathrm{F}_1'(r) + \mathrm{F}_1(r)\right) - \frac{\mathfrak{C}_1}{r^3} e^{-z_2 t} \tag{3.28}$$

$$e^e_{2r}(r,t) = -\frac{2}{r^3} e^{-z_2 t}\ddot{\widetilde{f}}_3(t) + \frac{2}{3r} e^{-z_1 t}\left(r\mathrm{F}_1'(r) - \mathrm{F}_1(r)\right) \tag{3.29}$$

$$e^\eta_r(r,t) = \frac{e^{-z_2 t}}{r^3}\left(-2z_2 \widetilde{f}_3(t) + \mathrm{C}_1\right) + \frac{3k_+ + 4\mu_+}{6r\mu_1} e^{-z_1 t}\left(r\mathrm{F}_1'(r) - \mathrm{F}_1(r)\right) \tag{3.30}$$

Writing down the initial conditions, we have:

$$\mathrm{F}_1(r) = -r f_2(0) - \frac{1}{r^2}\ddot{\widetilde{f}}_3(0), \qquad \mathrm{F}_1'(r) = -f_2(0) + \frac{2}{r^3}\ddot{\widetilde{f}}_3(0) \tag{3.31}$$

In initial material displacements are given by Lame formulae:

$$u^-(r,t) = \mathfrak{L}_-(t) r + \frac{\mathfrak{D}_-(t)}{r^2} \tag{3.32}$$

in our case of sphere, $u^-(r,t)$ is to be finite at $r = 0$, therefore $\mathfrak{D}_-(t) = 0$

To solve the problem we have to find $f_2(t)$, $\widetilde{f}_3(t)$ and $\mathfrak{L}_1(t)$ from the boundary conditions and the conditions at the interface. Therefore from (3.26), taking into account (3.19) and (3.32), we have:

$$\widetilde{f}_3(t) = \mathfrak{C}_2 \exp\left\{\frac{z_2\mathfrak{U}_2}{\mathfrak{U}_1} t\right\} - \frac{\left(k_- k_+ \vartheta^{tr} - \sigma_0(k_+ - k_-)\right)\mathrm{R}^3 a^3}{z_2\left(\mathfrak{U}_1 - \mathfrak{U}_2\right)} e^{z_2 t} + \frac{\mathfrak{C}_1}{2z_2} \tag{3.33}$$

$$\dot{\widetilde{f}}_3(t) = \frac{z_2\mathfrak{U}_2}{\mathfrak{U}_1}\mathfrak{C}_2 \exp\left\{\frac{z_2\mathfrak{U}_2}{\mathfrak{U}_1} t\right\} - \frac{\left(k_- k_+ \vartheta^{tr} - \sigma_0(k_+ - k_-)\right)\mathrm{R}^3 a^3}{\mathfrak{U}_1 - \mathfrak{U}_2} e^{z_2 t} \tag{3.34}$$

$$f_2(t) = -\frac{4k_-\mu_1 z_2}{\mathfrak{U}_1}\mathfrak{C}_2 \exp\left\{-\frac{z_2\left(\mathfrak{U}_1 - \mathfrak{U}_2\right)}{\mathfrak{U}_1} t\right\} + \frac{\left(k_+\vartheta^{tr} + \sigma_0\right)(3k_- + 4\mu_2)\mathrm{R}^3 - 4\mu_2 k_+ \vartheta^{tr} a^3}{3\left(\mathfrak{U}_1 - \mathfrak{U}_2\right)} \tag{3.35}$$

$$\mathfrak{L}_-(t) = \frac{4k_+\mu_1 z_2\left(\mathrm{R}^3 - a^3\right)}{\mathfrak{U}_1 a^3}\mathfrak{C}_2 \exp\left\{\frac{z_2\mathfrak{U}_2}{\mathfrak{U}_1} t\right\} + \frac{4\vartheta^{tr} k_+\mu_2\left(\mathrm{R}^3 - a^3\right) + \sigma_0(3k_+ + 4\mu_2)\mathrm{R}^3}{3\left(\mathfrak{U}_1 - \mathfrak{U}_2\right)} \tag{3.36}$$

$$\mathfrak{U}_1 = k_+(3k_- + 4\mu_+)\mathrm{R}^3 - 4\mu_+(k_+ - k_-)a^3, \qquad \mathfrak{U}_2 = 4\mu_1\left(k_+\mathrm{R}^3 - (k_+ - k_-)a^3\right)$$

where $\mathfrak{C}_2$ is an integration constant, can be found from the condition at the interface at the moment, when front is just came there: $\sigma_r^+(a,t_a) = \sigma_r^-(a,t_a)$:

$$\mathfrak{C}_2 = \frac{\left(k_- k_+ \vartheta^{tr} - (k_+ - k_-)\sigma_0\right)\mathrm{R}^3 a^3}{z_2\left(\mathfrak{U}_1 - \mathfrak{U}_2\right)} \exp\left\{\frac{z_2\left(\mathfrak{U}_1 - \mathfrak{U}_2\right)}{\mathfrak{U}_1} t_a\right\} \tag{3.37}$$

Integration constant $\mathfrak{C}_1$ can be found from the condition (3.9), writing down for (3.30):

$$\mathfrak{C}_1 = 2z_2 \widetilde{f}_3(t_a) \tag{3.38}$$

Then the strain density of the initial material "-" is

$$w_- = \frac{9}{2}k_-\mathfrak{L}_-(t)^2 \tag{3.39}$$

in the transformed material from (3.5) can be found as follows

$$w_+ = \frac{1}{2}\left(3f_2(t) - \vartheta^{tr}\right)^2 + \frac{4\mu_+}{a^3}\tilde{f}_3^2(t)e^{-2z_2 t} \tag{3.40}$$

and

$$\boldsymbol{\sigma}^- : [\![\varepsilon]\!] = 9k_-\mathfrak{L}_-(t)\left(f_2(t) - \mathfrak{L}_-(t)\right) \tag{3.41}$$

Substitution of (3.39) for w^-, (3.40) for w^+ and (3.41) into (1.30) gives χ as the quadratic function of external stress and transformation strain, elastic modulus of the constituents:

$$\frac{c_{eq}}{c_*} = \exp\left\{-\frac{n_-\mathscr{M}_-}{\rho_- \mathrm{R}_g\mathrm{T}}\left(\gamma - \frac{1}{2}k_+\left(3f_2(t) - \vartheta^{tr}\right)^2 - \frac{4\mu_+}{\mathrm{R}^3(1-\xi)^3}\tilde{f}_3^2(t)e^{-2z_2 t} + 9k_-\mathfrak{L}_-(t)\left(f_2(t) - \frac{\mathfrak{L}_-(t)}{2}\right)\right)\right\}$$

where $\xi = \dfrac{\mathrm{R}-a}{\mathrm{R}}$ is the thickness of the transformed layer divided by radius of the sphere. Then the substitution of (3.34), (3.35) and (3.36) into (3.1.2), gives χ as the quadratic function of external stress and transformation strain:

$$\chi(\sigma_0) = \frac{\mathrm{R}^6}{2\mathfrak{U}_1^2}\left((k_+ - k_-)\mathfrak{Q}\sigma_0^2 - 2k_+k_-\mathfrak{Q}\sigma_0\vartheta^{tr} - 8k_+k_-\mu_+\mathfrak{T}(\vartheta^{tr})^2\right) \tag{3.42}$$

where

$$\mathfrak{Q} = 3k_+(3k_- - 4\mu_+) + 4\mu_+(9k_- + 4\mu_+)$$
$$\mathfrak{T} = k_+\left((9k_- + 4\mu_+) - (1-\xi)^3(3k_- + 4\mu_+)\right) + 4\mu_+(1-\xi)^6(k_+ - k_-)$$

Substitution of (3.42) into (1.33) and (1.30) leads to the explicit dependencies of $\mathrm{A_{NN}}$ and c_{eq} at the reaction front on external stress and transformation strain, elastic modules of the constituents and chemical energies. In particularly,

$$\frac{c_{eq}}{c_*} = \exp\left\{-\frac{n_-\mathscr{M}_-}{\rho_-}\frac{(\gamma - \chi(\sigma_0))}{\mathrm{R}_g\mathrm{T}}\right\}$$

Then integration of the equation (3.16) leads to the kinetic equation:

$$\dot{\xi} = \frac{n_-\mathscr{M}_-}{\rho_-}\frac{k_* c_*}{1 + k^*\left(\dfrac{1-\xi}{\alpha} + \dfrac{\xi}{\mathrm{D}_0}\right)(1-\xi)}\left(1 - \exp\left\{-\frac{n_-\mathscr{M}_-}{\rho_-}\frac{(\gamma - \chi(\sigma_0))}{\mathrm{R}_g\mathrm{T}}\right\}\right)$$

3.1.3 Cylindrical front propagation

In this subsection we focus on the chemical reaction in axially-symmetric problem. As it was done in the previous Chapter 1 in Subsection 1.4.3., we consider initially a linear-elastic cylinder of radius R and length L under external stress σ_0 (Fig. 3.4). Assume L >> R. The displacement in a radial direction is a function on r alone and does not depend on upon z. Therefore, $\varepsilon_z = 0$, as we assume that tube material is compressible, then from (3.1) we have non zero $\boldsymbol{e}_z$. The diffusive material surrounds the cylinder. We suppose that reaction starts from the outer surface and transformed material forms a cylindrical layer of a thickness h from the body surface.

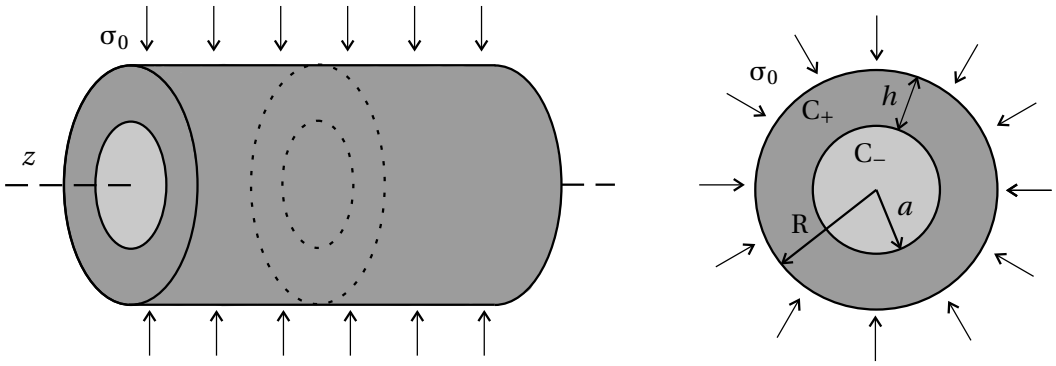

Figure 3.4: The cylindrical reaction front.

The solution for the diffusion problem and kinetic equation were solved in Section 1.4.3.(Eq. (2.25) and (2.26)). Here, we just recall the result:

The concentration of the diffusing constituent B_* at the reaction front is equal to

$$c(a) = \frac{c_* \dfrac{D_0}{k_*(1-\xi)} - c_{eq}\left(\ln(1-\xi) - \dfrac{D_0}{\alpha}\right)}{\dfrac{D_0}{1-\xi} + \dfrac{D_0}{\alpha} - \ln(1-\xi)}, \qquad D_0 = \frac{D}{R}, \qquad h = R - a, \qquad \xi = \frac{h}{R}$$

The reaction front velocity is given by the following equation

$$V_N = \frac{n_- \mathscr{M}_-}{\rho_-} \frac{c_* - c_{eq}}{\dfrac{1}{k_*} + \dfrac{1-\xi}{\alpha} - \dfrac{\ln(1-\xi)}{D_0}(1-\xi)} \tag{3.43}$$

Since the body's cylindrical geometry (cylindrical coordinates (r, φ, z)) and since the material is isotropic, the equilibrium and kinematic boundary conditions can be expressed as

$$\begin{gathered} \frac{d\sigma_r}{dr} + \frac{\sigma_r - \sigma_\varphi}{r} = 0 \\ \varepsilon_r = \frac{du}{dr}, \qquad \varepsilon_\varphi = \frac{u}{r}, \qquad \varepsilon_z = 0 \end{gathered} \tag{3.44}$$

Due to the axially-symmetric condition and from the condition $L >> R$, the only non zero component of displacement is radial. As viscosity does not produce any volume change, the volume variation is due to the elastic strain only

$$\varepsilon_r^+ + \varepsilon_\varphi^+ - \vartheta^{tr} = \frac{\sigma_r^+ + \sigma_\varphi^+ + \sigma_z^+}{3k_+} \tag{3.45}$$

Recall the viscoelastic equations. As the transformed material is described by the standard linear solid model, then we obtain:

$$\boldsymbol{\sigma}^+ = k_+\left(\vartheta^+ - \vartheta^{tr}\right)\mathbf{I} + 2\mu_1 \mathbf{e}_1^e + 2\mu_2 \mathbf{e}^+ = k_+\left(\vartheta^+ - \vartheta^{tr}\right)\mathbf{I} + 2\mu_1\left(\boldsymbol{\epsilon} - \frac{\vartheta^+}{3}\mathbf{I} - \mathbf{e}^\eta\right) + 2\mu_2\left(\boldsymbol{\varepsilon} - \frac{\vartheta^+}{3}\mathbf{I}\right) \tag{3.46}$$

$$\boldsymbol{\sigma}^+ = k_+\left(\vartheta^+ - \vartheta^{tr}\right)\mathbf{I} + 2\eta\dot{\mathbf{e}}^\eta + 2\mu_2 \mathbf{e}^+ = k_+\left(\vartheta^+ - \vartheta^{tr}\right)\mathbf{I} + 2\eta\left(\dot{\boldsymbol{\varepsilon}} - \frac{\dot{\vartheta}^+}{3}\mathbf{I} - \dot{\mathbf{e}}_1^e\right) + 2\mu_2\left(\boldsymbol{\varepsilon} - \frac{\vartheta^+}{3}\mathbf{I}\right) \tag{3.47}$$

where, taking into account (3.3)

$$e^e_{1r}+e^\eta_r=e^e_{2r}=\frac{1}{3}\left(2u'-\frac{u}{r}\right)=\frac{\eta}{\mu_1}\dot{e}^\eta_r+e^\eta_r,\qquad \dot{e}^e_{1r}+\frac{\mu_1}{\eta}e^e_{1r}=\frac{1}{3}\left(2\dot{u}'-\frac{\dot{u}}{r}\right) \tag{3.48}$$

$$e^e_{1\varphi}+e^\eta_\varphi=e^e_{2\varphi}=\frac{1}{3}\left(2\frac{u}{r}-u'\right)=\frac{\eta}{\mu_1}\dot{e}^\eta_\varphi+e^\eta_\varphi,\qquad \dot{e}^e_{1\varphi}+\frac{\mu_1}{\eta}e^e_{1\varphi}=\frac{1}{3}\left(2\frac{\dot{u}}{r}-\dot{u}'\right) \tag{3.49}$$

$$e^e_{1z}+e^\eta_z=e^e_{2z}=-\frac{1}{3}\left(u'+\frac{u}{r}\right)=\frac{\eta}{\mu_1}\dot{e}^\eta_z+e^\eta_z,\qquad \dot{e}^e_{1z}+\frac{\mu_1}{\eta}e^e_{1z}=-\frac{1}{3}\left(\dot{u}'+\frac{\dot{u}}{r}\right)$$

where the dot means differentiation w.r.t time t, and the dash differentiation w.r.t. position r.

From the condition (3.45) it follows:

$$e^e_{1r}+e^e_{1\varphi}+e^e_{1z}=0,\qquad \dot{e}^\eta_r+\dot{e}^\eta_\varphi+\dot{e}^\eta_z=0 \tag{3.50}$$

The equilibrium equation (3.44), taking into account (3.47), can be rewritten as follows:

$$\left(k_+ +\frac{4}{3}\mu_2\right)\left(u''+\frac{u'}{r}-\frac{u}{r^2}\right)+\frac{4}{3}\eta\left(\dot{u}''+\frac{\dot{u}'}{r}-\frac{\dot{u}}{r^2}\right)-2\eta\left(\left(\dot{e}^e_{1r}\right)'+\frac{1}{r}\left(\dot{e}^e_{1r}-\dot{e}^e_{1\varphi}\right)\right)=0 \tag{3.51}$$

We solve Partial Differential Equations (PDEs) (3.51), (3.48) and (3.49) together, with condition (3.50). These PDEs must be solved in combination with boundary conditions and initial conditions:

$$u_r(r,0)=0,\qquad u^+_r(a,t)=u^-_r(a,t),\qquad \sigma^+_r(a,t)=\sigma^-_r(a,t),\qquad \sigma^+_r(\mathrm{R},t)=\sigma_0 \tag{3.52}$$

the initial condition simply requires that there is no displacement in the beginning.

As it was written in the previous Section 3.1.2 for spherically-symmetric problem, such problem usually can be solved using the Laplace transformation. Such method takes into account only the initial conditions, but in our case, we are interested in taking into account the moment when the front passes through the body point. To make it possible we have to solve the problem in the general way, with more complex solution. The solution of non-linear system of PDEs will takes form:

$$u^+(r,t)=e^{-z_1t}\mathrm{F}_1(r)+\frac{e^{-z_1t}}{\eta(3k_++4\mu_+)}\left(r\int e^{z_1t}\mathrm{F}_2(t)dt+\frac{1}{r}\int e^{z_1t}\mathrm{F}_3(t)dt\right)$$

$$e^e_{1r}(r,t)=-\frac{z_2e^{-z_2t}}{\eta(3k_++4\mu_+)}\left(\int e^{(z_2-z_1)t}\left(\frac{1}{3}\int e^{z_1t}\mathrm{F}_2(t)dt-\frac{1}{r^2}\int e^{z_1t}\mathrm{F}_3(t)dt\right)dt\right)-\mathscr{C}_1e^{-z_2t}+$$
$$+\frac{e^{-z_1t}}{\eta(3k_++4\mu_+)}\left(\frac{1}{3}\int e^{z_1t}\mathrm{F}_2(t)dt-\frac{1}{r^2}\int e^{z_1t}\mathrm{F}_3(t)dt\right)+\frac{z_1e^{-z_1t}}{3(z_2-z_1)}\left(\frac{\mathrm{F}_1(r)}{r}-2\mathrm{F}_1'(r)\right)$$

$$e^\eta_r(r,t)=e^{-z_2t}\left(\int\frac{z_2e^{(z_2-z_1)t}}{\eta(3k_++4\mu_+)}\left(\frac{1}{3}\int e^{z_1t}\mathrm{F}_2(t)dt-\frac{1}{r^2}\int e^{z_1t}\mathrm{F}_3(t)dt\right)dt-\frac{z_2e^{(z_2-z_1)t}}{3(z_2-z_1)}\left(\frac{\mathrm{F}_1(r)}{r}-2\mathrm{F}_1'(r)\right)+\mathscr{C}_1\right)$$

$$e^e_{2r}(r,t)=\frac{e^{-z_1t}}{\eta(3k_++4\mu_+)}\left(\frac{1}{3}\int e^{z_1t}\mathrm{F}_2(t)dt-\frac{1}{r^2}\int e^{z_1t}\mathrm{F}_3(t)dt\right)-\frac{e^{-z_1t}}{3}\left(\frac{\mathrm{F}_1(r)}{r}-2\mathrm{F}_1'(r)\right)$$

$$z_1=\frac{\mu_1(3k_++4\mu_2)}{\eta(3k_++4\mu_+)},\qquad z_2=\frac{\mu_1}{\eta},\qquad \mu_+=\mu_1+\mu_2$$

$$e^e_{2\varphi}=\frac{e^{z_1t}}{\eta(3k_++4\mu_+)}\left(\frac{1}{3}\int e^{z_1t}\mathrm{F}_2(t)dt+\frac{1}{r^2}\int e^{z_1t}\mathrm{F}_3(t)dt\right)-\frac{e^{-z_1t}}{3}\left(\mathrm{F}_1'(r)-2\frac{\mathrm{F}_1(r)}{r}\right)$$

$$e^e_{2z}=-\frac{2e^{-z_1t}}{3\eta(3k_++4\mu_+)}\int e^{z_1t}\mathrm{F}_2(t)dt-\frac{e^{-z_1t}}{3}\left(\mathrm{F}_1'(r)+\frac{\mathrm{F}_1(r)}{r}\right)$$

where $F_1(r)$ is arbitrary function of r, what can be found from the initial conditions; $F_2(t)$ and $F_3(t)$ are arbitrary functions of t can be found from the boundary conditions; $\mathscr{C}_1$ is an integration constant.

Introduce the following notations: $f_{2,3}(t) = \dfrac{e^{-z_1 t}}{\eta(3k_+ + 4(\mu_1+\mu_2))} \int e^{z_1 t} F_{2,3}(t)\,dt$, $\int e^{z_2 t} f_{2,3}(t)\,dt = \widetilde{f}_{2,3}(t)$, then it follows $f_{2,3}(t) = \dot{\widetilde{f}}_{2,3}(t) e^{-z_2 t}$. Using such notation, we can rewrite our solution in more compact and simple form:

$$u^+(r,t) = e^{-z_1 t} F_1(r) + e^{-z_2 t}\left(r\dot{\widetilde{f}}_2(t) + \frac{1}{r}\dot{\widetilde{f}}_3(t)\right) \tag{3.53}$$

$$e^e_{1r}(r,t) = e^{-z_2 t}\left(-\frac{z_2}{3}\widetilde{f}_2(t) + \frac{1}{3}\dot{\widetilde{f}}_2(t) + \frac{z_2}{r^2}\widetilde{f}_3(t) - \frac{1}{r^2}\dot{\widetilde{f}}_3(t) - \mathscr{C}_1\right) + \frac{z_1 e^{-z_1 t}}{3(z_2 - z_1)}\left(\frac{F_1(r)}{r} - 2F_1'(r)\right) \tag{3.54}$$

$$e^\eta_r(r,t) = e^{-z_2 t}\left(\frac{z_2}{3}\widetilde{f}_2(t) - \frac{z_2}{r^2}\widetilde{f}_3(t) - \frac{z_2 e^{-z_1 t}}{3(z_2 - z_1)}\left(\frac{F_1(r)}{r} - 2F_1'(r)\right) + \mathscr{C}_1\right) \tag{3.55}$$

$$e^e_{2r}(r,t) = e^{-z_2 t}\left(\frac{1}{3}\dot{\widetilde{f}}_2(t) - \frac{1}{r^2}\dot{\widetilde{f}}_3(t)\right) - \frac{e^{-z_1 t}}{3}\left(\frac{F_1(r)}{r} - 2F_1'(r)\right)$$

$$e^e_{1\varphi}(r,t) = e^{-z_2 t}\left(-\frac{z_2}{3}\widetilde{f}_2(t) + \frac{1}{3}\dot{\widetilde{f}}_2(t) - \frac{z_2}{r^2}\widetilde{f}_3(t) + \frac{1}{r^2}\dot{\widetilde{f}}_3(t) - \mathscr{C}_1\right) - \frac{e^{-z_1 t}}{3r}\Big(z_2\left(-2F_1''(r) + F_1'(r) - F_1(r)\right) -$$

$$-\frac{1}{2\mu_1}\Big((3k_+ + 4\mu_+)r^2 F_1''(r) + (3k_+ + 4\mu_2 + 2\mu_1) r F_1'(r) - (3k_+ + 4\mu_2)F_1(r)\Big)\Big) \tag{3.56}$$

$$e^e_{2\varphi} = e^{-z_2 t}\left(\frac{\dot{\widetilde{f}}_2(t)}{3} + \frac{\dot{\widetilde{f}}_3(t)}{r^2}\right) - \frac{e^{-z_1 t}}{3}\left(F_1'(r) - 2\frac{F_1(r)}{r}\right) \tag{3.57}$$

$$e^e_{1z} = \frac{2e^{-z_2 t}}{3}\left(z_2\widetilde{f}_2(t) - \dot{\widetilde{f}}_2(t)\right) + e^{-z_1 t}\left(\frac{3(3k_+ + 4\mu_+)}{4\mu_1}\left(rF_1''(r) + F_1'(r) - \frac{F_1(r)}{r}\right) + F_1'(r) + \frac{F_1(r)}{r}\right) \tag{3.58}$$

$$e^e_{2z} = -\frac{2}{3}\dot{\widetilde{f}}_2(t)e^{-z_2 t} - \frac{e^{-z_1 t}}{3}\left(F_1'(r) + \frac{F_1(r)}{r}\right) \tag{3.59}$$

Writing down the initial conditions, we have

$$F_1(r) = -r\dot{\widetilde{f}}_2(0) - \frac{1}{r}\dot{\widetilde{f}}_3(0), \qquad F_1'(r) = -\dot{\widetilde{f}}_2(0) + \frac{1}{r^2}\dot{\widetilde{f}}_3(0)$$

In initial material displacements are given by Lame formulae

$$u^-(r,t) = \mathscr{A}_-(t)r + \frac{\mathscr{B}_-(t)}{r^2} \tag{3.60}$$

in our case of the cylinder u is to be finite at $r = 0$, therefore $\mathscr{B}_-(t) = 0$.

To solve the problem we have to find $\widetilde{f}_2(t)$, $\widetilde{f}_3(t)$ and $\mathscr{A}_-(t)$ from the boundary conditions and the conditions at the interface. Therefore, from (3.52), taking into account (3.46) and (3.60), solving

the system of differential equation (boundary conditions and conditions at the interface), we have

$$\widetilde{f}_2(t) = e^{z_2 t}\left(\frac{3k_+ + 4\mu_+}{4\mu_1 z_2}\dot{\widetilde{f}}_2(0)e^{-z_1 t} + \frac{3\left((k_+\vartheta^{tr} + \sigma_0)(k_- + \mu_2)\mathrm{R}^2 - k_+\mu_2\vartheta^{tr}a^2\right)}{2z_2\mathscr{P}_1}\right) + \mathscr{C}_2 e^{\mathscr{W}_1 t} + \mathscr{C}_3 e^{\mathscr{W}_2 t} - \frac{3}{4}\mathscr{C}_1 \tag{3.61}$$

$$\widetilde{f}_3(t) = e^{z_2 t}\left(\frac{3k_+ + 4\mu_+}{4\mu_1 z_2}\dot{\widetilde{f}}_3(0)e^{-z_1 t} - \frac{\mathrm{R}^2 a^2}{2z_2\mathscr{P}_2}\left(3k_- k_+\vartheta^{tr} - (3(k_+ - k_-) + \mu_2)\sigma_0\right)\right) - \left(\frac{k_+ - k_-}{k_-}(\mathrm{R}^2 - a^2) + \frac{2}{3}\mathrm{R}^2\right)\mathscr{C}_3 e^{\mathscr{W}_2 t} \tag{3.62}$$

$$\mathscr{A}_-(t) = \frac{(3k_+\mu_2\vartheta^{tr} + \sigma_0(3k_+ + 4\mu_2))\mathrm{R}^2 - 3k_+\mu_2\vartheta^{tr}a^2}{6\mathscr{P}_1\mathscr{P}_2} + \frac{2\mu_1\mu_+ z_2}{\mathscr{P}_2}(r^2 - a^2)\mathscr{C}_2 e^{(\mathscr{W}_1 - z_2)t} -$$
$$-\frac{\mu_1 z_2(r^2 - a^2)}{3k_-\mathscr{P}_2}\left((3k_+ - k_-)(3k_+ + \mu_+)\mathrm{R}^2 - 3k_+(3(k_+ - k_-) + \mu_+)a^2\right)\mathscr{C}_3 e^{(\mathscr{W}_2 - z_2)t} \tag{3.63}$$

where

$$\mathscr{P}_1 = (3k_+ + \mu_2)(k_- + \mu_2)\mathrm{R}^2 - \mu_2(3(k_+ - k_-) + \mu_2)a^2, \quad \mathscr{P}_2 = (3k_+ + \mu_+)(k_- + \mu_+)\mathrm{R}^2 - \mu_+(3(k_+ - k_-) + \mu_+)a^2$$
$$\mathscr{W}_1 = \frac{\mu_1 z_2}{\mathscr{P}_2}\left((k_- + \mu_+)\mathrm{R}^2 - \mu_+ a^2\right), \qquad \mathscr{W}_2 = \frac{\mu_1 z_2}{\mathscr{P}_2}\left((3k_+ + \mu_+)\mathrm{R}^2 - (3(k_+ - k_-) + \mu_+)a^2\right) \tag{3.64}$$

where $\mathscr{C}_2$ and $\mathscr{C}_3$ are integration constants, can be found from the conditions at the interface at the moments, when reaction front is just came there: $u^+(a,t_a) = u^-(a,t_a)$ and $\sigma_r^+(a,t_a) = \sigma_r^-(a,t_a)$:

$$\mathscr{C}_2 = -\frac{3e^{-(\mathscr{W}_1 - z_2)t_a}}{2\left((3k_+ - k_-)\mathrm{R}^2 - 3(k_+ - k_-)a^2\right)\mathscr{W}_1\mathscr{P}_1}\left((3k_+ - k_-)(k_- + \mu_2)(k_+\vartheta^{tr} + \sigma_0)\mathrm{R}^4 - (k_+(3k_+(k_- + 2\mu_2) -\right.$$
$$\left.-4k_-\mu_2)\vartheta^{tr} + (3k_+ - 4k_-)\mu_2\sigma_0)\mathrm{R}^2 a^2 + 3k_+(k_+ - k_-)\mu_2\vartheta^{tr}a^4\right) \tag{3.65}$$

$$\mathscr{C}_3 = -\frac{3\left(3k_- k_+\vartheta^{tr} - \left(3(k_+ - k_-) - \mu_2\right)\sigma_0\right)k_-\mathrm{R}^2 a^2 e^{-(\mathscr{W}_2 - z_2)t_a}}{2\left((3k_+ - k_-)\mathrm{R}^2 - 3(k_+ - k_-)a^2\right)\mathscr{W}_2\mathscr{P}_1} \tag{3.66}$$

Then the strain density of the initial material is

$$w_- = \frac{2}{3}(3k_- + \mu_-)\mathscr{A}_-^2 \tag{3.67}$$

in the transformed material we have

$$w_+ = k_+\left(\dot{\widetilde{f}}_2(t)e^{-z_2 t} - \dot{\widetilde{f}}_2(0)e^{-z_1 t} - \varepsilon^{tr}\right)^2 + \frac{2}{3}\mu_+\left(\left(\dot{\widetilde{f}}_2 e^{-z_2 t} - \dot{\widetilde{f}}_2(0)e^{-z_1 t}\right)^2 + \frac{3}{a^4}\left(\dot{\widetilde{f}}_3(t)e^{-z_2 t} - \dot{\widetilde{f}}_3(0)e^{-z_1 t}\right)^2\right) \tag{3.68}$$

and therefore

$$\boldsymbol{\sigma}^- : [\![\varepsilon]\!] = \frac{4}{3}(3k_- + \mu_-)\mathscr{A}_-(t)\left(\dot{\widetilde{f}}_2(t)e^{-z_2 t} - \dot{\widetilde{f}}_2(0)e^{-z_1 t} - \mathscr{A}_-(t)\right) \tag{3.69}$$

Substitution of (3.67), (3.68) and (3.69) into (1.30) gives χ as a quadratic function of external stress and transformation strain, elastic modulus of the constituents:

$$\chi(\sigma_0) = \chi(\sigma_0,\xi) = \frac{1}{2\mathscr{H}_1^2}\left((\mathscr{K}_+ - \mathscr{K}_-)\mathscr{H}_2\sigma_0^2 - 2\mathscr{K}_- k_+\mathscr{H}_2\vartheta^{tr}\sigma_0 - \mu_+ k_+\mathscr{H}_3(\vartheta^{tr})^2\right) \tag{3.70}$$

where

$$\mathscr{H}_1 = 3\mu_+(\mathscr{K}_+ - \mathscr{K}_-)(\xi^2 - 2\xi) - (\mathscr{K}_+ + 3\mu_+)\mathscr{K}_-, \quad \mathscr{H}_2 = 3(\mathscr{K}_+ + 3\mu_+)(\mathscr{K}_- + 3\mu_+), \quad \mathscr{K}_\pm = 3k_\pm + \mu_\pm$$
$$\mathscr{H}_3 = 9\mu_+(\mathscr{K}_+ - \mathscr{K}_-)(\mathscr{K}_- - \mu_+)\xi^2(\xi - 2)^2 - 2(\mathscr{K}_+ + 3\mu_+)\mathscr{K}_-\left(3(\mathscr{K}_- - \mu_+)\xi(\xi - 2) - 2\mathscr{K}_-\right)$$

Substitution of (3.70) into (1.30) and (1.33) leads to the explicit dependencies of A_{NN} and c_{eq} at the reaction front on external stress and transformation strain, elastic modules of the constituents and chemical energies. In particularly,

$$\frac{c_{eq}}{c_*} = \exp\left\{-\frac{n_-\mathscr{M}_-}{\rho_-}\frac{(\gamma-\chi(\sigma_0))}{R_gT}\right\}$$

Then integration of the equation (3.43) leads to the kinetic equation:

$$\dot{\xi} = \frac{n_-\mathscr{M}_-}{\rho_-}\frac{c_*}{\frac{1}{k_*}+\frac{1-\xi}{\alpha}-\frac{\ln(1-\xi)}{D_0}(1-\xi)}\left(1-\exp\left\{-\frac{n_-\mathscr{M}_-}{\rho_-}\frac{(\gamma-\chi(\sigma_0))}{R_gT}\right\}\right)$$

In this section, explicit or implicit kinetics equations were obtained. Now, they will be used and solved numerically in order to study reaction kinetics, stress relaxation behind the reaction front.

3.2 Equilibrium concentration, kinetics of the reaction front and blocking effect

Note, that resulting kinetics equations for each reaction front are the same, as it was in the case of elastic reaction product in Chapter 2. For planar reaction front, the equation (3.13) for χ is the same as equation (2.14); for spherical chemical reaction front the equation (3.42) is the same as (2.22); and for cylindrical front propagation the equation (3.70) is equal to (2.31). There are two reasons for it:

– we calculate the equilibrium concentration at the reaction front, from where we obtain χ;

– on the assumption (3.9) that we make, the viscous strains cannot occur instantaneously at the reaction, while the transformation and elastic strains appears instantaneously.

Therefore, from our assumption at the reaction front, we do not have the influence of the viscous deformations on the reaction velocity, but we have the stress relaxation behind the reaction front (see details bellow). This explains why the more simple Deal-Grove model works for the kinetics prediction, since constitutive model does not affect the reaction front propagation. However, the chemical transformation induces huge stresses at the reaction front (see details in the next section), and from the experimental observation it is shown that the chemical reaction generates stresses in the transformed layer, which causes the failure. Hence, to estimate the life-time of the considered solid and the stresses due to the chemical transformation, it is important to take into account the viscous and further plastic deformations.

Since the viscous deformations do not affect the reaction kinetics, therefore, the analysis of equilibrium concentration and kinetics of the reaction is determined by the elastic deformations and is performed in 2.2.

3.3 Stress relaxation behind the reaction front

The difference of molar volumes of initial material and transformed material is a source of volume expansion due to chemical reaction. Kinematic compatibility, i.e. displacement continuity at the reaction front, restricts the transformation strain and produces stresses which can be huge in the case of an elastic behavior of the reaction product. Viscoelastic assumption allows the strain in the transformed layer to be partly accommodated by the viscous deformation, making it possible that the volume increases due to the increase of the thickness of the transformed layer leading to the stress relaxation (see, e.g., [20, 30, 31, 73, 74]).

The transformation strain may produce huge stresses at the reaction front which would remain in a pure elastic problem statement and might cause fracture. In this section, one can see how narrow the high stresses domain can be and how fast the stresses may relax due to the viscous behavior of the reaction product at proper viscosities. This in turn demonstrates that, in

dependence of the viscosity, the stress relaxation can or cannot prevent damage accumulation and fracture at the reaction front.

3.3.1 Planar reaction front

To calculate stresses in the transformed material, i.e. behind the reaction front, according to (3.1), (3.2) and (3.3) one has to know time-evolution of volume strain ϑ^+ and deviators $\mathbf{e}_2 = \mathbf{e}^+$ and $\mathbf{e}^\eta$ or $\mathbf{e}_1^e$.

Substitution of $\varepsilon^+ - \dfrac{\vartheta^+}{3}\mathbf{I}$ and $\boldsymbol{\sigma}^+ - \sigma^+\mathbf{I}$ into Eq. (3.4) instead of $\mathbf{s}^+$ and $\mathbf{e}^+$ with the restrictions $\varepsilon_x^+ = \varepsilon_0$, $\varepsilon_z^+ = 0$, leads to the equations

$$-\left(1+\frac{\mu_2}{\mu_1}\right)\frac{\dot\vartheta^+}{3} + \frac{\mu_2}{\eta}\left(\varepsilon_0 - \frac{\vartheta^+}{3}\right) = \frac{1}{2\mu_1}\left(\dot\sigma_x^+ - \dot\sigma^+\right) + \frac{1}{2\eta}(\sigma_x^+ - \sigma^+), \tag{3.71}$$

$$-\left(1+\frac{\mu_2}{\mu_1}\right)\frac{\dot\vartheta^+}{3} - \frac{\mu_2}{\eta}\frac{\vartheta^+}{3} = \frac{1}{2\mu_1}\left(\dot\sigma_z^+ - \dot\sigma^+\right) + \frac{1}{2\eta}(\sigma_z^+ - \sigma^+). \tag{3.72}$$

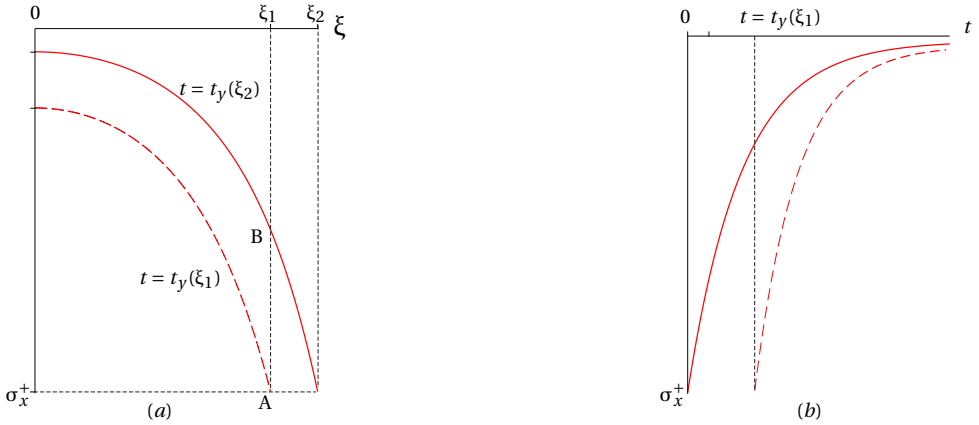

Figure 3.5: Stress relaxation behind the reaction front: (*a*) stress distributions behind the front for two front positions at times $t = t_y(\xi_1)$ and $t = t_y(\xi_2)$; (*b*) stress relaxation in points $\xi = 0$ and $\xi = \xi_1$ starting from the moments $t = t_y(0) = 0$ and $t = t_y(\xi_1)$, respectively.

Adding Eq. (3.71) and (3.72) and taking into account Eq. (3.2), we derive the differential equation for ϑ^+:

$$\dot\vartheta^+ + \frac{\vartheta^+}{\tau_+} - \frac{3(k_+\vartheta^{tr} + 2\mu_2\varepsilon_0)}{\tau_1\left(3k_+ + 4\mu_+\right)} = 0, \tag{3.73}$$

where

$$\tau_1 = \frac{\eta}{\mu_1}, \quad \tau_+ = \frac{(3k_+ + 4\mu_+)}{(3k_+ + 4\mu_2)}\frac{\eta}{\mu_1}.$$

The initial condition for Eq. (3.73) is the value $\vartheta^+(t_y)$ at time t_y; it is given by (3.11). Then the solution of Eq. (3.73) takes the form:

$$\vartheta^+(y,t) = \frac{6\mu_1 k_+(3\varepsilon_0 - 2\vartheta^{tr})}{\left(3k_+ + 4\mu_2\right)\left(3k_+ + 4\mu_+\right)}\exp\left(-\frac{t - t_y}{\tau_+}\right) + \frac{3(k_+\vartheta^{tr} + 2\mu_2\varepsilon_0)}{3k_+ + 4\mu_2}, \tag{3.74}$$

where the dependence $t_y = t_y(y)$ is given by (3.15). One can see that the volume strain in points behind the front increases or decreases with time depending on the sign of the difference $(3\varepsilon_0 - 2\vartheta^{tr})$.

Next step is to find e_x^+ and e_{1x}^e. Since

$$e_x^+ = \varepsilon_0 - \vartheta^+/3, \tag{3.75}$$

from Eq. (3.74) it directly follows that

$$e_x^+(y,t) = -\frac{2\mu_1 k_+ \left(3\varepsilon_0 - 2\vartheta^{tr}\right)}{\left(3k_+ + 4\mu_2\right)\left(3k_+ + 4\mu_+\right)} \exp\left(-\frac{t - t_y}{\tau_+}\right) + \frac{\varepsilon_0\left(3k_+ + 2\mu_2\right) - k_+\vartheta^{tr}}{3k_+ + 4\mu_2}. \tag{3.76}$$

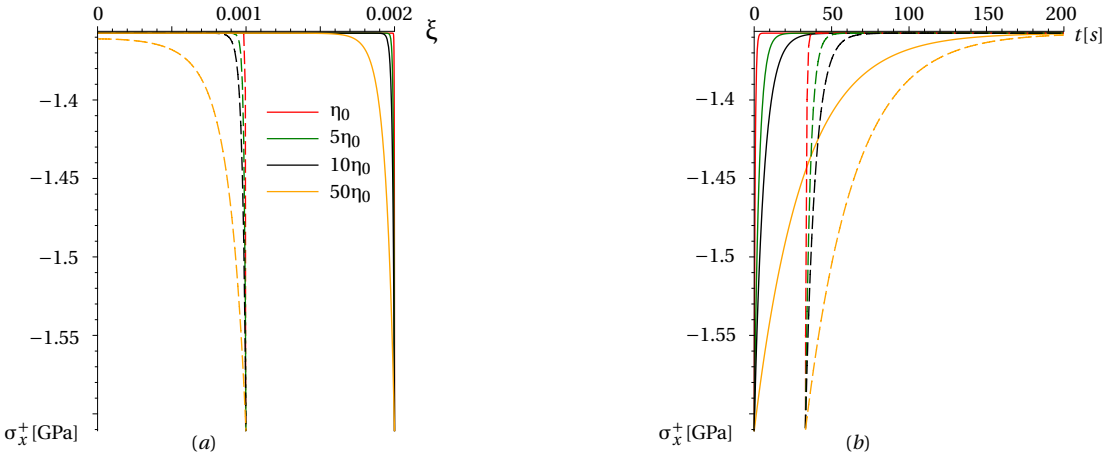

Figure 3.6: Planar reaction front: stress relaxation at various values of viscosity coefficient η for the standard linear solid model: (*a*) stress distributions behind the front for two front positions ξ = 0.001 (dashed lines) and ξ = 0.002 (solid lines), (*b*) stress relaxation in points ξ = 0 (solid lines) and for ξ = 0.005 (dashed lines) ; $\varepsilon_0 = 0$, $\eta_0 = 15.9$GPa·s. Solid and dashed curves of the same colour correspond to the same viscosity coefficient.

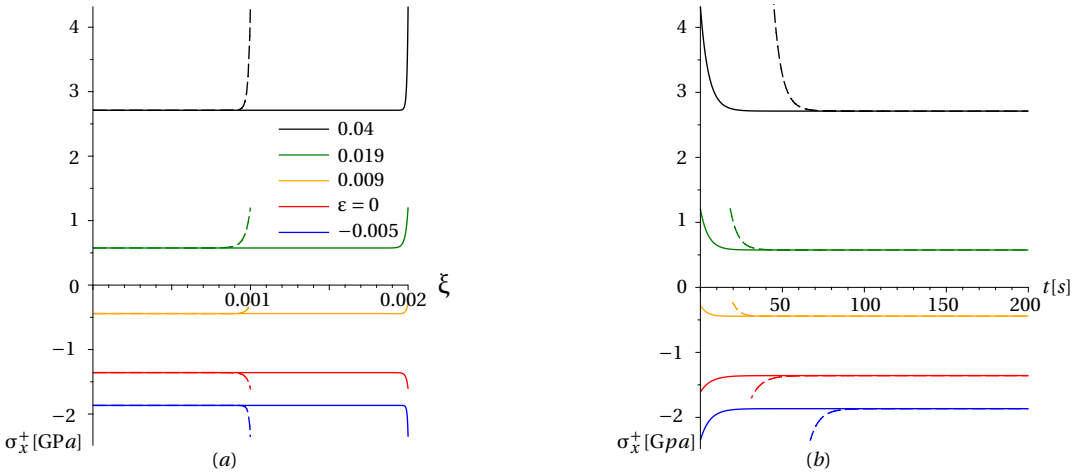

Figure 3.7: Planar reaction front: stress relaxation at various values of external strain ε_0: (*a*) stresses behind the reaction front; (*b*) stress relaxation in two points. Solid and dashed curves of the same colour correspond to the same external strains.

By constitutive equations (3.3),

$$\mathbf{e}_1^e = \tau_1 \dot{\mathbf{e}}^\eta = \tau_1(\dot{\mathbf{e}}^+ - \dot{\mathbf{e}}_1^e).$$

Then from (3.75) it follows that e_{1x}^e can be found from the equation

$$\dot{e}_{1x}^e + \frac{1}{\tau_1} e_{1x}^e = -\frac{\dot{\vartheta}^+}{3} \tag{3.77}$$

with the initial condition

$$e^e_{1x}(y,t_y) = e^+_x(y,t_y) = \varepsilon_0 - \frac{\vartheta^+(y,t_y)}{3}. \tag{3.78}$$

The condition (3.78) follows from Eq. (3.9) with $\vartheta^+(y,t_y)$ taken from Eq. (3.11).

After calculating the time derivative $\dot{\vartheta}^+$ from Eq. (3.74) and substituting it into the right hand side of Eq. (3.77) we come to the equation for e^e_{1x} that, with the initial condition (3.78), has a solution:

$$e^e_{1x}(y,t) = \frac{k_+(3\varepsilon_0 - 2\vartheta^{tr})}{2(3k_+ + 4\mu_+)} \exp\left(-\frac{t-t_y}{\tau_+}\right) + \frac{\varepsilon_0}{2}\exp\left(-\frac{t-t_y}{\tau_1}\right). \tag{3.79}$$

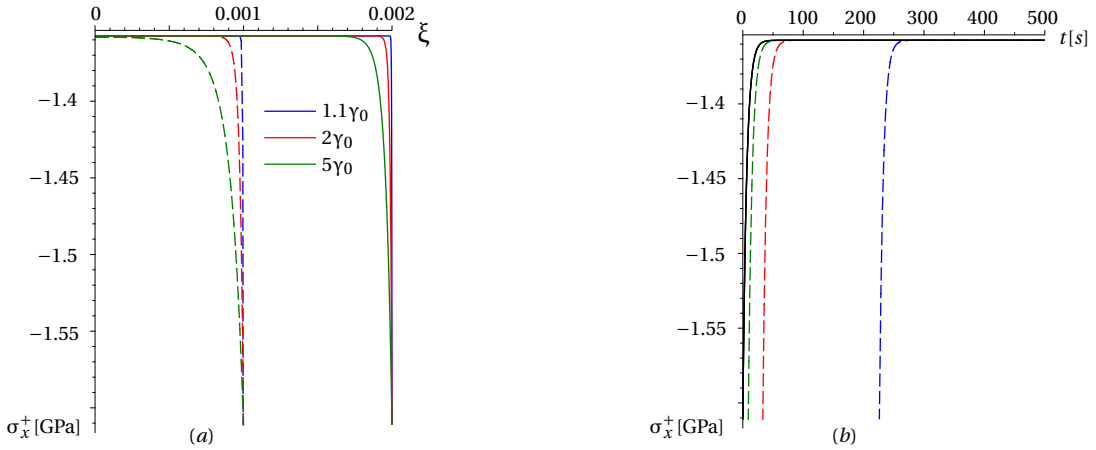

Figure 3.8: Planar reaction front: stress relaxation at various values of energy parameter γ for the standard linear solid model: (*a*) stresses behind the reaction front, (*b*) stress relaxation in two points $\xi = 0$ (solid lines) and for $\xi = 0.005$ (dashed lines). Solid and dashed curves of the same colour correspond to the same energy parameter.

Finally, from (3.74), (3.76) and (3.79) it follows that

$$\sigma^+_x(y,t) = \frac{9\mu_1 k_+^2\left(3\varepsilon_0 - 2\vartheta^{tr}\right)}{\left(3k_+ + 4\mu_2\right)\left(3k_+ + 4\mu_+\right)} \exp\left(-\frac{t-t_y}{\tau_+}\right) + \mu_1\varepsilon_0 \exp\left(-\frac{t-t_y}{\tau_1}\right) + \\ + \frac{2\mu_2\left(2(3k_+ + \mu_2)\varepsilon_0 - 3k_+\vartheta^{tr}\right)}{3k_+ + 4\mu_2} \tag{3.80}$$

Then at the reaction front

$$\sigma^+_x(y,t_y) = \frac{2\mu_+\left(2\left(3k_+ + \mu_+\right)\varepsilon_0 - 3k_+\vartheta^{tr}\right)}{3k_+ + 4\mu_+}$$

Since

$$\sigma^+_z(y,t) = 3k_+(\vartheta^+(t) - \vartheta^{tr}) - \sigma^+_x(t) = \\ = \frac{9\mu_1 {k_+}^2\left(3\varepsilon_0 - 2\vartheta^{tr}\right)}{(3k_+ + 4\mu_2)(3k_+ + 4\mu_+)} \exp\left(-\frac{t-t_y}{\tau_+}\right) - \mu_1\varepsilon_0 \exp\left(-\frac{t-t_y}{\tau_1}\right) + \frac{2\mu_2\left(3k_+\left(\varepsilon_0 - \vartheta^{tr}\right) - 2\mu_2\varepsilon_0\right)}{3k_+ + 4\mu_2} \tag{3.81}$$

at the reaction front

$$\sigma^+_z(y,t_y) = \frac{2\mu_+\left(\left(k_+ - 2\mu_+\right)\varepsilon_0 - k_+\vartheta^{tr}\right)}{3k_+ + 4\mu_+}$$

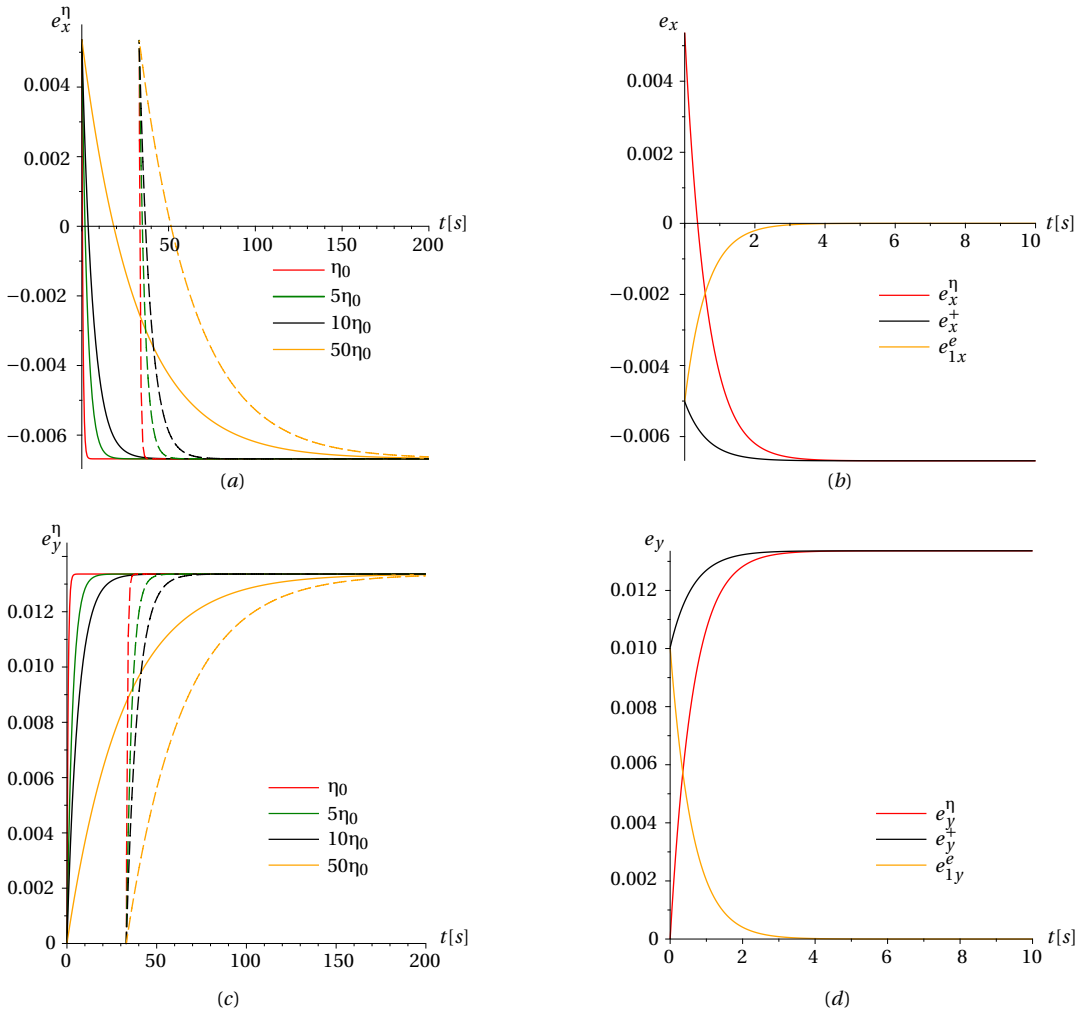

Figure 3.9: Planar reaction front: evolution and redistribution of viscous and elastic strains: (a) and (c) – evolution of viscous strains e_x^η and e_y^η in point $\xi = 0$ from the moment $t = 0$ and in the point y that is reached by the reaction front at time $t_y = 200s$ for various viscosity coefficients; (b) and (d) – relation between the inputs of elastic strains e_{1x}^e, e_{1y}^e and viscous strains e_x^η, e_y^η into total strains e_x^+, e_y^+.

For completeness, we also write down the formulas for strain the strains e_y^η and ε_y^+. To specify $\mathbf{e}^\eta$, note that from (3.3) it follows that

$$\mathbf{e}^\eta = \left(1 + \frac{\mu_2}{\mu_1}\right)\mathbf{e}^+ - \frac{1}{2\mu_1}\left(\boldsymbol{\sigma}^+ - \sigma^+\mathbf{I}\right) \tag{3.82}$$

Then, with $e_y^+ = \frac{2}{3}\vartheta^+ - \varepsilon_0$ and $\sigma_y = 0$, from (3.82) it follows that

$$e_y^\eta(y,t) = \frac{1}{2\mu_1}\left\{\left(k_+ + \frac{4}{3}\mu_+\right)\vartheta^+(y,t) - \left(k_+\vartheta^{tr} + 2\mu_+\varepsilon_0\right)\right\}$$

where the dependence of ϑ^+ is given by (3.74). The dependence $\varepsilon_y^+(y,t)$ follows from the equality $\varepsilon_y^+ = \vartheta^+ - \varepsilon_0$ and (3.74).

The distributions of stress σ_x^+ behind the reaction front at two moments $t_y(y)$ which correspond to the dimensionless front positions $\xi = \xi_1$ and ξ_2 are schematically shown in Fig. 3.5*a*. The stress σ_x^+ at $\xi = \xi_1$ relaxes from A to B during the time of the front propagation from ξ_1 to ξ_2. Stress relaxation in two points at $\xi = 0$ and $\xi = \xi_1$ starting from the moments $t = t_y(0) = 0$ and $t = t_y(\xi_1)$, respectively, is shown in Fig. 3.5*b*.

The results of quantitative studies of stress relaxation and strains evolution and the redistribution of various modes of strains are shown in Fig. 3.6, 3.7 and Fig. 3.9, respectively. Material

parameters are given in Table 2.1. Two sets of the stress distributions behind the reaction front at two moments t_y which correspond to the front positions $\xi = 0.001$ and $\xi = 0.002$, and two sets of stress relaxation curves for stresses in points $\xi = 0$ and $\xi = 0.005$ are shown for various viscosity coefficients η and various external strains ε_0. Fig. 3.7 shows how the curves are affected by external strain, in particular, how fast the limit residual "elastic" stress is reached.

Relaxation times τ_+ and τ_1 do not depend on energy parameter γ. But γ affects the front velocity and, thus, the front kinetics. Increasing γ increases the front velocity and decreases the time t_y, in other words, increasing γ "compresses" the time in Eq. (3.14) due to the increase of parameter Q. That is why stresses found for the same two front positions but at various γ have less time for the relaxation if γ increases. This tendency is reflected by the stress distributions shown in Fig. 3.8*b*. Note that the energy parameter depends on temperature, and the temperature may also affect stress relaxation via the viscosity coefficient.

Note that in experiments the thickness of the layer of the transformed material is usually observed which does not coincide with the front position predicted by the model. Fig. 3.9(b) demonstrates how residual strain $e_y^+ = \lim\limits_{t\to\infty} e_y^\eta$ is formed at various viscosity coefficients.

3.3.2 Spherical reaction front

For the case of the chemical reaction localized on spherical reaction front, we obtain the resulting equations for the deviators e_1^e and e^η. Substitution of (3.33), (3.34), (3.31) for $\widetilde{f_3}$, its time derivative and for F_1, into (3.28), and taking into account (3.38) and (3.37), leads to the equation

$$e_{1r}^e = \frac{2\left(k_+k_-\vartheta^{tr} - (k_+ - k_-)\sigma_0\right)\mathrm{R}^3(1-\xi)^3}{\left(k_+(3k_- + 4\mu_+) - 4\mu_+(k_+ - k_-)(1-\xi)^3\right)r^3}\exp\left\{-\frac{z_2\,(\mathfrak{U}_2 - \mathfrak{U}_1)}{\mathfrak{U}_1}(t - t_a)\right\} \tag{3.83}$$

Replacing $\widetilde{f_3}$ and F_1 by (3.33) and (3.31), respectively, in the formula (3.29), we obtain

$$e_r^\eta = \frac{\left(k_+k_-\vartheta^{tr} - (k_+ - k_-)\sigma_0\right)\mathrm{R}^3(1-\xi)^3}{\left(k_+(3k_- + 4\mu_2) - 4\mu_2(k_+ - k_-)(1-\xi)^3\right)r^3}\left(1 - 2\exp\left\{-\frac{z_2\,(\mathfrak{U}_2 - \mathfrak{U}_1)}{\mathfrak{U}_1}(t - t_a)\right\}\right) \tag{3.84}$$

To calculate stresses in the transformed material, i.e. behind the reaction front, we write down the equation (3.19) for the radial component, where the deviatoric strain parts are defined by formulas (3.83) and (3.84):

$$\sigma_r^+ = \frac{4\left(k_+k_-\vartheta^{tr} - (k_+ - k_-)\sigma_0\right)\mathrm{R}^3(1-\xi)^3}{\left(k_+(3k_- + 4\mu_2) - 4\mu_2(k_+ - k_-)(1-\xi)^3\right)r^3}\left(\mu_2 + \left(\mu_2 + \frac{3k_+k_-\mu_1(\mathrm{R}^3 - r^3)}{\mathfrak{U}_1}\right)\exp\left\{-\frac{z_2\,(\mathfrak{U}_2 - \mathfrak{U}_1)}{\mathfrak{U}_1}(t - t_a)\right\}\right) +$$
$$+ k_+\frac{(3k_- + 4\mu_2)\sigma_0 - 4\mu_2k_-\vartheta^{tr}(1-\xi)^3}{k_+(3k_- + 4\mu_2) - 4\mu_2(k_+ - k_-)(1-\xi)^3}$$

Likewise the calculations of tangential stress and strain can be obtained, taking into account that

$$e_{1\varphi}^e = -\frac{e_{1r}^e}{2}, \qquad e_\varphi^\eta = -\frac{e_r^\eta}{2}$$

From (3.20) we have the resulting formulae for σ_φ^+:

$$\sigma_\varphi^+ = -\frac{2\left(k_+k_-\vartheta^{tr} - (k_+ - k_-)\sigma_0\right)\mathrm{R}^3(1-\xi)^3}{\left(k_+(3k_- + 4\mu_2) - 4\mu_2(k_+ - k_-)(1-\xi)^3\right)r^3}\left(\mu_2 + \left(\mu_2 + \frac{3k_+k_-\mu_1(\mathrm{R}^3 - r^3)}{\mathfrak{U}_1}\right)\exp\left\{-\frac{z_2\,(\mathfrak{U}_2 - \mathfrak{U}_1)}{\mathfrak{U}_1}(t - t_a)\right\}\right) +$$
$$+ k_+\frac{(3k_- + 4\mu_2)\sigma_0 - 4\mu_2k_-\vartheta^{tr}(1-\xi)^3}{k_+(3k_- + 4\mu_2) - 4\mu_2(k_+ - k_-)(1-\xi)^3}$$

As it was mentioned in the case of planar reaction front, the chemical transformation generates stresses which can be huge. Viscoelastic assumption allows the strain in the transformed layer to

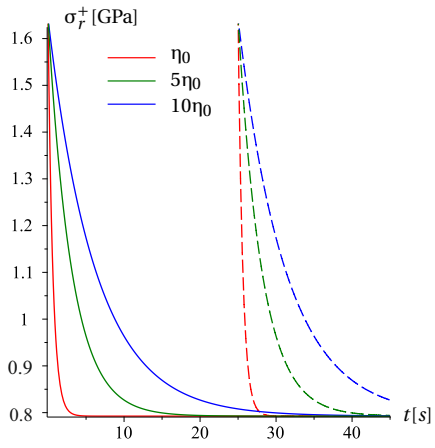

Figure 3.10: Spherical reaction front: stress relaxation at various values of viscosity coefficient η for the standard linear solid model: stress relaxation in points $\xi = 0$ (solid lines) and for $\xi = \xi(t = 100s)$ (dashed lines) ; $\eta_0 = 15.9$GPa·s. Solid and dashed curves of the same colour correspond to the same viscosity coefficient.

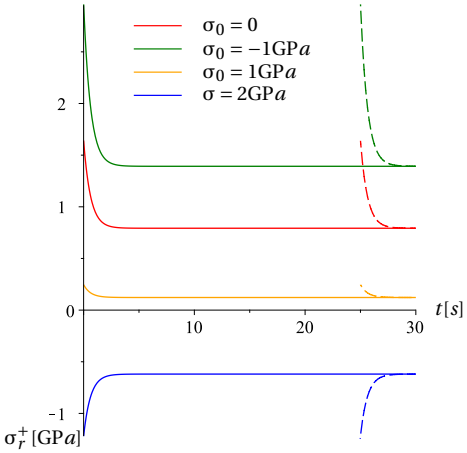

Figure 3.11: Spherical reaction front: stress relaxation at various values of external stress σ_0: stress relaxation in two points. Solid and dashed curves of the same colour correspond to the same external strains.

be partly accommodated by the viscous deformation, making it possible that the volume increases due to the increase of the thickness of the transformed layer leading to the stress relaxation.

The distributions of stress behind the reaction front at two moments t_a which correspond to the dimensionless front positions $\xi = \xi_1$ and ξ_2 are schematically shown in Fig. 3.5*a*. Stress relaxation in two points at $\xi = 0$ and $\xi = \xi_1$ starting from the moments $t = t_a(0) = 0$ and $t = t_a(\xi_1)$, respectively, is shown in Fig. 3.5*b*.

The results of quantitative studies of stress relaxation and strains evolution and the redistribution of various modes of strains are shown in Fig. 3.10, 3.11 and Fig. 3.12, respectively. Material parameters are given in Table 2.1. Two sets of stress relaxation curves for stresses in points $\xi = 0$ and $\xi = \xi(t = 100s)$ are shown for various viscosity coefficients η and various external stress σ_0. Fig. 3.11 shows how the curves are affected by external stress, in particular, how fast the limit residual "elastic" stress is reached.

Note that in experiments the thickness of the layer of the transformed material is usually observed which does not coincide with the front position predicted by the model. Fig. 3.12(b) demonstrates how residual strain $e_r^+ = \lim_{t\to\infty} e_r^\eta$ is formed at various viscosity coefficients.

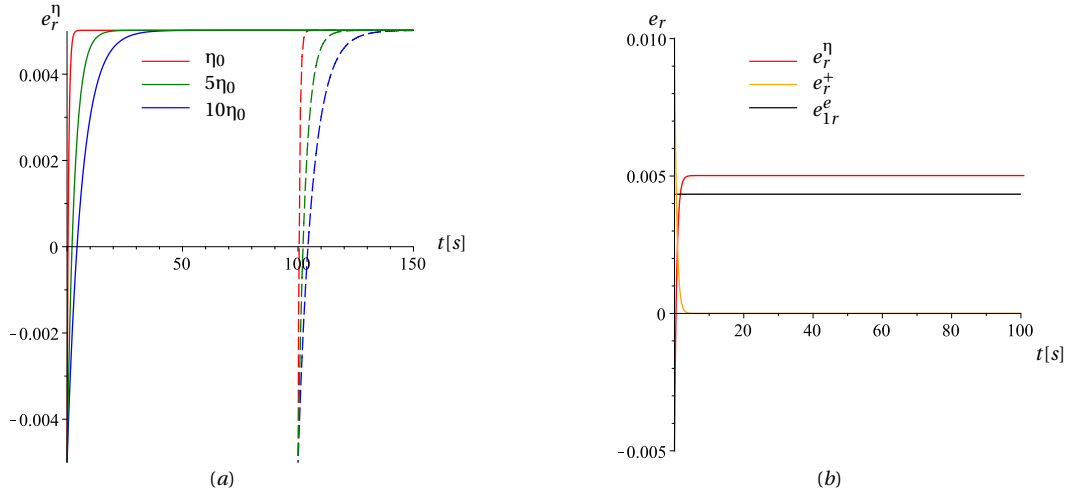

Figure 3.12: Spherical reaction front: Evolution and redistribution of viscous and elastic strains: (a) and – evolution of viscous strains e_r^η in point $\xi = 0$ from the moment $t = 0$ and in the point y that is reached by the reaction front at time $t_y = 100s$ for various viscosity coefficients; (b) – relation between the inputs of elastic strains e_{1r}^e and viscous strains e_r^η into total strains e_r^+.

3.3.3 Cylindrical reaction front

In cylindrical geometry, the resulting formulas are huge, so we provide here the more compact form of the results.

To calculate stresses in the transformed material, according to (3.46) one has to know time evolution of volume strain ϑ^+ and deviators $\mathbf{e}_2 = \mathbf{e}^+$ and $\mathbf{e}_1^e$ or $\mathbf{e}^\eta$.

Substitution of (3.61) and (3.62) into equations (3.54) and (3.55) for e_{1r}^e and e_r^η, respectively, leads to the formulas:

$$e_{1r}^e(r,t) = \frac{\mathscr{C}_2}{3}(\mathscr{W}_1 - z_2)e^{(\mathscr{W}_1 - z_2)t} + \mathscr{C}_3(\mathscr{W}_2 - z_2)\left(\frac{1}{3} + \frac{1}{r^2}\left(\frac{k_+ - k_-}{k_-}(\mathrm{R}^2 - a^2) + \frac{2}{3\mathrm{R}^2}\right)\right)e^{(\mathscr{W}_2 - z_2)t}$$

$$e_r^\eta(r,t) = \frac{(k_+\vartheta^{tr} + \sigma_0)(k_- + \mu_2)\mathrm{R}^2 - k_+\mu_2\vartheta^{tr}a^2}{2\mathscr{P}_1} + \frac{\mathrm{R}^2a^2}{2\mathscr{P}_2 r^2}\left(3k_+k_-\vartheta^{tr} - (3(k_+ - k_-) + \mu_2)\sigma_0\right) +$$
$$+ \frac{z_2}{3}\mathscr{C}_2 e^{(\mathscr{W}_1 - z_2)t} + \left(\frac{z_2}{3} + \frac{1}{r^2}\left(\frac{k_+ - k_-}{k_-}(\mathrm{R}^2 - a^2) + \frac{2}{3}\mathrm{R}^2\right)\right)\mathscr{C}_3 e^{(\mathscr{W}_2 - z_2)t}$$

where $\mathscr{C}_2$ and $\mathscr{C}_3$ are defined by (3.65) and (3.66) accordingly; $\mathscr{W}_1$ and $\mathscr{W}_2$ are determined by (3.64).

In the same way, from (3.56), (3.57) and (3.58), (3.59), we obtain the following equations for the strain deviatoric components:

$$e_{1\varphi}^e(r,t) = \frac{\mathscr{C}_2}{3}(\mathscr{W}_1 - z_2)e^{(\mathscr{W}_1 - z_2)t} + \mathscr{C}_3(\mathscr{W}_2 - z_2)\left(\frac{1}{3} - \frac{1}{r^2}\left(\frac{k_+ - k_-}{k_-}(\mathrm{R}^2 - a^2) + \frac{2}{3\mathrm{R}^2}\right)\right)e^{(\mathscr{W}_2 - z_2)t}$$

$$e_{2\varphi}^e(r,t) = \frac{(k_+\vartheta^{tr} + \sigma_0)(k_- + \mu_2)\mathrm{R}^2 - k_+\mu_2\vartheta^{tr}a^2}{2\mathscr{P}_1} - \frac{\mathrm{R}^2a^2}{2\mathscr{P}_2 r^2}\left(3k_+k_-\vartheta^{tr} - (3(k_+ - k_-) + \mu_2)\sigma_0\right) +$$
$$+ \frac{\mathscr{W}_1}{3}\mathscr{C}_2 e^{(\mathscr{W}_1 - z_2)t} + \mathscr{W}_2\left(\frac{1}{3} - \frac{1}{r^2}\left(\frac{k_+ - k_-}{k_-}(\mathrm{R}^2 - a^2) + \frac{2}{3}\mathrm{R}^2\right)\right)\mathscr{C}_3 e^{(\mathscr{W}_2 - z_2)t}$$

$$e_{1z}^e(r,r) = \frac{2}{3}\left((z_2 - \mathscr{W}_1)\mathscr{C}_2 e^{(\mathscr{W}_1 - z_2)t} + (z_2 - \mathscr{W}_2)\mathscr{C}_3 e^{(\mathscr{W}_2 - z_2)t}\right)$$

$$e_{2z}^e(r,t) = -\frac{1}{\mathscr{P}_1}\left((k_+\vartheta^{tr} + \sigma_0)(k_- + \mu_2)\mathrm{R}^2 - k_+\mu_2\vartheta^{tr}a^2\right) - \frac{2}{3}\left(\mathscr{W}_1\mathscr{C}_2 e^{(\mathscr{W}_1 - z_2)t} + \mathscr{W}_2\mathscr{C}_3 e^{(\mathscr{W}_2 - z_2)t}\right)$$

From (3.46), taking into account the resulting formulas for strain deviator, we conduct the

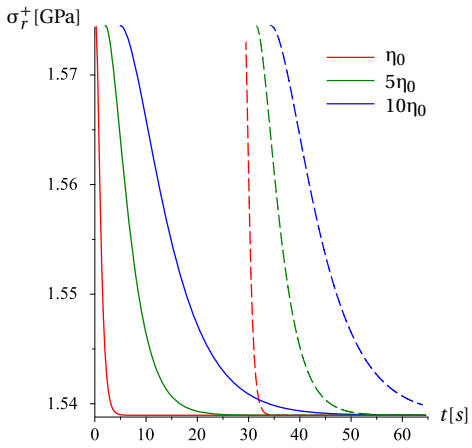

Figure 3.13: Cylindrical reaction front: stress relaxation at various values of viscosity coefficient η for the standard linear solid model: stress relaxation in points $\xi = 0$ (solid lines) and for $\xi = \xi(t = 30s)$ (dashed lines) ; $\eta_0 = 15.9\text{GPa}\cdot\text{s}$. Solid and dashed curves of the same colour correspond to the same viscosity coefficient.

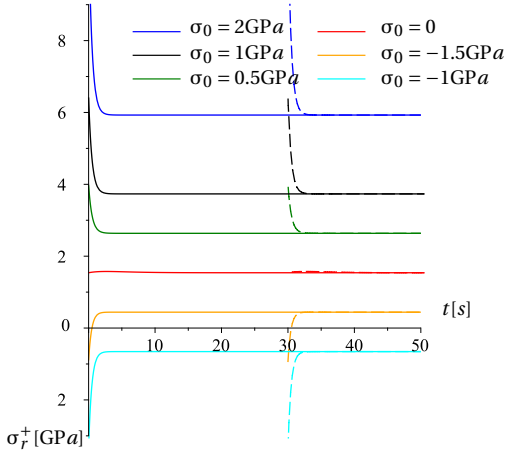

Figure 3.14: Cylindrical reaction front: stress relaxation at various values of external stress σ_0: stress relaxation in two points. Solid and dashed curves of the same colour correspond to the same external strains.

equations for stresses:

$$\sigma_r^+(r,t) = \frac{\mathscr{K}_+ - \mu_1}{\mathscr{P}_1}\left((k_- + \mu_2)(k_+\vartheta^{tr} + \sigma_0)\mathrm{R}^2 - k_+\mu_2\vartheta^{tr}a^2\right) - k_+\vartheta^{tr} - \frac{\mu_2\mathrm{R}^2a^2}{\mathscr{P}_2 r^2}\left(3k_+k_-\vartheta^{tr} - (3(k_+ - k_-) + \mu_2)\sigma_0\right) +$$
$$+\frac{2}{3}\mathscr{C}_2(\mathscr{W}_1\mathscr{K}_+ - \mu_1 z_2)e^{(\mathscr{W}_1 - z_2)t} + 2\mathscr{C}_3\left(\frac{\mathscr{W}_2\mathscr{K}_+ - \mu_1 z_2}{3} + \frac{1}{r^2}(\mu_+\mathscr{W}_2 - \mu_1 z_2)\left(\frac{k_+ - k_-}{k_-}(\mathrm{R}^2 - a^2)\frac{2}{3}\mathrm{R}^2\right)\right)e^{(\mathscr{W}_2 - z_2)t}$$

$$\sigma_\varphi^+(r,t) = \frac{\mathscr{K}_+}{\mathscr{P}_1}\left((k_+\vartheta^{tr} + \sigma_0)(k_- + \mu_2)\mathrm{R}^2 - k_+\mu_2\vartheta^{tr}a^2\right) - k_+\vartheta^{tr} - \frac{\mu_2\mathrm{R}^2a^2}{\mathscr{P}_2 r^2}\left(3k_+k_-\vartheta^{tr} - (3(k_+ - k_-) + \mu_2)\sigma_0\right) +$$
$$+\frac{2}{3}\mathscr{C}_2(\mathscr{K}_+\mathscr{W}_1 - \mu_1 z_2)e^{(\mathscr{W}_1 - z_2)t} + 2\mathscr{C}_3\left(k_+\mathscr{W}_2 + (\mu_+\mathscr{W}_2 - \mu_1 z_2)\left(\frac{1}{3} - \frac{1}{r^2}\left(\frac{k_+ - k_-}{k_-}(\mathrm{R}^2 - a^2) + \frac{2}{3}\mathrm{R}^2\right)\right)\right)e^{(\mathscr{W}_2 - z_2)t}$$

The results of quantitative studies of stress relaxation and strains evolution and the redistribution of various modes of strains are shown in Fig. 3.13, 3.14 and Fig. 3.15, respectively. Material parameters are given in Table 2.1. Two sets of stress relaxation curves for stresses in points $\xi = 0$ and $\xi = \xi(t = 30s)$ are shown for various viscosity coefficients η and various external stress

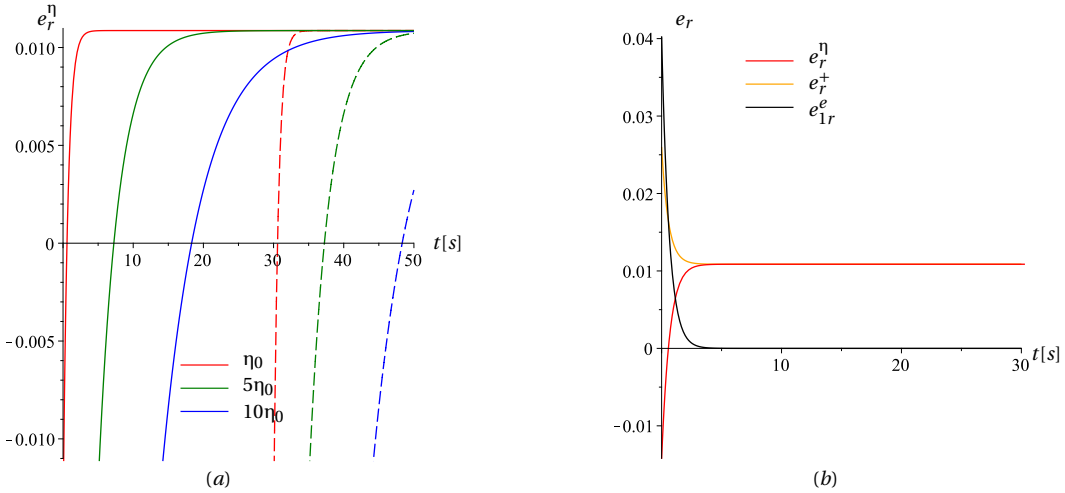

Figure 3.15: Cylindrical reaction front: evolution and redistribution of viscous and elastic strains: (a) and – evolution of viscous strains e_r^η in point $\xi = 0$ from the moment $t = 0$ and in the point y that is reached by the reaction front at time $t_y = 30s$ for various viscosity coefficients; (b) – relation between the inputs of elastic strains e_{1r}^e and viscous strains e_r^η into total strains e_r^+.

σ_0. Fig. 3.14 shows how the curves are affected by external strain, in particular, how fast the limit residual "elastic" stress is reached.

Note that in experiments the thickness of the layer of the transformed material is usually observed which does not coincide with the front position predicted by the model. Fig. 3.15(b) demonstrates how residual strain $e_r^+ = \lim\limits_{t\to\infty} e_r^\eta$ is formed at various viscosity coefficients.

3.4 Particular cases of viscoelastic behaviors

In this section we specify the equations for stresses and strains behind propagating reaction front for three rheological models which can be considered as particular cases of Standard Linear Solid Model and discuss the applicability of these models in the statement of mechanochemistry problems. We focus here only on the case of the planar reaction front, as for other two body's geometries the analysis would be similar.

3.4.1 Maxwell material

We obtain the Maxwell material, Fig. 3.2 *b*, from SLSM setting $\mu_2 = 0$ and $\mu_1 = \mu_+$. The formula (3.13) for χ_0 remains the same with new μ_+. The formulae (3.74), (3.76), (3.79), (3.80) (3.81) for strains ϑ^+, e_x^+, e_{1x}^e and stresses σ_x^+ and σ_z^+ behind the front become

$$\vartheta^+(y,t) = \vartheta^{tr} + \frac{2\mu_+\left(3\varepsilon_0 - 2\vartheta^{tr}\right)}{3k_+ + 4\mu_+}\exp\left(-\frac{t-t_y}{\tau_+}\right),$$

$$e_x^+(y,t) = \varepsilon_0 - \frac{\vartheta^{tr}}{3} - \frac{2\mu_+\left(3\varepsilon_0 - 2\vartheta^{tr}\right)}{3\left(3k_+ + 4\mu_+\right)}\exp\left(-\frac{t-t_y}{\tau_+}\right),$$

$$e_x^e(y,t) = \frac{k_+(3\varepsilon_0 - 2\vartheta^{tr})}{2(3k_+ + 4\mu_+)}\exp\left(-\frac{t-t_y}{\tau_+}\right) + \frac{\varepsilon_0}{2}\exp\left(-\frac{t-t_y}{\tau_1}\right),$$

and

$$\sigma_x^+(y,t) = \frac{3k_+\mu_+\left(3\varepsilon_0 - 2\vartheta^{tr}\right)}{3k_+ + 4\mu_+}\exp\left(-\frac{t-t_y}{\tau_+}\right) + \mu_+\varepsilon_0\exp\left(-\frac{t-t_y}{\tau_1}\right),$$

$$\sigma_z^+(y,t) = \frac{3k_+\mu_+\left(3\varepsilon_0 - 2\vartheta^{tr}\right)}{3k_+ + 4\mu_+}\exp\left(-\frac{t-t_y}{\tau_+}\right) - \mu_+\varepsilon_0\exp\left(-\frac{t-t_y}{\tau_1}\right),$$

where

$$\tau_1 = \frac{\eta}{\mu_+}, \quad \tau_+ = \frac{(3k_+ + 4\mu_+)}{3k_+}\frac{\eta}{\mu_+}.$$

3.4.2 Kelvin-Voigt material

Another particular case is the Kelvin-Voigt material (Fig. 3.2*c*). In this case

$$\mu_1 \to \infty,\ \mu_2 \to \mu_+, \tag{3.85}$$

$$\mathbf{e}^+ = \mathbf{e}^\eta = \mathbf{e}^e, \quad \boldsymbol{\sigma}^+ = k_+\left(\vartheta^+ - \vartheta^{tr}\right)\mathbf{I} + 2\mu_+\mathbf{e}^+ + 2\eta\dot{\mathbf{e}}^+. \tag{3.86}$$

Since the dash-pot element cannot deform simultaneously, at the reaction front $\mathbf{e}^\eta = \mathbf{e}^+ = 0$. Then this degenerative case can be realized only if $\varepsilon_0 = 0$. Then $w_- = 0$ and at the reaction front

$$\vartheta = \vartheta(y, t_y) = 0. \tag{3.87}$$

Then $\chi = w_+ = \frac{1}{2}k_+(\vartheta^+)^2$. Mechanics just subtracts $\frac{1}{2}k_+(\vartheta^+)^2$ from γ in the expression ofA_{NN}. Of course, this also directly follows from (3.13) and (3.1.1) if one takes (3.85).

The equation (3.73) for ϑ behind the front takes the form

$$\dot{\vartheta}^+ + \frac{\vartheta^+}{\tau} - \frac{3k_+}{4\eta}\vartheta^{tr} = 0, \quad \tau = \frac{4\eta}{3k_+ + 4\mu_+}.$$

The solution, satisfying the initial condition (3.87), is

$$\vartheta^+(y,t) = \frac{3k_+\vartheta^{tr}}{3k_+ + 4\mu_+}\left(1 - \exp\left(-\frac{t - t_y}{\tau}\right)\right). \tag{3.88}$$

The volume strain in points behind the front increases with time if $\vartheta^{tr} > 0$. Since $e_x^+ = e_z^+ = -\vartheta/3$, from (3.86) and (3.88) it follows that the stresses behind the front can be expressed via ϑ and relax as

$$\begin{aligned}\sigma_x^+(y,t) = \sigma_z^+(y,t) &= -\frac{2}{3}\eta\dot{\vartheta}^+ + \left(k^+ - \frac{2}{3}\mu_+\right)\vartheta^+ - k_+\vartheta^{tr} \\ &= -\frac{6k_+\mu_+\vartheta^{tr}}{3k_+ + 4\mu_+}\left(1 + \frac{3k_+}{4\mu_+}\exp\left(-\frac{t - t_y}{\tau}\right)\right).\end{aligned} \tag{3.89}$$

At the reaction front

$$\sigma_x^+ = \sigma_z^+ = -\frac{3}{2}k_+\vartheta^{tr}. \tag{3.90}$$

Of course, Eq. (3.88),(3.90) and (3.90) directly follow from (3.74), (3.80) if to take μ_1 and μ_2 from (3.85), but, since this case may be of a special interest, we presented the short derivations (3.86)–(3.89).

3.4.3 Pure linear-viscous material

The linear-viscous material (Fig. 3.2*d*) can be obtained by setting $\mu_+ = 0$ in above formulae. It can be considered only at the same restriction $\varepsilon_0 = 0$ as above. Then at the reaction front $w_- = 0$, $\chi = w_+ = \frac{1}{2}k_+(\vartheta^+)^2$,

$$\vartheta^+ = 0, \quad \sigma_x^+ = \sigma_z^+ = -\frac{3}{2}k_+\vartheta^{tr}$$

It is easy to see that the volume strain in points behind the front increases up to $\vartheta^{tr} > 0$ (decreases if $\vartheta^{tr} < 0$) with time as

$$\vartheta^+(y,t) = \vartheta^{tr}\left(1 - \exp\left(-\frac{t - t_y}{\tau}\right)\right), \quad \tau = \frac{4\eta}{3k_+}$$

and stresses relax as

$$\sigma_x^+(y,t) = \sigma_z^+(y,t) = -\frac{3}{2}k_+\vartheta^{tr}\exp\left(-\frac{t-t_y}{\tau}\right)$$

Note that the restriction $\varepsilon_0 = 0$ makes the Kelvin-Voigt and pure viscous materials rather unsuitable than suitable as rheological models, as opposed the Standard Linear Solid Model and the Maxwell material. This indicates that not every common rheological model can be used for reaction constituents in the considerations of coupled problems of mechanochemistry.

3.5 Conclusions

In this Chapter the stress-affected chemical reaction front propagation in deformable solid in the cases of a planar, spherical and cylindrical reaction fronts has been considered based on the concept of the chemical affinity tensor. The theoretical analysis is made for the case of elasto-viscous reaction product. The changing of the rheology of a solid constituent due to the localized chemical reaction was taken into account with the use of the Standard Linear Solid Model and its particular cases. The SLSM and Maxwell model allowed to obtain analytical solutions which gave us possibilities to study the specific effects of material parameters on stress relaxation behind the reaction front. On the other hand, the Kelvin-Voigt and pure viscous materials can hardly be considered as proper candidates for modeling the reaction products. Results show that viscous deformations do not affect directly the kinetics of the front in the case of the SLSM, since they do not have time to appear at the moment of the transformation. But they enable the possibility for a stress relaxation phenomenon behind the reaction front. Depending on the viscous and elastic parameters, this relaxation can be fast, and the high stresses region is localized in a narrow layer adjacent to the transformation front. Following these results, different perspectives could be drawn for coupled mechanochemistry simulations based on the chemical affinity tensor in order to be applied for more complex external loading and towards plasticity and viscoplasticity.

Chapter 4

The influence of plastic strains on chemical front propagation

Contents

In this chapter we focus on the effects of plasticity on the reaction front kinetics. We consider a plane with given external deformation, a sphere and cylinder subjected to a homogeneous external all-around loading. The chemical reaction starts from outer surface of body and is localized at a reaction front dividing the deformable body into two parts occupied by the initial linear elastic material and transformed elastoplastic material. We study the front propagation for elastoplastic material at various loading conditions. We study in detail interconnections between the reaction front propagation and the evolution of plastic domain, and discuss differences between the front behaviours in the cases of various constitutive models of the reaction product.

Before considering different cases, let us precise the framework. As it was precised before, the initial material is elastic, homogeneous, isotropic, compressible. We assume that the transformed material behaves as an elastic-perfectly plastic material in perfect von Mises type plasticity. Different boundary conditions will be considered: either a radial displacement u_0 (plane problem) or a normal loading σ_0 is fixed at the outer boundary of the body.

The stress deviator $\mathbf{s}$ for the initial material is defined by the following equation:

$$\mathbf{s}^- = 2\mu_- \mathbf{e}^-$$

To describe the elastoplastic behavior of the transformed material we consider an elastic-perfectly plastic model (see Fig. 4.1). In this case the deviatoric parts of stress and strain tensors in the transformed material are written as follows:

$$\mathbf{s}^+ = 2\mu_+ \mathbf{e}^{el} = 2\mu_+ \left(\mathbf{e}^+ - \mathbf{e}^{pl}\right), \qquad \mathbf{e}^+ = \mathbf{e}^{el} + \mathbf{e}^{pl} \tag{4.1}$$

where $\mu^{\pm}$ are shear moduli, $\mathbf{e}^{el}$ and $\mathbf{e}^{pl}$ are the elastic and plastic deviatoric components of the strain.

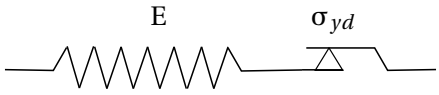

Figure 4.1: Rheological elastic-perfectly plastic model.

The initial part of the stress-strain curve for such material corresponds to a linear elastic behavior. Once the yield stress σ_{yd} is reached the material behaves as plastic, flowing at the constant stress σ_{yd}. To determine the yield stress that corresponds to the onset of plastic flow, we use the von Mises criterion. Von Mises criterion postulates that a given material is safe as long as the maximum value of the distortion energy per unit volume in that material remains smaller than the distortion energy per unit volume required to cause yield in a tensile-test specified of the same material. The yield condition is independent of hydrostatic pressure. The criterion suggests that plasticity begins when the second deviatoric stress invariant $J_2 = \frac{1}{2}\boldsymbol{s} : \boldsymbol{s}$ reaches a critical value. Prior to yield, material response is assumed to be elastic. Therefore for von Mises criterion, following the normality law for elasto-plastic stage we have:

$$\dot{\mathbf{e}}^{pl} = \dot{\lambda}\frac{\partial f}{\partial \boldsymbol{\sigma}^+}, \qquad \dot{\lambda} \geq 0, \qquad f(\boldsymbol{\sigma}) = \sqrt{3J_2} - \sigma_{yd} \leq 0$$

where $\dot{\lambda}$ is the plastic multiplier. And we obtain:

$$\dot{\mathbf{e}}^+ = \dot{\mathbf{e}}^{el} + \dot{\mathbf{e}}^{pl} = \frac{\dot{\mathbf{s}}^+}{2\mu_+} + \begin{cases} 0 & \text{if } \sqrt{3J_2} < \sigma_{yd} \\ \dot{\lambda}\dfrac{\partial f}{\partial \boldsymbol{\sigma}^+} & \text{if } \sqrt{3J_2} = \sigma_{yd} \end{cases} \tag{4.2}$$

where $\sigma_{yd} = \sqrt{3J_2}$ is the von Mises equivalent stress.

4.1 Reaction front kinetics

4.1.1 Planar reaction front propagation

To demonstrate the influence of plasticity, we consider in this section the simple plane strain problem for a chemical reaction in a plane layer of thickness H and length L >> H with a planar reaction front (Fig. 4.2). The reaction starts at the outer surface $y = 0$ of an initially elastic layer. The planar reaction front propagates in the y-direction, a transformed material forms a plane layer of the material of the thickness h. The lower $y = 0$ and upper $y = \mathrm{H}$ faces of the layer are traction free. Displacement u_0 at the edges $x = \pm\mathrm{L}$ prescribes the strain $\varepsilon_0 = u_0/\mathrm{L}$ in x-direction. Therefore, the strains have to satisfy the following conditions:

$$\varepsilon_z = \varepsilon_{xz} = \varepsilon_{yz} = 0, \quad \varepsilon_x = \varepsilon_0$$

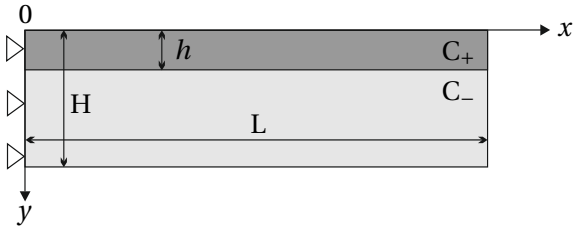

Figure 4.2: The planar reaction front.

Following the plane mechanochemical problem with elastic and viscoelastic reaction products in Chapter 2 and Chapter 3, correspondingly, the 3D Laplace diffusion problem is reduced to 1D scalar equation

$$\frac{d^2c}{dy^2} = 0, \quad y \in [0, h]$$

with boundary conditions

$$\mathrm{D}\,\frac{dc}{dy}\bigg|_{y=0} = \alpha(c(0) - c_*), \quad \mathrm{D}\,\frac{dc}{dy}\bigg|_{y=h} = -k_*(c(h) - c_{eq})$$

Hence, the concentration of the diffusing constituent B_* at the reaction front is equal to

$$c(h) = \frac{c_* + k_*\left(\dfrac{h}{\mathrm{D}} + \dfrac{1}{\alpha}\right)c_{eq}}{1 + k_*\left(\dfrac{h}{\mathrm{D}} + \dfrac{1}{\alpha}\right)}$$

Then, by Eq. (1.34), the reaction front velocity can be calculated as

$$\mathrm{V_N} = \frac{n_-\mathscr{M}_-}{\rho_-}\,\frac{c_* - c_{eq}}{\dfrac{1}{k_*} + \left(\dfrac{h}{\mathrm{D}} + \dfrac{1}{\alpha}\right)} \tag{4.3}$$

where the equilibrium concentration c_{eq}, defined by Eq. (1.32), depends on stresses and strains at the reaction front.

In the stress problem, the equilibrium equations and boundary conditions are satisfied if we take

$$\sigma_y = 0, \qquad \sigma_{xy} = 0$$

From the continuity of the displacement it follows that, at the reaction front

$$[[\varepsilon_x]] = 0$$

Then, from Eq. (3.7) and plane strains conditions it follows that $\boldsymbol{\sigma}_- : [[\boldsymbol{\varepsilon}]] = 0$ in the expression of the normal component of the chemical affinity tensor Eq. (1.29).

4.1.1.1 Elastic stage

We consider that the first stage corresponds to a situation where all materials, base and transformed, are elastic. This problem was solved already in 2.1.1, and we will use these results. For elastic stage, the stresses and strains in the base and transformed materials are defined by Eq.(2.7), (2.9), (2.11) and (2.12). It is worth mentioning that if the external deformation $\varepsilon_0(t) = \varepsilon_0$ is constant, the stresses and strains are constant in time and uniform. Here, in plasticity, we have to estimate $\dot{e}^{pl}$, this is rate-formulated problem. Then we need to introduce time-dependent external deformation $\varepsilon_0(t) = \mathscr{U} t$.

From (2.11) and (2.12), we have the equation to determine stresses in the transformed material:

$$\sigma_x^+ = \frac{2\mu_+\left(2(3k_+ + \mu_+)\mathscr{U} t - 3k_+\vartheta^{tr}\right)}{3k_+ + 4\mu_+} = \frac{\sigma_z^+}{\nu_+} = \frac{2\sigma_z^+(3k_+ + \mu_+)}{3k_+ - 2\mu_+} \tag{4.4}$$

Using the von Mises criterion, we define the yield stress from the second deviatoric stress invariant as follows

$$\sigma_{yd} = \sqrt{\sigma_x^{+2} - \sigma_x^+\sigma_z^+ + \sigma_z^{+2}} \tag{4.5}$$

or using (4.4) we can rewrite (4.5) as follows

$$\sigma_{yd} = \frac{\mu_+\left(2(3k_+ + \mu_+)\mathscr{U} t_* - 3k_+\vartheta^{tr}\right)}{(3k_+ + 4\mu_+)(3k_+ + \mu_+)}\sqrt{3\left(9k_+^2 + 6k_+\mu_+ + 4\mu_+^2\right)} \tag{4.6}$$

where t_* is the critical time, when the second stress invariant reaches the critical value (Fig. 4.3). It means that the plastic yield is reached when $\sqrt{\sigma_x^{+2} - \sigma_x^+\sigma_z^+ + \sigma_z^{+2}}$, increasing the function of $\varepsilon_0(t) = \mathscr{U} t$, is equal to σ_{yd}, the yield limit in one-dimensional tension. As the stresses are constant along all transformed layer, it will be fully transformed in the plastic zone immediately.

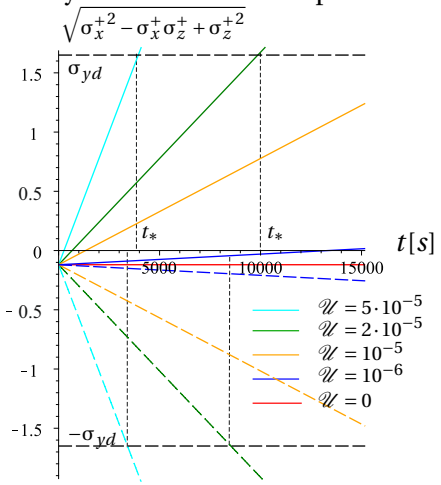

Figure 4.3: Influence of the magnitude $\mathscr{U}$ of external strain $\varepsilon_0(t) = \mathscr{U} t$ on the moment t_* when the second deviatoric stress invariant J_2 reaches the yield stress σ_{yd} (solid and dashed curves of the same colour correspond to the same $|\mathscr{U}|$, but solid line for $\varepsilon_0(t) = \mathscr{U} t$ and dashed line for the case of $\varepsilon_0(t) = -\mathscr{U} t$).

The strain energy density of initial and transformed material for the elastic stage are defined by (2.8) and (2.13), respectively:

$$w_- = \frac{2\mu_-\left(3k_- + \mu_-\right)}{3k_- + 4\mu_-}\varepsilon_0^2(t), \qquad w_+ = \frac{2\mu_+\left(\left(3k_+ + \mu_+\right)\varepsilon_0^2(t) - 3k_+\vartheta^{tr}\varepsilon_0(t) + k_+\vartheta^{tr2}\right)}{3k_+ + 4\mu_+} \tag{4.7}$$

where $\varepsilon_0(t) = \mathscr{U} t$. Therefore, as it was obtained in the Chapter 2, we have χ as the quadratic function of external and transformation strains and elastic constituents:

$$\chi_{el}(\varepsilon_0) = 2(G_+ - G_-)\varepsilon_0^2(t) - 3S_+\vartheta^{tr}\varepsilon_0(t) + S_+(\vartheta^{tr})^2 \tag{4.8}$$

where

$$G_{\pm} = \frac{\mu_{\pm}\left(3k_{\pm} + \mu_{\pm}\right)}{3k_{\pm} + 4\mu_{\pm}}, \quad S_{+} = \frac{2k_{+}\mu_{+}}{3k_{+} + 4\mu_{+}}$$

Substitution of (4.8) into Eq. (1.30) leads to the explicit dependencies of A_{NN} and c_{eq} at the reaction front on external and transformation strains, elastic modulus of the constituents and chemical energies for the elastic stage. Particularly,

$$\frac{c_{eq}}{c_*} = \exp\left\{-\frac{n_-\mathscr{M}_-}{\rho_-}\frac{(\gamma - \chi_{el}(\varepsilon_0))}{R_g T}\right\} \tag{4.9}$$

Note that at given ε_0 the equilibrium concentration does not depend on the front position.

4.1.1.2 Plastic state

In this section we find the stress and displacement field in the elastoplastic regime. When the second invariant of deviatoric stress reaches a critical value, the elastic transformed layer converts into a completely plastic one immediately. Therefore, only the plastic state will be in the transformed material. We will make the plastic analysis. The elastic equations are not valid anymore. The stress components for any point in the plastic layer can be determined only from the equilibrium equations and von Mises criteria of plasticity:

$$\frac{\partial \sigma_x}{\partial x} = 0, \qquad \sigma_{yd} = \sqrt{\sigma_x^{+2} - \sigma_x^{+}\sigma_z^{+} + \sigma_z^{+2}} \tag{4.10}$$

and strains can be found from:

$$\varepsilon_x = \frac{\partial u(x,y)}{\partial x} = \mathscr{U}\, t, \qquad \varepsilon_y = \frac{\partial u(x,y)}{\partial y} \tag{4.11}$$

Then solving the system of differential equations (4.10) and (4.11), taking into account (3.2) and (4.6), we obtain the following solution for plastic state:

$$\sigma_x^{pl} = -2\frac{\mu_+\left|2\mathscr{U}\, t_*(3k_+ + \mu_+) - 3k_+\vartheta^{tr}\right|\sqrt{9k_+^2 + 6k_+\mu_+ + 4\mu_+^2}}{(3k_+ + 4\mu_+)(3k_+ + \mu_+)} = -\frac{2\sqrt{3}}{3}\sigma_{yd}, \qquad \sigma_z^{pl} = -\frac{\sqrt{3}}{3}\sigma_{yd}$$

$$\varepsilon_x^{tot} = \mathscr{U}\, t, \quad \varepsilon_y^{tot} = -\frac{\sqrt{3}}{3k_+}\sigma_{yd} - \mathscr{U}\, t + \vartheta^{tr} \tag{4.12}$$

where $\varepsilon_{x,y}^{tot}$ are total strains in the plastic zone. Since plasticity does not produce any volume change, the volume variation is due to the elastic strain only. Knowing the stress in the plastic zone (4.12), we can calculate the elastic strains:

$$e_x^{el} = -\frac{\sqrt{3}\sigma_{yd}}{6\mu_+}, \qquad e_y^{el} = \frac{\sqrt{3}\sigma_{yd}}{6\mu_+} \tag{4.13}$$

Then from (4.1), we obtain the plastic deformations by subtracting the elastic strain to the total strain:

$$e_x^{pl} = \frac{\sqrt{3}(3k_+ + 2\mu_+)}{18k_+\mu_+}\sigma_{yd} + \mathscr{U}\, t - \frac{\vartheta^{tr}}{3}, \quad e_y^{pl} = -\frac{\sqrt{3}(3k_+ + 4\mu_+)}{18k_+\mu_+}\sigma_{yd} - \mathscr{U}\, t + \frac{2}{3}\vartheta^{tr}, \quad e_z^{pl} = \frac{\sqrt{3}}{9k_+}\sigma_{yd} - \frac{\vartheta^{tr}}{3} \tag{4.14}$$

Note, that in elastic stage the new transformed material is elastic. The layer thickness of new material grows due to the front propagation. The second stress invariant does not depend on the reaction front, but it depends on the external deformation. As it was mentioned before, to initiate

the plasticity in plane problem, we choose the external deformation increasing in time. Increasing of external deformation affect on the reaction rate as well as on J_2. When the second stress invariant reaches the critical value, all elastic transformed material becomes plastic. Following increasing of ε_0 has influence on the chemical reaction, that defines the velocity of plastic front (in this particular case they are the same).

For the elasto-plastic stage, the new material is elasto-plastic. The strain energy density of the initial elastic material B_- is

$$w_- = \frac{2\mu_-(3k_- + \mu_-)}{3k_- + 4\mu_-}\mathscr{U}^2 t^2 \tag{4.15}$$

The strain energy w_+ at the reaction front is found to be

$$w_+ = \frac{k_+^2 + \mu_+}{6k_+^2\mu_+}\sigma_{yd}^2 \tag{4.16}$$

Then substitution of (4.15) for w_- and obtained expression of w_+ into (1.31), gives χ for elasto-plastic stage:

$$\chi_{pl} = \frac{2\mu_-(3k_- + \mu_-)}{3k_- + 4\mu_-}\varepsilon_0^2 - \frac{k_+^2 + \mu_+}{6k_+^2\mu_+}\sigma_{yd}^2 \tag{4.17}$$

where $\varepsilon_0 = \mathscr{U} t$

Substitution of (4.17) into Eq. (1.30) leads to the explicit dependencies of A_{NN} and c_{eq} at the reaction front on external and transformation strains, elastic modulus of the constituents and chemical energies. Particularly,

$$\frac{c_{eq}}{c_*} = \exp\left\{-\frac{n_-\mathscr{M}_-}{\rho_-}\frac{(\gamma - \chi_{pl}(\varepsilon_0))}{R_g T}\right\} \tag{4.18}$$

4.1.2 Spherical reaction front propagation

In this section we focus on spherically- symmetric problem. We consider a sphere of radius R that is subjected to the reaction from the outer surface under external stress $\boldsymbol{\sigma}_0(t)$ (different cases for $\sigma_0(t)$ will be considered later). The spherical reaction front propagates in the direction of the center of sphere. Transformed materials forms a spherical layer of thickness h (Fig. 4.4). The chemical reaction is localized is on spherical reaction front of the radius $(R - h)$ and divides the sphere onto regions occupied by the initial and new materials.

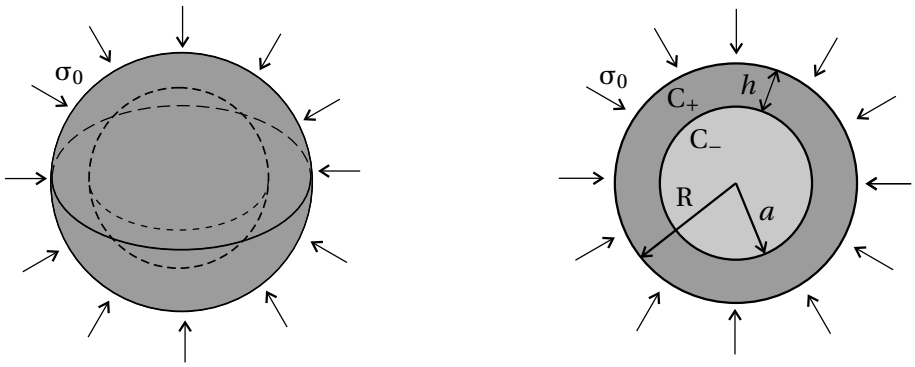

Figure 4.4: The spherical reaction front.

The solution of the diffusion problem for the spherical geometry was done in the Section 2.1.2. Here, we recall the resulting equations.The concentration of the diffusing constituent B_* at the

reaction front is equal to

$$c(a) = \frac{c_* + n_*^2 k_* \left(\frac{1-\xi}{\alpha} + \frac{\xi}{D_0} \right) (1-\xi) c_{eq}}{1 + n_*^2 k_* \left(\frac{1-\xi}{\alpha} + \frac{\xi}{D_0} \right) (1-\xi)}, \qquad h = R - a, \qquad \xi = \frac{h}{R}, \qquad D_0 = \frac{D}{R}$$

The reaction front velocity can be calculated as

$$V_N = \frac{n_- \mathscr{M}_-}{\rho_-} \frac{k_* n_*}{1 + n_*^2 k_* \left(\frac{1-\xi}{\alpha} + \frac{\xi}{D_0} \right) (1-\xi)} \left(c_* - c_{eq} \right) \tag{4.19}$$

The normal stresses σ_r, σ_φ satisfy the equilibrium equation

$$\frac{d\sigma_r}{dr} + 2\frac{\sigma_r - \sigma_\varphi}{r} = 0$$

and principal strains are

$$\varepsilon_r = \frac{du}{dr}, \qquad \varepsilon_\varphi = \varepsilon_\vartheta = \frac{u}{r} \tag{4.20}$$

where u is the radial displacement.

In the spherical geometry the conditions (4.2) can be rewritten as follows

$$\dot{\mathbf{e}}^+ = \dot{\mathbf{e}}^{el} + \dot{\mathbf{e}}^{pl} = \frac{\dot{\mathbf{s}}^+}{2\mu_+} + \begin{cases} 0 & \text{if } |\sigma_r^+ - \sigma_\varphi^+| < \sigma_{yd} \\ \dot{\lambda} \dfrac{\partial f}{\partial \boldsymbol{\sigma}^+} & \text{if } |\sigma_r^+ - \sigma_\varphi^+| = \sigma_{yd} \end{cases}$$

4.1.2.1 Elastic stage

We consider that the first stage corresponds to a situation where all materials, initial and transformed, are elastic (the external loading is moderate as the sphere is in an elastic state). Solution for this step was done in 2.1.2. Here we recall the main equations, what are needed for further calculations. More details of solution for this case can be found in 2.1.2.

Then the strains and stresses in the initial and transformed materials are determined by the following equations:

$$\varepsilon^- = A_- \mathbf{I}, \quad \boldsymbol{\sigma}^- = 3k_- A_- \mathbf{I} \tag{4.21}$$

$$\varepsilon^+ = \left(A_+ - 2\frac{B_+}{r^3} \right) \mathbf{e_r e_r} + \left(A_+ + \frac{B_+}{r^3} \right) (\mathbf{I} - \mathbf{e_r e_r}) \tag{4.22}$$

$$\boldsymbol{\sigma}^+ = \left(k_+ \left(3A_+ - \vartheta^{tr} \right) - 4\mu_+ \frac{B_+}{r^3} \right) \mathbf{e_r e_r} + \left(k_+ \left(3A_+ - \vartheta^{tr} \right) + 2\mu_+ \frac{B_+}{r^3} \right) (\mathbf{I} - \mathbf{e_r e_r}) \tag{4.23}$$

where $\mathbf{e}_r$ is a unit radial vector, and

$$B_+ = \frac{\left([\![k^{-1}]\!] \sigma_0(t) + \vartheta^{tr} \right) R^3 (1-\xi)^3}{-4\mu_+ [\![k^{-1}]\!] (1-\xi)^3 - \left(\frac{4\mu_+}{k_-} + 3 \right)}, \qquad A_+ = \frac{\sigma_0(t) + k_+ \vartheta^{tr} + 4\mu_+ \frac{B_+}{R^3}}{3k_+}, \qquad A_- = A_+ + \frac{B_+}{R^3 (1-\xi)^3}$$

where $\xi = \dfrac{h}{R}$ - is the relative thickness of the transformed material such as $\xi \in [0,1]$ or the degree of the chemical transformation and $h = R - a$; $[\![k]\!] = k_- - k_+$.

In order to evaluate the time and location of plastic flow onset, von Mises criterion, i.e. $|\sigma_r - \sigma_\varphi| = \sigma_{yd}$, is used. Taking into account (4.23), conducts to

$$|\sigma_r - \sigma_\varphi| = \frac{6\mu_+ \left|[\![k^{-1}]\!]\sigma_0(t) + \vartheta^{tr}\right| \mathrm{R}^3(1-\xi)^3}{\left(4\mu_+[\![k^{-1}]\!](1-\xi)^3 + \dfrac{4\mu_+}{k_-} + 3\right) r^3} \tag{4.24}$$

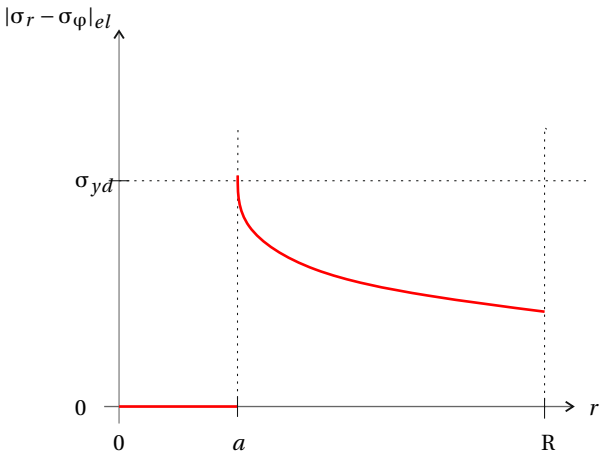

Figure 4.5: Change $\left|\sigma_r - \sigma_\varphi\right|$ along the radius of the sphere.

The plastic yield is reached when $|\sigma_r - \sigma_\varphi|$ *is equal to* σ_{yd} *when* ξ *is increasing and/or we increase* $\sigma_0(t)$*. Thus, both aspects* ξ *and* $\sigma_0(t)$ *have an action to influence plastic activity. Therefore, there are two ways to initiate plastic deformations:*

– evolution of the chemical transformation (through an increase in ξ *as internal source for activation of plasticity);*

– chemical front propagation and a simultaneously increase of the external loading $\sigma_0(t)$ *(the given stress as an external source for plasticity).*

Therefore, the plastic deformations in solid can be caused even only by chemical reaction.

The modulus $|\sigma_r - \sigma_\varphi|$ has a maximum at $r = a$ (Fig. 4.5), therefore initial plastic zone (if it appears) is located in $r = a$, what corresponds to the reaction front position. The maximum of the modulus is found out as:

$$|\sigma_r - \sigma_\varphi|_{max} = \frac{6\mu_+ \left|[\![k^{-1}]\!]\sigma_0(t) + \vartheta^{tr}\right|}{4\mu_+[\![k^{-1}]\!](1-\xi)^3 + \dfrac{4\mu_+}{k_-} + 3} \tag{4.25}$$

Note, that external loading can be different types: constant, increasing linearly in time, periodic, etc. Let's consider some cases more detailed:

Constant external loading $\sigma_0(t) = \sigma_0$

If the external loading σ_0 is constant, then $|\sigma_r - \sigma_\varphi|$ increases only due to the front propagation, i.e increasing of ξ. Then the value $|\sigma_r - \sigma_\varphi|_{max}$ reaches the yield stress σ_{yd}, when the thickness of the transformed material is equal to $h^*(t_*) = \xi^*(t_*)\mathrm{R}$, such as:

$$\frac{6\mu_+ \left|[\![k^{-1}]\!]\sigma_0 + \vartheta^{tr}\right|}{4\mu_+[\![k^{-1}]\!](1-\xi^*)^3 + \dfrac{4\mu_+}{k_-} + 3} = \sigma_{yd}$$

From where ξ^* is found out as:

$$\xi^*(t_*) = 1 - \sqrt[3]{\frac{\dfrac{6\mu_+|[\![k^{-1}]\!]\sigma_0 + \vartheta^{tr}|}{\sigma_{yd}} - \dfrac{4\mu_+}{k_-} - 3}{4\mu_+[\![k^{-1}]\!]}}$$

The situation of the chemical reaction in the sphere without any external loading, i.e $\sigma_0(t) = 0$, is the representative example of the case of the constant external loading. Note that in this case the plasticity can be induced only by the transformation strains.

When the front position $\xi < \xi^*$ the sphere remains in an elastic state. When $\xi = \xi^*$ the material of the sphere goes over into a plastic state on the surface $r = a$. A second (plastic) front appears at the reaction front, it has it own velocity and direction (more details will be given later). On further chemical transformation the region of plastic deformation is enlarged.

External loading as linear function of time, $\sigma_0(t) = \mathscr{S} t$

If σ_0 is a linear function of time, i.e $\sigma_0(t) = \mathscr{S} t$, then $|\sigma_r - \sigma_\varphi|$ increases due to the front propagation as well as increasing of σ_0 in time. Then the value $|\sigma_r - \sigma_\varphi|_{max}$ reaches the yield stress σ_{yd}, when the thickness of the transformed material is equal to $h^*(t_*) = \xi^*(t_*)\mathrm{R}$ and at the same time when $\sigma_0(t_*) = \mathscr{S} t_* = \sigma_0^*$:

$$6\mu_+ \frac{\left|[k^{-1}]\sigma_0^*(t_*) + \vartheta^{tr}\right|}{4\mu_+[k^{-1}](1-\xi^*(t_*))^3 + \dfrac{4\mu_+}{k_-} + 3} = \sigma_{yd}$$

where σ_0^* is the stress at which the plasticity begins at the reaction front. The equation to determine σ_0^* takes the following form

$$\sigma_0^*(t_*) = -\mathrm{sign}\left(\sigma_r - \sigma_\varphi\right) \frac{\sigma_{yd}\left(4\mu_+(k_- - k_+)(1-\xi^*(t_*))^3 - \left(4\mu_+ + 3k_-\right)k_+\right)}{6\mu_+(k_- - k_+)} - k_- k_+ \vartheta^{tr}$$

Note that in this case the yield stress is reached by the increasing of both external loading and the thickness of the transformed material (due to the chemical transformation), which both are time-dependent.

When the loading $\sigma_0(t) < \sigma^*$ the sphere remains in an elastic state. When $\sigma_0(t) = \sigma^*$ the material of the sphere goes over into a plastic state on the surface $r = a$. Similarly to how it was described above for the case of the constant external loading, the plastic reaction front arises at the reaction front, and with further propagation of the chemical reaction the plastic deformation region increases.

Harmonic external loading $\sigma_0(t) = \mathscr{Z}\sin(\omega t)$

If the external loading $\sigma_0(t)$ is the periodic function, i.e $\sigma_0(t) = \mathscr{Z}\sin(\omega t)$, then, as in the previous case, $|\sigma_r - \sigma_\varphi|$ increases due to the front propagation as well as increasing of $\sigma_0(t)$ in time. But it has to be mention, that as $\sigma_0(t)$ is a periodic function, it can decelerate and accelerate the reaction, and even block the reaction and further initiate it again, as well as it affects the moment when the value $|\sigma_r - \sigma_\varphi|_{max}$ reaches the yield stress σ_{yd}. It depends on the amplitude $\mathscr{Z}$ and frequency ω of the external loading. The yield stress is reached, when the thickness of the transformed material is equal to $h^*(t_*) = \xi^*(t_*)\mathrm{R}$ and at the same time when $\sigma_0(t) = \mathscr{Z}\sin(\omega t_*)$:

$$6\mu_+ \frac{\left|[k^{-1}]\mathscr{Z}\sin(\omega t_*) + \vartheta^{tr}\right|}{4\mu_+[k^{-1}](1-\xi^*(t_*))^3 + \dfrac{4\mu_+}{k_-} + 3} = \sigma_{yd} \tag{4.26}$$

Considering now these different cases, as the transformed material is elastic then in the elastic stage the strain energy density of the initial material B_- is

$$w^- = \frac{9}{2}k_-\mathfrak{A}_-^2 \tag{4.27}$$

in the transformed material it can be found as

$$w^+ = \frac{1}{2}k_+(3\mathfrak{A}_+ - \vartheta^{tr})^2 + 6\mu_+\left(\frac{\mathfrak{B}_+}{r^3}\right)^2 \tag{4.28}$$

and

$$\boldsymbol{\sigma}^{-} : [\![\varepsilon]\!] = 9k_{-}\mathfrak{A}_{-}(\mathfrak{A}_{+} - \mathfrak{A}_{-}) \tag{4.29}$$

Substitution of (4.27), (4.28) and (4.29) into Eq. (1.30) and (1.33) leads to the explicit dependencies of A_{NN} and c_{eq} at the reaction front on external stress and transformation strain, elastic modulus of the constituents and the chemical energies. In particular,

$$\frac{c_{eq}}{c_*} = \exp\left\{-\frac{n_-\mathscr{M}_-}{\rho_- R_g T}\left(\gamma + 9k_-\mathfrak{A}_-\left(\mathfrak{A}_+ - \frac{1}{2}\mathfrak{A}_-\right) - \frac{1}{2}k_+(3\mathfrak{A}_+ - \vartheta^{tr})^2 - 6\mu_+\frac{\mathfrak{B}_+^2}{R^6(1-\xi)^6}\right)\right\}$$

It gives χ as the quadratic function of external stress and transformation strain, front position and elastic modulus of the constituents:

$$\chi_{el}(\sigma_0, \xi) = \mathfrak{P}(k_+ - k_-)\sigma_0^2 - 2\mathfrak{P}k_+k_-\sigma_0\vartheta^{tr} - \mathfrak{K}(\vartheta^{tr})^2 \tag{4.30}$$

where

$$\mathfrak{P} = \frac{1}{\beta}\left(3k_+(3k_- - 4\mu_+) + 4\mu_+(9k_- + 4\mu_+)\right), \qquad \beta = 2\left(k_+(3k_- + 4\mu_+) - 4\mu_+(k_+ - k_-)(1-\xi)^3\right)^2$$

$$\mathfrak{K} = \frac{4\mu_+k_-k_+}{\beta}\left(k_+(9k_- + 4\mu_+) - 2k_+(3k_- + 4\mu_+)(1-\xi)^3 + 4\mu_+(k_+ - k_-)(1-\xi)^6\right)$$

Substitution of (4.30) into Eq. (1.30) and (4.30) leads to the explicit dependencies of A_{NN} and c_{eq} at the reaction front on external and transformation strains, elastic modules of the constituents and the chemical energies. In particularly,

$$\frac{c_{eq}}{c_*} = \exp\left\{-\frac{n_-\mathscr{M}_-}{\rho_-}\frac{(\gamma - \chi_{el}(\sigma_0, \xi))}{R_g T}\right\} \tag{4.31}$$

Note, that the external loading σ_0 can be given in different types: constant, time-dependent or harmonic.

Then the kinetic equation will take form:

$$\dot{\xi} = \frac{n_-\mathscr{M}_-}{\rho_-}\frac{k_*n_*}{1 + n_*^2k_*\left(\dfrac{1-\xi}{\alpha} + \dfrac{\xi}{D_0}\right)(1-\xi)}\left(1 - \exp\left\{-\frac{n_-\mathscr{M}_-}{\rho_-}\frac{(\gamma - \chi_{el}(\sigma_0, \xi))}{R_g T}\right\}\right) \tag{4.32}$$

4.1.2.2 Elasto-plastic state

In this section we find the stress and displacement field in the elastoplastic regime. We show that in this regime a second front (plastic front) appears. Two fronts have their own velocities and directions. We show that plastic zone expands in two directions. We determine the relation between the radius of the plastic zone, reaction front and external stress. We determine the limit stress that produces failure by excessive deformation.

When σ_0 is constant and the thickness h of the transformed material becomes larger than h^*, or σ_0 is linear time-dependent and is larger than σ^*, a natural assumption is that the plastic zone takes a region $a < r < \varsigma$, with ς a position of the plastic front, meanwhile the region $\varsigma < r < R$ remains in the elastic regime. The radial stress σ_r is continuous at the boundary between the elastic and plastic zone.

Elastic zone in the transformed material: $\varsigma < r < R$

The stresses in elastic transformed layer are defined by equation (4.23)

$$\sigma_r^{el} = 3k_+\mathscr{A}_+ - 4\mu_+\frac{\mathscr{B}_+}{r^3} - k_+\vartheta^{tr}$$

$$\sigma_\varphi^{el} = 3k_+\mathscr{A}_+ + 2\mu_+\frac{\mathscr{B}_+}{r^3} - k_+\vartheta^{tr}$$

where $\mathscr{A}^+$ and $\mathscr{B}^+$ are coming from the boundary conditions:

$$|\sigma_r^+ - \sigma_\varphi^+|\Big|_\varsigma = \sigma_{yd}, \qquad \sigma_r^{el}(\mathrm{R}) = \sigma_0$$

Hence we obtain

$$\mathscr{A}_+ = \frac{\sigma_0 + k_+\vartheta^{tr} - \operatorname{sign}(\sigma_r - \sigma_\varphi)\dfrac{2\sigma_{yd}\varsigma^3}{3\mathrm{R}^3}}{3k_+} \tag{4.33}$$

$$\mathscr{B}_+ = -\operatorname{sign}(\sigma_r - \sigma_\varphi)\frac{\sigma_{yd}\varsigma^3}{6\mu_+} \tag{4.34}$$

Then the stress components in the elastic zone are given by the equations:

$$\sigma_r^{el} = \sigma_0 + \frac{2}{3}\operatorname{sign}(\sigma_r - \sigma_\varphi)\,\sigma_{yd}\varsigma^3\left(\frac{1}{r^3} - \frac{1}{\mathrm{R}^3}\right)$$

$$\sigma_\varphi^{el} = \sigma_0 - \operatorname{sign}(\sigma_r - \sigma_\varphi)\frac{\sigma_{yd}\varsigma^3}{3}\left(\frac{2}{\mathrm{R}^3} + \frac{1}{r^3}\right)$$

Since the layer is elastic, then from (2.18), substituting (4.33) and (4.34) into it, we obtain the formula to calculate the displacements:

$$u^{el} = \frac{1}{3k_+}\left((\sigma_0 + k_+\vartheta^{tr})\mu_+ r - \operatorname{sign}(\sigma_r - \sigma_\varphi)\frac{\sigma_{yd}\varsigma^3}{6\mathrm{R}^3 r^2}(3k_+\mathrm{R}^3 + 4\mu_+ r^3)\right)$$

Plastic zone: $a < r < \varsigma$

We will study the plastic zone. The elastic formulation is not applicable anymore. Since the strain remains a priori undetermined, the stress components for any point in the plastic zone can be determined only from the equilibrium equations and the plasticity criterion

$$\frac{\partial\sigma_r^{pl}}{\partial r} + 2\frac{\sigma_r^{pl} - \sigma_\varphi^{pl}}{r} = 0, \qquad |\sigma_r - \sigma_\varphi| = \sigma_{yd} \tag{4.35}$$

We have the set of continuity equations:

$$\sigma_r^{pl}(a) = \sigma_r^-(a), \qquad u^{pl}(a) = u^-(a) \tag{4.36}$$

$$\sigma_r^{pl}(\varsigma) = \sigma_r^{el}(\varsigma), \qquad u^{pl}(\varsigma) = u^{el}(\varsigma) \tag{4.37}$$

So from (4.35) it follows that:

$$\frac{\partial\sigma_r^{pl}}{\partial r} + 2\frac{\sigma_{yd}}{r} = 0, \qquad \sigma_r^{pl} = -\operatorname{sign}(\sigma_r - \sigma_\varphi)\,2\sigma_{yd}\ln r + \mathscr{C}_1 \tag{4.38}$$

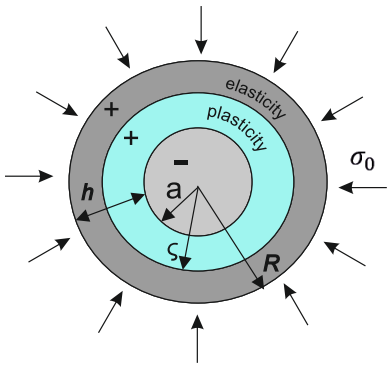

Figure 4.6: Elastic-plastic state.

where $\mathscr{C}_1$ is an integration constant, can be determined from the continuity of stress (4.37):

$$\mathscr{C}_1 = \sigma_0 + 2\text{sign}\left(\sigma_r - \sigma_\varphi\right)\sigma_{yd}\left(\frac{1}{3}\left(1 - \frac{\varsigma^3}{R^3}\right) + \ln\varsigma\right) \tag{4.39}$$

Displacements in the initial material are defined by $u^- = \mathscr{A}_- r$,where $\mathscr{A}_-$ is determined from the condition of stress continuity(4.36):

$$\mathscr{A}_- = \frac{1}{3k_-}\left(\sigma_0 + 2\text{sign}\left(\sigma_r - \sigma_\varphi\right)\sigma_{yd}\left(\ln\frac{\varsigma}{a} + \frac{1}{3}\left(1 - \frac{\varsigma^3}{R^3}\right)\right)\right)$$

In the plastic zone, substituting (B.6) into (B.4), we have in turn:

$$\sigma_r^{pl} = \sigma_0 - \text{sign}\left(\sigma_r - \sigma_\varphi\right)2\sigma_{yd}\left(\ln\frac{r}{\varsigma} - \frac{1}{3}\left(1 - \frac{\varsigma^3}{R^3}\right)\right) \tag{4.40}$$

$$\sigma_\varphi^{pl} = \sigma_0 - \text{sign}\left(\sigma_r - \sigma_\varphi\right)2\sigma_{yd}\left(\ln\frac{r}{\varsigma} + \frac{1}{3}\left(\frac{1}{2} + \frac{\varsigma^3}{R^3}\right)\right) \tag{4.41}$$

These stress components depend on ς, the radius of the plastic zone.

Due to the spherical symmetry, only the radial component of the displacement is not equal to zero. Using (3.2) and (4.20) we obtain the differential equation for the total radial displacement in the plastic zone:

$$\frac{3k_+\left(r^2u^{pl}\right)_r'}{r^2} = 3k_+\vartheta^{tr} - 6\text{sign}\left(\sigma_r - \sigma_\varphi\right)\sigma_{yd}\left(\ln\frac{r}{\varsigma} + \frac{\varsigma^3}{R^3}\right)$$

As a result, we obtain an expression to determine the total displacement in the plastic zone:

$$u^{pl} = \frac{k_+\vartheta^{tr} - 2\text{sign}\left(\sigma_r - \sigma_\varphi\right)\sigma_{yd}\left(\ln\frac{r}{\varsigma} - \frac{1}{3}\left(1 - \frac{\varsigma^3}{R^3}\right)\right)}{3k_+}r + \frac{\mathscr{C}_2}{r^2}$$

where $\mathscr{C}_2$ - is a constant, which, in turn, is found from the continuity of the displacement (4.37) at the plastic front $r = \varsigma$, that separates elastic and plastic zones in the transformed layer:

$$\mathscr{C}_2 = -\text{sign}\left(\sigma_r - \sigma_\varphi\right)\frac{\sigma_{yd}\left(3k_+ + 4\mu_+\right)}{18k_+\mu_+}\varsigma^3$$

Therefore, in the plastic zone:

$$u^{pl} = \frac{1}{3k_+}\left(k_+\vartheta^{tr} - \text{sign}\left(\sigma_r - \sigma_\varphi\right)2\sigma_{yd}r\left(\ln\frac{r}{\varsigma} - \frac{1}{3}\left(1 - \frac{\varsigma^3}{R^3}\right) + \frac{\left(3k_+ + 4\mu_+\right)}{12\mu_+}\frac{\varsigma^3}{r^3}\right)\right)$$

The radial displacement is continuous at the reaction front interface $r = a$, then from (4.36) we conduct the equation for the evolution of ς:

$$2\text{sign}\left(\sigma_r - \sigma_\varphi\right)[\![k]\!]\sigma_{yd}\ln\varsigma - 2\text{sign}\left(\sigma_r - \sigma_\varphi\right)\frac{\sigma_{yd}\varsigma^3}{3R^3}\left([\![k]\!] + \frac{k_-\left(3k_+ + 4\mu_+\right)}{4\mu_+\left(1-\xi\right)^3}\right) + \tag{4.42}$$

$$+\left(k_-k_+\vartheta^{tr} + [\![k]\!]\left(\sigma_0 + 2\text{sign}\left(\sigma_r - \sigma_\varphi\right)\sigma_{yd}\left(\frac{1}{3} - \ln\left(R(1-\xi)\right)\right)\right)\right) = 0$$

Note, that evolution of ς depends on external stress σ_0 as well as position of the chemical reaction front ξ. Therefore, the behavior of the external stress has a direct influence on the propagation of the plastic zone. We will consider it in more details later.

We know the total displacement in plastic zone, then we can calculate the total strain in the plastic zone:

$$\varepsilon_r = \frac{1}{3k_+}\left(k_+\vartheta^{tr} - \operatorname{sign}\left(\sigma_r - \sigma_\varphi\right)2\sigma_{yd}\left(\ln\frac{r}{\varsigma} + \frac{2}{3} + \frac{\varsigma^3}{3R^3} - \frac{(3k_+ + 4\mu_+)}{6\mu_+}\frac{\varsigma^3}{r^3}\right)\right) \tag{4.43}$$

$$\varepsilon_\varphi = \frac{1}{3k_+}\left(\frac{k_+\vartheta^{tr}}{r} - \operatorname{sign}\left(\sigma_r - \sigma_\varphi\right)2\sigma_{yd}\left(\ln\frac{r}{\varsigma} - \frac{1}{3}\left(1 - \frac{\varsigma^3}{R^3}\right) + \frac{(3k_+ + 4\mu_+)}{12\mu_+}\frac{\varsigma^3}{r^3}\right)\right) \tag{4.44}$$

Since plasticity does not produce any volume change, the volume variation is due to the elastic strain only:

$$e_r^+ - e_\varphi^+ = \frac{1}{2\mu_+}\left(\sigma_r^{pl} - \sigma_\varphi^{pl}\right) + e_r^{pl} - e_\varphi^{pl}$$

Knowing the stress in the plastic zone (4.40) and (4.41), we can calculate the elastic strains. Then from (4.1), we obtain the plastic deformation by subtracting the elastic strain to the total strain:

$$\mathbf{e}^p = \operatorname{sign}\left(\sigma_r - \sigma_\varphi\right)\cdot\frac{\sigma_{yd}\left(3k_+ + 4\mu_+\right)}{6\mu_+ k_+}\left(\frac{\varsigma^3}{r^3} - 1\right)\boldsymbol{\alpha} \tag{4.45}$$

where

$$\alpha = \frac{1}{3}\begin{pmatrix} 2 & 0 & 0 \\ 0 & -1 & 0 \\ 0 & 0 & -1 \end{pmatrix}$$

The derivative of the plastic deformation:

$$\dot{\boldsymbol{e}}^p = \operatorname{sign}\left(\sigma_r - \sigma_\varphi\right)\cdot\frac{\sigma_{yd}\left(3k_+ + 4\mu_+\right)}{2\mu_+ k_+}\frac{\varsigma^2\dot{\varsigma}}{r^3}\boldsymbol{\alpha}$$

Using the von Mises criteria (4.2) we obtain the equation for determining $\dot{\lambda}$

$$\dot{\lambda} = \operatorname{sign}\left(\sigma_r - \sigma_\varphi\right)\cdot\frac{\sigma_{yd}\left(3k_+ + 4\mu_+\right)}{3\mu_+ k_+}\frac{\varsigma^2\dot{\varsigma}}{r^3}, \quad \dot{\lambda} \geq 0$$

If we increase the external loading σ_0, the plastic zone will expand until it reaches the outer surface of the sphere. The solution (4.40) will then be valid up to $\varsigma = R$. Using the boundary condition, we have

$$\sigma_r^{pl} = -2\sigma_{yd} ln\frac{r}{R} + \sigma_0^{**}$$
$$\sigma_r^{pl}(R) = \sigma_0^{**}$$

This equation defines the limiting stress σ_0^{**}, at which the sphere is completely in the yield state. When the limit load σ_0^{**} is reached, the sphere loses its ability to resist increasing external forces.

The strain density of the initial material is

$$w_- = \frac{\sigma_v^2}{2k_-}\left(2\ln\frac{\varsigma}{a} + \frac{\sigma_0}{\sigma_{yd}} + \frac{2}{\varsigma^3} - \frac{2}{R^3}\right)^2 \tag{4.46}$$

in the transformed material it is found as follows

$$w_+ = \frac{2\sigma_{yd}^2}{9k_+}\left(3\ln\frac{r}{\varsigma} + \frac{\varsigma^3}{R^3}\right)^2 + \frac{\sigma_{yd}^2}{12\mu_+}\left(3\ln\frac{r}{\varsigma} + \frac{3\sigma_0}{\sigma_{yd}} - \frac{1}{2} + \frac{\varsigma^3}{R^3}\right)^2 \tag{4.47}$$

and jump at the reaction front:

$$\boldsymbol{\sigma}^{-} : [\![\boldsymbol{\varepsilon}]\!] = -\frac{4\sigma_{yd}^2}{k_+ k_-}\left(\ln\frac{\varsigma}{a}+\frac{\sigma_0}{2\sigma_{yd}}-\frac{1}{\mathrm{R}^3}+\frac{1}{\varsigma^3}\right)\left(\ln\frac{\varsigma}{a}(k_+-k_-)-\frac{k_+k_-\vartheta^{tr}}{2\sigma_{yd}}+\frac{k_+\sigma_0}{\sigma_{yd}}+k_+\left(\frac{1}{\varsigma^3}-\frac{2}{\mathrm{R}^3}\right)+\frac{k_-\varsigma^3}{3\mathrm{R}^3}\right) \tag{4.48}$$

Substitution of (4.46), (4.47) and (4.48) into equation (1.30) and (1.33) leads to the explicit dependence of $\mathrm{A_{NN}}$ and c_{eq} at the reaction front on external stress and transformation strain, elastic modulus of constituents and chemical energies:

$$\frac{c_{eq}^{pl}}{c_*}=\exp\left\{-\frac{n_-\mathscr{M}_-}{\rho_-\mathrm{R}_g\mathrm{T}}\left(\gamma+\frac{\sigma_{yd}^2}{2k_-}\left(2\ln\frac{\varsigma}{a}+\frac{\sigma_0}{\sigma_{yd}}+\frac{2}{\varsigma^3}-\frac{2}{\mathrm{R}^3}\right)^2-\frac{2\sigma_{yd}^2}{9k_+}\left(3\ln\frac{a}{\varsigma}+\frac{\varsigma^3}{\mathrm{R}^3}\right)^2-\frac{\sigma_{yd}^2}{12\mu_+}\left(3\ln\frac{a}{\varsigma}+\frac{3\sigma_0}{\sigma_{yd}}-\frac{1}{2}+\frac{\varsigma^3}{\mathrm{R}^3}\right)^2-\right.\right.$$
$$\left.\left.-\frac{4\sigma_{yd}^2}{k_+k_-}\left(\ln\frac{\varsigma}{a}+\frac{\sigma_0}{2\sigma_{yd}}-\frac{1}{\mathrm{R}^3}+\frac{1}{\varsigma^3}\right)\left(\ln\frac{\varsigma}{a}(k_+-k_-)-\frac{k_+k_-\vartheta^{tr}}{2\sigma_{yd}}+\frac{k_+\sigma_0}{\sigma_{yd}}+k_+\left(\frac{1}{\varsigma^3}-\frac{2}{\mathrm{R}^3}\right)+\frac{k_-\varsigma^3}{3\mathrm{R}^3}\right)\right)\right\} \tag{4.49}$$

Note, that c_{eq} is quadratic function of σ_0.

Then the kinetic equation will take form:

$$\dot{\xi}=\frac{n_-\mathscr{M}_-}{\rho_-}\frac{k_*n_*}{1+n_*^2k_*\left(\dfrac{1-\xi}{\alpha}+\dfrac{\xi}{\mathrm{D}_0}\right)(1-\xi)}\left(1-\frac{c_{eq}^{pl}}{c_*}\right) \tag{4.50}$$

4.1.3 Cylindrical front propagation

In this subsection we focus on the chemical reaction in axially-symmetric problem. We consider a linear-elastic cylinder of radius R and length L under external stress $\sigma_0(t)$ (Fig. 4.7). Assume L >> R, the stress along the longitudinal axis of the cylinder vanishes, $\sigma_z = 0$. The displacement in a radial direction is a function on r alone and does not depend on upon z. We assume that tube material is compressible.

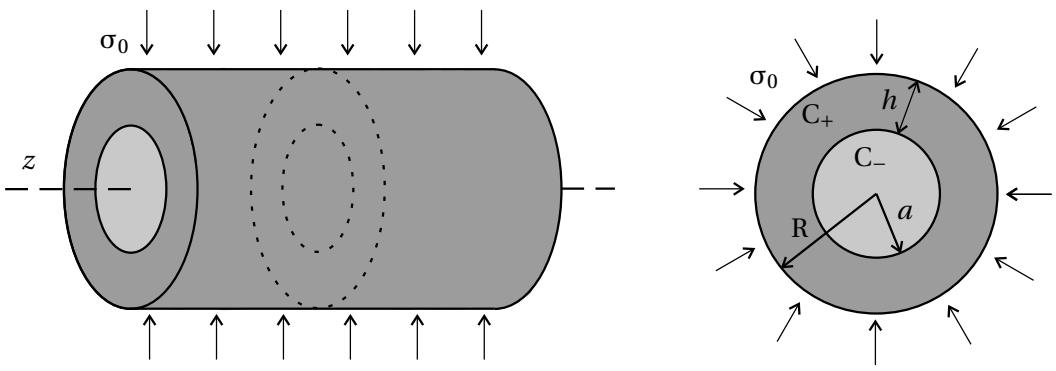

Figure 4.7: The cylindrical reaction front.

The diffusive material surrounds the cylinder. We suppose that reaction starts from the outer surface and transformed material forms a cylindrical layer of a thickness h from the body surface.

The solution for the diffusion problem and kinetic equation were solved in Section 2.1.3 (Eq. (2.25) and (2.26)). Here, we just recall the result:

The concentration of the diffusing constituent B_* at the reaction front is equal to

$$c(a)=\frac{c_*\dfrac{\mathrm{D}_0}{k_*(1-\xi)}-c_{eq}\left(\ln(1-\xi)-\dfrac{\mathrm{D}_0}{\alpha}\right)}{\dfrac{\mathrm{D}_0}{1-\xi}+\dfrac{\mathrm{D}_0}{\alpha}-\ln(1-\xi)},\qquad \mathrm{D}_0=\frac{\mathrm{D}}{\mathrm{R}},\qquad h=\mathrm{R}-a,\qquad \xi=\frac{h}{\mathrm{R}}$$

The reaction front velocity is given by the following equation

$$V_N = \frac{n_- \mathscr{M}_-}{\rho_-} \frac{c_* - c_{eq}}{\dfrac{1}{k_*} + \dfrac{1-\xi}{\alpha} - \dfrac{\ln(1-\xi)}{D_0}(1-\xi)} \tag{4.51}$$

Since the body's cylindrical geometry (cylindrical coordinates (r, φ, z)) and since the material is isotropic, the equilibrium and kinematic boundary conditions can be expressed as

$$\frac{d\sigma_r}{dr} + \frac{\sigma_r - \sigma_\varphi}{r} = 0 \tag{4.52}$$

$$\varepsilon_r = \frac{du}{dr}, \qquad \varepsilon_\varphi = \frac{u}{r}, \qquad \varepsilon_z = 0 \tag{4.53}$$

where u is the radial displacement. In the cylindrical coordinates the condition (4.2) can be written as follows:

$$\dot{\mathbf{e}}^+ = \dot{\mathbf{e}}^{el} + \dot{\mathbf{e}}^{pl} = \frac{\dot{\mathbf{s}}^+}{2\mu_+} + \begin{cases} 0 & \text{if } \sqrt{\frac{1}{2}\left((\sigma_r - \sigma_\varphi)^2 + (\sigma_\varphi - \sigma_z)^2 + (\sigma_r - \sigma_z)^2\right)} < \sigma_{yd} \\ \dot{\lambda}\dfrac{\partial f}{\partial \boldsymbol{\sigma}^+} & \text{if } \sqrt{\frac{1}{2}\left((\sigma_r - \sigma_\varphi)^2 + (\sigma_\varphi - \sigma_z)^2 + (\sigma_r - \sigma_z)^2\right)} = \sigma_{yd} \end{cases}$$

Since we assume in that $\sigma_z = 0$, then

$$\dot{\mathbf{e}}^+ = \dot{\mathbf{e}}^{el} + \dot{\mathbf{e}}^{pl} = \frac{\dot{\mathbf{s}}^+}{2\mu_+} + \begin{cases} 0 & \text{if } \sqrt{\sigma_r^2 + \sigma_\varphi^2 - \sigma_r\sigma_\varphi} < \sigma_{yd} \\ \dot{\lambda}\dfrac{\partial f}{\partial \boldsymbol{\sigma}^+} & \text{if } \sqrt{\sigma_r^2 + \sigma_\varphi^2 - \sigma_r\sigma_\varphi} = \sigma_{yd} \end{cases}$$

4.1.3.1 Elastic stage

Similar as it was done in the previous case for the sphere, we consider that the first stage corresponds to a situation where all materials, initial and transformed, are elastic. Solution for this problem was done in 2.1.3. Here we give only the main equations, that are needed for further solution. More details can be found in 2.1.3.

The strains and stresses in the initial and transformed materials are determined by the following equations:

$$\boldsymbol{\varepsilon}^- = \mathscr{A}_- \mathbf{I}, \qquad \boldsymbol{\sigma}^- = 2\left(k_- + \frac{\mu_-}{3}\right)\mathscr{A}_- \mathbf{I}$$

$$\varepsilon_r^+ = \mathscr{A}_+ - \frac{\mathscr{B}_+}{r^2}, \qquad \varepsilon_\varphi^+ = \mathscr{A}_+ + \frac{\mathscr{B}_+}{r^2}, \qquad \varepsilon_z^+ = 0$$

$$\sigma_r^+ = 2\left(k_+ + \frac{\mu_+}{3}\right)\mathscr{A}_+ - 2\mu_+\frac{\mathscr{B}_+}{r^2} - k_+\vartheta^{tr}, \qquad \sigma_\varphi^+ = 2\left(k_+ + \frac{\mu_+}{3}\right)\mathscr{A}_+ + 2\mu_+\frac{\mathscr{B}_+}{r^2} - k_+\vartheta^{tr} \tag{4.54}$$

where $\mathscr{A}_+$, $\mathscr{A}_-$ and $\mathscr{B}_+$ are given by the following formula:

$$\mathscr{B}_+ = \frac{3R^2}{\mathscr{G}}(1-\xi)^2\left(k_+\vartheta^{tr}(3k_- + \mu_-) - \sigma_0\left(3(k_+ - k_-) + (\mu_+ - \mu_-)\right)\right)$$

$$\mathscr{A}_+ = \frac{3}{\mathscr{G}}\left(3\mu_+(k_+\vartheta^{tr}(\xi^2 - 2\xi) - \sigma_0) - (3k_- + \mu_-)(k_+\vartheta^{tr} + \sigma_0)\right)$$

$$\mathscr{A}_- = \frac{3}{\mathscr{G}}\left(3k_+\mu_+\vartheta^{tr}(\xi^2 - 2\xi) - (3k_+ + 4\mu_+)\sigma_0\right)$$

where $\mathscr{G} = 6\mu_+(\xi^2 - 2\xi)\left(3(k_+ - k_-) + (\mu_+ - \mu_-)\right) - 2(3k_- + \mu_-)(3k_+ + 4\mu_+)$

In order to evaluate the time and location of plastic flow onset, von Mises criterion is used. Taking into account (4.54), this conduct to

$$\sqrt{\sigma_r^2+\sigma_\varphi^2-\sigma_r\sigma_\varphi}=\frac{\left(\begin{array}{l}\left(\mu_+^2(\mathscr{K}_+-\mathscr{K}_-)^2\dfrac{a^4}{r^4}+\dfrac{\mathscr{K}_+^2}{27}(\mathscr{K}_-+3\mu_+)^2\right)\sigma_0^2+k_+^2\mu_+^2\mathscr{K}_-^2\left(\dfrac{a^4}{r^4}+\dfrac{a^4}{3R^4}\right)\vartheta^{tr2}-\\ -2\mu_+k_+\mathscr{K}_-\left(\mu_+(\mathscr{K}_+-\mathscr{K}_-)\dfrac{a^4}{r^4}+\dfrac{\mathscr{K}_+}{9}(\mathscr{K}_-+3\mu_+)\right)\vartheta^{tr}\sigma_0\end{array}\right)}{\left(\mu_+\left(\mu_++k_+-\dfrac{\mathscr{K}_-}{3}\right)\left(1-\dfrac{a^2}{R^2}\right)+\dfrac{\mathscr{K}_-}{9}(3k_++4\mu_+)\right)^2} \tag{4.55}$$

where $\mathscr{K}_\pm=3k_\pm+\mu_\pm$.

From (4.55), we can deduce that the second invariant of deviatoric stress reaches a maximum at $r=a$. It means that the initial plastic zone (if it appears) is located in $r=a$, which corresponds to the chemical reaction front.

As it was presented in the previous case of the initially elastic sphere with elasto-plastic reaction product, the external loading $\sigma_0(t)$ can be of different types: it can be constant, a linear function of time or harmonic function.

From (4.55), if $\sigma_0(t)=\sigma_0$, then we can see that the $\sqrt{\sigma_r^2+\sigma_\varphi^2-\sigma_r\sigma_\varphi}$ can not increase via the external loading as it is constant. But from the formula (4.55), we see that the second stress invariant depends on reaction front position ξ. Then if the chemical reaction is initiated, then it induces internal stresses, which initiate the plasticity at the reaction front.

If $\sigma_0(t)=\mathscr{U}t$, then from (4.55) it follows that the second deviatoric stress invariant can reach yield stress at the moment $t=t_*$ due to the increasing of the external loading as well as the reaction propagation, such as: $\sigma_*=\mathscr{U}t_*$ and $\xi_*=\xi(t_*)$.

In the case of the harmonic external loading $\sigma_0(t)=\mathscr{Z}\sin(\omega t)$, this loading can accelerate, decelerate and even block the reaction as well as affects the initiation of plasticity.

In the elastic regime, the transformed material is elastic, and the strain densities of the initial and transformed materials are defined by

$$w^-=2\left(k_-+\frac{\mu_+}{3}\right)\mathscr{A}_-^2,\qquad w^+=\frac{1}{2}k_+\left(2\mathscr{A}^+-\vartheta^{tr}\right)^2+2\mu_+\left(\frac{\mathscr{A}_+^2}{3}+\frac{\mathscr{B}_+^2}{r^4}\right) \tag{4.56}$$

the jump condition can be written as follows

$$\boldsymbol{\sigma}^-:[\![\varepsilon]\!]=4\left(k_-+\frac{\mu_-}{3}\right)\mathscr{A}_-(\mathscr{A}_+-\mathscr{A}_-) \tag{4.57}$$

Substitution of (4.56) and (4.57) into Eq. (1.30) and (1.33) leads to the explicit dependencies of A_{NN} and c_{eq} at the reaction front on external stress and transformation strain, elastic modulus of the constituents and the chemical energies. In particularly,

$$\frac{c_{eq}^{el}}{c_*}=\exp\left\{-\frac{n_-\mathscr{M}_-}{\rho_-}\frac{(\gamma-\chi(\sigma_0,\xi))}{R_gT}\right\} \tag{4.58}$$

where χ is given as the quadratic function of external stress and transformation strain, front position and elastic modulus of the constituents:

$$\chi(\sigma_0,\xi)=\frac{1}{\mathscr{U}}\left((\mathscr{K}_+-\mathscr{K}_-)\mathscr{P}\sigma_0^2-2\mathscr{K}_-k_+\mathscr{P}\vartheta^{tr}\sigma_0-\mu_+k_+\mathscr{Q}(\vartheta^{tr})^2\right) \tag{4.59}$$

with

$$\mathscr{P}=3(3k_++4\mu_+)(\mathscr{K}_-+3\mu_+),\quad \mathscr{U}=2\left(3\mu_+(\mathscr{K}_+-\mathscr{K}_-)\xi(\xi-2)-(3k_++4\mu_+)\mathscr{K}_-\right)^2,\quad \mathscr{K}_\pm=3k_\pm+\mu_\pm$$
$$\mathscr{Q}=9\mu_+(\mathscr{K}_+-\mathscr{K}_-)(\mathscr{K}_--\mu_+)\xi^2(\xi^2-4\xi+4)-2(3k_++4\mu_+)\mathscr{K}_-\left(3(\mathscr{K}_--\mu_+)\xi(\xi-2)-2\mathscr{K}_-\right)$$

Then the kinetic equation in the elastic stage takes form:

$$\dot{\xi} = \frac{n_- \mathscr{M}_-}{\rho_-} \frac{1}{\dfrac{1}{k_*} + \dfrac{1-\xi}{\alpha} - \dfrac{\ln(1-\xi)}{D_0}(1-\xi)} \left(1 - \exp\left\{-\frac{n_- \mathscr{M}_-}{\rho_-} \frac{(\gamma - \chi(\sigma_0, \xi))}{R_g T}\right\}\right) \tag{4.60}$$

4.1.3.2 Elasto-plastic state

In this section we find the stress and displacement field in the elastoplastic regime. We show that in this regime the second front (plastic front) appears. Two fronts have their own velocities and directions. We show that plastic zone expands in two directions. We determine the relation between the radius of the plastic zone, reaction front and external stress.

When σ_0 is constant and the thickness h of the transformed material becomes larger than h^*, or σ_0 is linear time-dependent and is larger than σ^*, a natural assumption is that the plastic zone takes a region $a < r < \varsigma$, with ς a position of the plastic front, meanwhile the region $\varsigma < r < R$ remains in the elastic regime. The radial stress σ_r is continuous at the boundary between the elastic and plastic zone.

Elastic zone in the transformed material: $\varsigma < r < R$

The stresses in elastic transformed layer are defined by equations:

$$\sigma_r^{el} = 2\left(k_+ + \frac{\mu_+}{3}\right)A_+ - 2\mu_+ \frac{B_+}{r^2} - k_+ \vartheta^{tr}, \qquad \sigma_\varphi^{el} = 2\left(k_+ + \frac{\mu_+}{3}\right)A_+ + 2\mu_+ \frac{B_+}{r^2} - k_+ \vartheta^{tr} \tag{4.61}$$

where A_+ and B_+ are coming from the boundary conditions at the external surface and at the interface between the plastic and elastic zones in the transformed material:

$$\sqrt{\sigma_r^2 + \sigma_\varphi^2 - \sigma_r \sigma_\varphi}\Big|_\varsigma = \sigma_{yd}, \qquad \sigma_r^{el}(R) = \sigma_0$$

Therefore, we conduct formulas to determine A_+ and B_+:

$$A_+ = \frac{3\left((3R^4 + \varsigma^4)k_+ \vartheta^{tr} + 3R^4\sigma_0 + \varsigma^2\sqrt{(3R^4 + \varsigma^4)\sigma_{yd}^2 - 3R^4\sigma_0^2}\right)}{2\mathscr{K}_+(3R^4 + \varsigma^4)}, \quad B_+ = -\frac{\left(\varsigma^4\sigma_0 - \varsigma^2\sqrt{(3R^4 + \varsigma^4)\sigma_{yd}^2 - 3R^4\sigma_0^2}\right)R^2}{2\mu_+(3R^4 + \varsigma^4)} \tag{4.62}$$

Substitute (4.62) into (4.61), we obtain the equation for stress components in the elastic zone:

$$\sigma_r^{el} = \frac{R^2(3R^2r^2 + \varsigma^4)\sigma_0 - (R^2 - r^2)\sqrt{(3R^4 + \varsigma^4)\sigma_{yd}^2 - 3R^4\sigma_0^2}}{(3R^4 + \varsigma^4)r^2} \tag{4.63}$$

$$\sigma_\varphi^{el} = \frac{R^2(3R^2r^2 - \varsigma^4)\sigma_0 + (R^2 + r^2)\sqrt{(3R^4 + \varsigma^4)\sigma_{yd}^2 - 3R^4\sigma_0^2}}{(3R^4 + \varsigma^4)r^2} \tag{4.64}$$

Since the considering zone is elastic, then from (2.27), substituting (4.62) into it, we obtain the equation for displacement in the elastic zone:

$$u^{el} = \frac{\left(\mathscr{K}_+R^2 + 3\mu_+r^2\right)\sqrt{(3R^4 + \varsigma^4)\sigma_{yd}^2 - 3R^4\sigma_0^2} + 3k_+\mu_+r^2(3R^4 + \varsigma^4)\vartheta^{tr} + R^2(9\mu_+R^2r^2 - \mathscr{K}_+\varsigma^4)\sigma_0}{2\mu_+\mathscr{K}_+(3R^4 + \varsigma^4)r}$$

Plastic zone: $a < r < \varsigma$

We will study the plastic zone. The elastic formulation is not applicable anymore. Since the strain remains a priori undetermined, the stress components for any point in the plastic zone can be determined only from the equilibrium equations and the plasticity criterion

$$\frac{d\sigma_r^{pl}}{dr} + \frac{\sigma_r^{pl} - \sigma_\varphi^{pl}}{r} = 0, \qquad \sqrt{\sigma_r^2 + \sigma_\varphi^2 - \sigma_r\sigma_\varphi} = \sigma_{yd} \tag{4.65}$$

We have the set of continuity equations:

$$\sigma_r^{pl}(a) = \sigma_r^{-}(a), \qquad u^{pl}(a) = u^{-}(a) \tag{4.66}$$

$$\sigma_r^{pl}(\varsigma) = \sigma_r^{el}(\varsigma), \qquad u^{pl}(\varsigma) = u^{el}(\varsigma) \tag{4.67}$$

From von Mises criterion we have

$$\sigma_\varphi^{pl} = \frac{1}{2}\left(\sigma_r^{pl} \pm \sqrt{4\sigma_{yd}^2 - 3\sigma_r^{pl\,2}}\right) \tag{4.68}$$

To determine the proper sign of the radical in (4.68), we note, that in the elastic region, from (4.63) and (4.64) we have

$$2\sigma_\varphi^{el} - \sigma_r^{el} = \frac{3R^2(R^2r^2 - \varsigma^4) + (3R^2 + r^2)\sqrt{(3R^4 + \varsigma^4)\sigma_{yd}^2 - 3R^4\sigma_0^2}}{(3R^4 + \varsigma^4)r^2} > 0, \quad r \in [\varsigma, R]$$

which must be valid at the elastic-plastic interface. Thus, from (4.68) we have

$$\sigma_\varphi^{pl} = \frac{1}{2}\left(\sigma_r^{pl} + \sqrt{4\sigma_{yd}^2 - 3\sigma_r^{pl\,2}}\right) \tag{4.69}$$

Therefore, substituting (4.69) into equilibrium equation (4.65), we obtain

$$\frac{d\sigma_r^{pl}}{dr} + \frac{1}{2r}\left(\sigma_r^{pl} - \sqrt{4\sigma_{yd}^2 - 3\sigma_r^{pl\,2}}\right) = 0$$

We can solve this differential equation by separation of variables in integration:

$$\int \frac{d\sigma_r^{pl}}{\sqrt{4\sigma_{yd}^2 - 3\sigma_r^{pl\,2}} - \sigma_r^{pl}} = \int \frac{dr}{2r} + \mathscr{C}_1$$

where $\mathscr{C}_1$ is integration constant, can be conducted from the continuity of stress (4.67) at $r = \varsigma$. After integration the radial stress can be determined from:

$$\sigma_r^{pl} = -\frac{2\sigma_{yd}}{\sqrt{3}\mathscr{J}}, \qquad \mathscr{J} \geq 1 \tag{4.70}$$

where $\mathscr{J}$ is defined by the equation:

$$\ln(\mathscr{J}) + 2\sqrt{3}\arctan\left(\sqrt{\mathscr{J} - 1}\right) - 2\ln\left(3\sqrt{\mathscr{J} - 1} + \sqrt{3}\right) - 4\ln r = \mathscr{C}_1 \tag{4.71}$$

From the continuity of stress at $r = \varsigma$, we obtain $\mathscr{C}_1$:

$$\mathscr{C}_1 = 2\sqrt{3}\arctan\left(\frac{\sqrt{3}}{3}\left(\frac{\sqrt{\mathscr{Y}}}{\sigma_0 R^2\varsigma^2(3R^2 + \varsigma^2) - \sqrt{\sigma_{yd}^2(3R^4 + \varsigma^4) - 3R^4\sigma_0^2}(R^2 - \varsigma^2)}\right)\right) +$$
$$+2\ln\left(\frac{2\sigma_{yd}^2(3R^4 + \varsigma^4)}{3(\sigma_0 R^2\varsigma^2(3R^2 + \varsigma^2) - \sqrt{\sigma_{yd}^2(3R^4 + \varsigma^4) - 3R^4\sigma_0^2}(R^2 - \varsigma^2) + \sqrt{\mathscr{Y}})}\right) \tag{4.72}$$

$$\mathscr{Y} = 6R^2\varsigma^2\sigma_0(2R^4 + (R^2 - \varsigma^2)^2)\sqrt{\sigma_{yd}^2(3R^4 + \varsigma^4) - 3R^4\sigma_0^2} + 3(\sigma_0^2 - \sigma_{yd}^2)(3(R^4 - \varsigma^4)^2 - R^4\varsigma^4(9R^4 - \varsigma^4)) +$$
$$+\sigma_{yd}^2(9R^4(R^4 - 2R^2\varsigma^6 + 3\varsigma^8) + 4\varsigma^{12} - 3\varsigma^4(R^2 - \varsigma^2)^2)$$

Displacement in initial material are defined by $u^- = \mathscr{A}_- r$, where $\mathscr{A}_-$ is conducted from the stress continuity (4.66) at the reaction front $r = a$:

$$\mathscr{A}_- = -\frac{1}{3\mathscr{K}_-}\left(\sqrt{3}\sigma_{yd}\,\mathrm{RootOf}\left(\mathscr{X}^2\mathscr{H} - 9\right)\mathscr{H}\right)$$

$$\mathscr{H} = \cos\left(\mathrm{RootOf}\left(\sqrt{3}\mathscr{C}_1 + \sqrt{3}\ln\left(3(a^4\cos(\mathscr{X})^2)\right) + 2\sqrt{3}\ln\left(\frac{\cos(\mathscr{X}) + \sqrt{3}\,\mathrm{sign}\left(\frac{\sin(\mathscr{X})}{\cos(\mathscr{X})}\right)\sin(\mathscr{X})}{\cos(\mathscr{X})}\right) - 6\mathscr{X}\right)\right)^2$$

where RootOf represents the roots of expression with respect to its single variable or $\mathscr{X}$, respectively. Note, that it was not possible to obtain the explicit form of the equation, but it is possible to calculate it numerically.

In plastic zone, substituting (4.71) and (4.72) into (4.70), and then substitute the result of (4.70) into (4.69), we obtain the equations for stresses in the plastic zone:

$$\sigma_r^{pl} = -\frac{2\sigma_{yd}}{\sqrt{3\mathscr{J}}}, \qquad \mathscr{J} \geq 1, \qquad \sigma_\varphi^{pl} = \frac{\sigma_{yd}}{\mathscr{J}}\left(\sqrt{\mathscr{J}^2 - 1} - \sqrt{\frac{\mathscr{J}}{3}}\right)$$

These stresses components are depend on ς, the radius of the plastic zone (it comes from $\mathscr{J}$, which depends on $\mathscr{C}_1$, that is defined by (4.72) and depends on ς). The radial displacements are continuous at the reaction front, $r = a$, therefore, from (4.66) we obtain the formula for the evolution of ς.

Due to the cylindrical geometry (axial symmetry), only radial component of the displacement is considered. Using (3.2) and (4.53), we conduct the differential equation for the total radial displacement in the plastic zone:

$$\frac{3k_+(r^2u^{pl})'_r}{r^2} = 3k_+\vartheta^{tr} + \frac{\sigma_{yd}}{\mathscr{J}}\left(\sqrt{\mathscr{J}^2 - 1} - \sqrt{3\mathscr{J}}\right)$$

Therefore, equations in this part have complex and implicit form. Hence it is not possible to obtain analytical solution. This problem can be solved numerically using Runge-Kutta method. Taking into account the discontinuity conditions at the plastic and reaction front and since plasticity does not produce any volume change, the volume variations is due to the elastic strain only, therefore, we have the following system of differential equations with boundary conditions:

$$\dot{\xi} = \frac{n_-\mathscr{M}_-}{\rho_-}\frac{1}{\frac{1}{k_*} + \frac{1-\xi}{\alpha} - \frac{\ln(1-\xi)}{D_0}(1-\xi)}\left(1 - \frac{c_{eq}^{pl}}{c_*}\right), \qquad \xi(t_*) = \xi_* \tag{4.73}$$

$$\frac{c_{eq}^{pl}}{c_*} = \exp\left\{-\frac{n_-\mathscr{M}_-}{\rho_- R_g T}\left(\gamma + \frac{2}{3}\mathscr{K}_-\mathscr{A}_-^2 - \frac{k_+}{2}\left(\vartheta^+ - \vartheta^{tr}\right)^2 - \mu_+ e^{el} : e^{el} - \boldsymbol{\sigma}_- : [\![\varepsilon]\!]\right)\right\} \tag{4.74}$$

$$\sigma_r^{pl} = -\frac{2\sigma_{yd}}{\sqrt{3\mathscr{J}}}, \qquad \mathscr{J} \geq 1, \qquad \sigma_\varphi^{pl} = \frac{\sigma_{yd}}{\mathscr{J}}\left(\sqrt{\mathscr{J}^2 - 1} - \sqrt{\frac{\mathscr{J}}{3}}\right)$$

$$\frac{3k_+(r^2u^{pl})'_r}{r^2} = 3k_+\vartheta^{tr} + \frac{\sigma_{yd}}{\mathscr{J}}\left(\sqrt{\mathscr{J}^2 - 1} - \sqrt{3\mathscr{J}}\right)$$

$$u^- = \mathscr{A}_- r$$

$$u^{pl}(a) = u^-(a), \qquad \sigma_r^{pl}(\varsigma) = \sigma_r^{el}(\varsigma), \qquad u^{pl}(\varsigma) = u^{el}(\varsigma)$$

$$\sigma_r^{pl} + \sigma_\varphi^{pl} = 3k_+(\vartheta^+ - \vartheta^{tr}), \qquad e_r^{el} + e_\varphi^{el} + e_z^{el} = \frac{1}{2\mu_+}\left(\sigma_r^{pl} + \sigma_\varphi^{pl}\right)$$

In the next section, numerical integration of these explicit or implicit equations will be done. It will allow to study in details the kinetics and the evolution of two fronts: the chemical and plastic ones.

4.2 Equilibrium concentration, kinetics of the reaction front and blocking effect

4.2.1 Planar reaction front

In this Section, the dependencies of the reaction front position and of the reaction front velocity on time, which are deduced from (4.3), will be presented finally at various values of amplitude of external strain ε_0 and energy parameter γ. The effect of elastic moduli was studied in details in Chapter 2 in Section 2.2. The main differences with the previous chapters are: the time-depending external strain is given instead of the constant one, therefore, even in the elastic stage; the equilibrium concentration c_{eq} in (4.9) depends on time; and there are two stages - elastic and elasto-plastic that have different kinetics .

By (4.3), the reaction front can propagate only if the stress-strain state at the front and the energy parameter are such that $c_{eq} < c_*$. We study further how the condition $c_{eq} < c_*$ is affected by the parameters. By (4.9), this is possible only if the transformation strain, external strains, elasticity parameters and the energy parameter are such that $\chi < \gamma$. Initially, we study the elastic stage, when the transformed and initial materials are elastic. We consider external deformation growing in time linearly: $\varepsilon_0(t) = \mathscr{U} t$. Therefore, at initial moment we have $\varepsilon_0(t = 0) = 0$. It means that by (2.14), in the considered case this condition takes the same form as it was in Section 2.2:

$$\chi(\varepsilon_0) - \gamma = 2(G_+ - G_-)\varepsilon_0^2 - 3S_+\vartheta^{tr}\varepsilon_0 - \left(\gamma - \gamma_0\right) < 0,$$

where

$$\gamma_0 = S_+(\vartheta^{tr})^2$$

is the critical value of the parameter γ in the sense that the reaction front may propagate at the external strain $\varepsilon_0 = 0$ only if

$$\gamma > \gamma_0.$$

A detailed analysis for the initial moment $t = 0$, is presented in Section 2.2 for the case $\varepsilon_0(t) = \varepsilon_0$ (in particular, the results for $\varepsilon_0(t) = 0$ can be found in 2.2). It shows how the initial conditions can initiate/block the chemical reaction depending on the elastic modulus, energetic parameter γ and different values of $\varepsilon_0(t) = \varepsilon_0$. Note, that for the results for the constant external deformation can be used as well for the case $\varepsilon_0(t) = \mathscr{U} t$: the different values of constant $\varepsilon_0(t) = \varepsilon_0$ can be corresponded to $\varepsilon_0(t) = \mathscr{U} t$ with given magnitude $\mathscr{U}$ at some moment of time such as these two values of external deformation are equal.

Note, that χ in (4.8) is a quadratic function of ε_0, which is given as $\varepsilon_0(t) = \mathscr{U} t$. Consequently χ is a quadratic function of time. The elasto-plastic stage appears when the second invariant of deviatoric stress reaches the yield stress:

$$\sigma_{yd} = \sqrt{\sigma_x^{+2} - \sigma_x^+\sigma_z^+ + \sigma_z^{+2}}$$

From where we obtain

$$\varepsilon_{cr} = \mathscr{U} t_* = \frac{1}{2(3k_+ + \mu_+)}\left(\frac{\sigma_{yd}(3k_+ + 4\mu_+)(3k_+ + \mu_+)}{\mu_+\sqrt{3\left(9k_+^2 + 6k_+\mu_+ + 4\mu_+^2\right)}} + 3k_+\vartheta^{tr}\right) \tag{4.75}$$

where ε_{cr} is the critical value of the external strain, that is reached at the moment $t = t_*$, when $\sqrt{3J_2} = \sigma_{yd}$. It means that for external strain $\varepsilon_0 \in [-\varepsilon_{cr}, \varepsilon_{cr}]$ the elastic stage takes place, and the

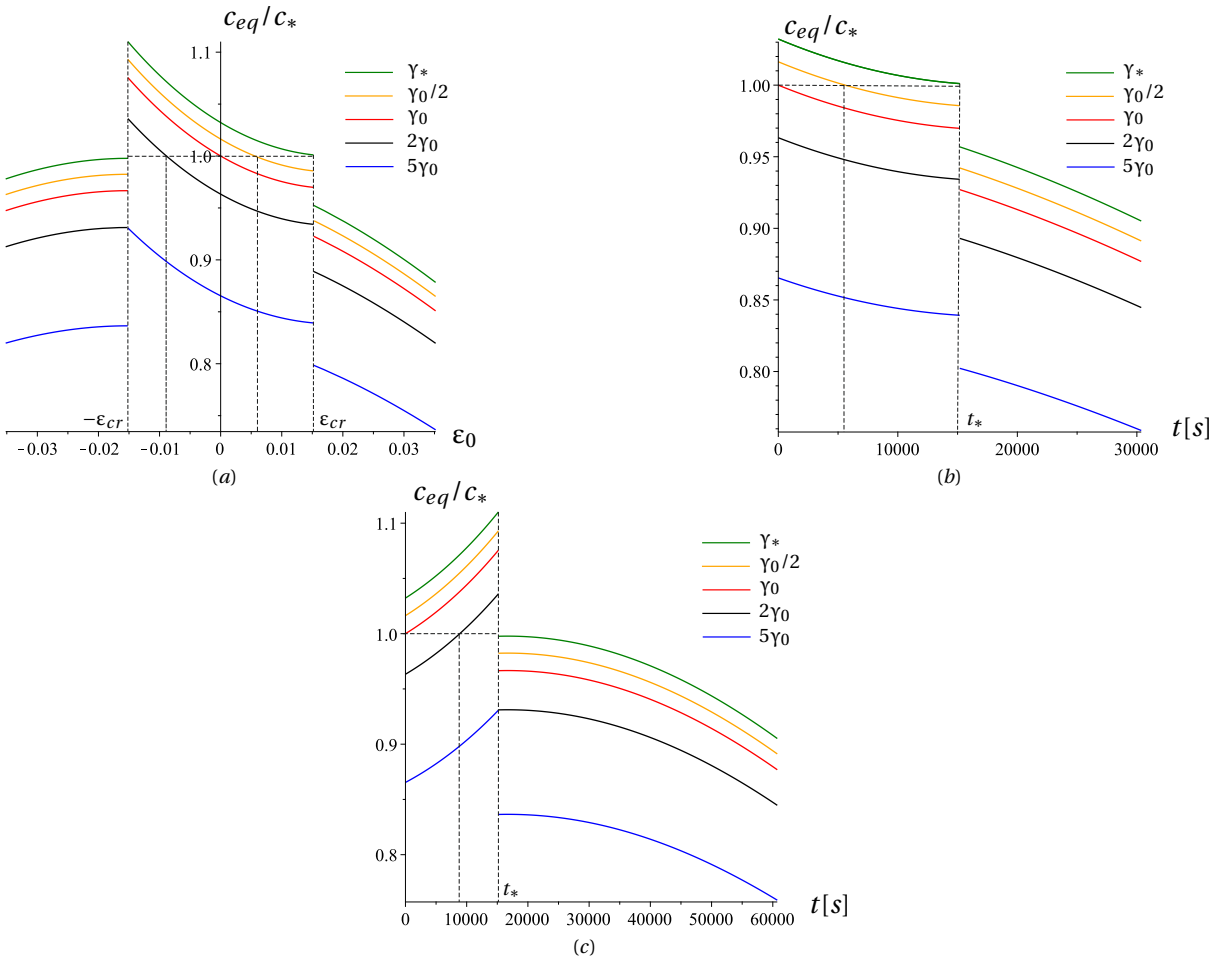

Figure 4.8: Planar reaction front: dependencies of the equilibrium concentration on (*a*) external strain ε_0 and (*b*), (*c*) on time for different values of the energy parameter γ ((*b*) for $\varepsilon_0 = 10^{-6}t$; (*c*) for $\varepsilon_0 = -10^{-6}t$) for the case $G_+ > G_-$. We observe something what could be associated to a jump, but it is not, it corresponds to instantaneous decrease.

equilibrium concentration is defined by (4.9), where ξ comes from the equation (4.8). When ε_0 reaches $|\varepsilon_{cr}|$ the elasto-plastic stages begins and all transformed elastic material transforms in plastic. Therefore for $\varepsilon_0 \in (-\infty, -\varepsilon_{cr}] \cup [\varepsilon_{cr}, \infty)$ (in the limit of small deformation assumption; finite strain is not part of this work and would necessities further developments) the equilibrium concentration c_{eq} is conducted from (4.18), where χ is defined by (4.17).

Fig. 4.8a and Fig. 4.9a reflect the competition between strain and chemical energies at $G_+ > G_-$ and $G_+ < G_-$, respectively. If $\gamma = \gamma_0$ then the dependence of c_{eq}/c_* on ε_0 passes trough the point $\varepsilon_0 = 0$, c_{eq}/c_*. In the case of elastic stage $\varepsilon_0 \in [-\varepsilon_{cr}, \varepsilon_{cr}]$ and $\gamma = \gamma_0$ then the front may propagates only at tension. When the external strain reaches $|\varepsilon_{cr}|$ reaction goes, even in compression, and reaction velocity increases. We see on Fig. 4.8a and Fig. 4.9a the instantaneous concentration decrease at $\varepsilon_0 = |\varepsilon_{cr}|$, it corresponds to the increase of elastic strain energy due to the plastification of the material. In the elasto-plastic stage the dependence c_{eq}/c_* changes the behaviour, initiates the reaction if it was blocked, and even accelerates the front propagation. One can see how increasing γ results in enlarging the interval allowed strains ε_0 (see the curves for $\gamma = 2\gamma_0$ and $\gamma = 5\gamma_0$) and how decrease of γ shortens and shifts the interval of the strains at $\gamma_* < \gamma < \gamma_0$.

Note, that the plastification in transformed layer changes also the elastic strain energy in initial material.

As the external deformation is given as $\varepsilon_0(t) = \mathscr{U}t$, therefore, the c_{eq}/c_* depends on time. From (4.75) follows, that for time $t \le t_*$, the elastic stage takes place and the equilibrium concentration is defined by (4.9), where ξ comes from the equation (4.8). For the instant $t = t_*$ the

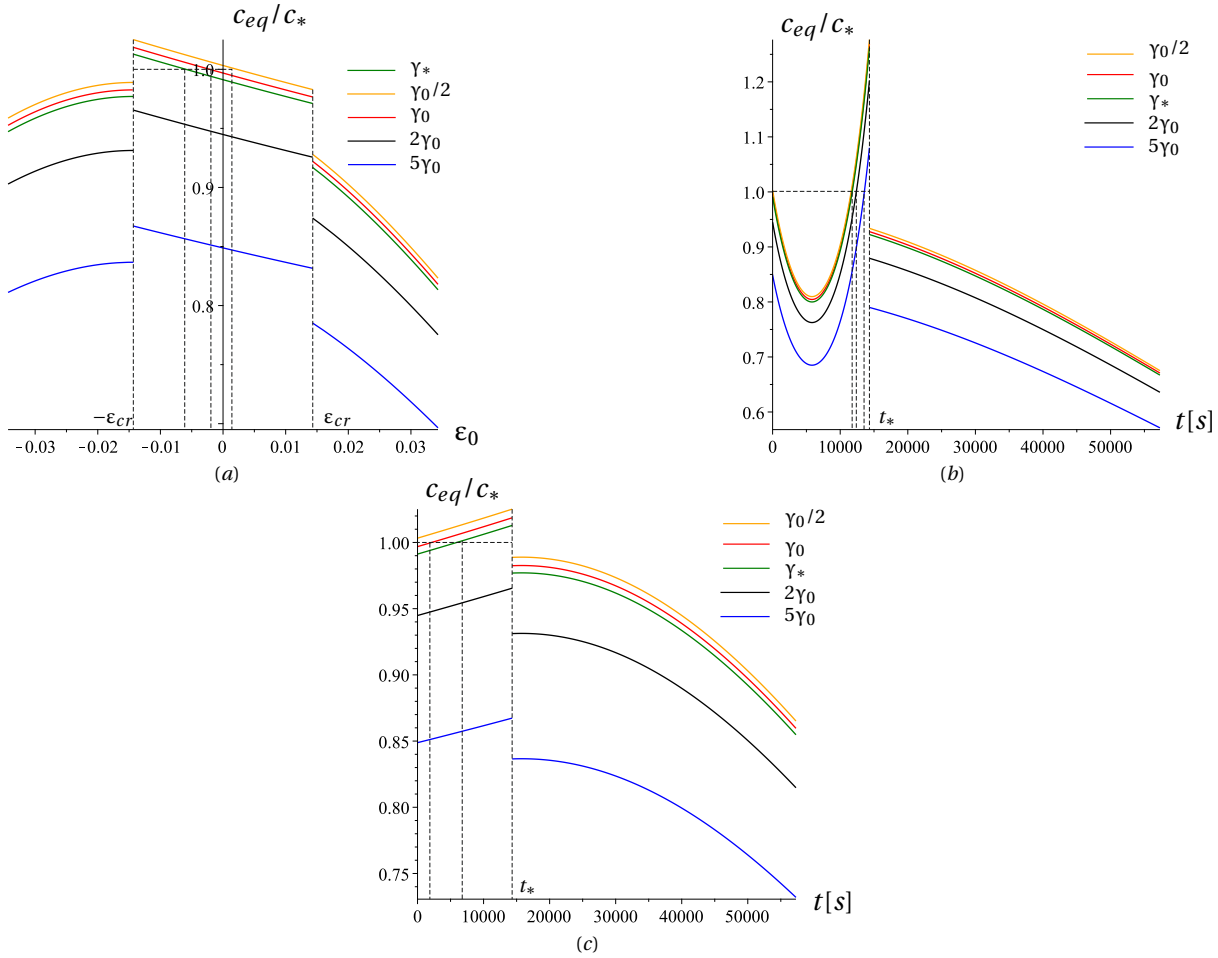

Figure 4.9: Planar reaction front: dependencies of the equilibrium concentration on (*a*) external strain ε_0 and (*b*), (*c*) on time for different values of the energy parameter γ ((*b*) for $\varepsilon_0 = 10^{-6}t$; (*c*) for $\varepsilon_0 = -10^{-6}t$) for the case $G_+ < G_-$. We observe something what could be associated to a jump, but it is not, it corresponds to instantaneous decrease.

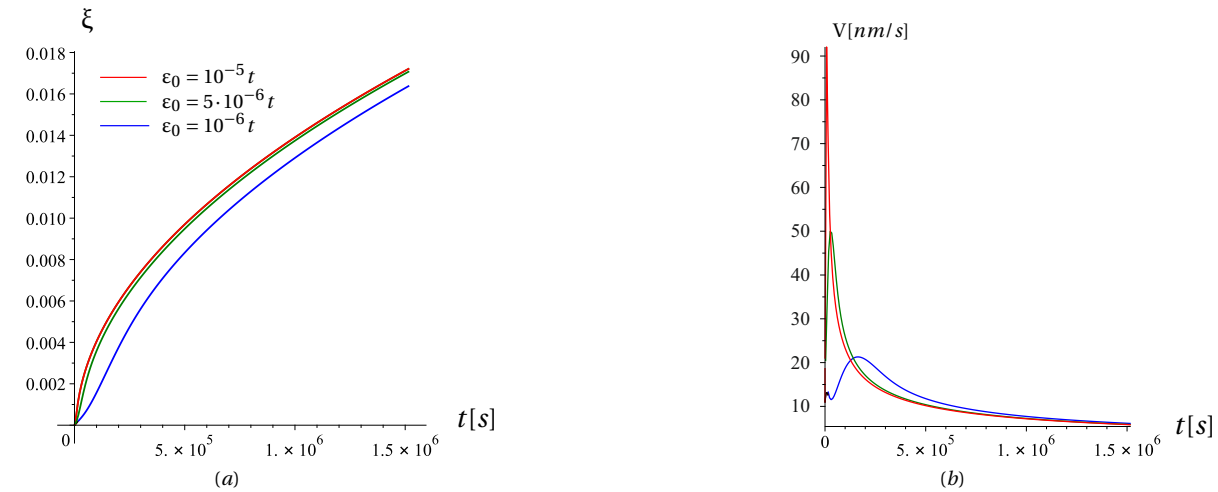

Figure 4.10: Planar reaction front: dependencies of the front position (*a*) and the front velocity (*b*) on time at various values of the amplitude $\mathscr{U}$ of external strain $\varepsilon_0(t) = \mathscr{U}\,t$ for the case $G_+ > G_-$.

elasto-plastic stages begins and the equilibrium concentration c_{eq} is defined by (4.18), where χ is defined by (4.17).

On Fig. 4.8b,c and Fig. 4.9b,c the dependence of the equilibrium concentration on time are shown at $G_+ > G_-$ and $G_+ < G_-$, respectively. If $\gamma = \gamma_0$, then the dependence of c_{eq}/c_* on time

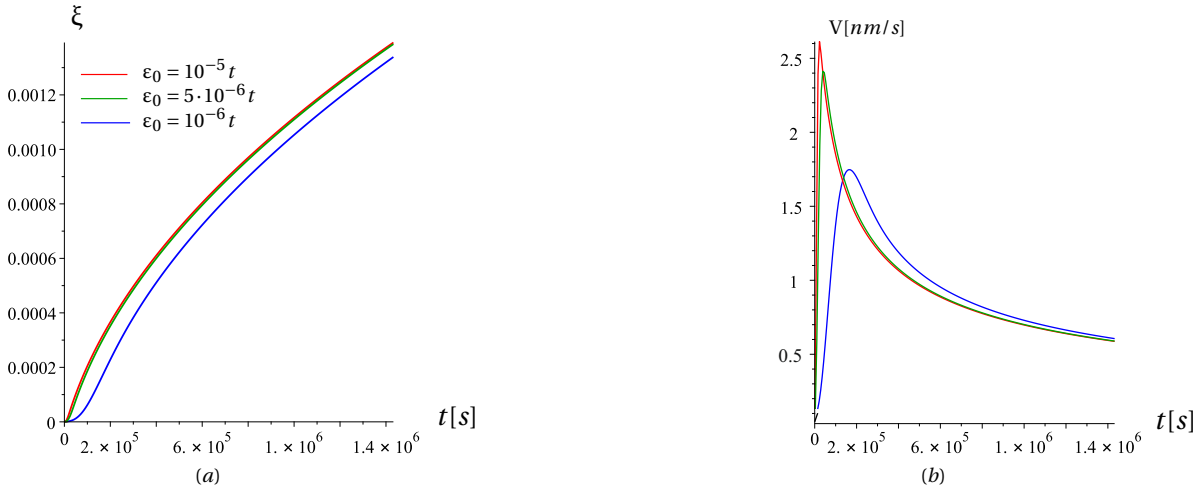

Figure 4.11: Planar reaction front: dependencies of the front position (a) and the front velocity (b) on time at various values of the amplitude $\mathscr{U}$ of external strain $\varepsilon_0(t) = \mathscr{U} t$ for the case $G_+ < G_-$.

passes through the point $t = 0$, $c_{eq}/c_* = 1$. In the case of tension external strain (e.g. $\varepsilon = 10^{-6} t$ Fig. 4.8b) in the case of elastic stage $t \in [0, t_*]$ and $\gamma = \gamma_0$ then the front propagates and the reaction velocity accelerates. When the time reaches the moment $t = t_*$ reaction is activated, even the reaction may start even at $\gamma_* < \gamma < \gamma_0$ and reaction velocity increases. One can see how increasing γ results in increasing of the reaction kinetics (see the curves for $\gamma = 2\gamma_0$ and $\gamma = 5\gamma_0$) and how decrease of γ may block the reaction at $\gamma_* < \gamma < \gamma_0$.

In the case of compressive external loading (e.g. $\varepsilon = -10^{-6} t$ Fig. 4.8c and Fig.4.9c) in the case of elastic stage $t \in [0, t_*]$ and $\gamma_* < \gamma < \gamma_0$ the reaction is blocked. When the time reaches the moment $t = t_*$ reaction initiates and front velocity increases. One can see how increasing γ results in enlarging the interval allowed time (see the curves for $\gamma = 2\gamma_0$ and $\gamma = 5\gamma_0$).

The dependence of the front position and the front velocity on time for various magnitude ε_0 are shown in Fig.4.10 and Fig. 4.11 at $G_+ > G_-$ and $G_+ < G_-$, respectively. One can see how the strains can retard or accelerates the reaction front.

4.2.2 Spherical reaction front

In this section, the dependencies of the reaction position on time and of the reaction front velocity on the front position in a sphere will be presented finally for various values and types of the external stresses σ_0. Since, by (4.19), the reaction front velocity increases if c_{eq}/c_* decreases and, respectively, the velocity decreases if c_{eq}/c_* increases. The influence of various parameters on the reaction front behavior can be predicted qualitatively if one knows how the parameters affect the equilibrium concentration. The effect of elastic modulus for the case of the constant external loading was studied in details in Chapter 2 in Section 2.2.

Constant external loading $\sigma_0(t) = \sigma_0$

If the external loading σ_0 is constant, then $|\sigma_r - \sigma_\varphi|$ increases only due to the front propagation, i.e increasing of ξ. Then the value $|\sigma_r - \sigma_\varphi|_{max}$ reaches the yield stress σ_{yd}, when the thickness of the transformed material is equal to $h^*(t_*) = \xi^*(t_*)\mathrm{R}$, such as:

$$\frac{6\mu_+ \left| [\![k^{-1}]\!]\sigma_0 + \vartheta^{tr} \right|}{4\mu_+ [\![k^{-1}]\!] (1-\xi^*)^3 + \dfrac{4\mu_+}{k_-} + 3} = \sigma_{yd}$$

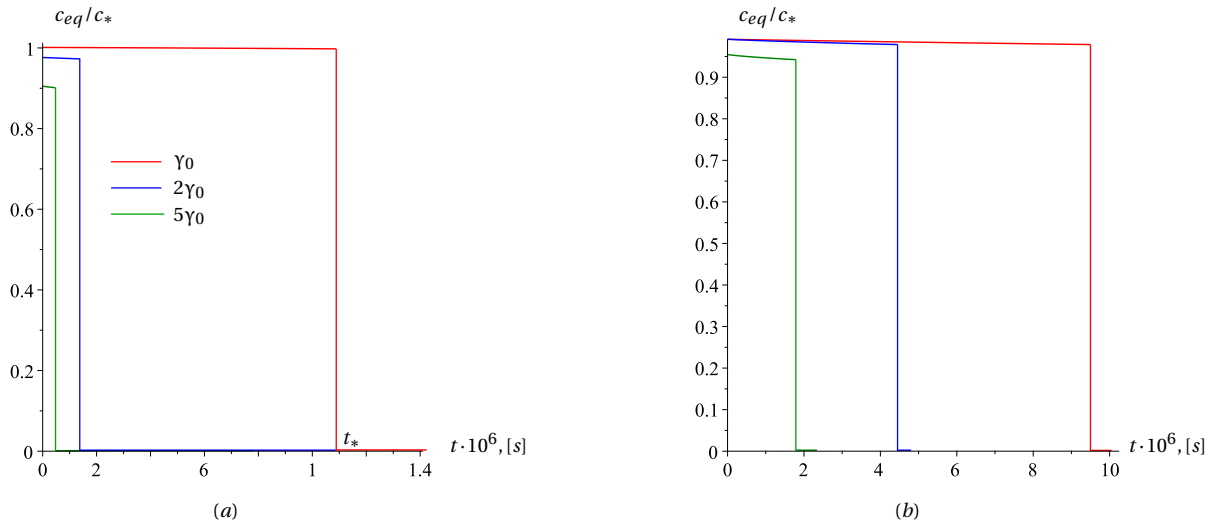

Figure 4.12: Spherical reaction front: dependencies of the equilibrium concentration on time at $\sigma_0(t) = \sigma_0 = 0$ for the case: (a) $k_+ > k_-$ and (b) $k_+ < k_-$ for different values of the energy parameter γ.

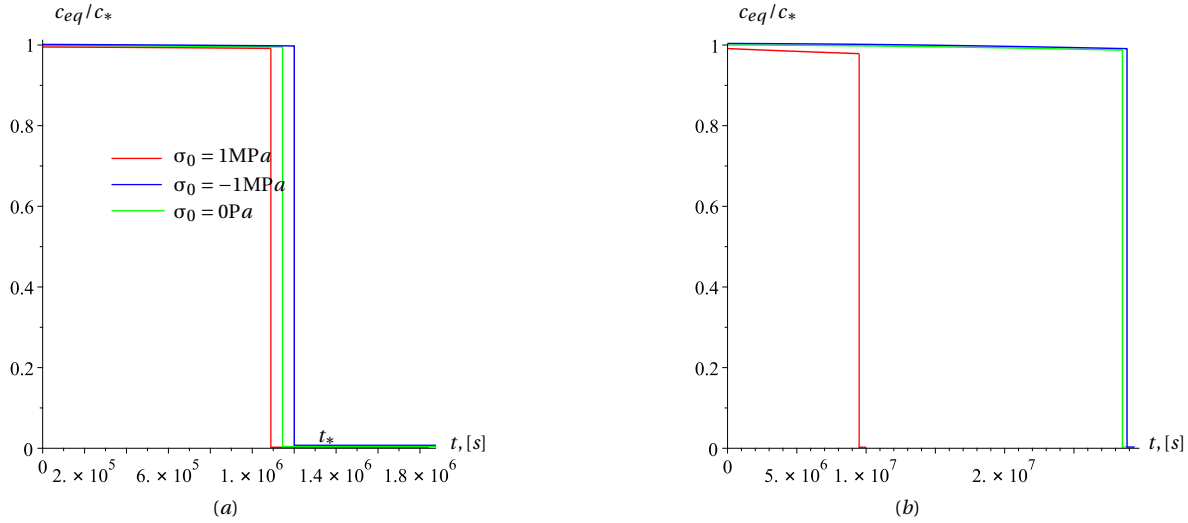

Figure 4.13: Spherical reaction front: dependencies of the equilibrium concentration on time (a) for the case $k_+ > k_-$ and (b) for the case $k_+ < k_-$ for different magnitude of external loading $\sigma_0(t) = \sigma_0$.

From where ξ^* is found out as:

$$\xi^*(t_*) = 1 - \sqrt[3]{\frac{6\mu_+|[\![k^{-1}]\!]\sigma_0 + \vartheta^{tr}|}{\sigma_{yd}} - \frac{4\mu_+}{k_-} - 3}{4\mu_+[\![k^{-1}]\!]} \tag{4.76}$$

where t_* is the moment when the thickness of the transformation reaches the critical value ξ^* and this in turn makes $\sqrt{3J_2} = \sigma_{yd}$. It means that for the thickness of the transformed layer $\xi \in [0, \xi^*]$ the elastic stage takes place and the equilibrium concentration can be found from (4.31), where ξ comes from (4.32). When $\xi = \xi^*$ the elasto-plastic stage begins. For $\xi \in [\xi^*, 1]$ the equilibrium concentration c_{eq} is given by (4.49).

In order to study the propagation of the reaction front we study further how the condition $c_{eq} < c_*$ is affected by the reaction front propagation and external loading. By (4.31), this is possible only if the transformation strain, external stress, elasticity parameters and the energy parameter are such that $\chi_{el} < \gamma$. As initially the elastic stage takes place, therefore, we use the results that we

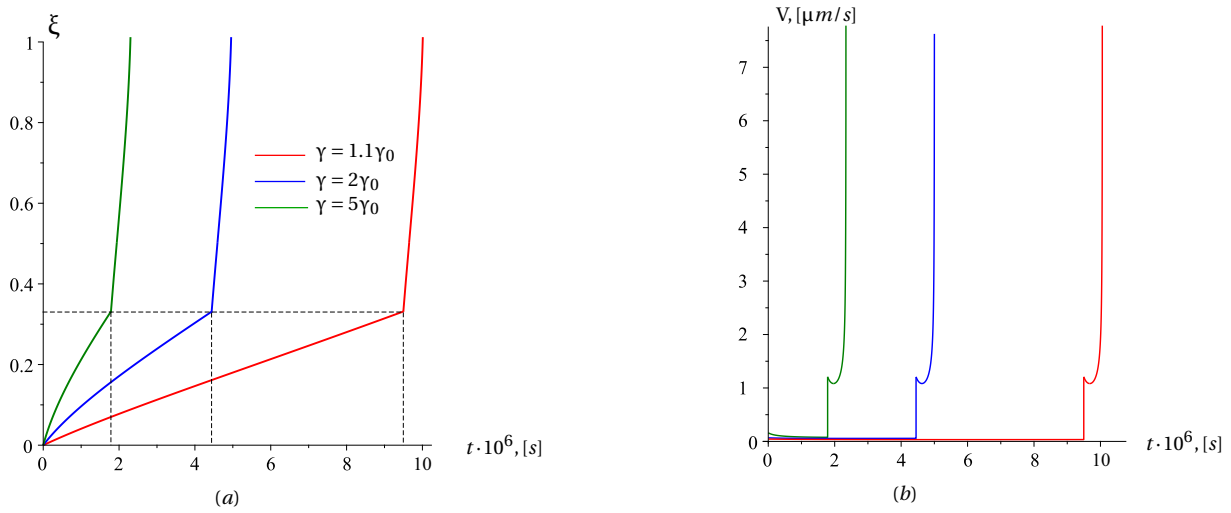

Figure 4.14: Spherical reaction front: dependencies of the dimensionless front position on time (*a*) and (c) (Fig.c is zoomed Fig.a), and the front velocity on the front position (b) at various values of energy parameter γ for the case $k_+ < k_-$, $\sigma_0(t) = \sigma_0 = 0$

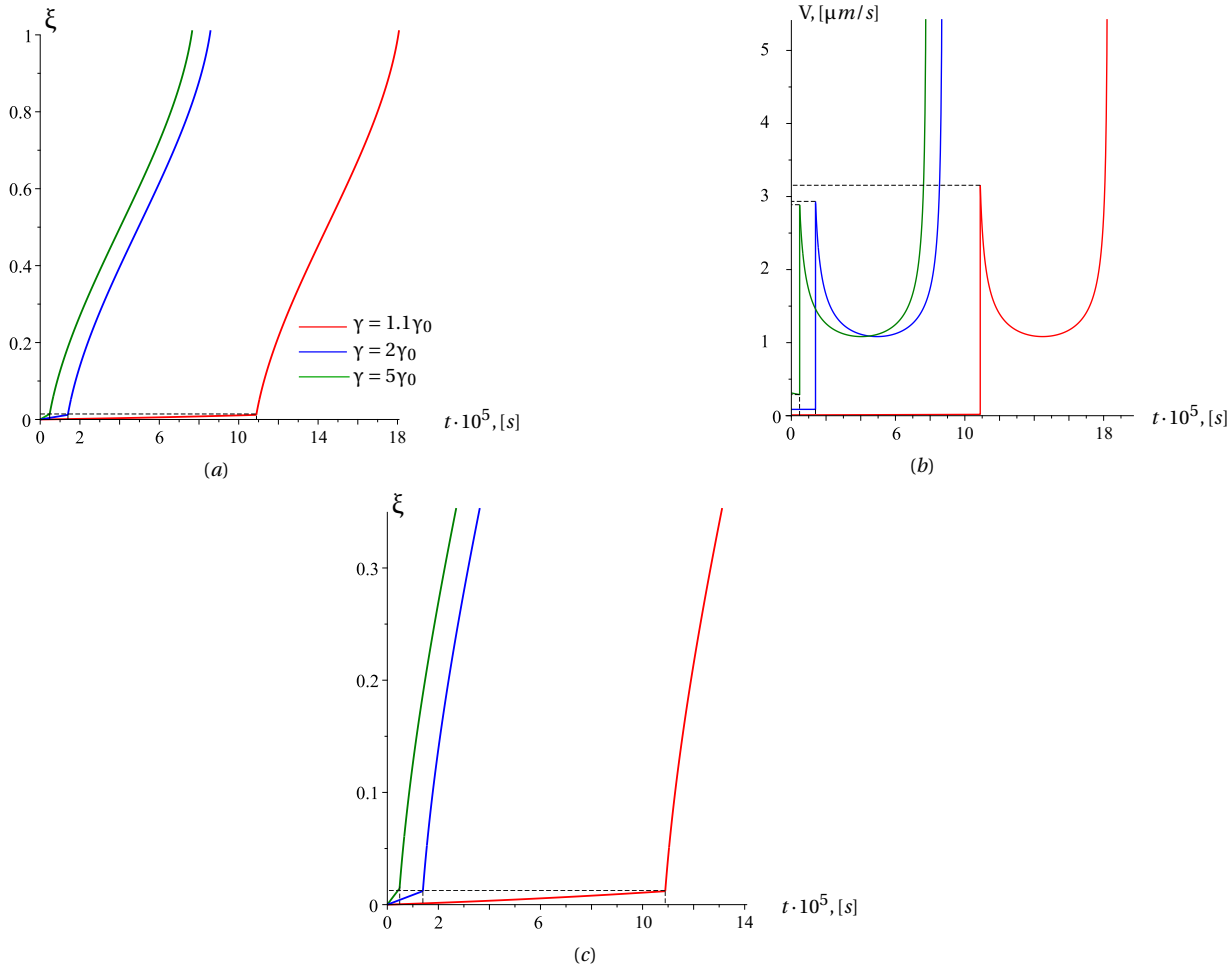

Figure 4.15: Spherical reaction front: dependencies of the dimensionless front position on time (*a*) and (c) (Fig.c is zoomed Fig.a), and the front velocity on the front position (b) at various values of energy parameter γ for the case $k_+ > k_-$, $\sigma_0(t) = \sigma_0 = 0$

obtained in Chapter 2 in Section 2.2: by (4.30), in the considered case this condition takes the form

$$\chi(\sigma_0,\xi)-\gamma=\mathfrak{P}(k_+-k_-)\sigma_0^2-2\mathfrak{P}k_+k_-\sigma_0\vartheta^{tr}-(\gamma-\gamma_0)<0$$

where

$$\gamma_0=\mathfrak{K}(\vartheta^{tr})^2$$

is the critical value of the parameter γ in the sense that the reaction front can start from the outer surface at $\sigma_0=0$ only if

$$\gamma>\gamma_0$$

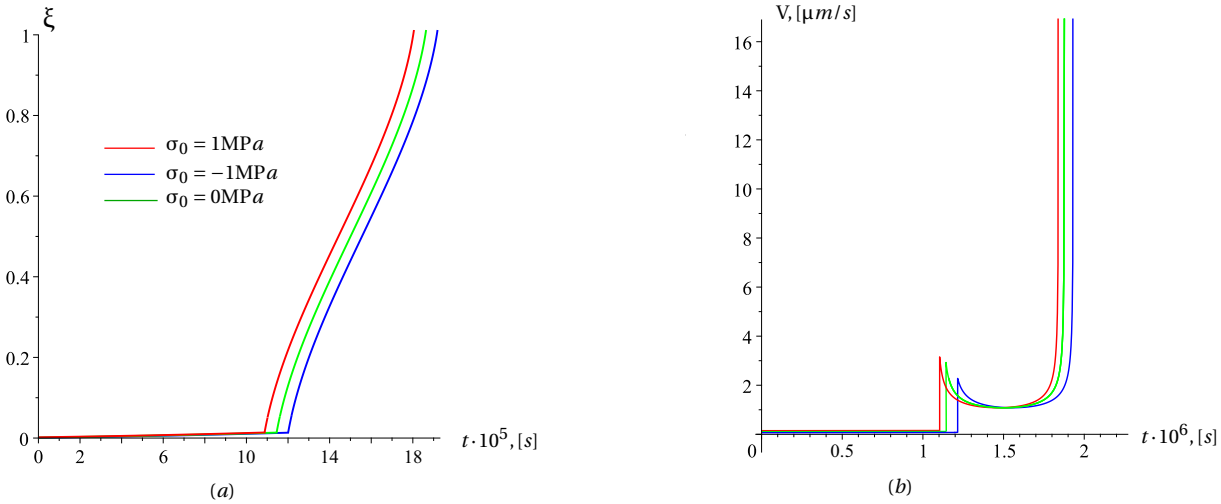

Figure 4.16: Spherical reaction front: kinetics of the reaction front at various values of external loading $\sigma_0(t)=\sigma_0$ for the case $k_+>k_-$. Dependencies of the dimensionless front position on time (a) and (c), and the front velocity on the front position (b)

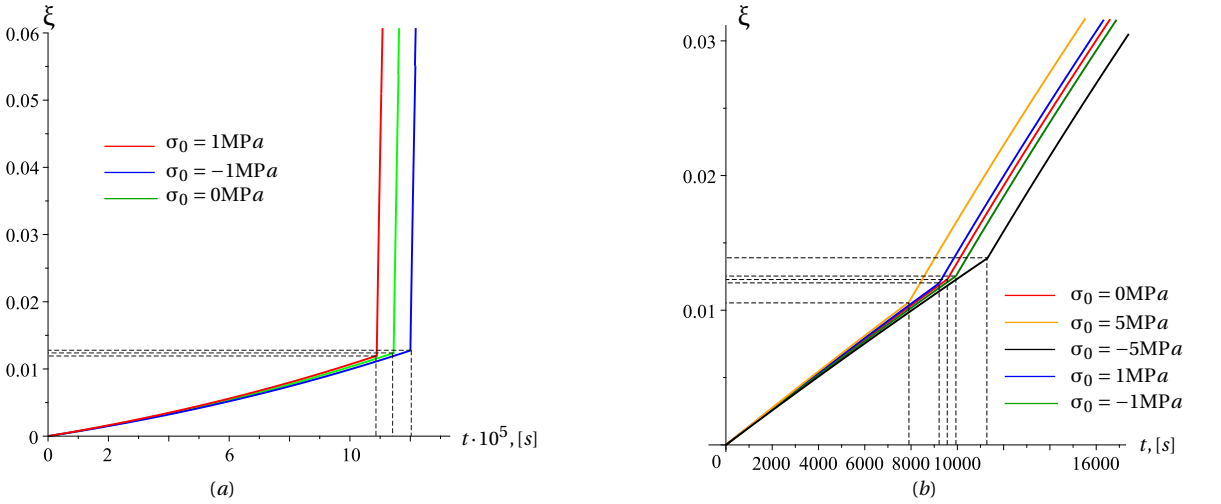

Figure 4.17: Spherical reaction front: kinetics of the reaction front at various values of external loading $\sigma_0(t)=\sigma_0$ for the case $k_+>k_-$: (a) at $\gamma=1.1\gamma_0$ and (b) at $\gamma=10\gamma_0$

On Fig. 4.12 the dependence of the equilibrium concentration c_{eq} on time at various values of energy parameter γ is presented at $k_+>k_-$ and $k_+<k_-$ in 4.12(a) and 4.12(b), respectively.

If $\gamma = \gamma_0$ at $t \in [0, t_*]$ the sphere is in an elastic case, and the solution corresponds to the results obtained in Chapter 2 in Section 2.2: the reaction front propagates and its velocity increases. At the instant $t = t_*$, the elasto-plastic stage takes place: the reaction goes, even if it was blocked before and the speed of the reaction front propagation increases significantly. Note, that the bigger energetic parameter γ, the faster elasto-plastic stage becomes and the higher reaction rate.

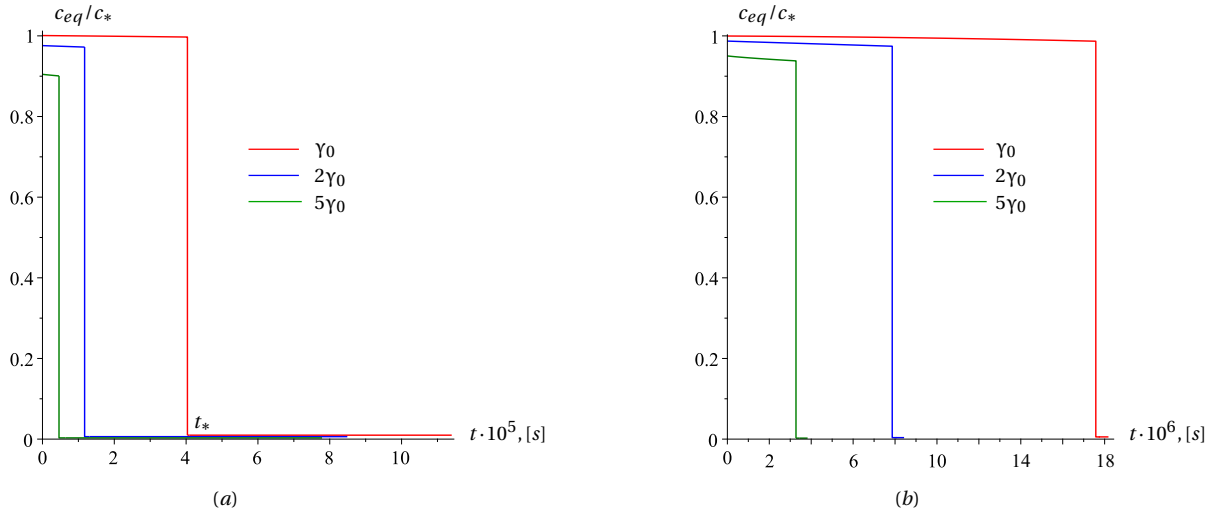

Figure 4.18: Spherical reaction front: dependencies of the equilibrium concentration on time (a) for the case $k_+ > k_-$ and (b) for the case $k_+ < k_-$ for different values of the energy parameter γ, $\sigma_0(t) = 50t$.

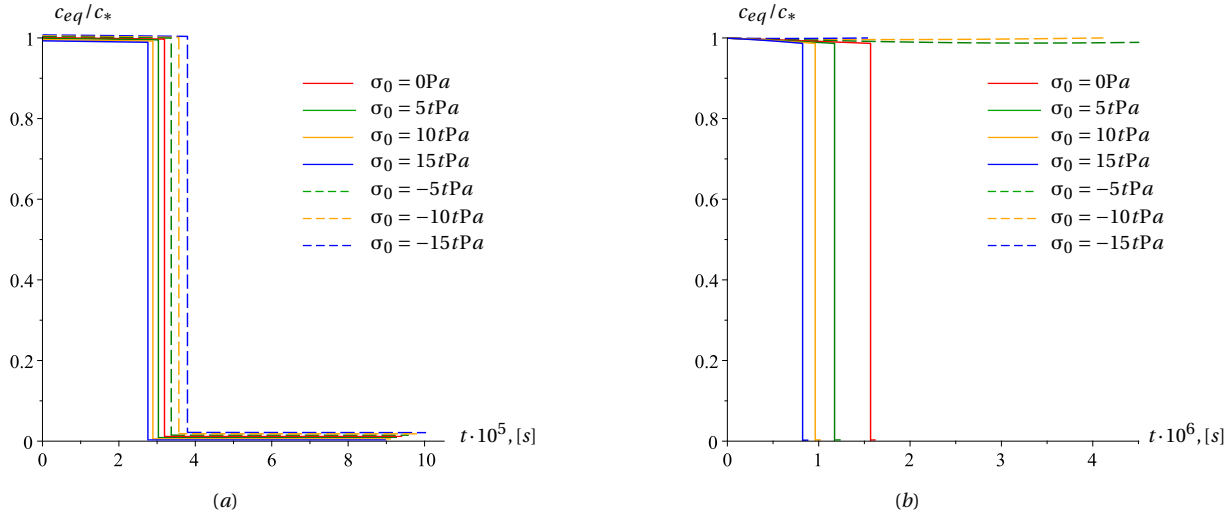

Figure 4.19: Spherical reaction front: dependencies of the equilibrium concentration on time (a) for the case $k_+ > k_-$ and (b) for the case $k_+ < k_-$ for different magnitude $\mathscr{S}$ of external loading $\sigma_0(t) = \mathscr{S}t$.

The influence of the applied external stress σ_0 on the equilibrium concentration c_{eq} is demonstrated on Fig. 4.13. For $\gamma = \gamma_0$ at $t \in [0, t_*]$ the elastic stage takes place and at tensile stress the reaction initially blocked and starts with time, while at $\sigma_0 = 0$ and at compressing stress the reaction goes and velocity of the reaction front accelerates. Note, that the higher the external loading, the faster becomes the instant t_* - the start of the plastification of the sphere. At $t = t_*$ the elasto-plastic stage takes place, and the equilibrium concentration instantaneously and significantly decreases, and the reaction kinetics increases. In the case for $k_+ > k_-$, the elastoplastic regime occurs faster, than for the case $k_+ < k_-$.

The dependence of the reaction front position and its velocity on time for different values energy parameter γ and various magnitude of the external loading σ_0 are demonstrated in Fig. 4.15 –

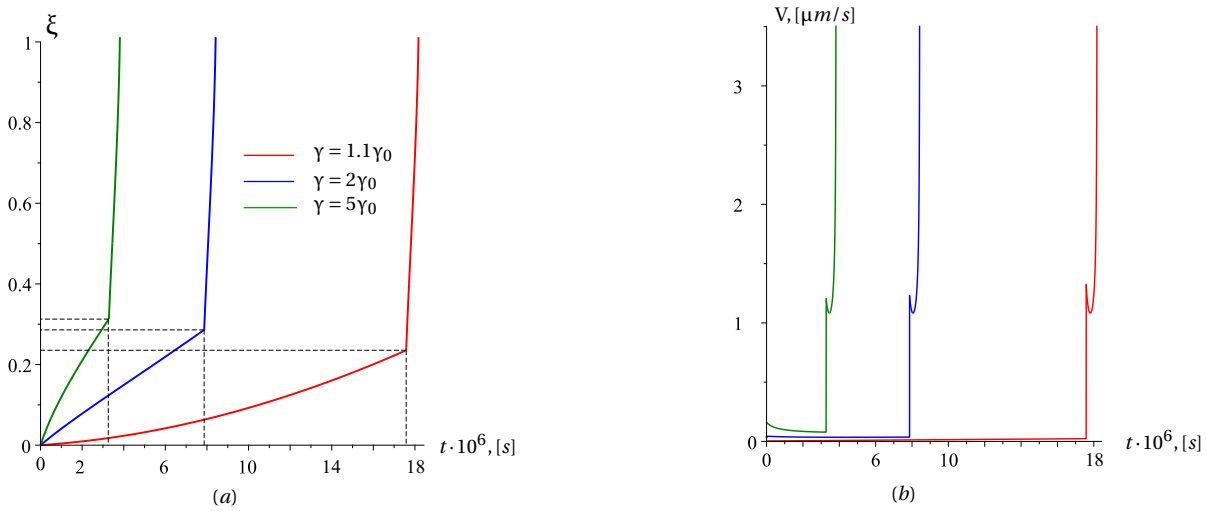

Figure 4.20: Spherical reaction front: dependencies of the dimensionless front position on time (*a*) and (c) (Fig.c is zoomed Fig.a), and the front velocity on the front position (b) at various values of energy parameter γ for the case $k_+ < k_-$, $\sigma_0(t) = 50t$

Fig. 4.17. From equation (4.76), the plastification of the transformed material becomes at the moment t_*, when the thickness of the transformed layer reaches value ξ_*. Therefore, in Fig. 4.15 and Fig. 4.14, the elasto-plastic stage takes place as earlier as greater value of energy parameter γ. The reaction kinetics accelerates with beginning of the material plastification. As it was mentioned before, in the case for $k_+ > k_-$, the elastoplastic regime occurs faster, than for the case $k_+ < k_-$. Therefore, the thickness of the transformed layer, which is needed to pass to elastoplastic state, is less for the case $k_+ > k_-$ and, than in the case $k_+ < k_-$.

The influence of the value of the external loading σ_0 on the reaction front kinetics is shown in Fig 4.16 and in zoomed Fig. 4.17. The external compression increase the velocity of the reaction and the elasto-plastic stage becomes earlier then in the case for $\sigma_0 = 0$, while the tensile loading decelerates the reaction propagation and the yield stress is reached later. Note, that external stress affects as well the moment t_* of transformed material plastification, as the critical thickness ξ_* of transformed layer (see Fig. 4.17).

Important to emphasise that the greater value of yield stress σ_{yd}, the later becomes the moment $t = t_*$ of the beginning of the elastoplastic regime, or can not occurs at all.

External loading as linear function of time $\sigma_0(t) = \mathscr{S} t$

If the external loading is a linear function of time $\sigma_0(t) = \mathscr{S} t$, then there are two "sources" to increase $|\sigma_r - \sigma_\varphi|$: ξ (degree of chemical transformation) is increasing and/or we increase the magnitude of σ_0. Therefore, both aspects ξ and σ_0 have action on plastic activity. The moment t_*, when $|\sigma_r - \sigma_\varphi|$ reaches the yield stress σ_{yd} and $\xi(t_*) = \xi^*$ and $\sigma_0(t_*) = \mathscr{S} t_*$, is found from the condition:

$$6\mu_+ \frac{\left|[k^{-1}]\mathscr{S} t_* + \vartheta^{tr}\right|}{4\mu_+[k^{-1}](1-\xi^*)^3 + \dfrac{4\mu_+}{k_-} + 3} = \sigma_{yd} \tag{4.77}$$

Similarly to what was done for the constant loading and in the case of the plate, for the time $t \in [0, t_*]$ such as the relative thickness of the transformed layer $\xi \in [0, \xi_*]$ and the external loading $|\sigma_0(t)| \in [0, |\mathscr{S}|\, t_*]$, the sphere is in an elastic state. And the study of the equilibrium concentration and reaction front propagation comes from the equations (4.31) and (4.32), respectively.

At the moment $t = t_*$ the external loading reaches the value $\sigma_0(t_*) = \mathscr{S} t_*$, while the degree of the chemical transformation becomes $\xi(t_*) = \xi_*$, and they are both valid to the equation (4.77).

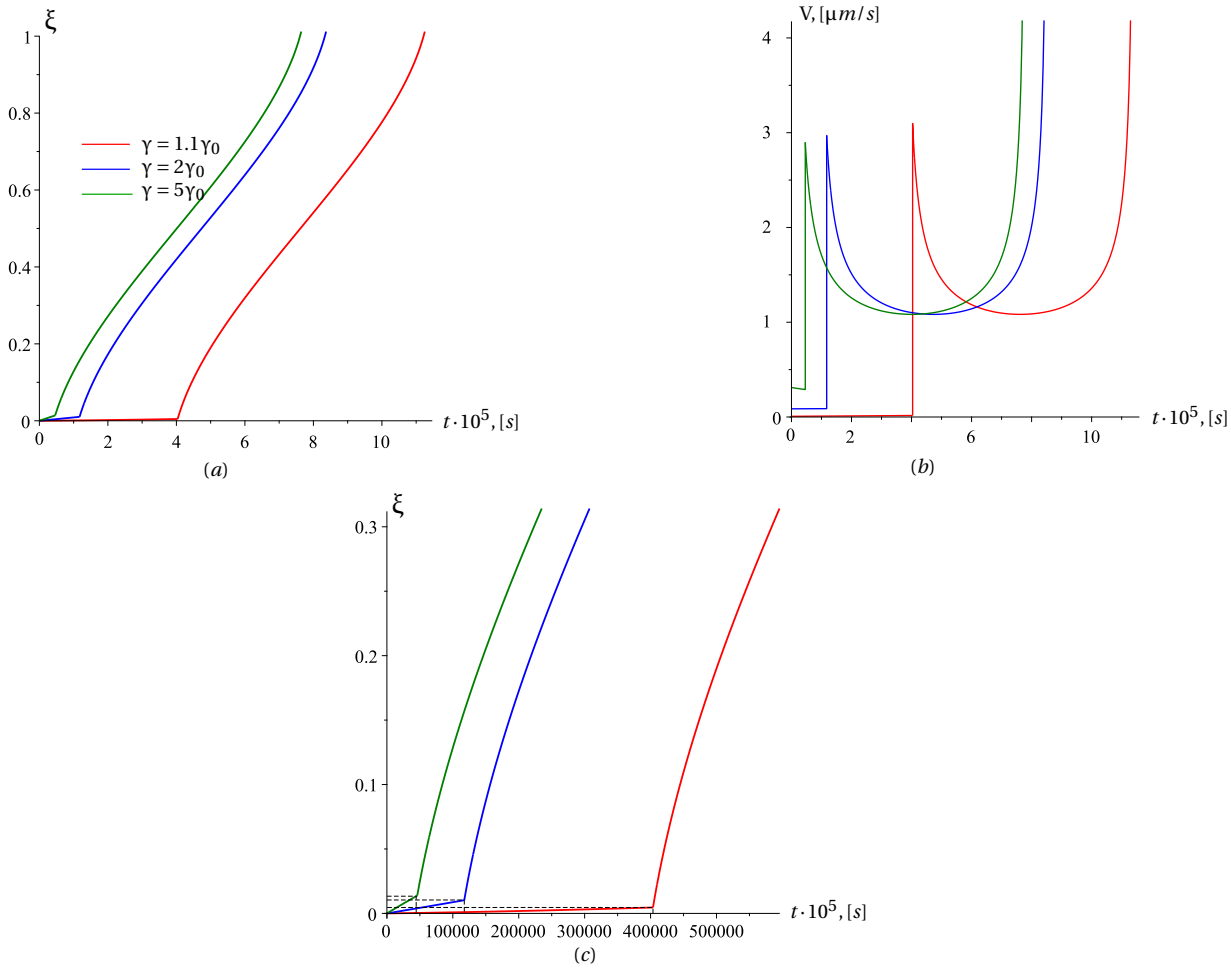

Figure 4.21: Spherical reaction front: dependencies of the dimensionless front position on time (*a*) and (c) (Fig.c is zoomed Fig.a), and the front velocity on the front position (b) at various values of energy parameter γ for the case $k_+ > k_-$, $\sigma_0(t) = 50t$

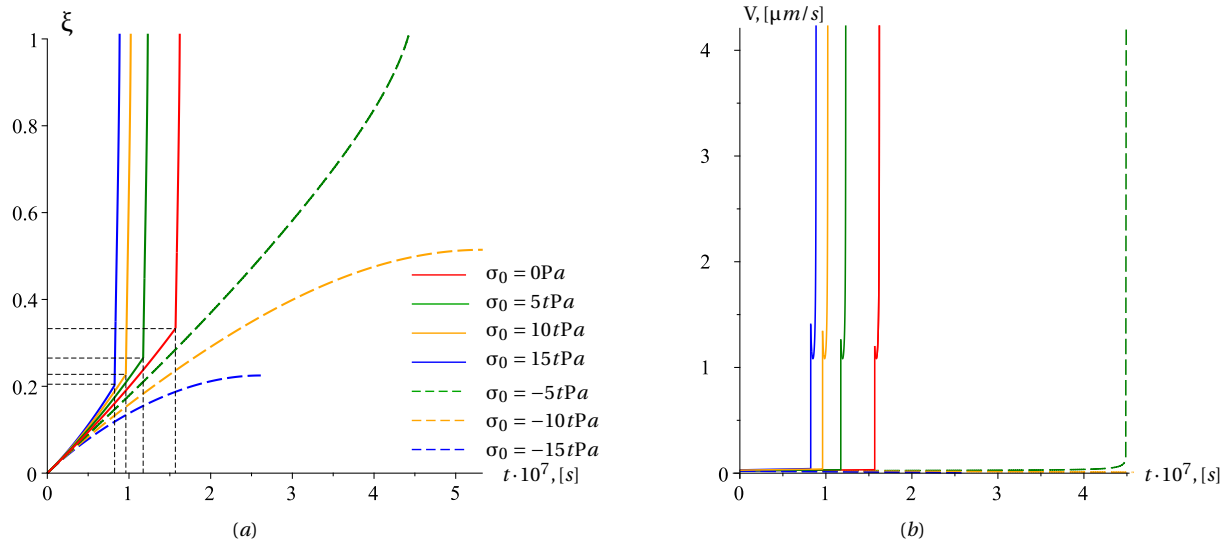

Figure 4.22: Spherical reaction front: kinetics of the reaction front at various values of external loading $\sigma_0(t) = \mathscr{S}t$ for the case $k_+ < k_-$. Dependencies of the dimensionless front position on time (*a*) and (c), and the front velocity on the front position (b)

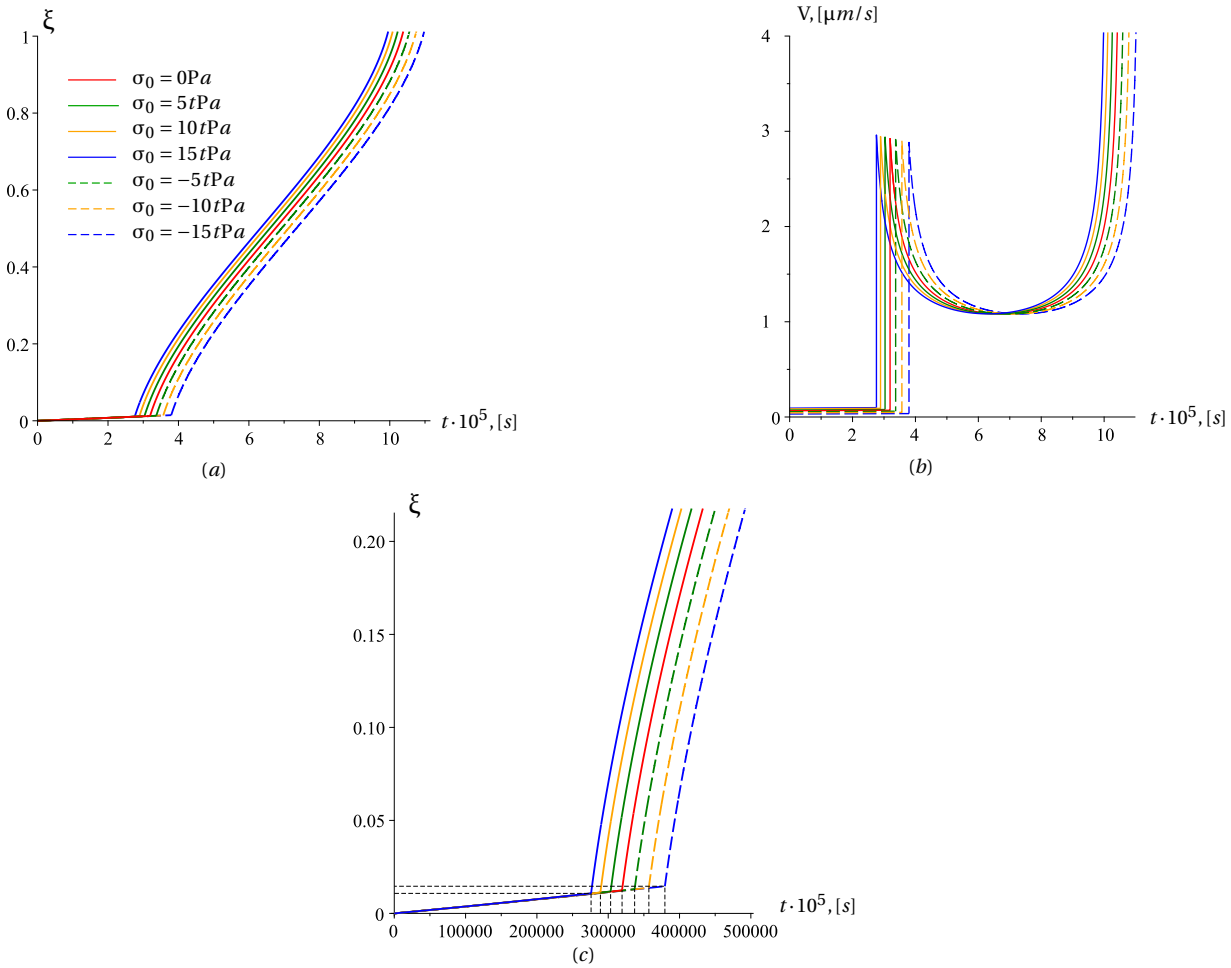

Figure 4.23: Spherical reaction front: kinetics of the reaction front at various values of external loading $\sigma_0(t) = \mathscr{S}t$ for the case $k_+ > k_-$. Dependencies of the dimensionless front position on time (*a*) and (c), and the front velocity on the front position (b)

This means that elastoplastic regime occurs and develops for $t \geq t_*$. The equilibrium concentrations is defined by (4.49), and the reaction kinetics is obtained from (4.50).

The dependence of the equilibrium concentration c_{eq} on time is demonstrated in Fig. 4.18 and Fig. (4.19) at various values of energy parameter γ and for different magnitude $\mathscr{S}$ of external loading $\sigma_0(t) = \mathscr{S}t$, respectively. Similarly to the case $\sigma_0(t) = \sigma_0$, the elasto-plastic regime takes place faster with increasing of the energy parameter γ and in the case of $k_+ > k_-$ (see Fig. 4.18(a),(b)).

The influence of the external loading $\sigma_0(t) = \mathscr{S}t$ on the reaction front propagation is shown in Fig. 4.19. The greater the magnitude $\mathscr{S}$ of the external loading, the faster the reaction kinetics. In the case $k_+ > k_-$, the elastoplastic state takes place faster, than for $k_+ < k_-$ (see Fig. 4.19). For $k_+ > k_-$ (Fig. 4.19(a)), the reaction is initially blocked for the tensile external loading. The bigger value of $|\mathscr{S}|$ for external tension the longer reaction would be blocked, however, the reaction propagation initiates the reaction. It means that in this case the influence of the reaction front propagation on the equilibrium concentration c_{eq} is stronger, than the effect of external loading $\sigma_0(t) = \mathscr{S}t$ on the reaction kinetics.

For the case $k_+ < k_-$ (Fig. 4.19(b)), the external compressive stress has greater influence than for $k_+ > k_-$. Moreover, for tensile load is unlikely to be possible as well as the reaction can be blocked at some moment. The greater the tensile external loading $\sigma_0(t)$, the faster the reaction will be blocked. It can be observed that for the smaller value of yield stress σ_{yd}, there is a possibility to initiate the plastification of the material and to delay the blocking of the reaction for tensile external loading.

4.2.3 Cylindrical reaction front

In the same way, as for the planar and spherical reaction fronts, the dependencies of equilibrium concentration and chemical reaction kinetics on time for the cylindrical reaction front is studied in this section.

The second deviatoric stress invariant J_2 in this case is equal to $J_2 = \sqrt{\sigma_r^2 + \sigma_\varphi^2 - \sigma_r \sigma_\varphi}$. Therefore, using von Mises criterion, it follows that the plasticity at the reaction front begins at the moment $t = t_*$, such as

$$\frac{\left(\begin{array}{l}\left(\mu_+^2(\mathscr{K}_+ - \mathscr{K}_-)^2 + \dfrac{\mathscr{K}_+^2}{27}(\mathscr{K}_- + 3\mu_+)^2\right)\sigma_0^2(t_*) + k_+^2\mu_+^2\mathscr{K}_-^2\left(1 + \dfrac{(1-\xi(t_*))^4}{3}\right)\vartheta^{tr2} - \\ -2\mu_+ k_+ \mathscr{K}_-\left(\mu_+(\mathscr{K}_+ - \mathscr{K}_-) + \dfrac{\mathscr{K}_+}{9}(\mathscr{K}_- + 3\mu_+)\right)\vartheta^{tr}\sigma_0(t_*)\end{array}\right)}{\left(\mu_+\left(\mu_+ + k_+ - \dfrac{\mathscr{K}_-}{3}\right)\left(1 - (1-\xi(t_*))^2\right) + \dfrac{\mathscr{K}_-}{9}(3k_+ + 4\mu_+)\right)^2} = \sigma_{yd} \tag{4.78}$$

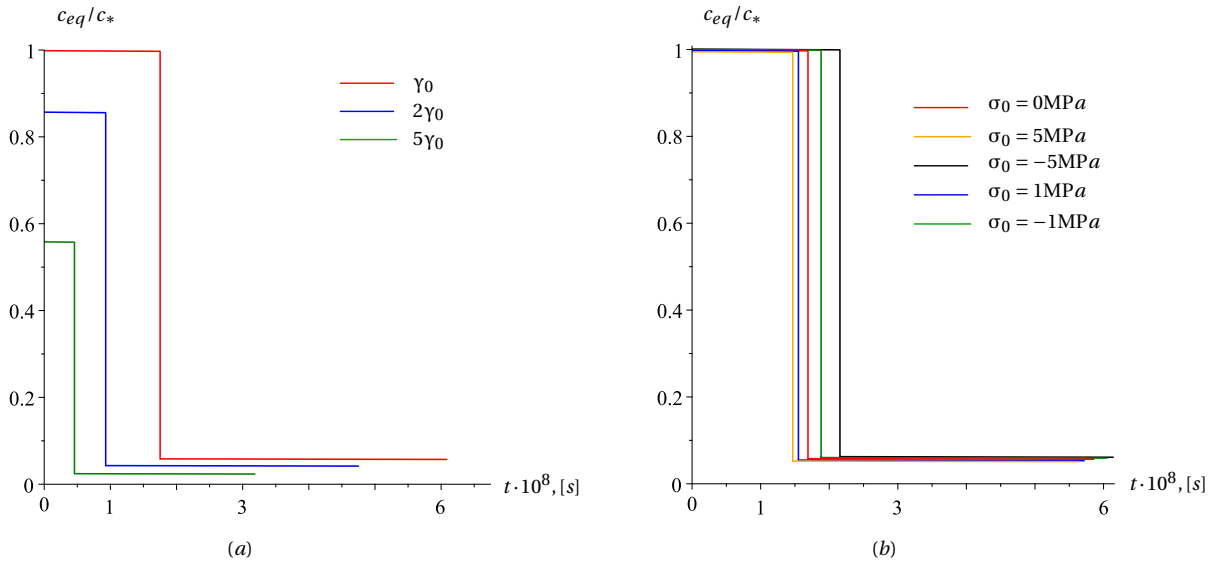

Figure 4.24: Cylindrical reaction front: dependencies of the equilibrium concentration on time for the case $\mathscr{K}_+ > \mathscr{K}_-$ for(a) different values of the energy parameter γ at $\sigma_0(t) = 0$ and (b) various values of external loading $\sigma_0(t) = \sigma_0$.

Prior to yield $t \in [0, t_*]$, the cylinder is in elastic state, and the equilibrium concentration c_{eq} and the reaction kinetics are obtained from (4.58) and (4.60). From the yield criterion (4.78), the yield stress σ_{yd} can be reached due to the reaction front propagation (ξ is increasing) and/or due to the change of the external stress $\sigma_0(t)$. If the external load is constant $\sigma_0(t) = \sigma_0$, hence the elasto-plastic stage can be initiated by the chemical transformation. In the case of $\sigma_0(t) = \mathscr{S}t$, at the instant $t = t_*$ the external stress $\sigma_0(t_*) = \mathscr{S}t_*$ and the relative thickness of the new transformed material $\xi(t_*) = \xi_*$ are such as the yield stress is reached (the criterion (4.78) is valid) and the material behaves as plastic. For elasto-plastic stage the reaction kinetics and the equilibrium concentration are found from (4.73) and (4.74), accordingly.

The dependencies of the equilibrium concentration on time for various values of the energy parameter γ are shown in Fig. 4.24(a) and in Fig. 4.26(a) for different types of the external loading. The greater value of γ the faster reaction goes. In the case of the constant external loading, decreasing the energy parameter γ the elasto-plastic stage takes place later (see Fig. 4.24(a)). As parameter γ depends on the temperature as well, therefore, changing its value can delay or accelerates the moments of the material yielding. For $\sigma_0(t) = \mathscr{S}t$, the dependence c_{eq}/c_* on time decreases with increasing of γ (Fig. 4.26(a)), and the yield stress is reached earlier, than in the case

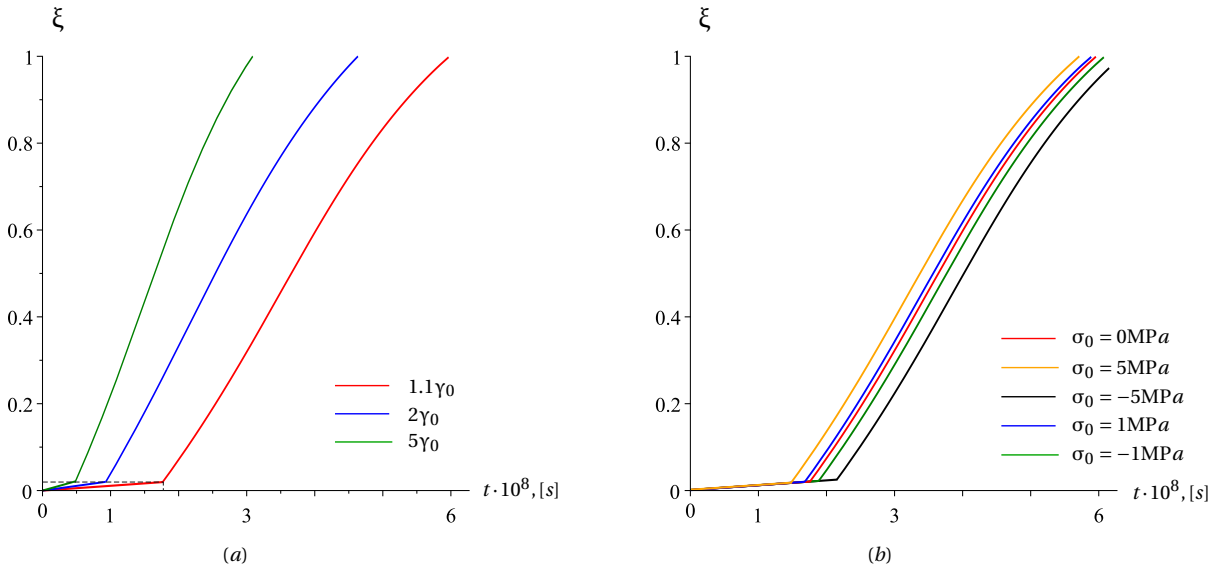

Figure 4.25: Cylindrical reaction front: kinetics of the reaction front for the case $\mathscr{K}_+ > \mathscr{K}_-$ at (a) various values of energy parameter γ at $\sigma_0(t) = \sigma_0 = 0$ and (b) at different values of external stress $\sigma_0(t) = \sigma_0$ at $\gamma = 1.1\gamma_0$.

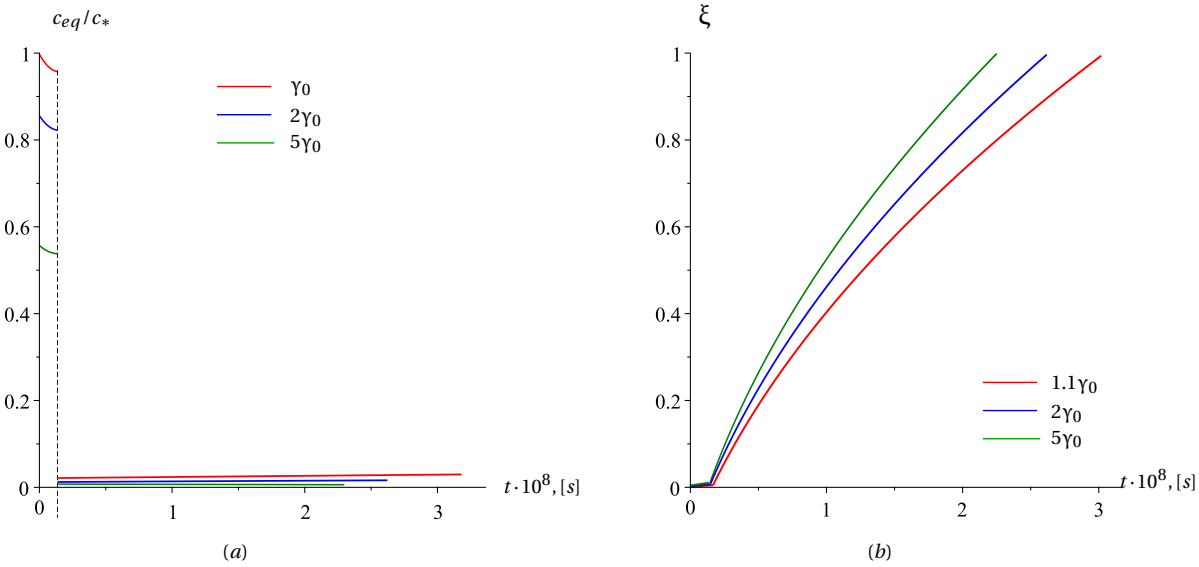

Figure 4.26: Cylindrical reaction front: (a) dependencies of the equilibrium concentration on time and (b) kinetics of the chemical reaction front for different values of the energy parameter γ for the case $\mathscr{K}_+ > \mathscr{K}_-$ and $\sigma_0(t) = \mathscr{S}t$.

of the constant external loading. In Fig. 4.25 and Fig. 4.26(b) the kinetics of the reaction front is presented for various values of γ, for different magnitude and types of the external loading.

Note, that in the case $\mathscr{K}_+ < \mathscr{K}_-$ the yield stress is not reached. It can be possible only at smaller values of σ_{yd}. As it was not possible to obtain the resulting formulas in the case of the elasto-plastic transformed material for the chemical reaction in the cylinder, it was not possible to make more detailed analysis.

4.3 Plastic front evolution and plastic deformations

In this section the evolution of the plastic front, mechanism of the reaction front propagation for the case of the elastoplastic transformed material and plastic deformations are studied.

To describe the chemical reaction in solid, we consider two-phases model with moving in-

terface. The reaction between solid and diffusing reactant starts at the outer surface of the deformable body. The reaction front is localized at the interface dividing the initial and transformed materials. The reaction front moves due to the consumption of the diffusive reactant, which diffuses through the transformed material from the outer surface to the reaction front. In Fig.4.27 and Fig. 4.28 are demonstrated such mechanism of the chemical reaction evolution in solids with different geometry. Such reaction evolution was in the case of the reaction with elastic and viscoealstic reaction product, which were studied in details in Chapter 2 and Chapter 3.

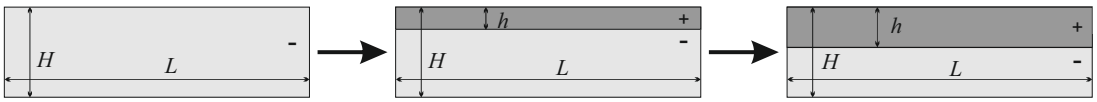

Figure 4.27: Evolution of the planar reaction front.

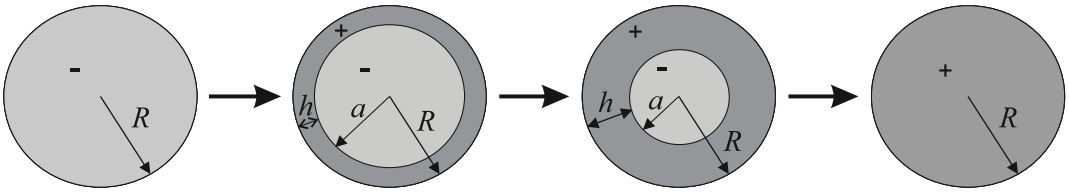

Figure 4.28: Evolution of the spherical reaction front in the case of the elastic and viscoelastic transformed materials.

In this Chapter we consider the case of the chemical reaction with elastoplastic reaction product. In section 4.1.1 we studied propagation of the reaction front in plate with given external deformation $\varepsilon_0 = \mathscr{U} t$, which increases linearly with time. Such choice of the boundary condition was motivated by initiating of the yielding of the material in plate. In the elastic state, the reaction product is elastic and the reaction propagates in the same way as presented in Fig. 4.27. As result, when the second deviatoric stress invariant reaches the value equal to yield stress, at that moment elastic transformed layer becomes fully plastic. Further mechanism is similar to the one in the cases of elastic and viscoelastic reaction product in Fig. 4.27, and it is demonstrated in Fig. 4.29. The plastic deformations were found before (see equation (4.14)). In Fig. 4.30 are shown the plastic deformations e_x^{pl} and e_y^{pl} at various magnitude of given external deformation $\varepsilon_0 = \mathscr{U} t$.

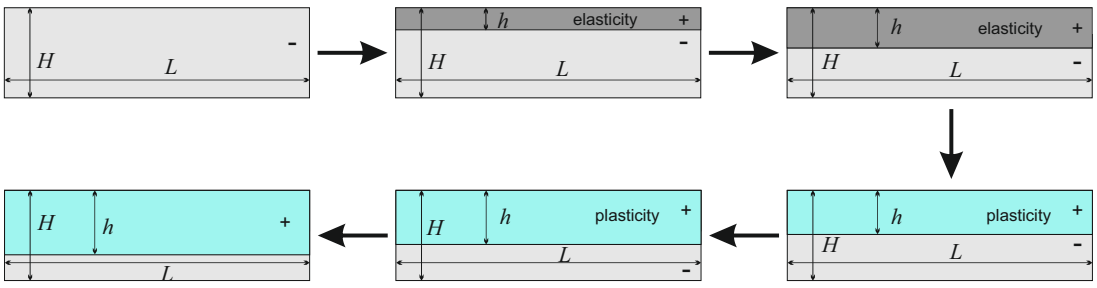

Figure 4.29: Evolution of the planar chemical reaction front in the case of the elasto-plastic transformed material with given deformations $\varepsilon_0(t) = \mathscr{U} t$ at the plate edges.

Note, that if the stress σ_0 is given as boundary condition at the short sides of the plate, then the second front, a plastic front, appears. In this case the stresses satisfy the integral equilibrium

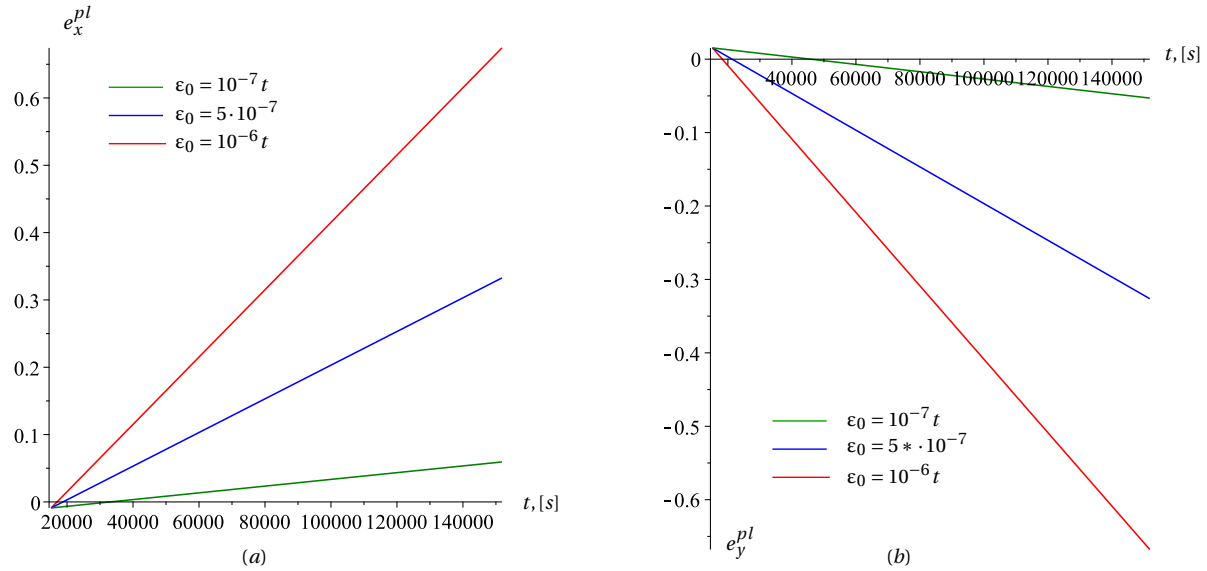

Figure 4.30: Planar reaction front: Plastic deformations (a) e_x^{pl} and (b) e_y^{pl} at various magnitude of the external deformation $\varepsilon_0(t) = \mathscr{U} t$.

conditions

$$\int_0^h \sigma_x^+ dy + \int_h^H \sigma_x^- dy = H\sigma_0, \qquad \int_0^h y\sigma_x^+ dy + \int_h^H y\sigma_x^- dy = \frac{H^2}{2}\sigma_0$$

This case corresponds to the plate bending. Such effect appears due to the chemical transformation. To solve such problem we suppose that $\varepsilon_x = \mathscr{A} y + \mathscr{B}$ (assuming the planar sections hypothesis). Von Mises criterion in this case takes the following form

$$|\sigma_x^+|\sqrt{\nu_+^2 - \nu_+ - 1} = \left| \frac{E_+}{1-\nu_+^2}(\mathscr{A} y + \mathscr{B} - \vartheta^{tr}) \right| = \sigma_{yd} \tag{4.79}$$

As $y \in [0, h]$, the equation (4.79) has a maximum at $y = h$. It means that the initial plastic zone (if it appears) is located at $y = h$, which corresponds to the reaction front. In elasto-plastic stage there are two different fronts: the reaction front and the plastic one. The plastic front propagates in inverse direction to the reaction front, and its propagation velocity is proportional to the reaction kinetics. As results, the plastic zone expands in both directions and, more likely, occupied the all transformation layer. Such evolution of the plastic and the reaction fronts is shown in Fig. 4.31. Different scenarios are possible for the case of the unloading due to the stress relaxation, reversible chemical reaction or harmonic external loading.

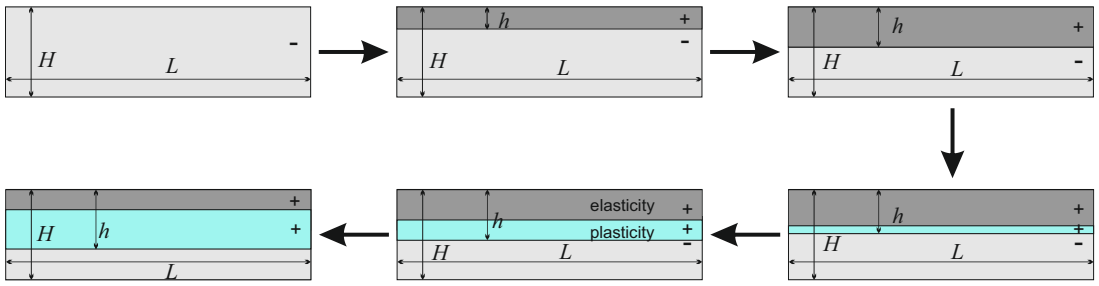

Figure 4.31: Evolution of the planar chemical reaction front in the case of the elasto-plastic transformed material with given loading σ_0 at the plate edges.

Evolution of the spherical and cylindrical reaction fronts for the elastic and viscoelastic reaction products is presented in Fig. 4.28. The reaction starts at the outer surface and propagates to

the center of the sphere or to the axis of the cylinder. As the spherical and cylindrical problems are very similar, and in the case of the reaction in cylinder the equations are very complex and explicit, therefore, in order to analyse the reaction mechanism for the case of the elasto-plastic transformed material, we focus only on the spherical reaction front propagation.

As it was already shown in Fig. 4.5 and from the equation (4.24), the yield stress is reached at the reaction front $r = a$ (see equations (4.24) and (B.2)). Thus the second (plastic) front appears in elasto-plastic regime and the plastic zone (if it appears) starts at the reaction front (see Fig. 4.32). The reaction and plastic fronts have their own kinetics and direction of propagation. The evolution of the plastic front $r = \varsigma$ is defined be the equation (4.42). This equation represents the relation between two fronts. The dimensionless positions of the reaction front and plastic fronts in time are shown in Fig. 4.33. Therefore, the plastic front propagates outwards to the reaction front, and the plastic zone expands in two directions. Such evolution of the plastic zone is shown in Fig. 4.32. Regarding to (4.55), the same mechanism would be for the cylindrical reaction front.

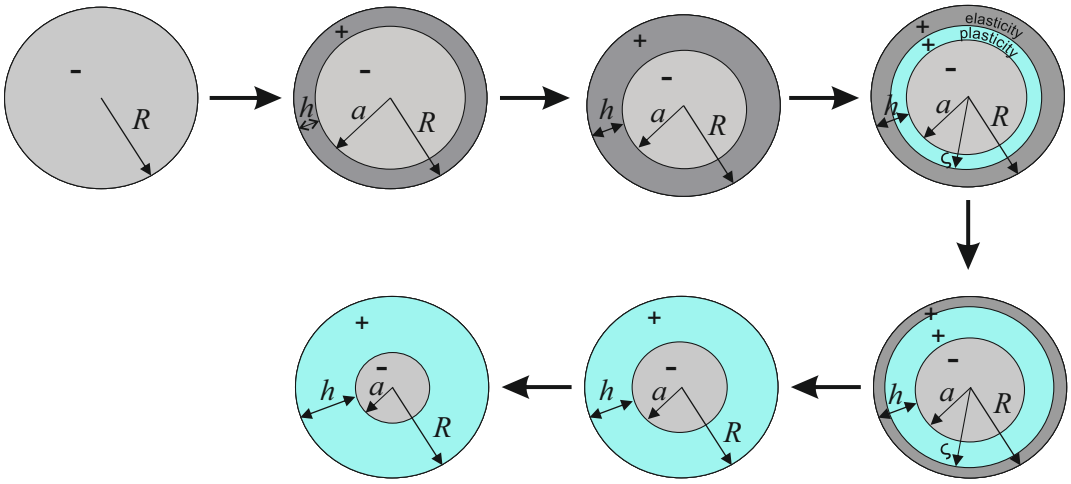

Figure 4.32: Evolution of the spherical reaction front for the elasto-plastic transformed material.

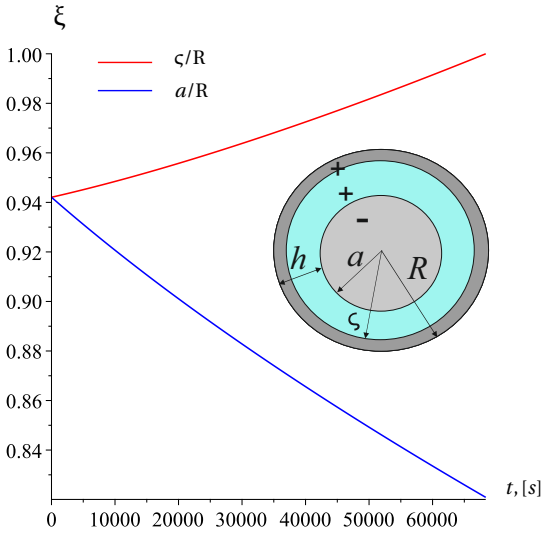

Figure 4.33: Spherical reaction front: dimensionless positions of the reaction and plastic fronts in time.

At the elastic stage the strains and stresses in the initial and transformed materials are determined by the equations (4.21), (4.22) and (4.23). In Fig. 4.34 the evolution for the radial and

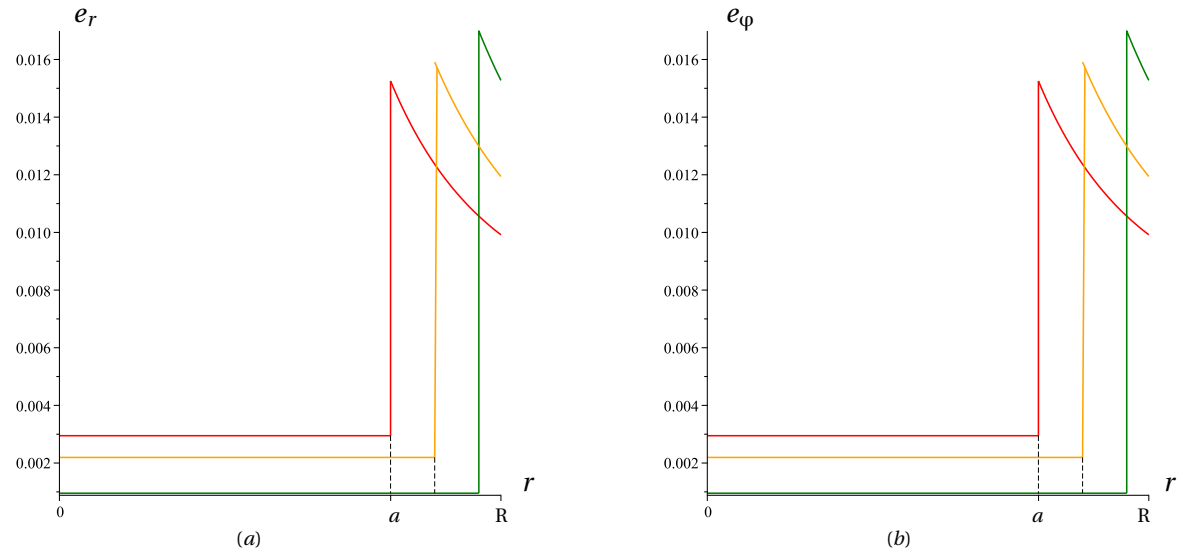

Figure 4.34: Spherical reaction front: evolution of elastic (a) radial and (b) tangential strains for different reaction front positions at the elastic stage.

tangential elastic strains is shown for different positions of the front at the elastic stage. The distribution of the radial and tangential stresses along the radius is demonstrated in Fig. 4.35.

At the elasto-plastic stage, the plastic deformations and stresses are defined by equations (4.45) and (4.40) and (4.41), respectively. The total strains in the plastic zone can be found from (4.43) and (4.44).

The relation between the inputs of elastic strains e_r^{el}, e_φ^{el} and plastic strains e_r^{pl}, e_φ^{pl} into total strains e_r^+ and e_φ^+ is shown in Fig. 4.36. In Fig. 4.37 the evolution of the radial ε_r and tangential ε_φ strains along the radius of the sphere is shown for different positions of reaction and plastic fronts. The highest magnitude of the radial and tangential strains is achieved at the reaction front for all positions of the reaction and plastic front, while with the front propagation this magnitude increases.

The evolution of the second deviatoric stress invariant along the radius of the sphere is shown in Fig. 4.38(a). In Fig. 4.37(b),(c) the profile of the radial ε_r and tangential ε_φ stresses along the radius of the sphere for different positions of reaction and plastic fronts is presented. The radial and tangential stresses reach their maximum at the reaction front for all positions of the reaction and plastic front.

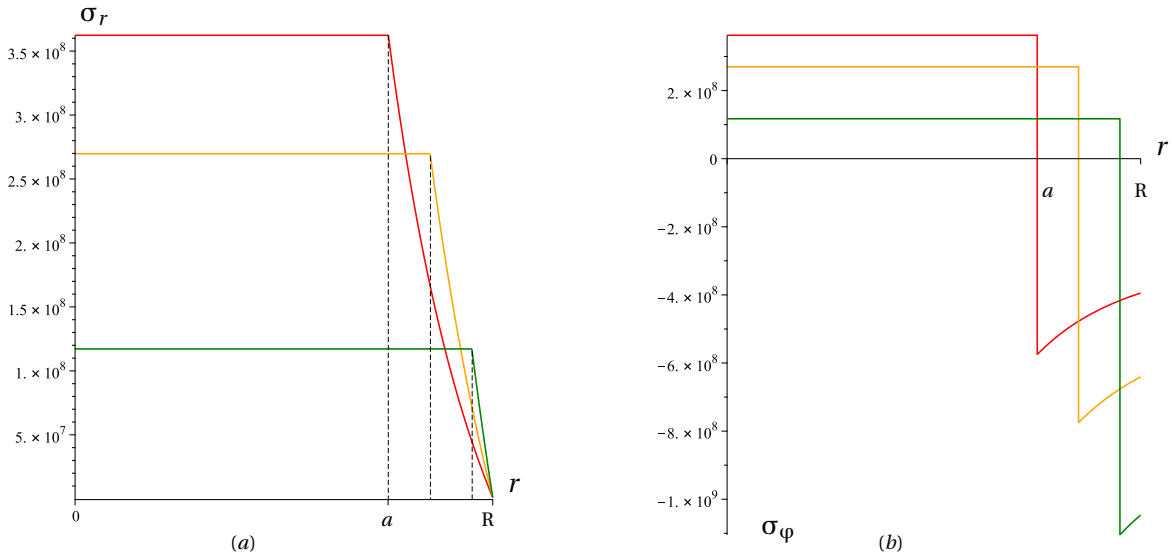

Figure 4.35: Spherical reaction front: profile of (a) the radial stress and (b) the tangential stress at different positions of the reaction and plastic fronts at the elastic stage.

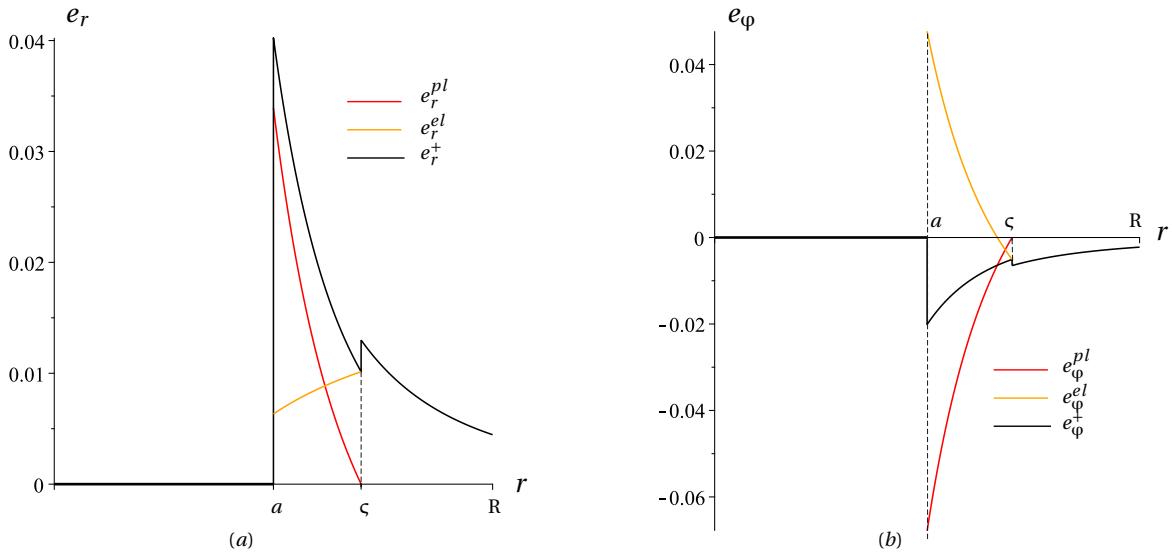

Figure 4.36: Spherical reaction front: Redistribution of plastic and elastic strains, relation between the inputs of elastic strains e_r^{el}, e_φ^{el} and plastic strains e_r^{pl}, e_φ^{pl} into total strains e_r^+ and e_φ^+.

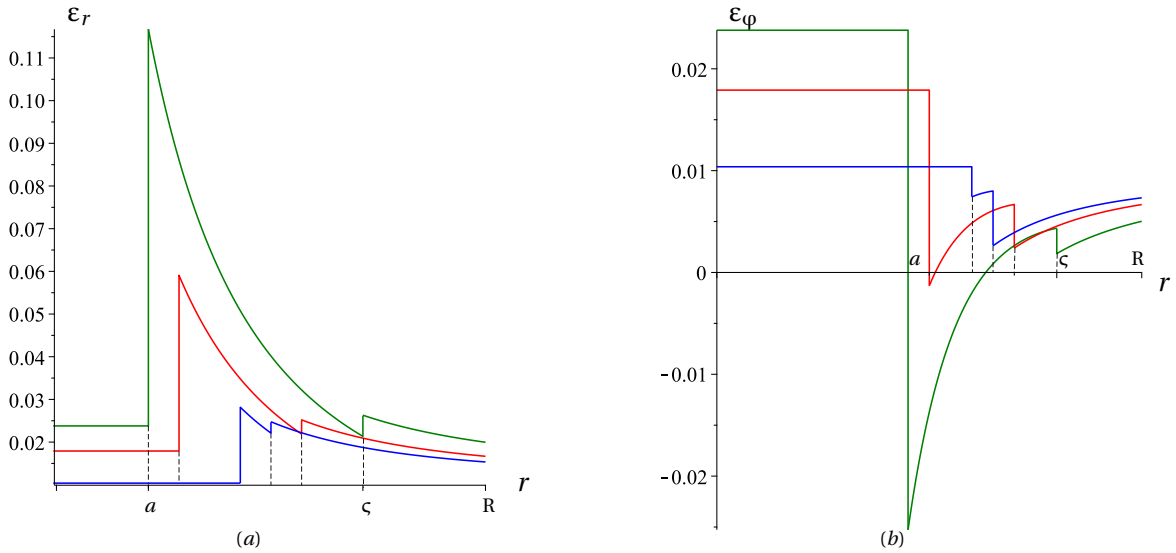

Figure 4.37: Spherical reaction front: Evolution of the radial ε_r and tangential ε_φ strains: different colors correspond to the different positions of the reaction and plastic fronts.

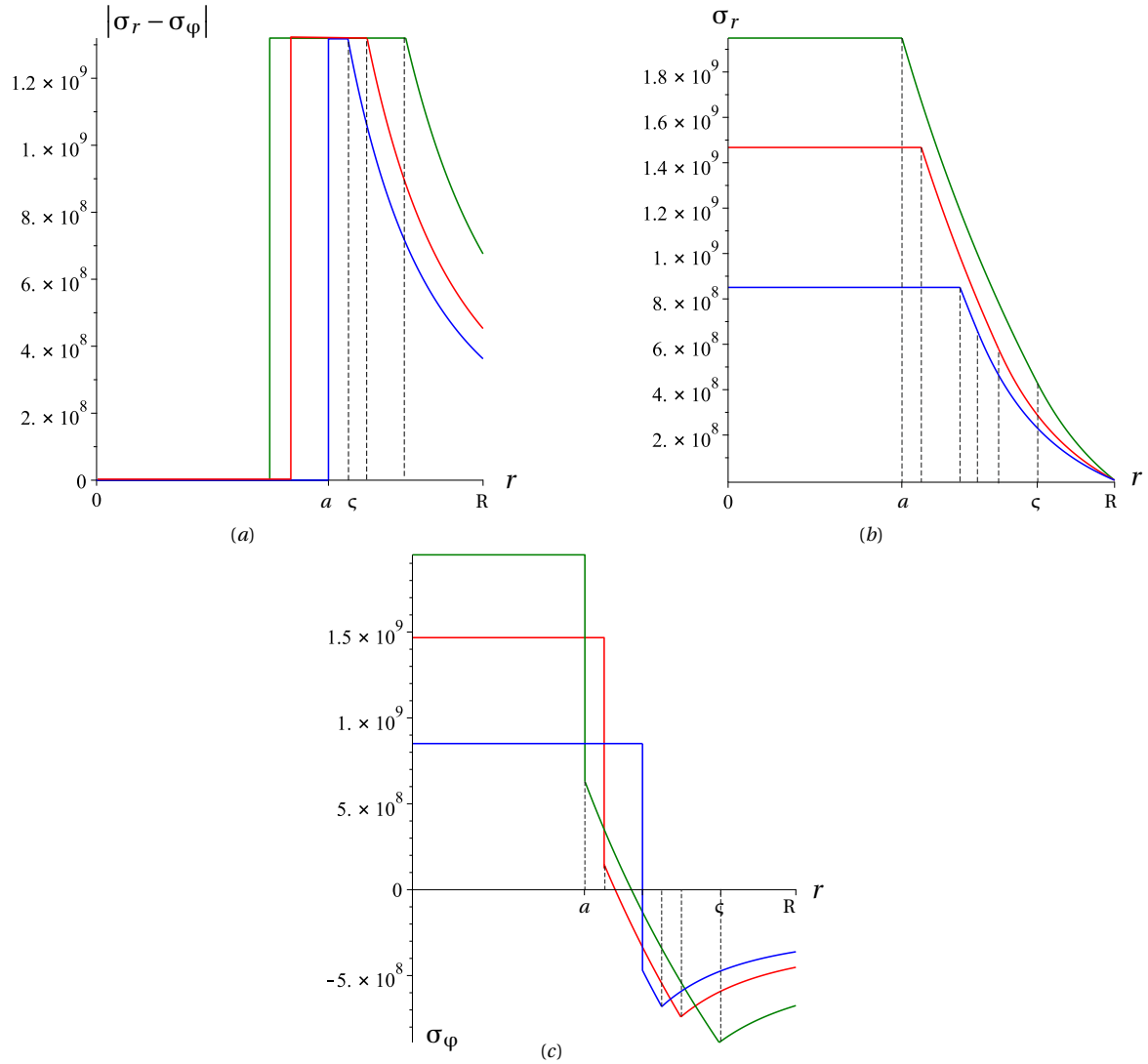

Figure 4.38: Spherical reaction front: profile of the second deviatoric stress invariant(a), the radial stress (b) and the tangential stress (c) at different positions of the reaction and plastic fronts.

4.4 Conclusions

In this Chapter the stress-assisted chemical reaction front propagation in deformable solid in the cases of a planar, spherical and cylindrical reaction fronts for the elastoplastic reaction product has been considered. Theoretical analysis is conducted for the case of elastic-perfectly plastic transformed material. The reaction kinetics is studied. The different mechanism of the chemical reaction front propagation in comparison with the cases of elastic and viscoelastic reaction product is studied. The importance of the type of the boundary condition for the initiation of the plastic deformation in the material is studied. It is discussed that even due to only chemical reaction, the yield stress can be achieved and the plastification of the material take place. It is shown that in the case of the planar front propagation, the choice of the boundary condition leads to the two different situation for elasto-plastic stage (if it appears). The elastoplastic solution follows the elastic solution (see Chapter 2) until the thickness of the transformed layer and/or the external loading become high enough for plastic flow to occur. It is shown that for the case of given deformations, when the yield stress is reached, the elastic transformed material becomes fully plastic, while for the given stresses, the plastic front appears. Also the plastic front appears for the spherical and cylindrical reaction front propagation in the elasto-plastic regime. Two fronts have their own velocities and directions. We showed that the plastic zone expands in two directions. We determined the relation between the reaction front and plastic front. It is shown that yielding of the material accelerates the reaction.

To our knowledge, this precise analysis of chemical fronts simultaneously with the plastic zones evolution consists in new original results in mechanochemistry.

Chapter 5

Experiments and Comparisons

Contents

This chapter concerns experimental works on the oxidation of pure nickel specimens and two different types of comparisons.

The first part of this chapter is devoted to the high-temperature oxidation experiments of pure nickel specimens in order to:

– validate some of the assumptions and precise some limits of the presented models;

– complete existing data and extract new data in order to compare with the different proposed models;

– determine oxidation kinetics.

In the second part two types of comparisons are made:

– experimental data with the different rheological models proposed in the previous chapters;

– models between each others, in order to show the influence of solids geometry, mechanical properties and constitutive law on the reaction front propagation.

5.1 Experiments: Oxidation of Nickel Balls and Wires

This section concerns high-temperature oxidation experiments of nickel. Two different types of specimen shapes were investigated: spheres and cylinders. These geometries are chosen in order to compare to the spherical and cylindrical geometry of the chosen models (see previous chapters). Specimens were produced from high purity nickel. Oxidation was conducted in the air under 800°C during different time.

This section describes the nickel oxidation studied and the different techniques used to analyze their morphological and crystallography during the oxidation process and heat treatment.

We will start by describing the different types of Nickel specimens used to carry out this work. To be able to analyse the experimental results, we will describe the samples preparations of the specimens, different characterization techniques used. In a second part, we provide a set of experimental data and observations for the oxidation of pure nickel withing large duration range (100h-500h). The evolution of oxide thickness in time is measured and presented. Characterization of the morphology and microstructure of NiO scales is presented.

5.1.1 State of the art

In this chapter we will not be completely exhaustive on all possible paper on nickel oxidation kinetics, we just choose some representative works. The oxidation of pure nickel is considered in this study as one the example of high-temperature oxidation of pure metals and in order to compare with theoretical assumption.

Nickel is one of the base metals in superalloys, and it is widely used in engineering applications. Ni-base alloys have big attention for high-temperature use due to their good mechanical properties, resistance to corrosion at high-temperature application and to fatigue crack initiation and growth during cyclic loading [36]. However, NiO usually does not provide such corrosion resistance [75], but it shows good mechanical, thermal, optical electrical and magnetic properties. The important examples, where detailed modeling of nickel oxidation kinetics is crucial, are: the high-performance solar absorbing coatings [1, 62], the solid oxide fuel cells [45, 55, 84, 113, 133, 158], ceramic matrix composites [101, 102]. The detailed review on nickel oxide application is done in [24].

However, the main studies of nickel oxidation were concerned to the experimental works (i.e., [133, 158]) and the mechanism of oxidation is not well investigated.

For the oxidation of metals there are few basic diffusion-dependent models. The first one and the earliest is the Tammann and Pilling and Bedworth parabolic law [114, 139]. This model is based on the assumption that the oxide thickness is proportional to square root of the time at a given time of the oxidation process, what was observed from the experiments. This model also assumes that the concentrations in the interface and in the outer surface are independent of the oxide thickness. In the case of thin films, the reaction velocity decreases with increasing of the

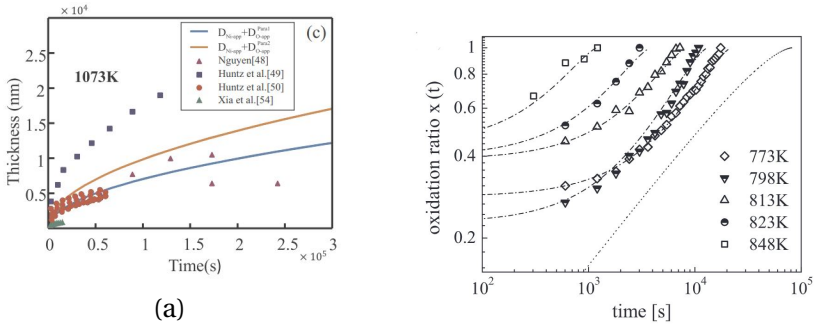

Figure 5.1: Oxidation kinetics: some examples from literature (a) from [149] and (b) from [45]

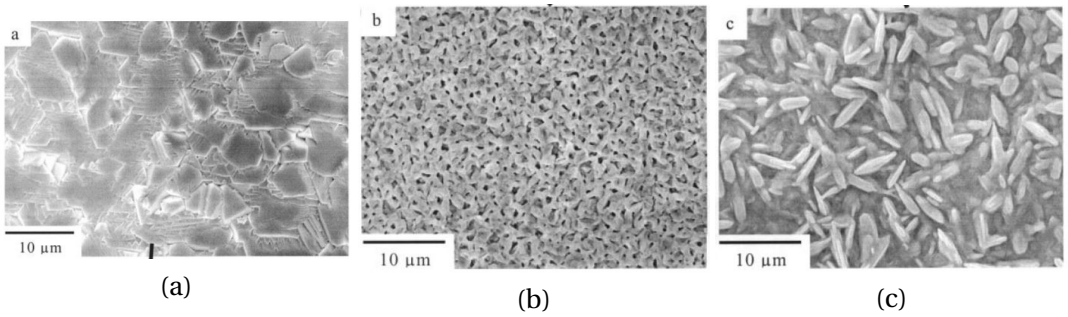

Figure 5.2: NiO surface morphologies [111]: faceted grains (a), cellular (b), and platelets (c).

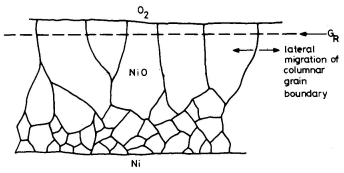

Figure 5.3: Schematical diagram NiO scale grain structure from [5].

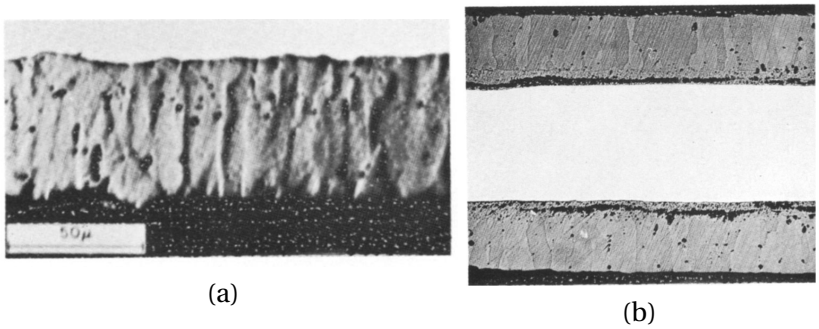

Figure 5.4: Morphology of (a) simplex compact and (b) duplex scales formed during nickel oxidation [35].

oxide thickness in agreement with logarithmic rate. The first model for logarithmic kinetics was proposed by Tammann and Koster [140], motivation for such choice was to fit the experimental results. To explain the growth of moderately thin flat films on the metal surfaces, Cabrera and Mott [16] suggested the model where the oxidation is limited by field-facilitated activated jumps

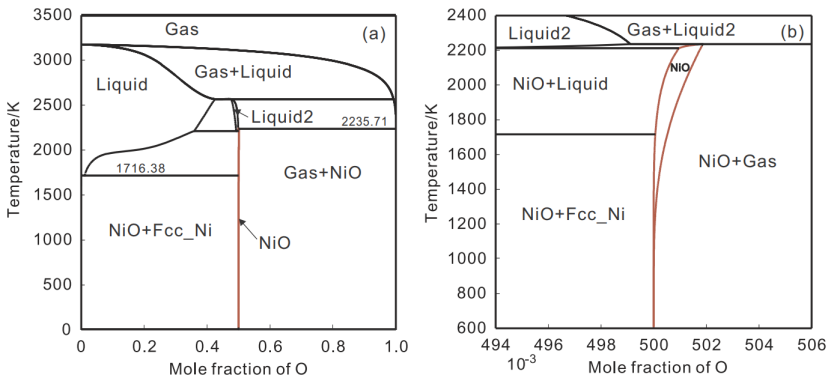

Figure 5.5: Phase diagram of binary Ni-O system [149].

of metal ions at the metal-oxide interface. The reaction kinetics in this case follow an inverse logarithmic law. Another commonly used model for thick oxide films was proposed by Wagner [146–148]. This model is based on the assumption that metal oxidation proceeds mainly via diffusion of charged particles. Wagner's theory is based essentially on the linear diffusion equation for charged particles. Wagner assumed that a neutral oxide evolves during growth. This requires that the number of equivalents of positively charged cations moving through the oxide in unit time has to be equal to the number of equivalents of negatively charged anions and electrons moving through the film in unit time. This assumption can be used to eliminate the electric field from the three transport equations for the three species. Now, These models are widely use and extended to another geometry, to more general case etc (see i.e. [33, 110, 150, 160]).

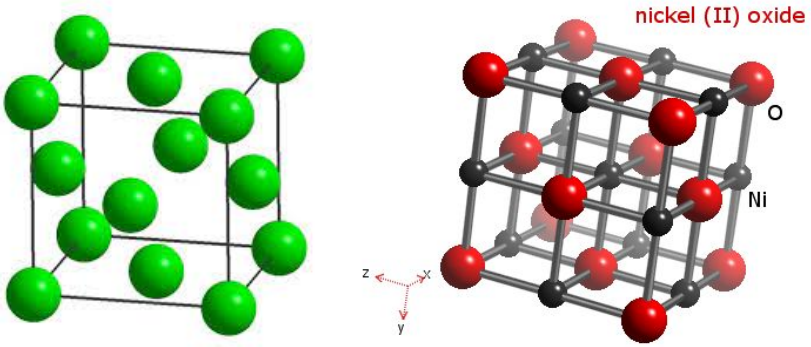

(a) (b)

Figure 5.6: Cubic crystal structure for: (a) Ni and (b) NiO

The kinetic of nickel oxidation were studied theoretically and numerically in [45, 49, 62, 82, 101, 102, 110, 123, 149] (see some examples in Fig. 5.1). In most of the works big attention was given to calculate the parabolic rate constant, and the oxidation of nickel was described by the parabolic law (Fig. 5.1a). In [45] the non-linear oxidation of Ni particle is studied (Fig. 5.1). In [113] the viscoelastic behavior of the nickel oxide was considered and pseudoplasticity of NiO is discussed. The residual stresses and plastic deformations, which appear during nickel oxidation, are studied in [35, 36, 94, 112].

Many parameters such as metal purity, surface preparation and orientation are known to significantly effect the growth kinetics, the external morphology and the internal microstructure of theses scales. The experimental studies of oxide scales shows three different surface morpholigies [5, 36, 82, 111]: faceted grains, platelets and cellular (see Fig. 5.2). The faceted grains are mostly found for oxidation at the temperature higher than 900°C. Such structure is characterized by the large and compact scales. Cellular morphology observed was noticed for oxidation at $450-800$°C.

They are always thicker than the faceted ones. The specimen's surface in this case is characterized by a large open porosity. The platelets oxide scales were detected for oxidation at 600 – 900°C. They have disc shape, and were observed only on top of either cellular or faceted oxide scales. Three different microstructures of nickel oxide were obtained in [5, 35, 36, 49, 82, 94, 111]: simplex compact, duplex and simplex porous (see one of the first results in Fig. 5.4). The simplex compact is presented as single compact layer, it was observed for the experiments of the oxidation of nickel at temperature higher than 900°C. At lower temperature the simplex porous was obtained. It is characterized by the large open porosity on the top of oxide layer and high density of smaller pores at the reaction interface. For the oxidation at temperature range of 600 – 800°C, the oxide layer has duplex microstructure [5, 35, 82, 111]. It consist of two layers: porous and fine-grain inner layer and cellular or more compact columnar outer one. One of the first representation of duplex structure was obtained in [5, 35], and it is shown in Fig. 5.3.

From the phase diagram of Ni-O system [149] (see Fig. 5.5), it can be noted that for the temperature below 1250 K the composition of nickel oxide is 50% of Ni and 50% of O. Above this temperature there is an excess of oxygen inside of NiO. Pure nickel has FCC structure with interplanar space equal to 0.352nm (Fig. 5.6a). In Fig. 5.6b it is shown, that NiO structure is FCC with every octaedric sides occupied by an atom of oxygen with interplanar space equal to 0.4177nm.

5.1.2 Microstructural characterization by electron microscope

In this parts, we will describe the equipment and techniques we used for the characterization of our specimens :

– Scanning Electron Microscopy (SEM - QUANTA 650 - *FEI*) to characterize the morphology of the oxide layer and to reveal interface between the NiO and Ni,

– Energy-dispersive X-ray spectroscopy (EDXS - X-ACT 10mm² - *Oxford Instrument*) for the chemical composition,

– Electron backscatter diffraction (EBSD - SYMMETRY - *Oxford Instrument*) techniques in SEM to characterize the crystallographic orientation of the grains.

5.1.2.1 SEM for morphological study

Scanning electon microscopy SEM is a device that use the interaction between electron (produce by the SEM) and the specimen material.

SEM is mosly use with two different electrons detectors.

Everhart and Thornley detector (ETD) that collect the secondary electrons (SE). These electrons are produced by an inelastic interaction and give some contrasts linked with the topography of the specimen.

Backscattered electron detector (BSED) that will collect Backscatterd electrons (BSE). These electrons are produced by an elastic interaction between the electrons from the SEM beam and the atoms present in the specimen. The atoms with high atomic number Z have higher probability to interact. This result as pictures with contrasts linked to the chemistry of the specimen. Under some specific beam conditions, it's also possible to have qualitative contrasts linked to the cristallography.

5.1.2.2 Chemical analyzes in Energy-Dispersive X-ray Spectroscopy (EDXS)

Energy Dispersive X-Ray Spectroscopy (EDS or EDXS) is a microanalysis technique that is used in combination with SEM to obtain the chemical composition of the specimens.

The beam of SEM locally interacts with atoms, exciting their electrons. Hence the electrons jumps from the inner shell to the outer ones, or even can be ejected, creating some holes. When an electron come back to its stable state, it emits an X-ray photon, which has an energy characteristic of the atom. These X-ray photons are capt and analysed by the EDS detector. The 'Maps' of elements distribution, that are presented bellow are acquired by combining SEM scan with EDS. The software used for EDXS acquisition and data post-processing is AZtec (*Oxford instruments*).

Table 5.1: Name of the wire specimens and time oxidation

Specimen	W1	W2	W3	W4	W5
Oxidation time, [h]	100	200	300	400	500

5.1.2.3 Crystallographic analysis

Electron Backscatter Diffraction (EBSD) is the technique used in SEM to acquire the local crystallographic information. We can construct maps that describe the structure of the specimen by combining SEM scanning with EBSD data. This technique uses the diffraction properties of the electrons ,when they interact with periodic structure, such as crystals. Electron, that satisfy the Bragg's condition, is diffracted in cone starting from interaction point. The intersection of these cones and EBSD camera form Kikuchi patterns characteristic of the material and crystal orientation. These patterns are compared with theoretical ones for the material by using software, in order to determine the crystallographic orientation. The software used for the acquisition of the EBSD is Aztec (*Oxford instruments*) and the post-processing of maps have been performed using HKL Channel 5 (*Oxford instruments*)

5.1.3 Wires

In this section we focus on the experiments high-temperature oxidation on pure Ni wires. The wires were oxidized in the air at 800°C for 5 different duration in order to obtain the evolution of the oxide growth with time. The studies of the surface morphology, the internal structure and the growth of the oxide thickness are presented.

5.1.3.1 Experimental procedure and specimen preparation

This experiment is performed for 5 different wires. The specimens have approximately 1 mm diameter and 10 cm length (see Fig 5.7). This length was chosen to be able to measure the mass gain. Before the high-temperature oxidation, the specimens were ultrasonically cleaned: first in acetone and then ethanol, and dried. EDXS analysis was performed in order to check the contamination of the samples before the oxidation.

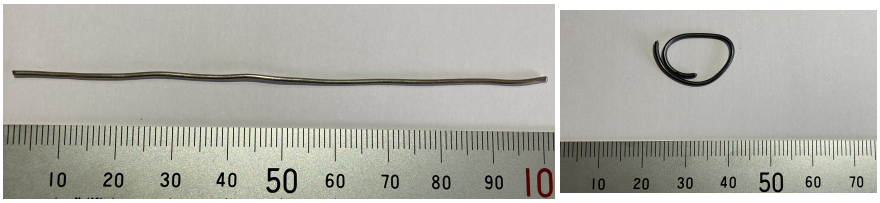

(a) (b)

Figure 5.7: Photos of the wires: (a) before oxidation and (b) after oxidation

Each wire was oxidized during different time (see Table 5.1). This part of the experiment was performed at Onera Chatillon. Wires were oxidized in laboratory air at 800°C for 100, 200, 300, 400 and 500 hours in "Pyrox" furnace. The initial mass and mass gain for every 100h of each sample are presented in Table 5.2. To characterize the morphology and microstructure of the oxide, several steps were required. First, the morphology of the oxide scales was observed in SEM. More details concerning the surface morphology will be presented in the result part (see 5.3.2). Before further observation, the specimens were set in epoxy resin in order to study their cross-sections. Therefore, the samples were cut and their surfaces were manually polished. The protocol consisted of mechanical polishing to a "mirror" finish, down to 4000-grade SiC-paper, followed by

Table 5.2: Change of mass of wires during the oxidation

	Time	W1	W2	W3	W4	W5
	initial	1.07503	1.07581	1.07192	1.0765	1.0722
	100h	1.08434	1.08509	1.0815	1.08589	1.08198
Mass, [g]	**200h**		1.08967	1.08623	1.09065	1.08676
	300h			1.09041	1.09501	1.09098
	400h				1.0987	1.09462
	500h					1.20496

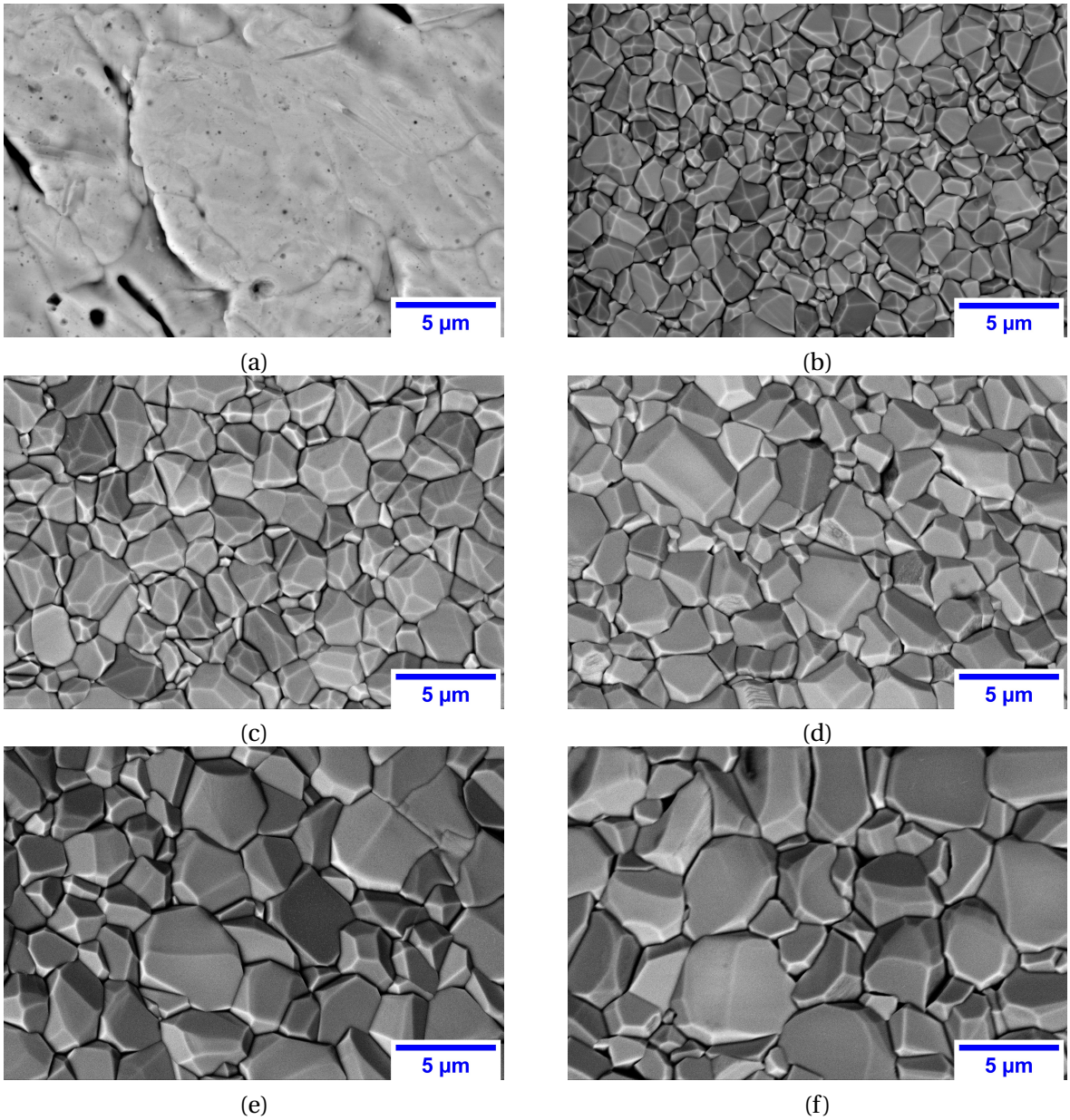

Figure 5.8: BSE pictures of NiO surface morphology as a function of oxidation duration: (a) before oxidation, and after (b) 100h, (c) 200h, (d) 300h, (e) 400h, (f)500h.

polishing with 3 µm and 1 µm diamond paste and finishing polishing with OP-AA (Active Oxide Alumina Polishing Suspension, *Struers*) in vibratory polishing machine VibroMet 2, *Buehler* dur-

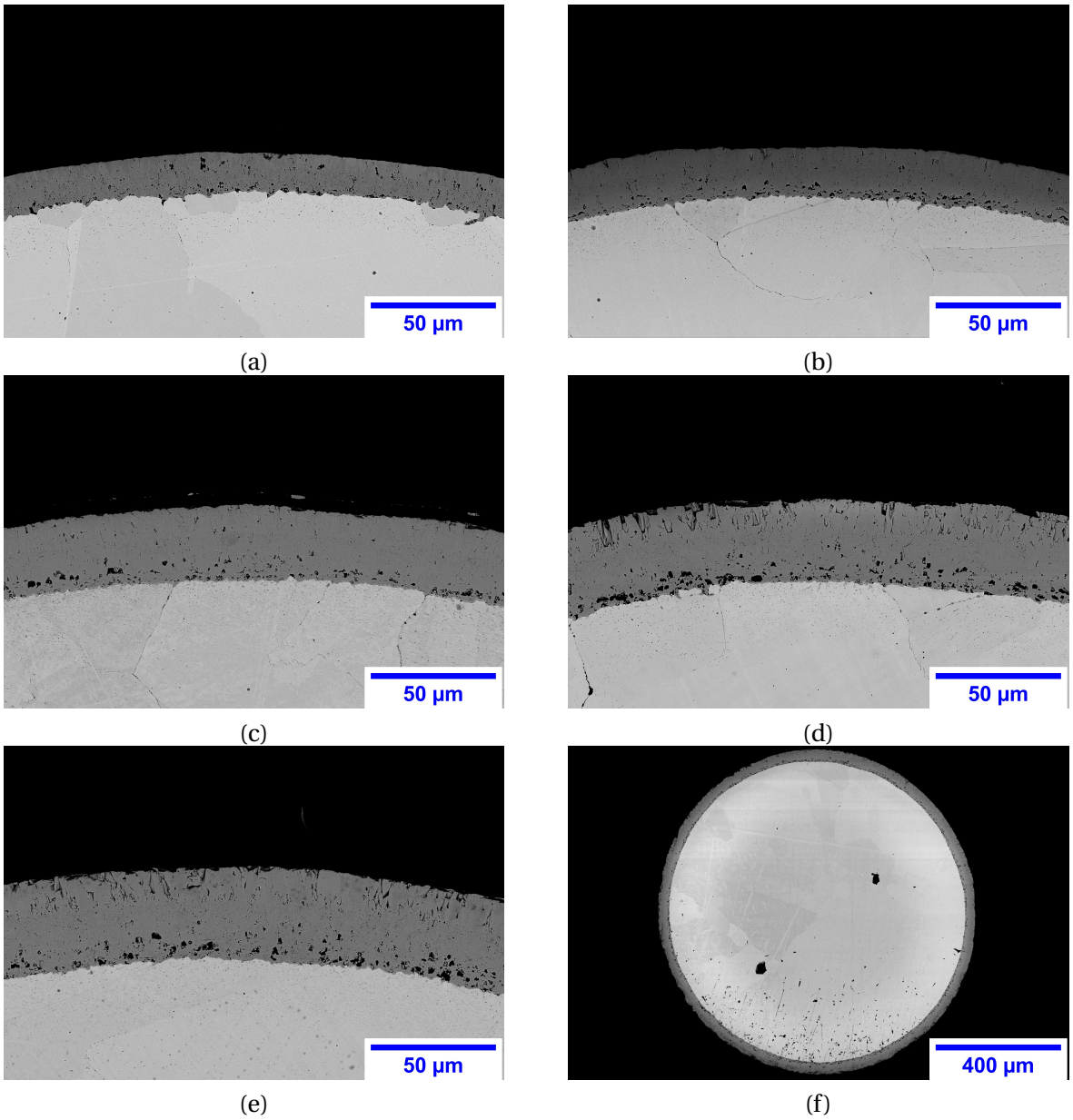

Figure 5.9: BSE images of NiO thickness as a function of oxidation duration: (a) 100h (b) 200h, (c) 300h, (d) 400h, (e) and (f) 500h.

ing 40 min. In addition, for the specimen 'W-4' the preparation using cross-section Ion-polishing in PECS II *Gatan* has been performed at 8keV during 13h. Such preparation was made in order to avoid hardening effect link to the mechanical polishing and to obtain the microstructure of oxide layer by EBSD.

Note, that polishing of such specimens is a difficult step, due to the differences in material characteristics between two materials (Ni and NiO). Moreover, mention that our experimental work was carried out in order to validate the analytical model of Ni oxidation but not the oxide formation itself.

5.1.3.2 Results

First, we made EDXS analysis of the specimen surface to be sure that no other elements are present apart from Ni. Therefore, the oxide surface morphology was investigated by scanning electron microscopy. The scales morphology evolution in time is illustrated in Fig. 5.8. Within the investigated ranges of oxidation time (100h-500h), SEM examinations of oxide exhibited the faceted grains only,

Table 5.3: Oxide thickness measurements for Ni wires. Experimental data

Time, [h]	0h	100h	200h	300h	400h	500h
Oxide thickness, [μm]	0	14.9451	22.7125	28.9574	32.6975	37.8676

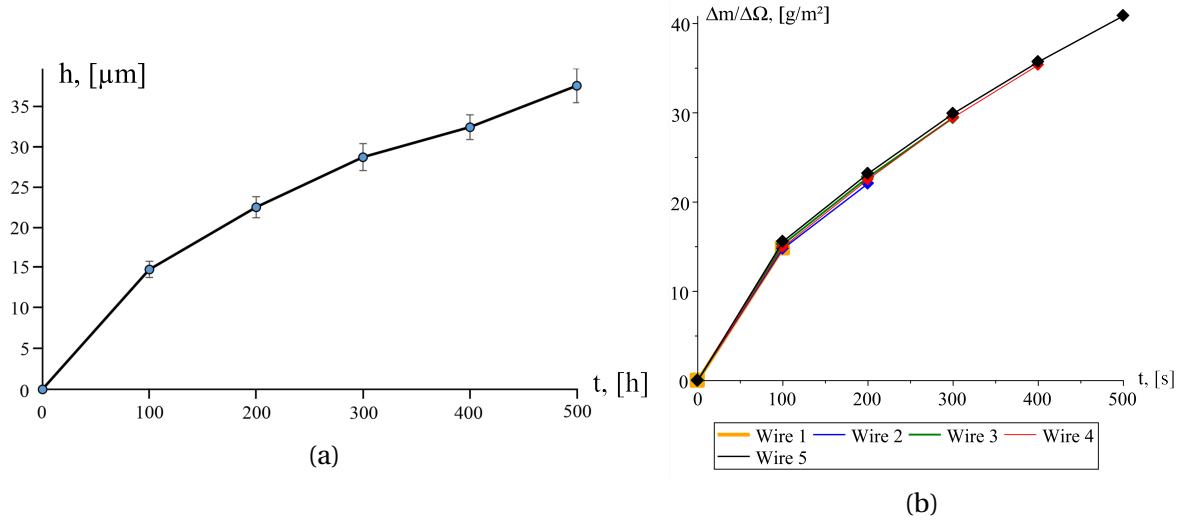

Figure 5.10: (a) Growth of oxide layer in time, based on the experimental data from Fig. 5.9 and Table 5.3, (b) evolution of weight gain per unit area in time

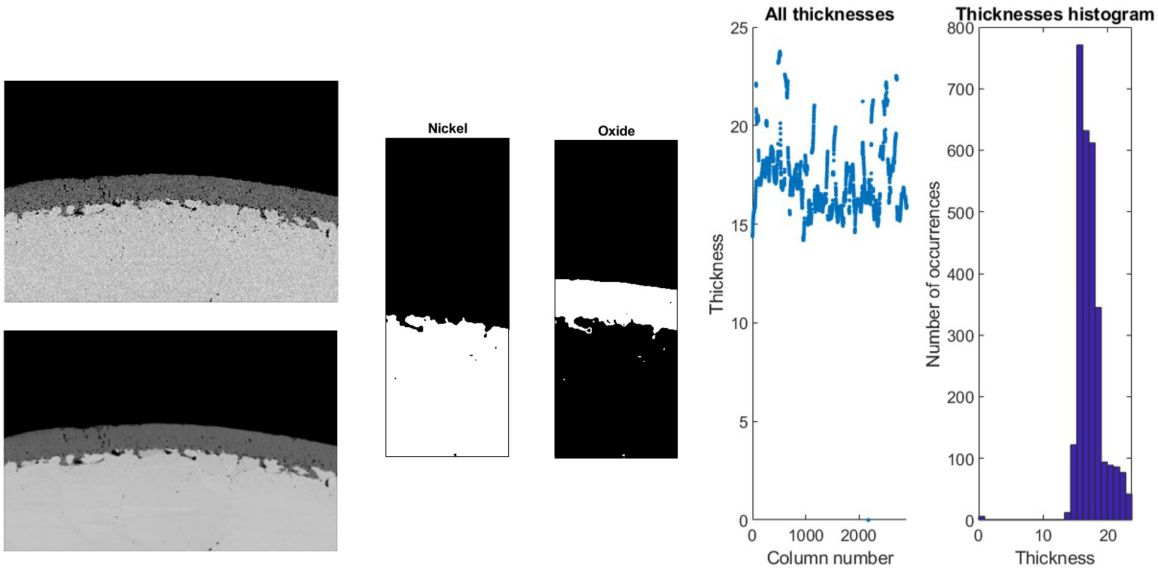

Figure 5.11: Matlab script results

we do not have neither cellular no platelets morphology or growing oxide scales[111]. The size of oxide grains increases with test duration.

The cross-section were prepared for SEM observation in order to assess the thickness and sub-surface morphology of the oxide layer. Fig. 5.9 shows a typical cross-section through the oxide and its evolution in time. The differences in contrast correspond to different chemical composition. On Fig. 5.9f, is presented full cross-section of the specimen, that was oxidized during 500 hours. As we have the roughness of the external oxide surface and reaction interface, a Matlab script (see a *'Note...'* below) was developed in order to make more precise measurements and get statistical data of the oxide thickness. This script is based on postprocessing of images. The mean value

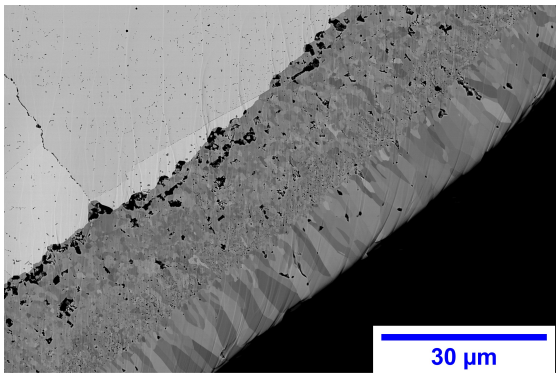

Figure 5.12: BSE image: internal microstructure of NiO (after 400h oxidation)

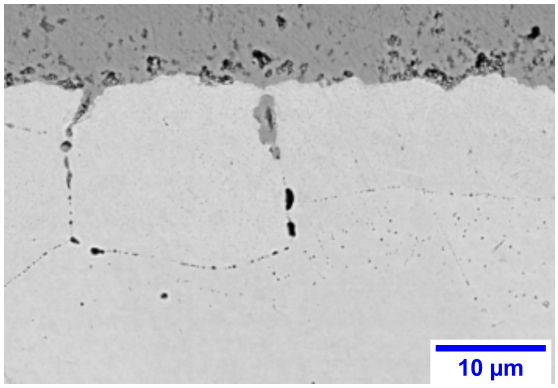

(a)

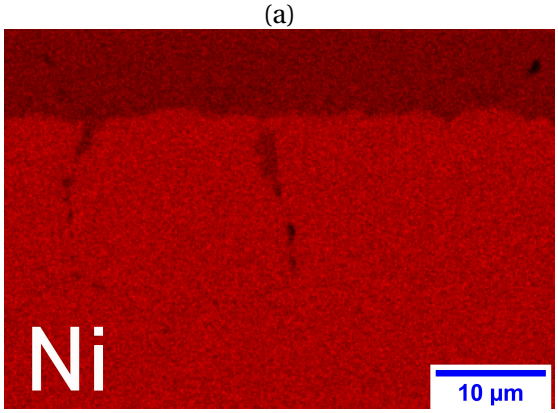

(b)

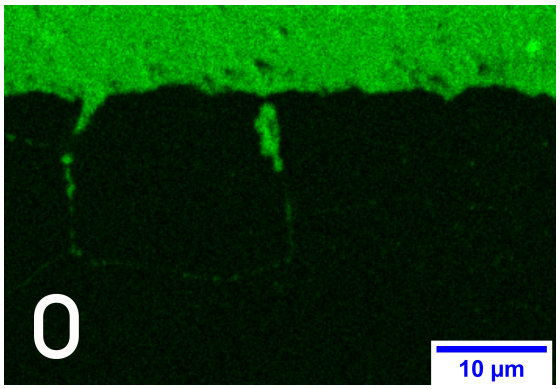

(c)

Figure 5.13: SEM Backscattered electron image (a) and EDXS element map (for the specimen oxidized during 100h)

was chosen as the current thickness and the standard deviation was obtained in order to calculate an error estimate. The resultant measurements for oxide growth are shown in Table 5.3 and in Fig. 5.10a. The weight per unit are in time, based on the results from Table 5.2 is shown on Fig. 5.10b.

Note on a Matlab script for oxide measurements

There are two reasons why we needed to write this code: discontinuities at the reaction front (we wanted to obtain the more accurate data) and a circular cross-section of the specimens (no possible to use existing software).

First of all, note that the oxide layer is not uniform. Therefore, the image needs be edited before the following steps: we make the gaussian filtering of image. Since the cross-sections of the samples are circular, the next step is to decompose the image of it into a finite number of small sub-images,

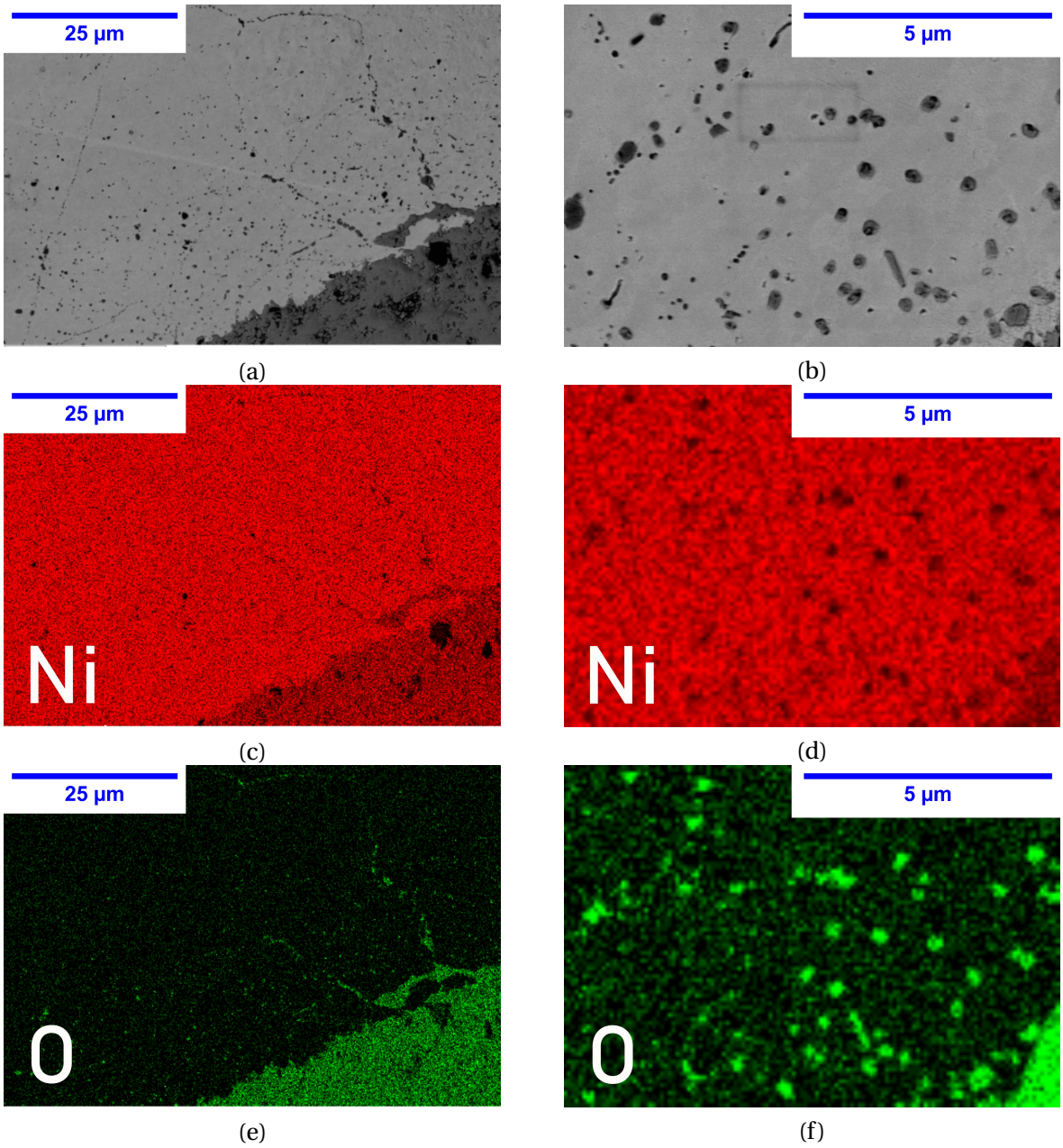

Figure 5.14: Local BSE image (a) and (b) and EDXS element map (b), (c), (e) and (f) (for the specimen oxidized during 400h).

so that in each sub-image the curvature of the cross-section is small and hence the reaction front can be approximated locally a linear. Then we rotate the image to make the reaction front horizontally on it: for this we draw a line along the interface between two materials, and the program identifies the required angle from the line positions and rotate the image. Since the image is greyscale, we use a gray threshold to determine the oxide (also the pixels dilation is used for it). The last step is to draw a line along which all columns should be measured. Therefore, different thickness are automatically estimated (see Fig. 5.11). The evolution of oxide thickness and standard deviation are obtained from this analysis.

On Fig. 5.12 is shown the BSE picture of internal microstructure for nickel oxide. This image was made for the specimen W4, that was oxidized during 400h. Such good contrast in oxide layer was possible to obtain after Ion Polishing during 13h. Such way of specimen's preparation gave the possibility to have the diffraction in oxide layer and to obtain further the EBSD map. On Fig. 5.12

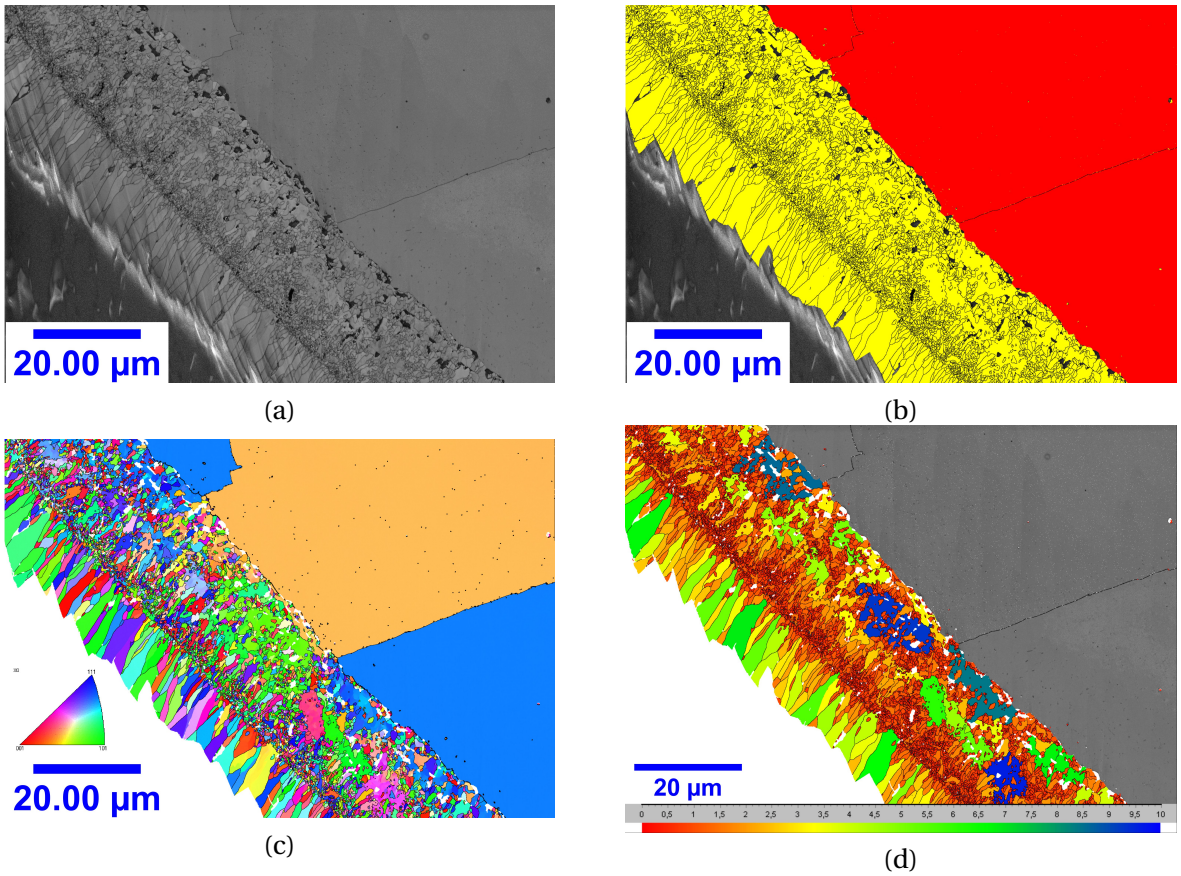

Figure 5.15: EBSD Map of nickel oxide and nickel after 400h: (a) Band contrast, (b) Phases, (c) IPFX and (d) grain size.

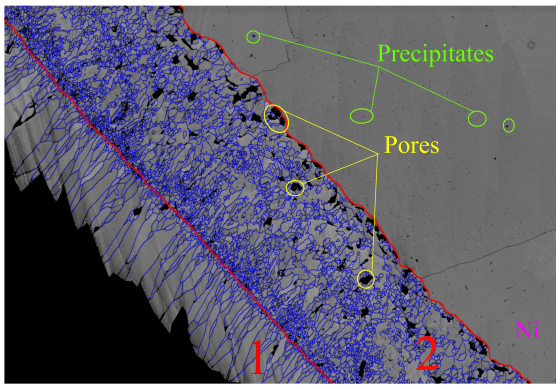

Figure 5.16: EBSD band contrast map. 1 – the outer nickel oxide layer, 2 – the inner oxide layer, blue color corresponds to grain boundaries.

we see that NiO has duplex microstructure: the compact columnar outer layer and porous and fine-grains inner layer. The interface between these two layer corresponds the initial wire surface before the oxidation.

A qualitative map of the chemical composition of the specimen's cross-section was performed via EDXS analysis on an Oxford Instruments. A energy dispersive spectrometric analysis showed that its composition corresponds to nickel and nickel oxide, respectively, no other elements were found apart from Ni and O. Fig. 5.13 shows as SEM picture of examined cross-section and element maps for Ni and O for the specimen oxidized 100h. We see that oxygen diffusion rate increase along grain boundaries. This acquisition have been performed with an acceleration voltage of 15 keV and a beam current of 2.4 nA.

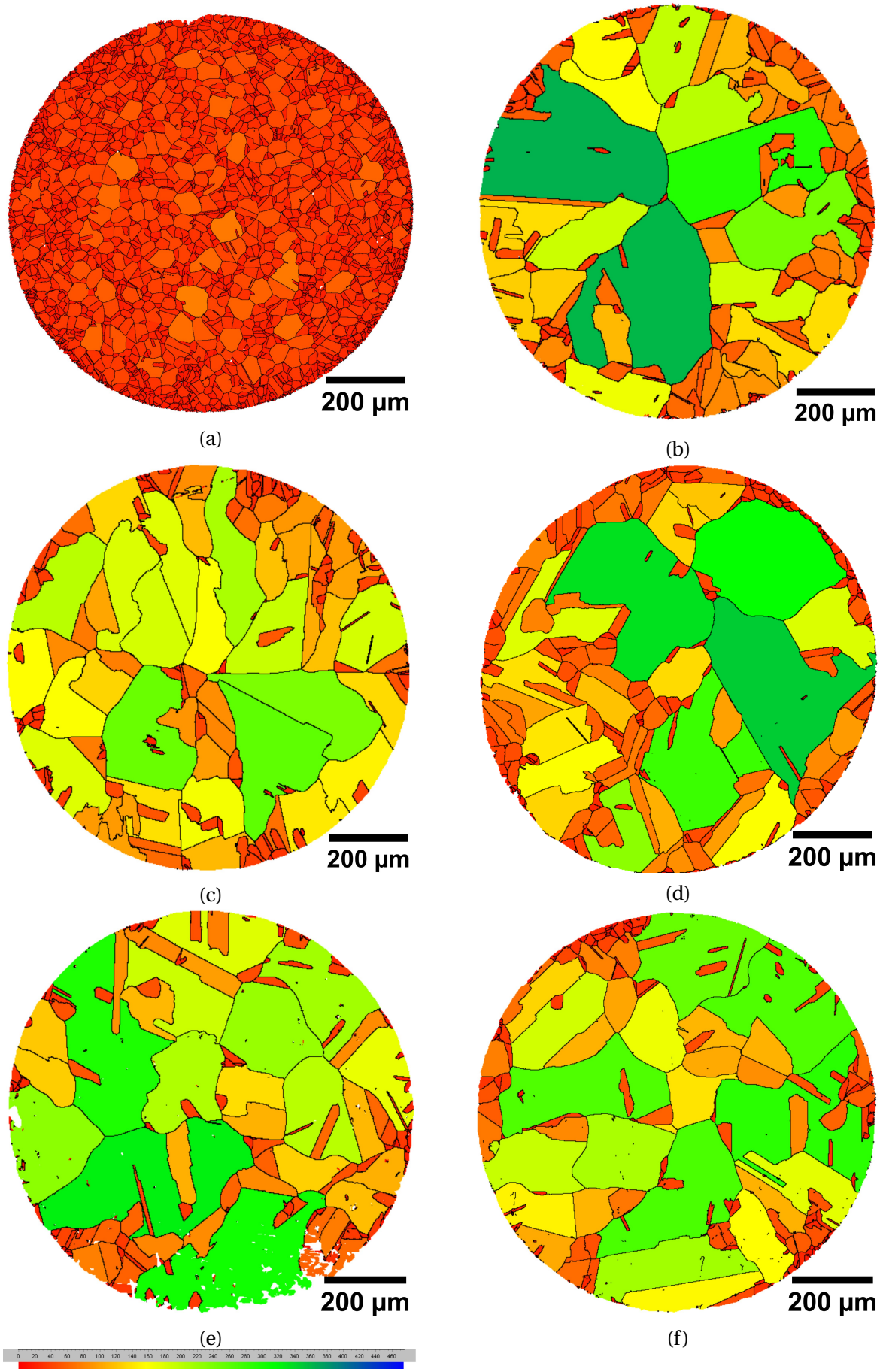

Figure 5.17: EBSD Map of Nickel wires during oxidation: (a) 0h, (b) 100h, (c) 200h, (d) 300h, (e) 400h and (f) 500h.

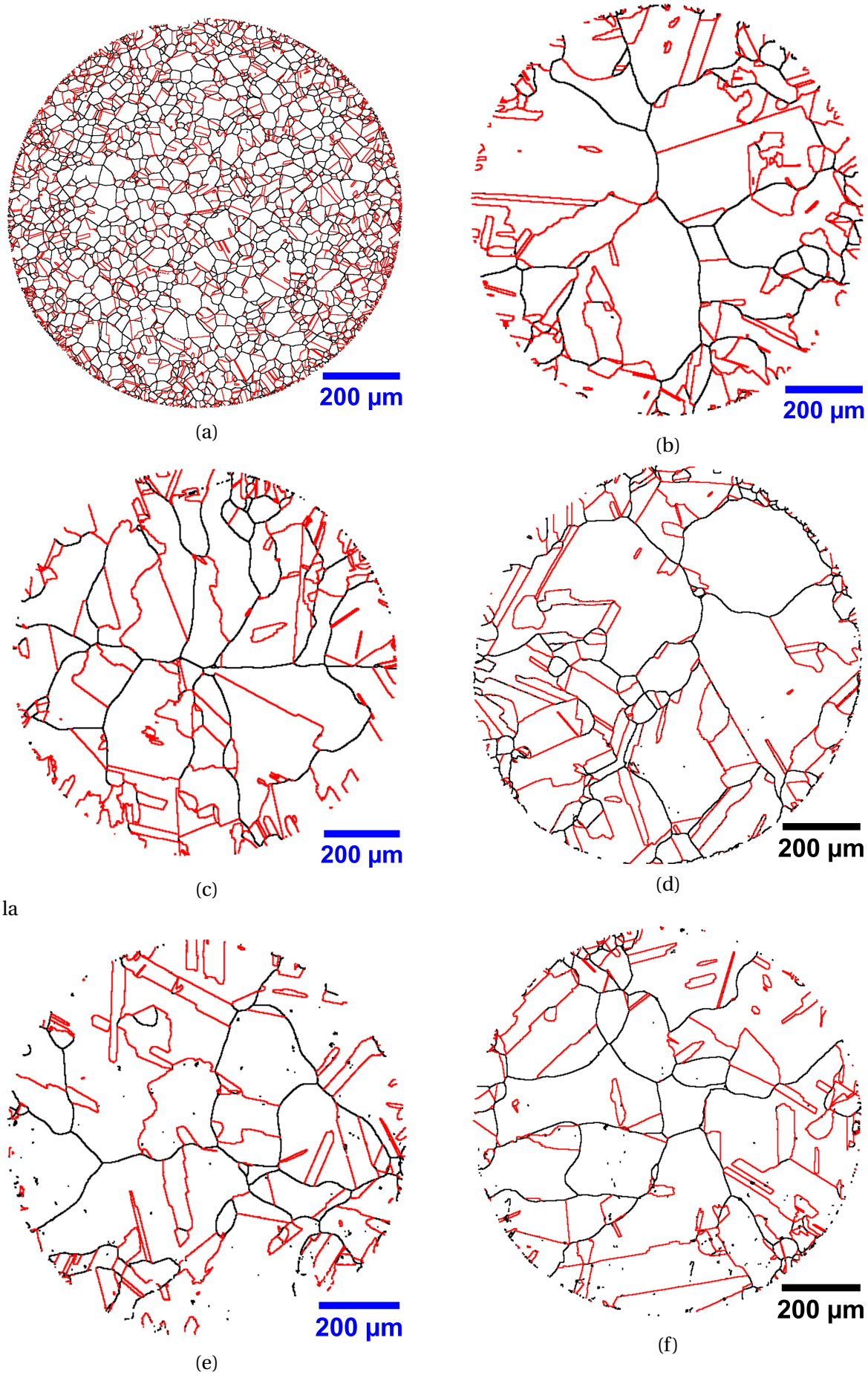

la

Figure 5.18: EBSD grain boundary maps showing grain boundaries with a misorientation higher than 10° in black and twin boundaries in red: (a) 0h, (b) 100h, (c) 200h, (d) 300h, (e) 400h and (f) 500h.

Table 5.4: Thickness measurements of the compact columnar outer layer of NiO for Ni wires. Experimental data

Time, [h]	0h	100h	200h	300h	400h	500h
Average oxide outer layer thickness, [μm]	0	7.2199	9.9102	13.2843	13.8001	16.4698
% of the total NiO layer thickness	0	44.9	43.6	45.9	42.2	43.0

On Fig. 5.14 are presented BSE pictures and EDXS elements maps for the wire oxidized during 400h. From BSE image 5.14a, we can see that there is some layer inside of Ni where plenty of aligned precipitates. The pic. 5.14b is the zoomed area of image 5.14a, for which a local accurate EDX analyse of long time acquisition was performed. The nickel precipitates measured by EDXS (see image5.14d,f) correspond to nickel oxide. We can see that oxygen diffuse inside of the material, and along the grain boundaries. These precipitates could be related to some preferential structure of the dislocation or to a plane for the oxygen diffusion. No specific features can be verified at least at SEM scale examinations. More detailed investigations of microstructure and oxide precipitation inside of Ni by TEM examination of scale cross-section would be required to confirm these observations.

Note, that we did not do any heat treatment before the test, so the microstructure is not stable between the initial state and the further ones. It should be pointed out, that the alignments don't seem to be linked to the wire initial microstructure. In order to verify the microstructure evolution under the heat treatment, EBSD maps have been performed on the 5 wires cross-sections. For these acquisitions, the acceleration voltage was 25 keV and the beam current was 5.6 nA. EBSD maps are presented on Fig. 5.17 and grain boundaries on Fig. 5.18. Grain boundaries were defined as minimum 10° misorientation. On EBSD map, that is presented on Fig. 5.17, we can see that the reference wire (non-oxidized) has the small grains. For every specimens after the heat treatment the grain size is much larger than for non-oxidized one. After 100h the structure is practically stabilized, and grain size (qualitatively) does not change significantly. Note that is was not possible to make statistical analysis of grain sizes for the wire because of the small amount of grains and the presence of many scratch on some specimens.

EBSD map for oxide layer is presented on Fig. 5.15. On images 5.15a,b we can see the micrsostructure of oxide layer. For this acquisition, we have adapted the beam conditions in order to improve the spatial resolution of the EBSD. The acceleration voltage was 15 keV and the beam current was 2.4 nA. The difference between inner and outer oxide layer is very clear. The inner layer has plenty of fine grains that become smaller and smaller (see Fig. 5.16 and Fig. 5.15d) as the distance between the NiO and the Ni increase. In Fig. 5.16 (denoted by number 1) it is also clearly visible that the grains from the outer layer have an epitaxial growth with a columnar shape. Porosities in the inner oxide layer could be the consequences of the diffusion of nickel thought the oxide layer in order to form the outer layer. Note, that the small NiO grains which are close the to reaction interface, have the same orientation as grains of Ni in image. 5.15c. The map presented in Fig. 5.15b present the phase map. It make easier to localize the interface between the oxide layer and the nickel grains. Note that it was possible to index the diffraction patterns of some precipitates. They correspond to NiO and confirm the EDXS results presented before.

In order to precise the following qualitative results for kinetics of nickel oxidation and since it is parabolic (see Fig.5.10), we determine the parabolic rate constant k_p from the experimental results. Oxidation kinetics were taken by using the well-known formula for parabolic kinetics:

$$t = \mathrm{A} + \mathrm{B}\triangle m + \mathrm{C}\triangle m^2 \tag{5.1}$$

where $\triangle m$ is the mass gain per unit area. The parabolic constant k_p is defined as coefficient C in equation (5.1). The equation (5.1) can be applied to whole process of oxidation in order to calculate a global value of k_p, and may be applied to only to a small part of the process to determine the

local k_p (for given time, scale thickness). Based on the experimental data from Table. 5.2 for mass gain every 100h for every wire, and taking into account that length of wires is $10cm$ and radius is $1mm$, we obtain:

$$k_p \in [3.003543643 \cdot 10^{10}, 4.383968374 \cdot 10^{10}][g^2 \cdot m^{-4} \cdot s^{-1}] \tag{5.2}$$

From the experimental results for the internal microstructure of the oxide Fig.5.15, there are outer and internal layers of NiO. The nature of these two layers corresponds two different mechanism of the oxide growth. The inner layer growths due to the diffusion of the oxygen in nickel, while the outer layer expands as result of the nickel diffusion outward of the initial specimen surface. The outer layer has the compact columnar microstructure (see Fig. 5.14). We measure manually which part of the whole oxide layer is occupied by the outer one. We measured it manually in 10 points for each wire, therefore, data are not very accurate. The resultant measurements for each specimens are presented in Table 5.4. The outer oxide layer constitutes a substantially constant fraction of the total oxide thickness for each wire. Therefore, it gives the idea that the growth of the outer layer relates to the reaction front kinetics.

From these different results, it's possible to differentiate several oxidation mechanisms, each one having its own kinetics.

Based on the EDXS and EBSD observation, it must be emphasized that the diffusion along grain boundaries is clearly the fastest mechanism and allow the oxide formation much deeper than the main oxide layer. It's important to note that the diffusion rate along the twin boundaries is slower than for other ones.

As soon as the oxide formed on the surface of the sample, we can observe precipitation of nano-crystallites up to 30-40 µm inside the nickel. It was motioned, that from EDXS analyse, these precipitates correspond to NiO. The nucleation of these precipitate shows that the oxygen diffuse deeper than the reaction front. It seems that they are aligned, but we were not able to understand the reasons. Furthermore, the precipitates are also visibly deeper in the metal along the grain boundaries. It was impossible to deeply investigate the origin of these precipitates in nickel because of the limitation of SEM. TEM examination of cross-section as required area inside of nickel and close to oxide layer would be required to investigate and confirm these observations.

5.1.4 Balls

In the previous section we made the experiment on the wires, which were homogeneous. In this part we try to analyze more complex structure (see in Fig. 5.19), based on the obtained results for wires.

This section examines the oxidation of pure nickel balls. The oxidation was performed in the air at 800°C for 5 different duration in order to obtain the evolution of the oxide growth in time. Investigations of surface morphology, internal structure and growth of the oxide thickness are presented.

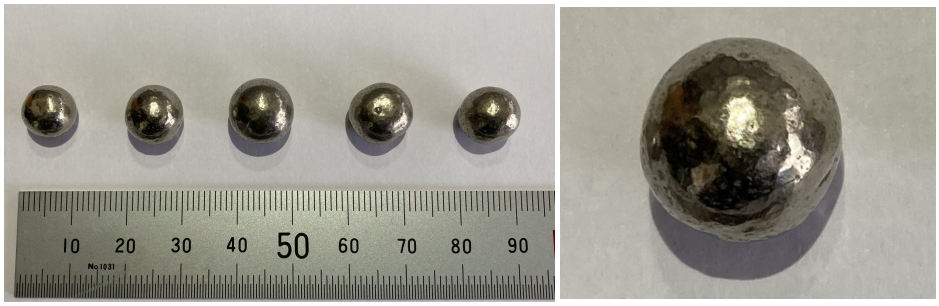

Figure 5.19: Photo of the balls before oxidation

Table 5.5: Name of the balls specimens, time oxidation and the average diameter after oxidation

Specimen	B1	B2	B3	B4	B5
Oxidation time, [h]	100	200	300	400	500
Average diameter after oxidation, [mm]	9.98	10.31	9.5	9.02	9.9

5.1.4.1 Experimental procedure and specimen preparation

This experiment is performed for 5 different balls. The specimens have approximately a spherical shape with surface defects (Fig. 5.19). The approximate diameter of balls is varying from $9mm$ to $10.3mm$ (see more details in Table 5.5). Such balls were manufactured by electroless deposition layer by layer Fig. 5.20 (with different thickness of each layer). This method of metal coating developing creates Ni nanospikes arrays [52, 105]. EDXS analysis was performed in order to check the contamination of the samples before the oxidation.

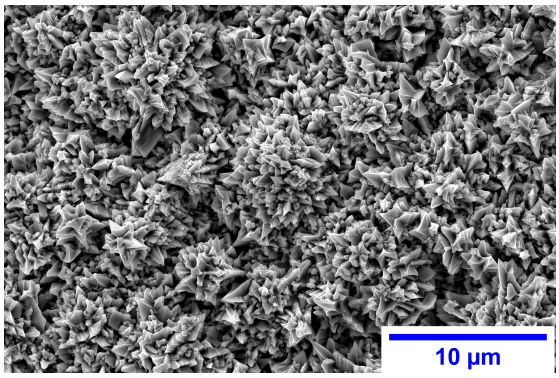

Figure 5.20: SE image of the nickel balls surface before the oxidation.

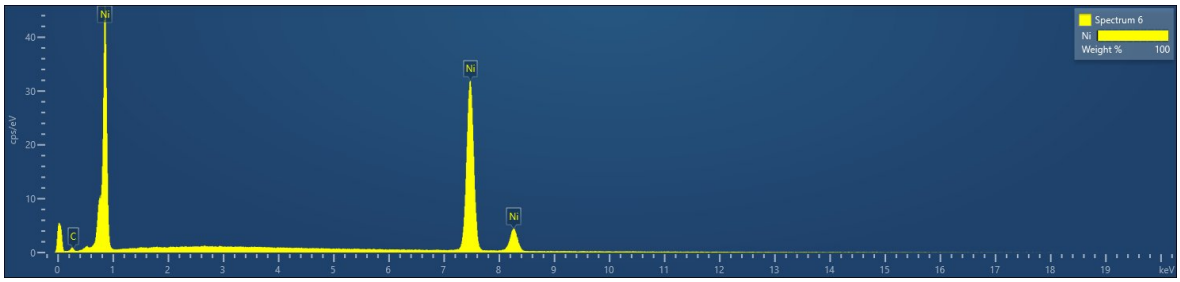

Figure 5.21: EDX spectrum shown the Ni was detected in samples

Each balls was oxidized during different time (see Table 5.5). This part of the experiment was also performed at Onera Chatillon. Balls were oxidized in laboratory air at 800°C for 100, 200, 300, 400 and 500 hours in "Pyrox" furnace. The balls mass was measured before oxidation and every 100 h for each specimen. The mass change measurements are presented in Table 5.6. Analogously as it was made for wires, to characterize the morphology and microstructure of the oxide, several steps were required. First, the morphology of the oxide scales was observed in SEM. More details for the surface morphology will be presented in the result part. Before further observation, the specimens were set in epoxy resin in order to study their cross-sections. Therefore, the samples were cut in the middle and their surfaces were manually polished. The protocol consisted of mechanical polishing to a "mirror" finish, down to 4000-grade SiC-paper, followed by polishing with 3 µm and 1 µm diamond paste and finishing polishing with OP-S(Colloidal silica suspension, *Struers*) in vibratory polishing machine VibroMet 2, *Buehler* during 45 min.

Table 5.6: Mass change of nickel balls during the oxidation

	Time	B1	B2	B3	B4	B5
Mass, [mg]	**initial**	3778.53	4541.46	3832.4	3199.43	4198.92
	100h	3781.37	4545.08	3836.17	3202.87	4202.21
	200h		4545.92	3837.01	3203.68	4203.87
	300h			3837.40	3203.92	4205.13
	400h				3204.16	4206.06
	500h					4206.50

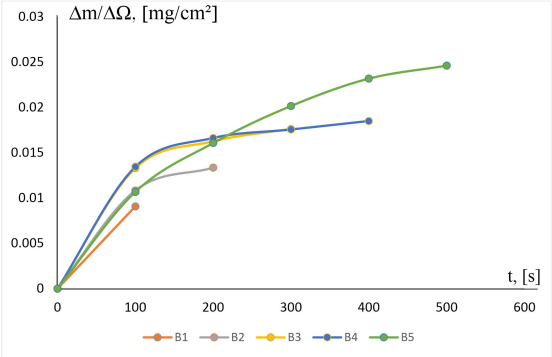

Figure 5.22: Evolution of the change in the mass of nickel balls per unit area in time

5.1.4.2 Results

The half balls were prepared for SEM observation in order to access the thickness of oxide layer. First, we made EDXS analysis of the specimen surface to be sure that no other elements are present apart from nickel (see Fig. 5.21).

Therefore, the oxide surface morphology was examined by scanning electron microscopy. The scales morphology evolution in time is illustrated in Fig. 5.23. Within the investigated range of oxidation duration (100h-500h), SEM examinations of oxide exhibited the faceted grains, platelets on the top of faceted grains, as reported in literature [36, 111]. This figure also shows coating of oxide scales by needle-shaped oxides of varying thickness and length, which tend to be clustered in islands. A large number of such oxide can be seen in Fig. 5.24. EDXS analysis of the needles revealed Cr and O (see Fig. 5.25). Similar oxide particles and needle-like oxide were observed and described in [18, 36, 63, 108, 115, 132].

The cross-section were prepared for SEM observation in order to assess the thickness and sub-surface morphology of the oxide layer. EDXS analysis of the ball cross-section was performed. According to EDXS analysis (see Fig. 5.27), the Cr_2O_3 is detected only on the top of nickel oxide scales. Fig. 5.28 shows a typical cross-section through the oxide and its evolution in time. The differences in contrast correspond to different chemical composition. As we have the roughness of the external oxide surface and reaction interface, in this experiment there are more significant surface defects due to the manufacturing method (see i.e., Fig. 5.20 and Fig. 5.28) then in the case of nickel wires oxidation, the Matlab code was developed in order to make more precise measure-

Table 5.7: Oxide thickness measurements for Ni balls.Experimental data

Time, [h]	0h	100h	200h	300h	400h	500h
Oxide thickness, [μm]	0	6.3604	8.1073	10.5940	12.9184	16.2345

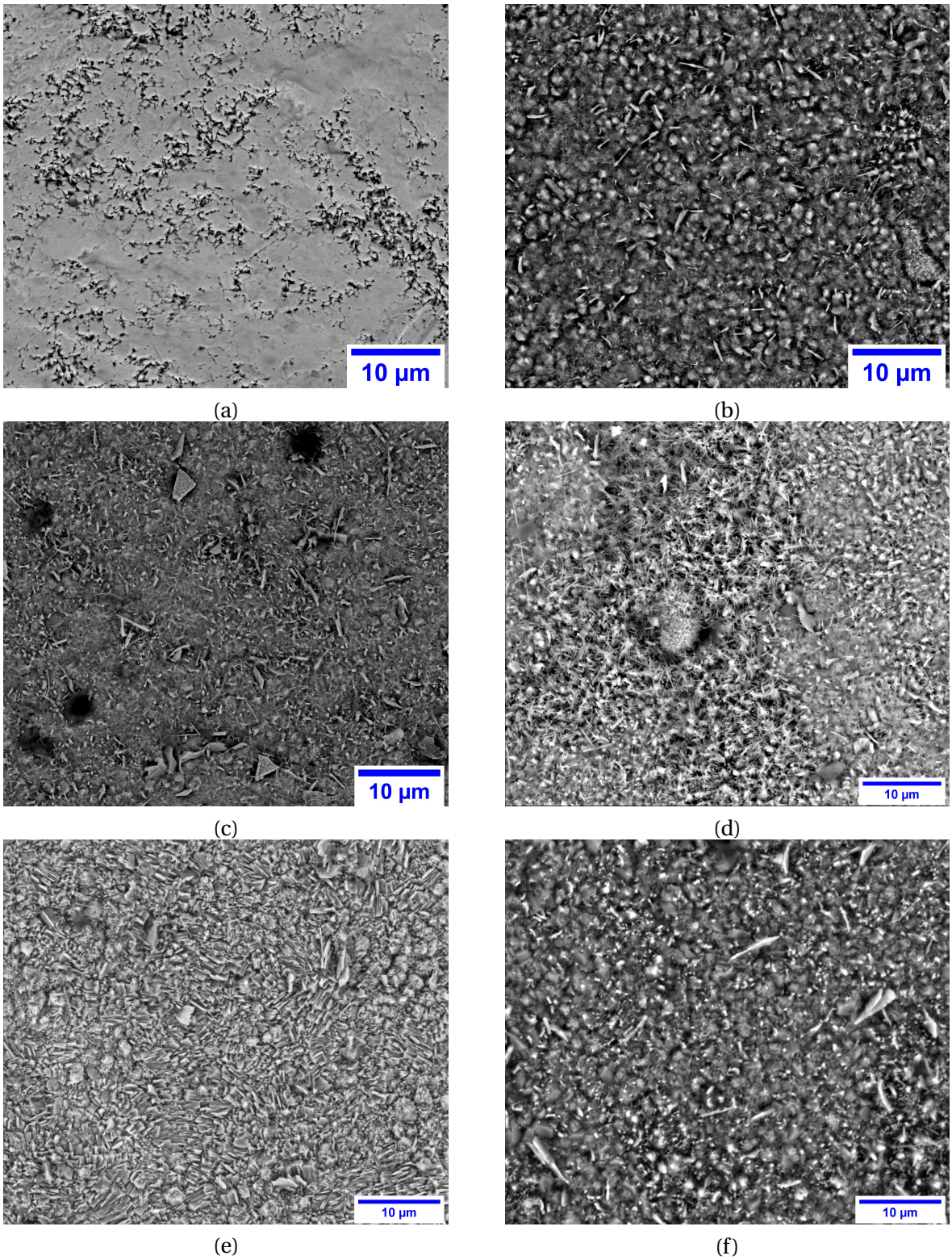

Figure 5.23: BSE pictures of NiO surface morphology as a function of oxidation duration for nickel balls: (a) before oxidation, and after (b) 100h, (c) 200h, (d) 300h, (e) 400h, (f) 500h.

ments of the oxide thickness. The details of the program, how it works and analyse the images, see in the *Note* in the previous part. The mean value was chosen a s the current thickness and the standard deviation was obtained in order to obtain an error estimate. The resultant measurements for oxide growth are presented in Table 5.7 and on Fig. 5.26a. As the radius of balls was different for each specimens, it make sense to present oxide thickness divided by the radius of each ball in order to be able to see the common tendency in oxidation process, as the radius plays an important

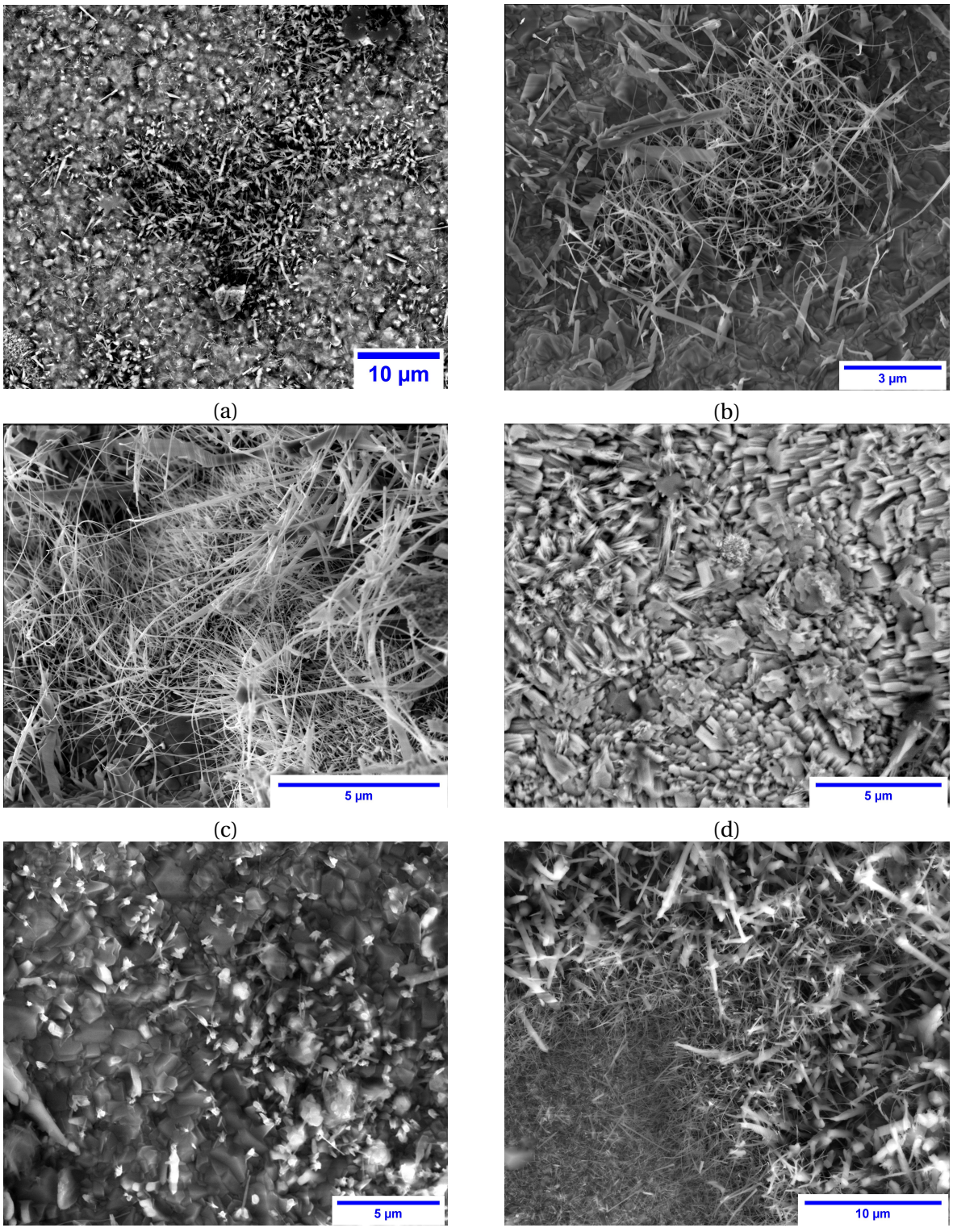

Figure 5.24: BSE pictures of surface of the oxide scale covered with Cr_2O_3 for nickel balls: after (a) 100h (b) 200h, (c) 300h, (d) 400h, (e) and (f) 500h.

role in diffusion process and therefore has an influence on the reaction kinetics (see Fig. 5.26b). We can notice from the experimental data, that the kinetics is not parabolic, and can be described by logarithmic law.

On Fig. 5.29 is shown the BSE picture of internal microstructure for nickel oxide. This image was made for the specimen B4, that was oxidized 400h. On Fig. 5.29 we see that NiO has duplex

microstructure: the compact columnar outer layer and porous and fine-grains inner layer. The interface between these two layer corresponds the initial ball surface before the oxidation.

The same as for the test for nickel wire, we did not heat treatment before testing, therefore the microstructure is not stable between the initial and the subsequent states. In order to verify the microstructure evolution under the heat treatment in time, EBSD maps have been performed on the 5 ball's cross-sections. For these acquisitions, the acceleration voltage was 25 keV and the beam current was 5.6 nA. EBSD maps are presented in Fig. 5.31. For analysis we make a choice minimum 10° misorientation to define the grain boundary. From stereographic projection (Fig. 5.30), it has to be noted that the samples have a crystallographic texture aligned with the radius.

The EBSD map shown in Fig. 5.31, we can see that the reference ball (unoxidized) has a lot of fine grains. For every specimens after the heat treatment, the grain size is significantly larger than for non-oxidized one. After 100h the grain size is completely different from the initial. The grains are able to grow through the layers of the initial ball structure; practically nothing remains of the original structure. After 100h the structure is practically stabilized, and the grain size does not change significantly.

Since the nickel balls were of different sizes (see Table 5.5) with many surface defects (such as roughness, chemical contamination, porosity etc.) and due to the mass change during the oxidation (see in Fig. 5.22 and Table 5.6), we should note that there is no general tendency in kinetics. Therefore, this makes it not possible to make a more detailed analysis compared to the case of nickel wires in the previous section.

This experiment shows us the influence of the surface morphology on the diffusion process and the kinetics of the chemical reaction.

5.1.5 Discussions

The roughness of the reaction interface and of the outer oxide surface decreases with increasing temperature [111]. This give us the incentive that at higher temperature our theoretical model can work more accurately.

The oxidation kinetics in the case of nickel wires is parabolic, and for the nickel balls it can be described by logarithmic law. The comparison of the morphological and microstructural features is difficult due to the differences in the specimen purity, the manufacturing methods, the surface preparation etc.

The experiment on the oxidation of nickel wires shows that the oxide has a two-layers microstructure and each layer has its own kinetics. Therefore, there are two reaction fronts:

– the reaction front, which is localized at the interface between Ni and NiO. Its kinetics determines the growth of the inner oxide layer due to the diffusion of oxygen through the entire oxide to this reaction front;

– the second front associated with the expansion of the oxide outward from the original specimen surface (the outer oxide layer). This process is related to nickel diffusion to the outside of the sample. Its kinetics is associated with the chemical reaction front propagation.

Hence, the theoretical model has to take into account the second reaction front. In the approach we use, this volumetric expansion is introduced via ε^{tr}. In the future work, we can modify this chemical transformation deformations to make them dependent on the chemical reaction front velocity.

The nickel precipitates can be associated with the oxygen diffusion and oxide formation. But to check this hypothesis, a more detailed analysis by TEM have to be investigated.

As we can see, there are few mechanisms of oxidation: the growth of the main oxide layer (due to the diffusion of oxygen through whole oxide layer to the reaction front and the diffusion of the nickel outwards of the original specimen surface), the diffusion of oxygen along the nickel grain and twin boundaries and NiO precipitates. The diffusion along the grain boundaries is the fastest process during the oxidation and it is important to include this mechanism in the theoretical model to predict the possible crack initiation and failure of the solid. In our theoretical model

we did not take into account the grain boundaries, then it gives us the motivation to improve the diffusion model in given approach.

Since we did not do any heat treatment before the oxidation, the microstructure between the initial state and the further ones is not stable. And it makes not possible to take into account the influence of the initial microstructure on the diffusion along the grain boundaries, but we can use the experimental data to predict the kinetics along the GBs. To model the kinetics of the oxygen diffusion along the grain boundaries for the initial microstructure, the set of the experiment with heat treatment before the oxidation has to be preformed.

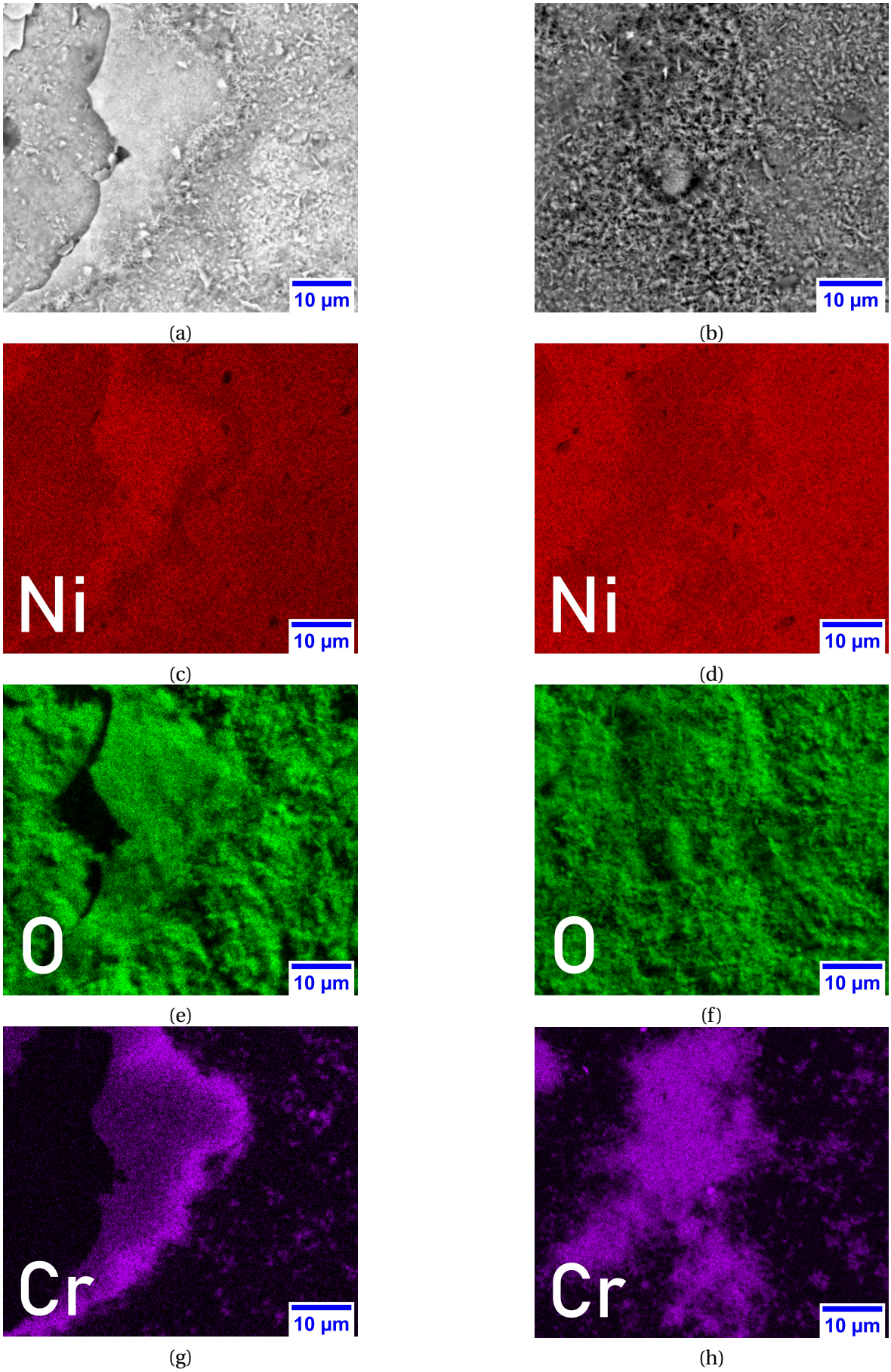

Figure 5.25: BSE images (a) and (b) and EDXS element maps (b) - (h) for the ball oxidized 300h.

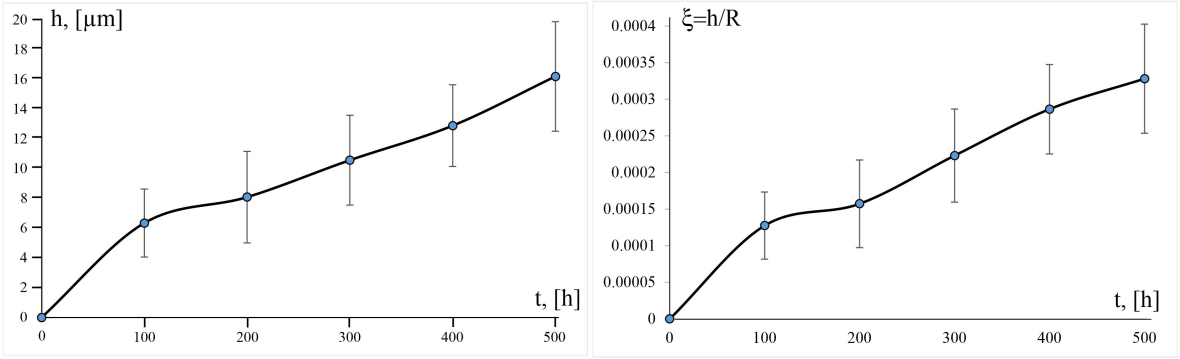

(a) (b)

Figure 5.26: Growth of oxide layer in time for balls, based on the experimental data from Fig. 5.28 and Table 5.7: (a) actual measurements, (b) relative oxide thickness (divided by the radius of each ball)

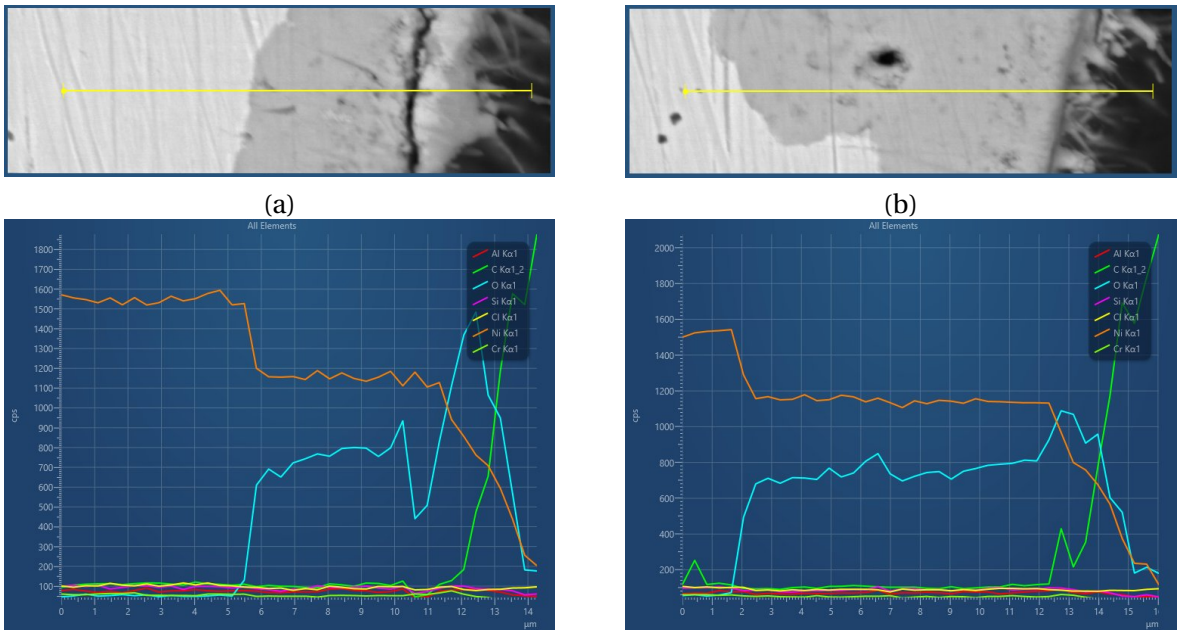

(a) (b)

(c) (d)

Figure 5.27: BSE images (a) and (b) and line-profile EDXS (c) and (d) for the ball oxidized 100h.

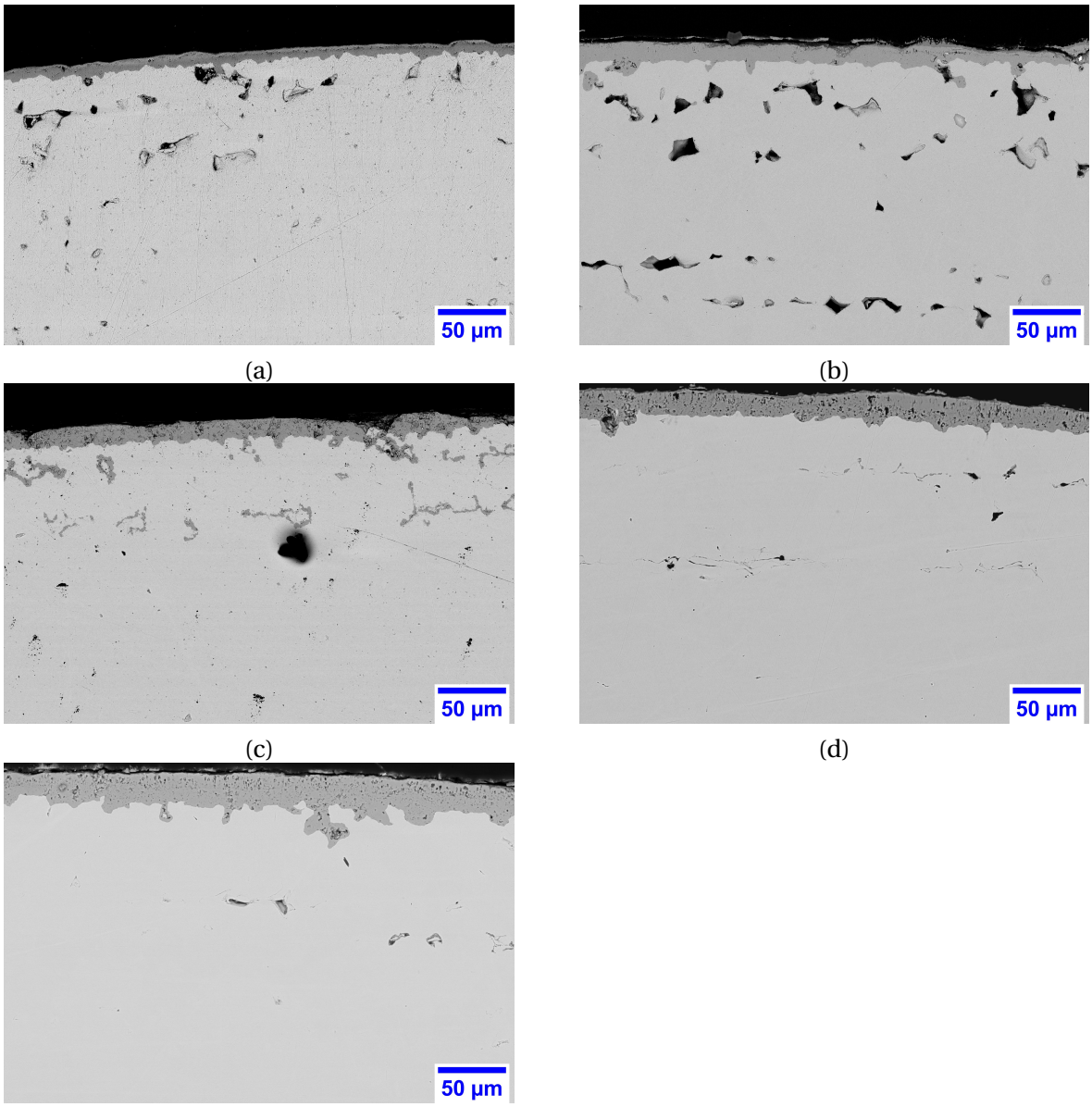

Figure 5.28: Nickel Balls: BSE images of NiO thickness as a function of oxidation duration: (a) 100h (b) 200h, (c) 300h, (d) 400h and (e) 500h.

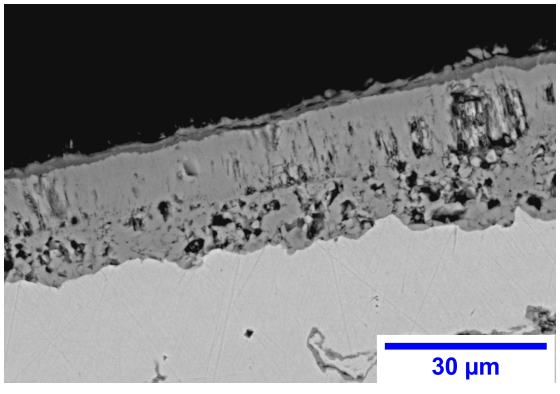

Figure 5.29: Nickel Balls: BSE image: internal microstructure of NiO (after 400h oxidation)

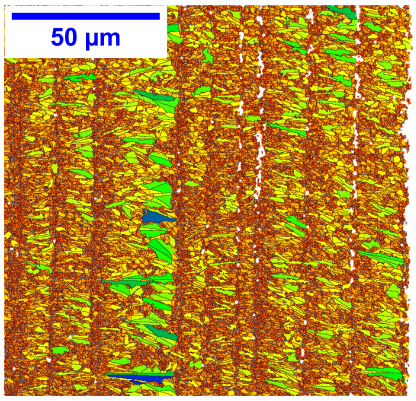

(a)

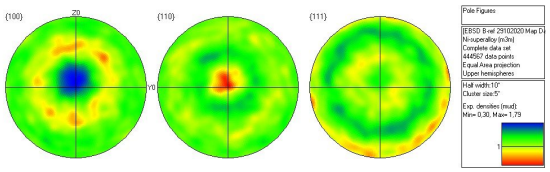

a)

Figure 5.30: (a) EBSD Map and (b) Pole figure displaying crystallographic texture for Nickel ball before oxidation

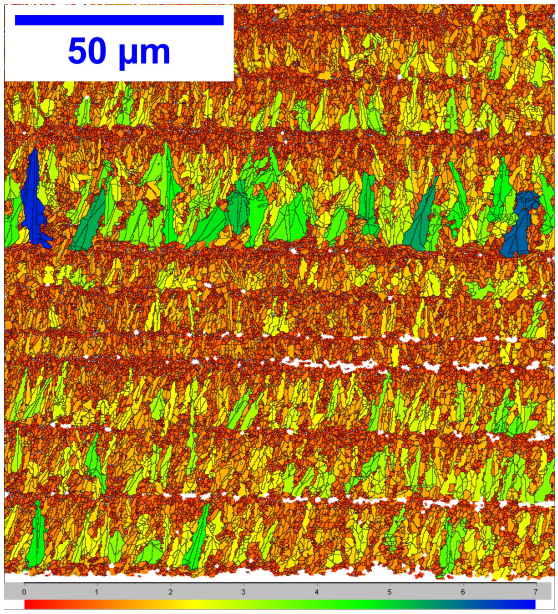

(a)

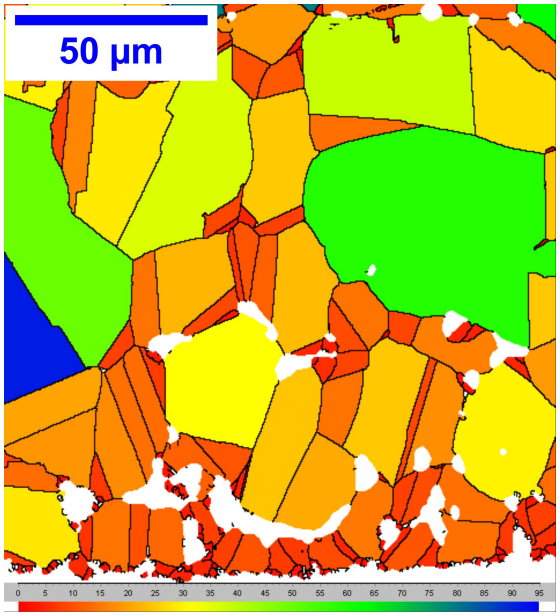

(b)

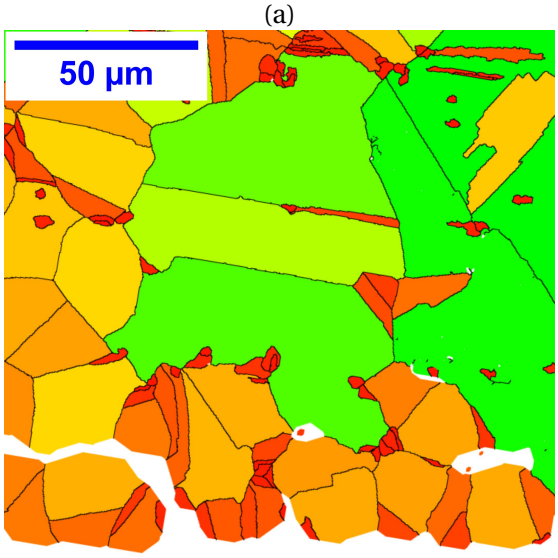

(c)

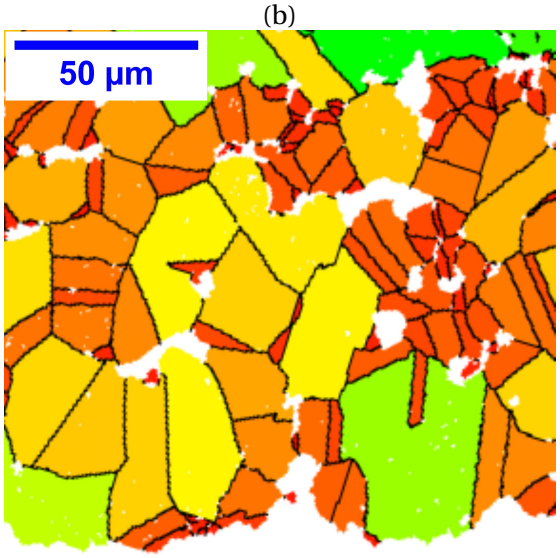

(d)

Figure 5.31: EBSD Map of Nickel balls during oxidation: (a) 0h, (b) 100h, (c) 300h and (d) 500h. The legend for grain size for balls after oxidation is common for all specimens and presented in pic.(b)

5.2 Comparisons

In this section we make two types of comparisons:

-– models between each others, in order to show the influence of solids geometry, mechanical properties, type of the loading and constitutive law on the reaction front propagation;

-– experimental data with different proposed models, in order to validate the model and to show the constitutive law impact.

5.2.1 Models comparison: influence of the constitutive law, elastic modulus, solids geometry and types of loading on the reaction front propagation

In this part we make the comparison between models and obtained results in order to show the influence of the constitutive law, elastic modulus, solids geometry and types of loading on the reaction front propagation.

5.2.1.1 Influence of the elastic modulus on the reaction propagation

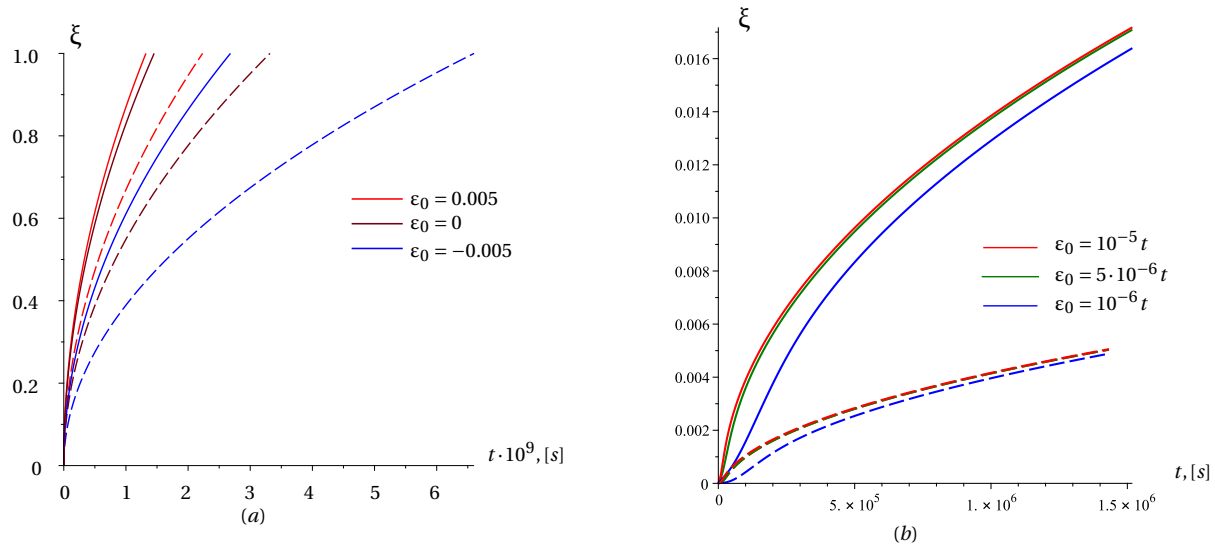

Figure 5.32: Kinetics of the planar reaction front with (a) elastic and (b) elasto-plastic reaction product at various values of external tension ε_0 for the case $G_+ > G_-$ (solid lines) and for the case $G_- > G_+$ (dashed lines).

As it was shown in the previous chapters, the mechanical parameters, such as bulk and shear modulus, k_+ and μ_+ respectively, affect the equilibrium concentration c_{eq} and hence the reaction kinetics (see more details in sections 2.2, 3.2 and 4.2). Here, we study how the elastic modulus affect the reaction front propagation.

In Chapter 3, it was shown that the viscous deformations do not affect the reaction kinetics in the case of viscoelastic reaction product. Therefore, for the case of the viscoelastic transformed material, the chemical reaction propagates with the same velocity as for the case of a pure elastic reaction product (see more details in Section 3.2).

In the case of the planar reaction front with elastic, the reaction kinetics is defined by Eq.(2.16) in the form of parabolic law. The character of the equilibrium concentration c_{eq} (2.15) depend on the relation between G_+,G_- and S_+ (see section 2.2), where $G_\pm = \dfrac{\mu_\pm\left(3k_\pm + \mu_\pm\right)}{3k_\pm + 4\mu_\pm}$ and $S = \dfrac{2k_+\mu_+}{3k_+ + 4\mu_+}$. We illustrate how the sign of the difference $(G_+ - G_-)$ and the value of the parameter S_+ affect the reaction front kinetics (Fig. 5.32a). By (2.14) and (2.16) the elastic moduli and external strain affect the parabolic kinetic via the influence on the coefficient Q, i.e. via changing the time-scale due to changing the parameters S_+ and the difference $(G_+ - G_-)$.

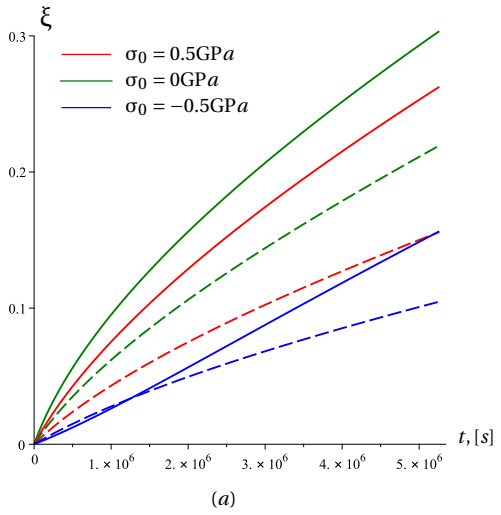

Figure 5.33: Kinetics of the spherical reaction front with elastic reaction product at various values of external stress σ_0 for the case $k_+ > k_-$ (solid lines) and for the case $k_- > k_+$ (dashed lines).

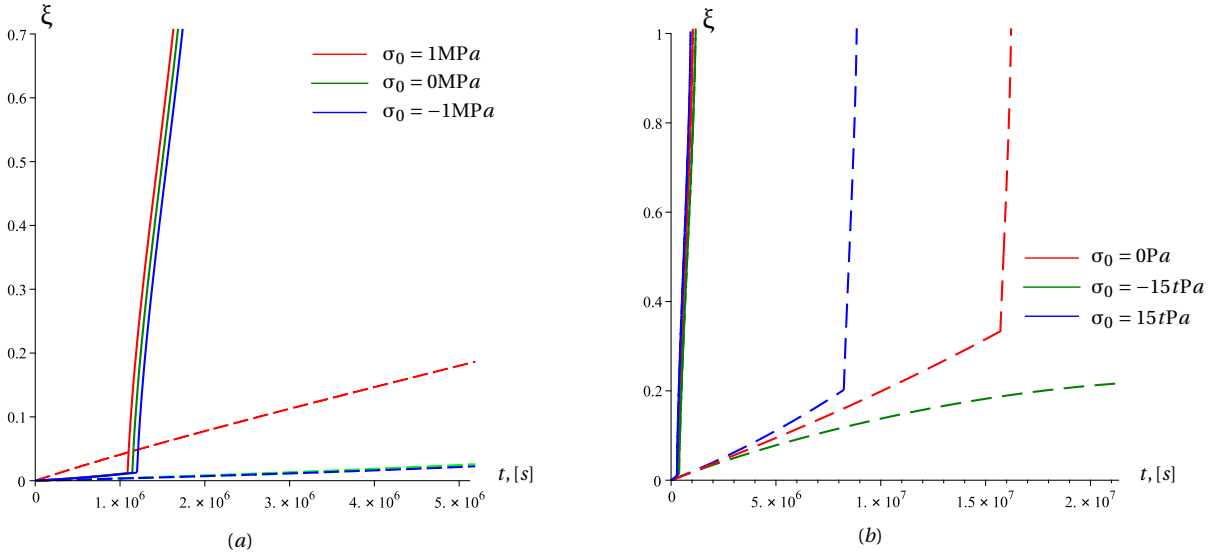

Figure 5.34: Kinetics of the spherical reaction front with elasto-plastic reaction product at various values of external stress (a) $\sigma_0(t) = \sigma_0$ and (b) $\sigma_0(t) = \mathscr{S}t$ for the case $k_+ > k_-$ (solid lines) and for the case $k_- > k_+$ (dashed lines).

If $\varepsilon_0 = 0$ the difference $(G_+ - G_-)$ itself does not affect the front kinetics, and the front propagates slowly in the case $G_+ < G_-$ just because the value S_+ is smaller than in the case $G_+ > G_-$ at elastic moduli taken in this example (see Tables 2.1, 2.2). Note that S_+ is defined by the elastic moduli of the transformed material only.

One case also compare quantitatively how the external strain affects the kinetics if the elastic moduli of the solid constituents are such that $G_+ > G_-$ or $G_+ < G_-$. In particular, the front propagates at $G_+ < G_-$ slower than at $G_+ > G_-$ as it was due to the different values of S_+, but the difference is grater at compression and smaller at tension in comparison with the case $\varepsilon_0 = 0$.

Same comparison can be done for the case of planar reaction front with the elasto-plastic reaction product, using the Eq.(4.8) and (4.9) for the elastic stage and Eq.(4.17) and (4.18) for the plastic stage (Fig. 5.32b). From the quantitative comparison it follows, that in the case $G_+ > G_-$ front propagates much faster that at $G_- > G_+$ due to the differences in elastic modulus of initial and transformed materials (see Eq.(4.17)).

For the spherical reaction front with elastic transformed material, from the Eq.(2.22) and (2.17)

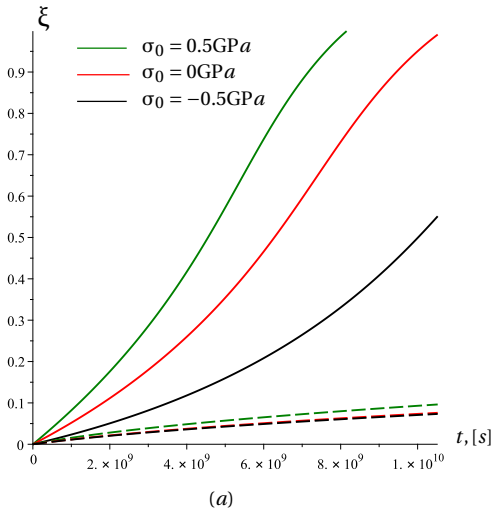

(*a*)

Figure 5.35: Kinetics of the cylindrical reaction front with elastic reaction product at various values of external stress σ_0 for the case $\mathscr{K}_+ > \mathscr{K}_-$ (solid lines) and for the case $\mathscr{K}_- > \mathscr{K}_+$ (dashed lines).

it can be noticed, that the character of c_{eq} depends on the relation between $\mathfrak{P}$ and $\mathfrak{K}$ and the sign of $(k_+ - k_-)$. In Fig. 5.33 the influence of the $\mathfrak{P}$ and $\mathfrak{K}$ and the sign of $(k_+ - k_-)$ on the reaction front kinetics is shown. By (2.22) and (2.17), the reaction kinetics depends on the elastic modulus, external stress and the reaction front position. The reaction propagates according to the parabolic and logarithmic laws (depending on the elastic modulus, see details in section 2.2).

From the equation (2.22), at $\sigma_0 = 0$ the difference $(k_+ - k_-)$ itself and the parameter $\mathfrak{P}$ do not affect the reaction kinetics, there is the influence of the parameter $\mathfrak{K}$ on it. In the case of $k_+ > k_-$ the reaction propagates faster than in the case $k_+ < k_-$ due to the greater value of $\mathfrak{K}$ in this case. The quantitative comparison at various values of external stress σ_0 of the kinetics for the cases $k_+ > k_-$ and $k_+ < k_-$ shows that in the case $k_+ > k_-$ the reaction front propagates faster, than for the case $k_- > k_+$.

The analysis of the spherical reaction front with the elasto-plastic reaction product is carried out in the same way as for the case of the elastic reaction product (Fig. 5.34). Two different types of the external loading are considered: $\sigma_0(t) = \sigma_0$ and $\sigma_0(t) = \mathscr{S} t$.

Note, that for the constant loading $\sigma_0(t) = \sigma_0$, in the initial stage of the chemical transformation at $\sigma_0 = 0$, the reaction kinetics is faster for the case $k_- > k_+$, than for the case $k_+ > k_-$ (Fig. 5.34a). This initial stage corresponds to the moment, when the solid in both cases is in the elastic state. However, since in the case $k_+ > k_-$ the plastic stage takes place, the reaction fronts propagates much faster, than for $k_- > k_+$. Note, that it was discussed in the chapter 4, that the plastification of the material at the same conditions becomes earlier in the case of $k_+ > k_-$. At given external tension or compression, the reaction propagates slower at $k_- > k_+$.

In the case of external loading as linear function of time, $\sigma_0(t) = \mathscr{S} t$, the chemical reaction propagates much faster in the case of $k_+ > k_-$, than for the case $k_- > k_+$ (Fig. 5.34b).

In the same manner, in Fig. 5.35 is shown that for cylindrical reaction front the reaction kinetics is faster for the case of $\mathscr{K}_+ > \mathscr{K}_-$, than for the case $\mathscr{K}_+ > \mathscr{K}_-$ (see (2.31) and (2.33)). Note, that cylindrical reaction front propagates according to the parabolic and exponential laws (depending on the elastic modulus, more details can be found in section 2.2).

All these analysis show how much the reaction front propagation is affected by constitutive law and by elastic parameters.

5.2.1.2 Impact of the solids geometry on the reaction kinetics

In this part we analyse the influence of the solids geometry on the reaction front propagation.

In the case of elastic reaction product, the kinetics of the reaction front for various solids ge-

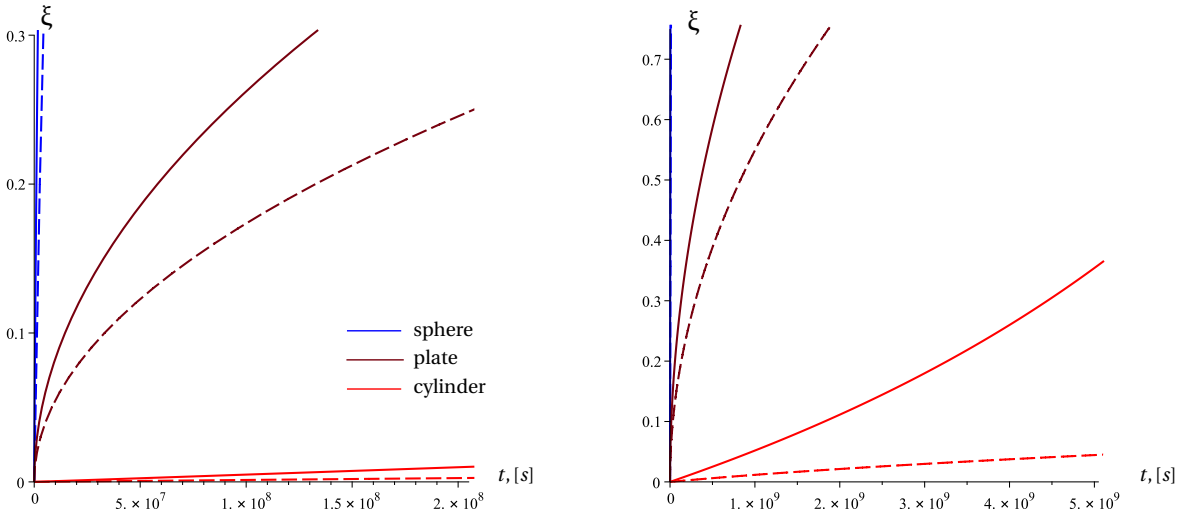

Figure 5.36: Influence of the solids geometry on the kinetics of reaction front with elastic reaction product at $\sigma_0 = 0$ for the case $\mathscr{K}_+ > \mathscr{K}_-$ (solid lines) and for the case $\mathscr{K}_- > \mathscr{K}_+$ (dashed lines).

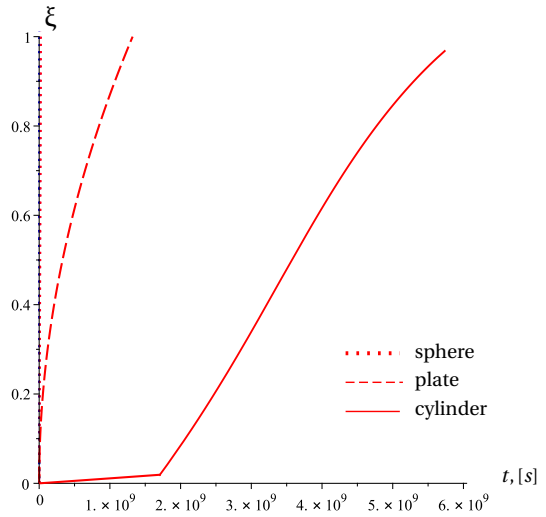

(*a*)

Figure 5.37: Influence of the solids geometry on the kinetics of reaction front with elasto-plastic reaction product at $\sigma_0 = 0$ for the case $\mathscr{K}_+ > \mathscr{K}_-$.

ometries is presented in Fig. 5.36 for different ratio of the elastic modulus (see the previous subsection). It is shown that in the case of the spherical reaction front propagates with highest velocity among the fronts of presented geometries. The kinetics of the cylindrical front is the slowest one, and it demonstrates two different behaviours for the cases of $\mathscr{K}_+ > \mathscr{K}_-$ and $\mathscr{K}_+ < \mathscr{K}_-$, respectively. The comparison was made for the sphere and cylinder of the same radius R = $1mm$ and for the plate with thickness of H = $0.5mm$.

For elasto-plastic transformed material the kinetics for the spherical, cylindrical and planar reaction front is shown in Fig. 5.37. Similarly to the case of the elastic reaction product, the planar reaction front propagates faster than the cylindrical one and slower than the spherical reaction front.

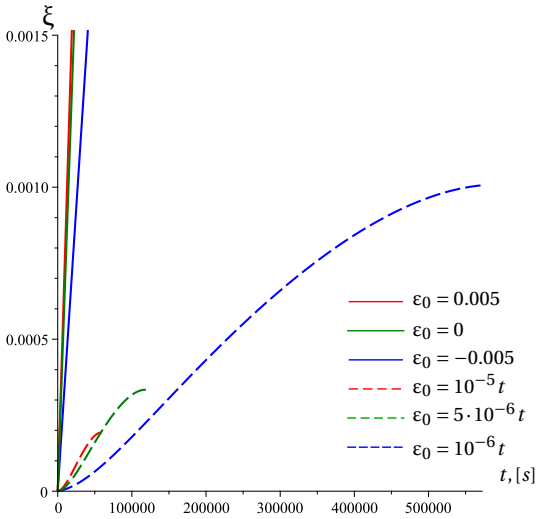

(*a*)

Figure 5.38: Kinetics of planar reaction front with elastic reaction product at various external deformation $\varepsilon_0 = 0$ for $G_+ > G_-$.

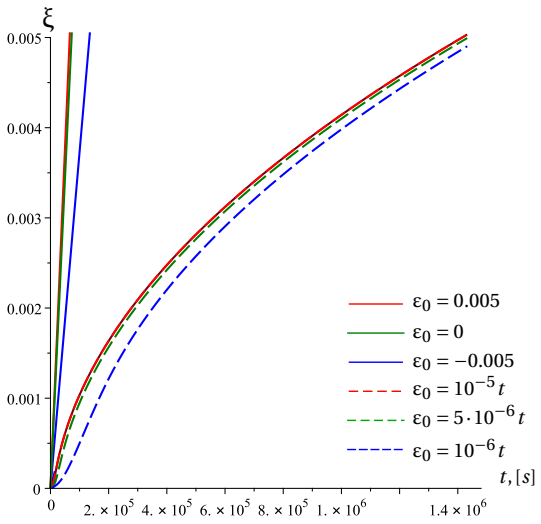

(*a*)

Figure 5.39: Kinetics of planar reaction front with elastic (at $\varepsilon_0(t) = \varepsilon_0$) and elasto-plastic (at $\varepsilon_0(t) = \mathscr{U} t$) reaction products for $G_+ > G_-$.

5.2.1.3 Influence of the constitutive law and of the type of loading on the reaction front propagation

In the case of the planar reaction front with elastic reaction product, we consider two types of the given external deformation: $\varepsilon_0(t) = \varepsilon_0$ and $\varepsilon_0(t) = \mathscr{U} t$ (Fig. 5.38). It can be noticed, that for constant external deformation the kinetics is faster than at time-dependent external deformation. Moreover, in the case of time-dependent loading the reaction front can be blocked. Note, that as higher the magnitude $\mathscr{U}$ of the external loading $\varepsilon_0(t) = \mathscr{U} t$ as faster the reaction will be blocked.

In Fig. 5.39 is shown the influence of the constitutive law on the front propagation for the planar front. It can be noticed, that for the case of the elasto-plastic reaction product the kinetics of the chemical reaction is much slower than for the case of elastic transformed material.

For the chemical reaction propagates from the surface of the sphere, we consider the different types of the loading for elastic and elasto-plastic reaction products (see Fig. 5.40). One can see that for the case of time-dependent external loading $\sigma_0(t) = \mathscr{S} t$ the reaction propagates faster,

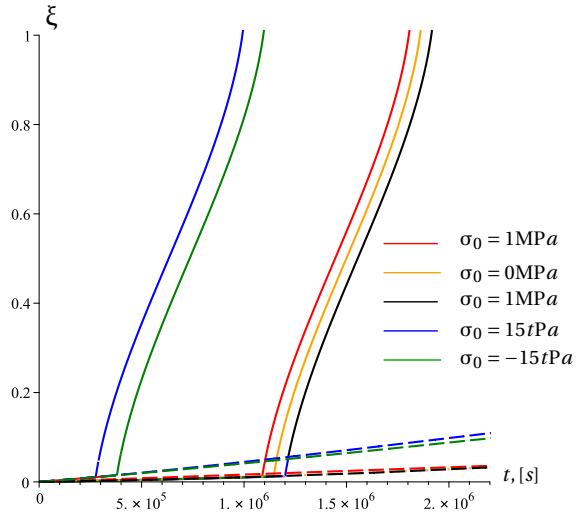

(*a*)

Figure 5.40: Kinetics of spherical reaction front with elastic (dashed lines) and elasto-plastic (solid lines) reaction products at various external loading $\sigma_0(t)$ for $k_+ > k_-$.

than for the constant external stress $\sigma_0(t) = \sigma_0$ both for elastic and elasto-plastic transformed material. In the case of the elasto-plastic reaction product (solid lines in Fig. 5.40), the reaction kinetics is faster, than for elastic transformed material (dashed lines in Fig. 5.40). This underlines the complexity of the reaction two fronts (transformation and plastic) act.

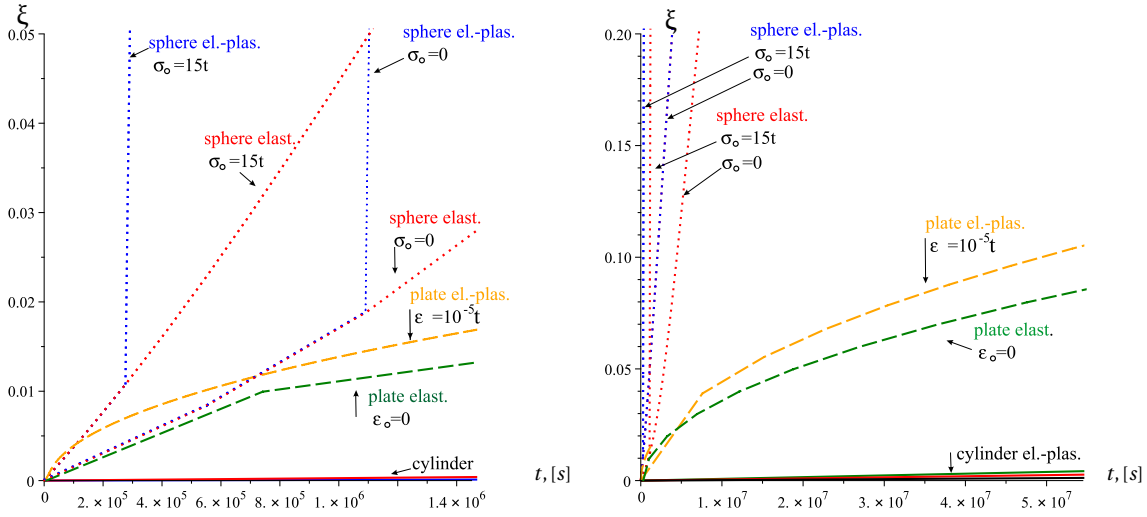

(*a*) (*b*)

Figure 5.41: The influence of the solids geometry and constitutive law on the kinetics of the chemical reaction at $\sigma_0(t) = 0$ and for the case $\mathscr{K}_+ < \mathscr{K}_-$.

In summary of this part, the scheme of the influence of the solids geometry and constitutive law on the kinetics of the chemical reaction is shown in Fig. 5.41. One can see, that the spherical reaction front propagates faster than planar and cylindrical fronts both for elastic and elasto-plastic transformed material. However, for the initial stage of the chemical transformation (Fig. 5.41a), the dependence of reaction kinetics on the solid geometry is more complex and very 'sensitive' to the external conditions (temperature through the energy parameter γ, external loading, etc.). In the case of the cylindrical reaction front the kinetics is much slower than for the spherical and planar fronts.

Note, that as it was discussed in Section 3.2, predicting stresses due to chemical transformation and taking into account viscous and plastic deformations, very important to estimate the lifetime of the considered solid. The evolution of the viscous strains and the stress relaxation behind the reaction front can be found in section 3.2. The redistribution of the plastic and elastic strains and stresses profiles at different positions of the reaction front are conducted in Section 4.3.

5.2.2 Comparison of experimental and theoretical results

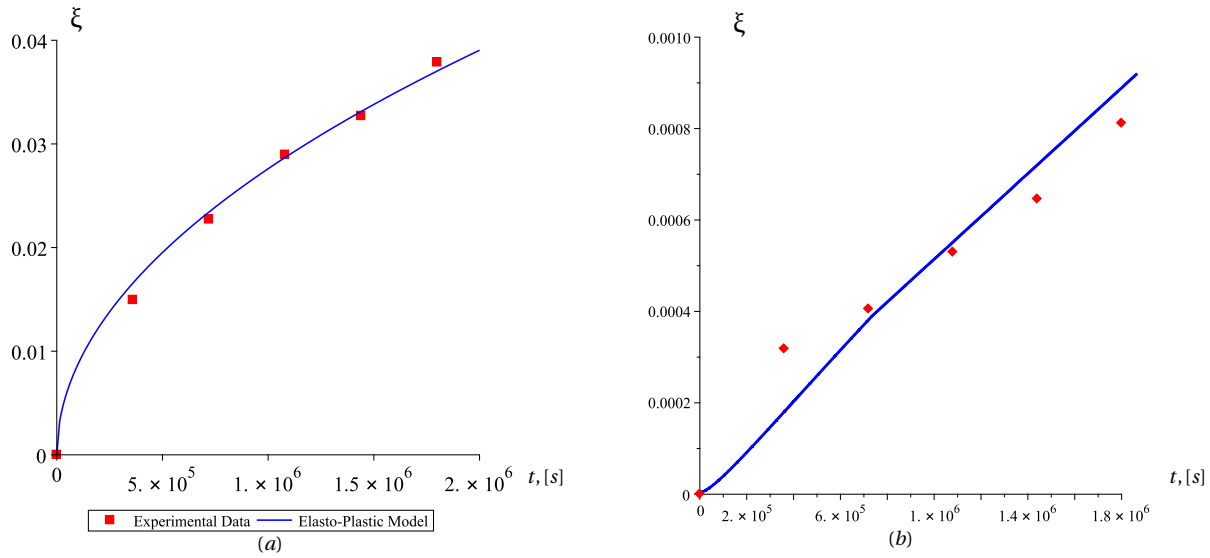

Figure 5.42: Oxidation of pure nickel. Comparison of the experimental data with theoretical models: (a) nickel wires and (b) nickel balls.

In this part we compare the experimental data with the models proposed in the previous chapters.

In order to plot the theoretical curve, we use some data coming from the literature since the investigation on the nickel oxidation were performed mostly experimentally.

The diffusion of oxygen inside of nickel and nickel oxide were studied and discussed in [4, 5, 110, 112, 131, 145, 149]. The coefficient of diffusion for nickel oxidation as well as solubility of the oxygen in solid nickel can be found in these articles. The mechanical properties of nickel and nickel oxides were obtained in [1, 35, 94, 113], Young's modulus, Poisson's ratio and yield stress for Ni and NiO are given in these articles.

As it was discussed in Chapter 1 in the general framework, the energy parameter γ, depending on the temperature, is defined empirically. We approximate this energy by the energy formation of NiO at 800°C, divided by the molar volume of NiO, since the unit of energy parameter γ is energy density per unit volume. The value of the energy formation for NiO is given in [136] at various temperature.

In Fig. 5.10 we can notice, that the kinetics fits very well a parabolic evolution. Hence we will use only the relation between parameters, that give us such parabolic kinetics and in the case of the cylindrical reaction front it corresponds to the case $\mathscr{K}_- > \mathscr{K}_+$. In Fig. 5.42a is shown the results for the cylindrical front propagation with elasto-plastic reaction product. The theoretical curve for elastic transformed material is much lower than the experimental data. Note, that with our theoretical model we can describe the experimental curve very accurately. The values of the parameters used in the simulation: $D = 6.75 \cdot 10^{-16} cm^2 s^{-1}$, $E_+ = 172 GPa$, $\nu_+ = 0.35$, $E_- = 190 GPa$, $\nu_- = 0.305$, $\rho_- = 8.9 g/cm^3$.

We can notice from the experimental data for the oxidation of the nickel balls (Fig. 5.26), that the kinetics is not parabolic, and can be described by logarithmic type law, which corresponds

with our theoretical models for the case to the spherical front propagation. The theoretical curve corresponds to the solution for the spherical reaction front with elasto-plastic transformed material. In this case, we are able to obtain a relative confirmation of the theoretical results with the experimental one, since large variation of the thickness for this set of the experiment is observed.

Indeed, as it was mentioned in the experimental part of this chapter, and it was noted in the literature, that the surface preparation, purity of the samples have big influence on the reaction kinetics. Since here, nickel balls were of different sizes (see Table 5.5) and with many surface defects, it affect the diffusion process and then the kinetics of the oxidation. Therefore, in the case of balls, model and experiments give only a relative accordance and more test are necessary to validate these final results. In order to do it, it needs to conduct one more experiment for balls with the same radius and smooth surface.

5.3 Conclusions

In the first part of this chapter high-temperature oxidation of pure nickel wires and balls were conducted.

A high temperature oxidation of pure nickel wires and balls were performed. The evolution of oxide thickness in time is measured and presented. The morphological and microstructural evolution of NiO scales are obtained. The scale morphology is faceted. The oxide scales have duplex microstructure. The evolution of nickel microstructure during the oxidation is presented. The constant parabolic rate is obtained in the case of nickel wires oxidation. Different mechanisms of oxidation are shown and discussed.

In the second part of this chapter, two types of comparisons are made: between models and experiments and between models.

The effect of the elastic modulus on the reaction front kinetics is presented for each geometry of solid and for the cases of elastic and elasto-plastic transformed materials. It is shown that the reaction front propagation is affected by the constitutive laws and by elastic parameters. The influence of the solids geometry on the reaction kinetics is investigated. The planar reaction front propagates faster than cylindrical one and slower than the spherical reaction front. The influence of the constitutive law and of the type of loading on the reaction front propagation for various solids geometry is investigated.

The comparisons of the experimental data with proposed models are made. The experimental results of nickel wires oxidation can be described accurately by the model for cylindrical reaction front with elasto-plastic reaction product. Since the nickel balls were of different sizes and with many surface defects, model and experiment give only a relative accordance.

Conclusion

The stress-affected chemical reaction front propagation in inelastic (viscous, plastic) deformable solid has been considered based on the concept of the chemical affinity tensor. For the case of an inelastic component the chemical reaction is obtained and investigated by analytical solutions of the simplest boundary value problems describing the propagation of plane, cylindrical, and spherical fronts of reaction. It was shown how the stress-strain state and the geometry of the solid affect the kinetics of the chemical reaction. Using the notion of the equilibrium concentration, the effects of acceleration is studied, as well as the slowing down and blocking of the reaction by external loading and material parameters. The stresses and deformations, induced by chemical transformations, have been determined. Their impact on the deformation and strength properties of the materials have been predicted. Resulting from the chemical affinity tensor a kinetic equation is formulated, which determines the dependence of the rate of a chemical reaction front propagation in visco-elastic and elastic-plastic bodies from the stress-strain state.

The stress-affected chemical reaction front propagation in deformable solid in the cases of a planar, spherical and cylindrical reaction fronts has been considered for elastic bodies in Chapter 2. The accurate mathematical analysis of the influence of various parameters on the reaction front behavior is conducted. The planar reaction front propagates only according a parabolic law. In the case of the spherical reaction front, the kinetics can be logarithmic and parabolic, depending on the relations between the combinations of elastic moduli of solid reactants. For the reaction in cylindrical element an exponential kinetics law was observed as well as a parabolic one. These different results are consistent with some experimental data coming from literature.

The third chapter is devoted to the stress-assisted chemical reactions with viscoelastic reaction product and a model for analytical studies of stress relaxation behind the reaction front is developed. Results show that viscous deformations of the reaction product do not affect directly the kinetics of the front in the case of the Standard Linear Solid Model if the external strain acts in the plane of the interface, since they do not have time to appear at the moment of the transformation. But they enable the possibility for a stress relaxation phenomenon behind the reaction front. Depending on the viscous and elastic parameters, this relaxation can be fast, and the high stresses region is localized in a narrow layer adjacent to the transformation front. Note also that other external loadings are possible, at which stress relaxation can restart the initially blocked reaction front. The changing of the rheology of a solid constituent due to the localized chemical reaction was taken into account with the use of the Standard Linear Solid Model and its particular cases. The SLSM and Maxwell model allowed to obtain analytical solutions which gave us possibilities to study the specific effects of material parameters on stress relaxation behind the reaction front. On the other hand, the Kelvin-Voigt and pure viscous materials can hardly be considered as proper candidates for modeling the reaction products.

The effects of plasticity on the reaction front kinetics were investigated in Chapter 4. The stress-assisted chemical reaction front propagation in deformable solid in the cases of a planar, spherical and cylindrical reaction fronts for the elastic-perfectly plastic transformed material has been also considered. It is shown that the chemical reaction has differ mechanism from the reaction with elastic and viscoelastic reaction product. These mechanism are presented and described. It is shown that even only chemical transformation cans induce the plastic deformations. The influence of the boundary condition for the initiation of the plastic deformation in the material is studied. For the planar reaction front, the choice of the boundary condition leads to two different situation for elasto-plastic stage (if it appears). It is shown that for the case of given deformations, when the yield stress is reached, the elastic transformed material becomes fully plastic, while for given stresses, a plastic front appears. In the case of the spherical and cylindrical reaction front propagation the plastic front appears in the elasto-plastic regime. Two fronts have their own velocities and directions. The plastic zone expands in two directions. The relation between the reaction front and plastic front is determined. It is shown that yielding of the material accelerates the reaction.

As a result, the proposed models are compared with each other in Chapter 5. It is shown that the kinetics of the chemical reaction front is affected by the constitutive laws, type of the external

loading and by elastic parameters. The influence of the solids geometry on the reaction kinetics is investigated. The planar reaction front propagates faster than cylindrical one and slower than the spherical reaction front.

Finally, experimental high temperature oxidation of pure nickel wires and balls experiments were conducted. The experimental data for the oxide thickness evolution in time were obtained and compared with proposed theoretical models. It is shown that the oxidation of nickel wires demonstrates a parabolic kinetics, while for the nickel balls it is more a logarithmic one. The comparison of experimental results of nickel wires oxidation with proposed models shows that the experiments can be described accurately by the model for cylindrical reaction fronts with elasto-plastic reaction product. Since the nickel balls were of different sizes and with many surface defects, model and experiment give only a relative accordance, which has to be confirmed.

In summary, we can see the influence of the solids geometry, constitutive laws, boundary conditions and mechanical properties on the reaction front propagation for inelastic constitutive laws. As these simple geometries correspond to industrial applications, then the obtained results could be used for the developments of the optimal design of nano-anodes in Li-ion batteries with specific capacity, to develop the theoretical basis for the control of the size of the transformed material (e.g., oxide, lithiated silicon) and geometry of the nano-structure. These analytical solutions could also be used to check numerical procedures and for the estimation of the impacts of the transformation and inelastic strains on the thickening during the front propagation in the experiments.

Following these results, different perspectives could be drawn for coupled mechanochemistry simulations based on the chemical affinity tensor:

– be applied for more complex external loading and geometry;

– be extended it to viscoplasticity;

– numerical implementation of models of chemical propagation fronts in inelastic bodies. Our approach has a deal with the sharp interface, that makes such simulations significant and difficult to realize;

– extend to thermo-elasticity, thermo-viscosity and thermo-plasticity with strong thermo-chemo-mechanical couplings;

– develop new diffusion model, in order not to be limited with this simple stationary one;

– to take into account the diffusion along the grain boundaries by taking into account the microstructure features;

– introduce the second reaction front, in accordance with the expansion of the material outwards (see the discussions at the end of Section 5.1). In the approach we use, this volumetric expansion is introduced via ϑ^{tr}. In the future work, we could modify this chemical transformation deformations to make them dependent on the chemical reaction front velocity;

– conduct experiments with cyclic thermal and mechanical loadings.

Appendix A

Solution for Laplace transformation

For analysis it is best to work with dimensionless quantities. In the case of a sphere the outer radius R is the only length parameter in the problem. Hence, there is no other choice but to define a dimensionless distance and dimensionless displacement by

$$u = \frac{u_r}{\mathrm{R}}, \qquad x = \frac{r}{\mathrm{R}} \tag{A.1}$$

We solve PDEs by mapping them onto Laplace space w.r.t. time $t \leftrightarrow p$ and then finding a solution of the corresponding Ordinary Differential Equation (ODE). The Laplace transform of the displacement will be identified by a bar, $\bar{u} = \bar{u}(x,p)$, $\bar{\mathrm{e}}_1^e = \bar{\mathrm{e}}_1^e(x,p)$, and we may write according to the usual rules of Laplace transforms:

$$\left(k^+ + \frac{4}{3}\mu_2 + \frac{4}{3}\eta p\right)\left(\bar{u}''(x,p) + \frac{2}{x}\bar{u}'(x,p) - 2\frac{\bar{u}(x,p)}{x^2}\right) - \frac{4}{3}\eta\left[u''(x,0) + \frac{2}{x}u'(x,0) - 2\frac{u(x,0)}{x^2}\right] -$$
$$-2\eta p\left(\left(\bar{e}_{1r}^e\right)'(x,p) + \frac{2}{x}\left(\bar{e}_{1r}^e(x,p) - \bar{e}_{1\varphi}^e(x,p)\right)\right) + 2\eta\left[\left(e_{1r}^e\right)'(x,0) + \frac{2}{x}\left(e_{1r}^e(x,0) - e_{1\varphi}^e(x,0)\right)\right] = 0, \tag{A.2}$$

$$\left(p + \frac{\mu_1}{\eta}\right)\bar{e}_{1r}^e(x,p) - e_{1r}^e(x,0) = \frac{2p}{3}\left(\bar{u}'(x,p) - \frac{\bar{u}(x,p)}{x}\right) - \frac{2}{3}\left[u'(x,0) - \frac{u(x,0)}{x}\right], \tag{A.3}$$

$$\left(p + \frac{\mu_1}{\eta}\right)e_{1\varphi}^e(x,p) - e_{1\varphi}^e = \frac{p}{3}\left(\frac{\bar{u}(x,p)}{x} - \bar{u}'(x,p)\right) - \frac{1}{3}\left[\frac{u(x,0)}{x} - u'(x,0)\right] \tag{A.4}$$

The terms in brackets drops out. We can give two reasons for that. The first is the initial condition, according to which the displacement (and all its derivative) shall vanish initially. Second, we note that these very terms represents the (stationary) ODEs, which is then zero to begin with. The solution of the remaining system of ODEs for $\bar{u}(x,p)$ and $\bar{\mathrm{e}}_1^e(x,p)$. We may write:

$$\bar{u}^+(x,p) = \bar{\mathrm{F}}_1(p)x + \frac{\bar{\mathrm{F}}_2(p)}{x^2}, \qquad \bar{e}_{1r}^e(x,p) = -\frac{2p\eta\bar{\mathrm{F}}_1(p)}{x^3\left(p\eta+\mu_1\right)}, \qquad \bar{e}_{1\varphi}^e(x,p) = \frac{p\eta\bar{\mathrm{F}}_1(p)}{x^3\left(p\eta+\mu_1\right)} \tag{A.5}$$

where $\bar{\mathrm{F}}_1(p)$, $\bar{\mathrm{F}}_2(p)$ are arbitrary functions, what can be found from the boundary conditions at the interface. In initial material displacements are given by Lame formulae:

$$u^-(x,t) = \mathrm{A}_-(t)x + \frac{\mathrm{B}_-(t)}{x^2}, \qquad \bar{u}^-(x,p) = \bar{\mathrm{A}}_-(p)x + \frac{\bar{\mathrm{B}}_-(p)}{x^2} \tag{A.6}$$

in the case of sphere u^- is to be finite at $r = 0$, therefore $\mathrm{B}_-(t) = \bar{\mathrm{B}}_-(p) = 0$.

In order to determine the arbitrary functions $\mathrm{F}_1(p)$, $\mathrm{F}_2(p)$ and $\bar{\mathrm{A}}^-(p)$ we have to transform the boundary conditions (3.26) into Laplace space:

$$\begin{aligned}
&\bar{u}^+(\xi,p) = \bar{u}^-(\xi,p): && \mathrm{F}_1(p)\xi + \frac{\mathrm{F}_2(p)}{\xi^2} = \bar{\mathrm{A}}_-(p)\xi, \qquad \xi = \frac{a}{\mathrm{R}} \\
&\sigma_r^+(\xi,p) = \sigma_r^-(\xi,p): && 3k^+\mathrm{F}_1(p) - \frac{4}{\xi^3}\left(\frac{\mu_1\eta p}{\eta p+\mu_1} + \mu_2\right)\mathrm{F}_2(p) - k^+\vartheta^{tr} = 3k^-\bar{\mathrm{A}}_-(p), \\
&\sigma_r^+(1,p) = \sigma_0: && 3k^+\mathrm{F}_1(p) - 4\left(\frac{\mu_1\eta p}{\eta p+\mu_1} + \mu_2\right)\mathrm{F}_2(p) - k^+\vartheta^{tr} = \sigma_0
\end{aligned} \tag{A.7}$$

Then we have:

$$\bar{\mathrm{F}}_1(p) = \frac{\Upsilon_1}{3\Phi} + \frac{4\Upsilon_2\mu_1^2k^-\xi^3}{\eta\Phi^2\left(p+\mathrm{Q}\right)}, \quad \bar{\mathrm{F}}_2(p) = \frac{\Upsilon_2\xi^3}{\Phi} + \frac{\Upsilon_2\mu_1^2\left(\xi^3\left(k^+-k^-\right)-k^+\right)}{\eta\Phi^2\left(p+\mathrm{Q}\right)}, \quad \bar{\mathrm{A}}_-(p) = \frac{\Upsilon_3}{3\Phi} + \frac{4\Upsilon_2\mu_1^2k^+\left(\xi^3-1\right)}{\eta\Phi^2\left(p+\mathrm{Q}\right)} \tag{A.8}$$

where

$$\Upsilon_1 = 4(\mu_1+\mu_2)k^+\vartheta^{tr}\xi^3 - \left(\sigma_0 + k^+\vartheta^{tr}\right)\left(3k^- + 4\left(\mu_1+\mu_2\right)\right)$$

$$\Upsilon_2 = k^+k^-\vartheta^{tr} - \sigma_0\left(k^+ - k^-\right), \qquad \mathrm{Q} = \frac{\mu_1\Upsilon_4}{\eta\Phi}$$

$$\Upsilon_3 = 4\left(\mu_1+\mu_2\right)k^+\vartheta^{tr}\left(\xi^3-1\right) - \sigma_0\left(3k^- + 4\left(\mu_1+\mu_2\right)\right)$$

$$\Phi = 4\left(k^+ - k^-\right)\left(\mu_1+\mu_2\right)\xi^3 - k^+\left(3k^- + 4\left(\mu_1+\mu_2\right)\right)$$

$$\Upsilon_4 = 4\mu_2\left(k^+ - k^-\right)\xi^3 - k^+\left(3k^- + 4\mu_2\right)$$

Take the inverse Laplace transform, reminding that $\frac{1}{p-z} \xrightarrow{\mathrm{L}^{-1}} e^{zt}$:

$$\mathrm{F}_1(t) = \frac{\Upsilon_1}{3\Phi} + \frac{4\Upsilon_2\mu_1^2k^-\xi^3}{\eta\Phi^2}\exp\{-\mathrm{Q}t\}, \quad \mathrm{F}_2(t) = \frac{\Upsilon_2\xi^3}{\Phi} + \frac{\Upsilon_2\mu_1^2\left(\xi^3\left(k^+-k^-\right)-k^+\right)}{\eta\Phi^2}\exp\{-\mathrm{Q}t\} \tag{A.9}$$

$$\mathrm{A}_-(t) = \frac{\Upsilon_3}{3\Phi} + \frac{4\Upsilon_2\mu_1^2k^+\left(\xi^3-1\right)}{\eta\Phi^2}\exp\{-\mathrm{Q}t\} \tag{A.10}$$

Analogously, from (A.5) using (A.8), we obtain:

$$\tilde{e}^e_{1r}(p) = -\frac{2\Upsilon_2}{r^3\Phi} + \frac{2}{r^3}\frac{\Upsilon_2\Upsilon_4\mu_1\xi^3}{\eta\Phi^2\left(p+\mathrm{Q}\right)}, \qquad e^e_{1r}(t) = -\frac{2\Upsilon_2}{r^3\Phi} + \frac{2}{r^3}\frac{\Upsilon_2\Upsilon_4\mu_1\xi^3}{\eta\Phi^2}\exp\{-\mathrm{Q}t\} \tag{A.11}$$

Appendix B

Influence of plastic strains on a chemical reaction front propagation in spherically-symmetric problems of mechanochemistry with given displacement u_0

The solution of the spherically-symmetric problem of mechanochemistry with elastic reaction product is given in [42]. As it was shown in Chapter 3, the viscous strain do not affect the reaction kinetics, then the kinetics is the same as in the case of the elastic transformed material.

Here, we give the solution of the chemical reaction propagating in the sphere radius R with given displacement u_0 at the outer surface. The spherical reaction front propagates in the direction of the center of sphere. Transformed materials forms a spherical layer of thickness h. The chemical reaction is localized is on spherical reaction front of the radius $(\mathrm{R}-h)$ and divides the sphere onto regions occupied by the initial and new materials.

The solution of the diffusion problem for the spherical geometry was done in [42]. Here, we recall the resulting equations.The concentration of the diffusing constituent B_* at the reaction front is equal to

$$c(a)=\frac{c_*+n_*^2k_*\left(\dfrac{1-\xi}{\alpha}+\dfrac{\xi}{\mathrm{D}_0}\right)(1-\xi)c_{eq}}{1+n_*^2k_*\left(\dfrac{1-\xi}{\alpha}+\dfrac{\xi}{\mathrm{D}_0}\right)(1-\xi)},\qquad h=\mathrm{R}-a,\qquad \xi=\frac{h}{\mathrm{R}},\qquad \mathrm{D}_0=\frac{\mathrm{D}}{\mathrm{R}}$$

The reaction front velocity can be calculated as

$$\mathrm{V_N}=\frac{n_-\mathscr{M}_-}{\rho_-}\frac{k_*n_*}{1+n_*^2k_*\left(\dfrac{1-\xi}{\alpha}+\dfrac{\xi}{\mathrm{D}_0}\right)(1-\xi)}\left(c_*-c_{eq}\right)$$

The normal stresses σ_r, σ_φ satisfy the equilibrium equation

$$\frac{d\sigma_r}{dr}+2\frac{\sigma_r-\sigma_\varphi}{r}=0$$

and principal strains are

$$\varepsilon_r=\frac{du}{dr},\qquad \varepsilon_\varphi=\varepsilon_\vartheta=\frac{u}{r}$$

where u is the radial displacement.

In the spherical geometry the conditions (4.2) can be rewritten as follows

$$\dot{\mathbf{e}}^+=\dot{\mathbf{e}}^{el}+\dot{\mathbf{e}}^{pl}=\frac{\dot{\mathbf{s}}^+}{2\mu_+}+\begin{cases}0 & \text{if } |\sigma_r^+-\sigma_\varphi^+|<\sigma_{yd}\\ \dot{\lambda}\dfrac{\partial f}{\partial\boldsymbol{\sigma}^+} & \text{if } |\sigma_r^+-\sigma_\varphi^+|=\sigma_{yd}\end{cases}$$

Elastic stage

We consider that the first stage corresponds to a situation where all materials, initial and transformed, are elastic (the external loading is moderate as the sphere is in an elastic state). Solution for this step was done in 2.1.2. Here we recall the main equations, what are needed for further calculations.

Then the strains and stresses in the initial and transformed materials are determined by the following equations:

$$\boldsymbol{\varepsilon}^-=\mathrm{A}^-\mathbf{I},\quad \boldsymbol{\sigma}^-=3k_-\mathrm{A}^-\mathbf{I}$$

$$\boldsymbol{\varepsilon}^+=\left(\mathrm{A}^+-2\frac{\mathrm{B}^+}{r^3}\right)\mathbf{e_r}\mathbf{e_r}+\left(\mathrm{A}^++\frac{\mathrm{B}^+}{r^3}\right)(\mathbf{I}-\mathbf{e_r}\mathbf{e_r})$$

$$\boldsymbol{\sigma}^+=\left(k_+\left(3\mathrm{A}^+-\varepsilon^{tr}\right)-4\mu_+\frac{\mathrm{B}^+}{r^3}\right)\mathbf{e_r}\mathbf{e_r}+\left(k_+\left(3\mathrm{A}^+-\varepsilon^{tr}\right)+2\mu_+\frac{\mathrm{B}^+}{r^3}\right)(\mathbf{I}-\mathbf{e_r}\mathbf{e_r})\qquad\text{(B.1)}$$

where where $\mathbf{e}_r$ is a unit radial vector, and A^-, B^-, A^+ and B^+ are found from the boundary conditions and conditions at the reaction front:

$$B^+ = \frac{\left(\frac{3u_0[\![k]\!]}{R} - k_+\vartheta^{tr}\right)R^3(1-\xi)^3}{4\mu_+ + 3k_- + 3[\![k]\!](1-\xi)^3}$$

$$A^+ = \frac{\frac{(4\mu_+ + 3k_-)u_0}{R} + k_+\vartheta^{tr}(1-\xi)^3}{4\mu_+ + 3k_- + 3[\![k]\!](1-\xi)^3}$$

$$A^- = \frac{\frac{(4\mu_+ + 3k_-)u_0}{R} + k_+\vartheta^{tr}(1-\xi)^3 + \left(\frac{3u_0[\![k]\!]}{R} - k_+\vartheta^{tr}\right)\frac{R^3}{a^3}(1-\xi)^3}{4\mu_+ + 3k_- + 3[\![k]\!](1-\xi)^3}$$

where $\xi = \frac{h}{R}$ - is the relative thickness of the transformed material such as $\xi \in [0,1]$ or the degree of the chemical transformation and $h = R - a$; $[\![k]\!] = k_- - k_+$.

In order to evaluate the time and location of plastic flow onset, von Mises criterion, i.e. $|\sigma_r - \sigma_\varphi| = \sigma_{yd}$, is used. Taking into account (4.23), conducts to

$$|\sigma_r - \sigma_\phi| = 6\mu_+ \left| \frac{\frac{3u_0[\![k^{-1}]\!]}{R} + \frac{\vartheta^{tr}}{k_-}}{3[\![k^{-1}]\!] - \frac{4\mu_+ + 3k_-}{k_+k_-(1-\xi)^3}} \right| \frac{R^3}{r^3}$$

The modulus $|\sigma_r - \sigma_\varphi|$ has a maximum at $r = a$ (Fig. 4.5), therefore initial plastic zone (if it appears) is located in $r = a$, what corresponds to the reaction front position. The maximum of the modulus is found out as:

$$|\sigma_r - \sigma_\phi|_{max} = \frac{6\mu_+ \left| \frac{3u_0[\![k^{-1}]\!]}{R} + \frac{\vartheta^{tr}}{k_-} \right|}{\frac{4\mu_+ + 3k_-}{k_+k_-} - 3[\![k^{-1}]\!](1-\xi)^3} \tag{B.2}$$

If the external displacement u_0 is constant, then $|\sigma_r - \sigma_\varphi|$ increases only due to the front propagation, i.e increasing of ξ. Then the value $|\sigma_r - \sigma_\varphi|_{max}$ reaches the yield stress σ_{yd}, when the thickness of the transformed material is equal to $h^*(t_*) = \xi^*(t_*)R$, such as:

$$\frac{6\mu_+ \left| \frac{3u_0[\![k^{-1}]\!]}{R} + \frac{\vartheta^{tr}}{k_-} \right|}{\frac{4\mu_+ + 3k_-}{k_+k_-} - 3[\![k^{-1}]\!](1-\xi^*)^3} = \sigma_{yd}$$

From where ξ^* is found out as:

$$\xi^*(t_*) = 1 - \sqrt[3]{\frac{4\mu_+ + 3k_+}{3(k_+ - k_-)} - \frac{2\mu_+}{[\![k^{-1}]\!]\sigma_{yd}} \left| \frac{3u_0[\![k^{-1}]\!]}{R} + \frac{\vartheta^{tr}}{k_-} \right|}$$

When the front position $\xi < \xi^*$ the sphere remains in an elastic state. When $\xi = \xi^*$ the material of the sphere goes over into a plastic state on the surface $r = a$. A second (plastic) front appears at the reaction front, it has it own velocity and direction. On further chemical transformation the region of plastic deformation is enlarged.

If u_0 is a linear function of time, i.e $u_0(t) = \mathscr{S}t$, then $|\sigma_r - \sigma_\varphi|$ increases due to the front propagation as well as increasing of u_0 in time. Then the value $|\sigma_r - \sigma_\varphi|_{max}$ reaches the yield stress σ_{yd},

when the thickness of the transformed material is equal to $h^*(t_*) = \xi^*(t_*)\mathrm{R}$ and at the same time when $u_0(t_*) = \mathscr{S} t_* = u_0^*$:

$$u_0^* = \mathscr{S} t_* = \operatorname{sign}\left(\sigma_r - \sigma_\varphi\right) \frac{\sigma_{yd}\mathrm{R}}{18\mu_+}\left(3\left(1-\xi^*\right)^3 + \frac{4\mu_+ + 3k_-}{[\![k]\!]}\right) + \frac{k_+ \mathrm{R}\vartheta^{tr}}{3[\![k]\!]}$$

When the displacement $u_0(t) < u^*$ the sphere remains in an elastic state. When $u_0(t) = u^*$ the material of the sphere goes over into a plastic state on the surface $r = a$. Similarly to how it was described above for the case of the constant external loading, the plastic reaction front arises at the reaction front, and with further propagation of the chemical reaction the plastic deformation region increases.

Elasto-plastic state

In this section we find the stress and displacement field in the elastoplastic regime. We show that in this regime a second front (plastic front) appears. Two fronts have their own velocities and directions. We show that plastic zone expands in two directions. We determine the relation between the radius of the plastic zone, reaction front and external stress. We determine the limit stress that produces failure by excessive deformation.

When u_0 is constant and the thickness h of the transformed material becomes larger than h^*, or u_0 is linear time-dependent and is larger than u^*, a natural assumption is that the plastic zone takes a region $a < r < \varsigma$, with ς a position of the plastic front, meanwhile the region $\varsigma < r < \mathrm{R}$ remains in the elastic regime. The radial stress σ_r is continuous at the boundary between the elastic and plastic zone.

Elastic zone in the transformed material: $\varsigma < r < \mathrm{R}$

The stresses in elastic transformed layer are defined by equation (B.1):

$$\sigma_r^e = 3k_+\mathrm{A}^+ - 4\mu_+\frac{\mathrm{B}^+}{r^3} - k_+\vartheta^{tr}$$
$$\sigma_\varphi^e = 3k_+\mathrm{A}^+ + 2\mu_+\frac{\mathrm{B}^+}{r^3} - k_+\vartheta^{tr}$$

where A^+ and B^+ from the boundary conditions:

$$|\sigma_r^+ - \sigma_\varphi^-|\Big|_\varsigma = \sigma_{yd}, \qquad u|_\mathrm{R} = u_0$$

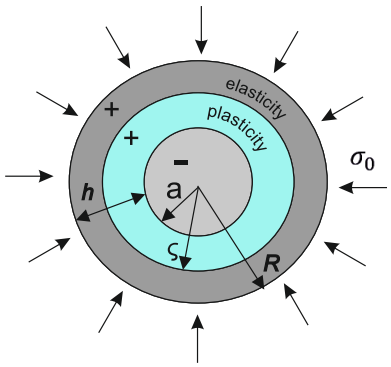

Figure B.1: Elasto-plastic state.

Hence we obtain

$$\mathrm{B}^{+} = -\operatorname{sign}\left(\sigma_r - \sigma_\varphi\right)\frac{\sigma_{yd}\varsigma^3}{6\mu_+}$$
$$\mathrm{A}^{+} = \frac{u_0}{\mathrm{R}} + \operatorname{sign}\left(\sigma_r - \sigma_\varphi\right)\frac{\sigma_{yd}\varsigma^3}{6\mu_+\mathrm{R}^3}$$

Then the stress components in the elastic zone are given by the equations:

$$\sigma_r^e = \frac{3k_+u_0}{\mathrm{R}} - k_+\vartheta^{tr} + \operatorname{sign}\left(\sigma_r - \sigma_\varphi\right)\frac{\sigma_{yd}\varsigma^3}{6\mu_+}\left(\frac{4\mu_+}{r^3} + \frac{3k_+}{\mathrm{R}^3}\right)$$
$$\sigma_\phi^e = \frac{3k_+u_0}{\mathrm{R}} - k_+\vartheta^{tr} - \operatorname{sign}\left(\sigma_r - \sigma_\varphi\right)\frac{\sigma_{yd}\varsigma^3}{6\mu_+}\left(\frac{2\mu_+}{r^3} - \frac{3k_+}{\mathrm{R}^3}\right)$$

Plastic zone: $a < r < \varsigma$

We will study the plastic zone. The elastic formulation is not applicable anymore. Since the strain remains a priori undetermined, the stress components for any point in the plastic zone can be determined only from the equilibrium equations and the plasticity criterion

$$\frac{\partial\sigma_r^{pl}}{\partial r} + 2\frac{\sigma_r^{pl} - \sigma_\varphi^{pl}}{r} = 0, \qquad \left|\sigma_r - \sigma_\varphi\right| = \sigma_{yd}$$

We have the set of continuity equations:

$$\begin{aligned}\sigma_r^{pl}(a) &= \sigma_r^{-}(a), \qquad u^{pl}(a) = u^{-}(a)\\ \sigma_r^{pl}(\varsigma) &= \sigma_r^{el}(\varsigma), \qquad u^{pl}(\varsigma) = u^{el}(\varsigma)\end{aligned} \tag{B.3}$$

So from (4.35) it follows that:

$$\frac{\partial\sigma_r^{pl}}{\partial r} + 2\frac{\sigma_{yd}}{r} = 0, \qquad \sigma_r^{pl} = -\operatorname{sign}\left(\sigma_r - \sigma_\varphi\right)2\sigma_{yd}\ln r + \mathscr{C}_1 \tag{B.4}$$

where $\mathscr{C}_1$ is an integration constant, can be determined from the continuity of stress (B.3):

$$\mathscr{C}_1 = 3k_-\mathrm{A}^{-} + \operatorname{sign}\left(\sigma_r - \sigma_\varphi\right)\cdot 2\sigma_{yd}\ln a \tag{B.5}$$

Using the another one boundary condition $\sigma_r^p(\varsigma) = \sigma_r^e(\varsigma)$, we obtain:

$$-3k_-\mathrm{A}^{-} + \frac{3k_+u_0}{\mathrm{R}} - k_+\vartheta^{tr} = \operatorname{sign}\left(\sigma_r - \sigma_\varphi\right)\sigma_{yd}\left(2\ln\frac{a}{\varsigma} - \frac{\varsigma^3}{6\mu_+}\left(\frac{4\mu_+}{\varsigma^3} + \frac{3k_+}{\mathrm{R}^3}\right)\right) \tag{B.6}$$

Substitute (**??**) to (B.6), we obtain equation for A^{-}

$$\mathrm{A}^{-} = \frac{1}{3k_-}\left(\frac{3k_+u_0}{\mathrm{R}} - k_+\vartheta^{tr} + \operatorname{sign}\left(\sigma_r - \sigma_\varphi\right)\sigma_{yd}\left(\frac{\varsigma^3}{6\mu_+}\left(\frac{4\mu_+}{\varsigma^3} + \frac{3k_+}{\mathrm{R}^3}\right) + 2\ln\frac{\varsigma}{a}\right)\right) \tag{B.7}$$

Due to the spherical symmetry, only the radial component of the displacement is not equal to zero. Taking into account $\sigma^{+} = k_+\left(\vartheta^{+} - \vartheta^{tr}\right)$, $\varepsilon_r = \dfrac{du}{dr}$ and $\varepsilon_\varphi = \dfrac{u}{r}$, we obtain the differential equation for the total displacement in plastic zone:

$$\frac{3k_+\left(r^2u^p\right)_r'}{r^2} = \frac{9k_+u_0}{\mathrm{R}} + 3\left(\sigma_r - \sigma_\varphi\right)\sigma_{yd}\left(\frac{k_+\varsigma^3}{2\mu_+\mathrm{R}^3} + \ln\frac{\varsigma^2}{r^3} - \frac{1}{3}\right)$$

As a result, we obtain an expression for determining the total displacement in plastic zone::

$$u^p = \frac{u_0}{\mathrm{R}} r + \operatorname{sign}\left(\sigma_r - \sigma_\varphi\right) \frac{\sigma_{yd}}{3k_+} \left(\frac{2}{3} + \frac{k_+ \varsigma^3}{2\mu_+ \mathrm{R}^3} + 2\ln\frac{\varsigma}{r} \right) r + \frac{\mathscr{C}_2}{r^2}$$

where $\mathscr{C}_2$ - is a constant, we find it from the boundary condition.

Take into account (**??**) and (B.7), rewrite (B.5) and obtain a formula for σ_r^p:

$$\sigma_r^p = \frac{3k_+ u_0}{\mathrm{R}} - k_+ \vartheta^{tr} + \operatorname{sign}\left(\sigma_r - \sigma_\varphi\right) \sigma_{yd} \left(\frac{2}{3} + \frac{k_+ \varsigma^3}{2\mu_+ \mathrm{R}^3} + 2\ln\frac{\varsigma}{r} \right) \tag{B.8}$$

Using the condition of the continuity of the displacement $u^p(\varsigma) = u^e(\varsigma)$, we obtain a formulae for determining the constant $\mathscr{C}_2$

$$\frac{u_0}{\mathrm{R}}\varsigma + \operatorname{sign}\left(\sigma_r - \sigma_\varphi\right) \frac{\sigma_{yd}\varsigma}{6\mu_+} \left(\frac{\varsigma^3}{\mathrm{R}^3} - 1 \right) = \frac{u_0}{\mathrm{R}}\varsigma + \left(\sigma_r - \sigma_\varphi\right) \frac{\sigma_{yd}\varsigma}{3k_+} \left(\frac{2}{3} + \frac{k_+ \varsigma^3}{2\mu_+ \mathrm{R}^3} \right) + \frac{\mathscr{C}_2}{\varsigma^2}$$

$$\mathscr{C}_2 = -\operatorname{sign}\left(\sigma_r - \sigma_\phi\right) \cdot \frac{\sigma_{yd}\left(3k_+ + 4\mu_+\right)}{18k_+\mu_+} \varsigma^3$$

Using the condition of the continuity of the displacement at the interface $u^p(a) = u^-(a)$, we obtain the equation for ς

$$a\left(\frac{u_0}{\mathrm{R}} \left(\frac{k_+}{k_-} - 1 \right) - \frac{k_+ \vartheta^{tr}}{3k_-} \right) = \operatorname{sign}\left(\sigma_r - \sigma_\varphi\right) \frac{\sigma_{yd}}{3} \left(a[\![k^{-1}]\!] \left(\frac{2}{3} + \frac{k_+ \varsigma^3}{2\mu_+ \mathrm{R}^3} + 2\ln\frac{\varsigma}{a} \right) - \frac{\left(3k_+ + 4\mu_+\right)\varsigma^3}{6k_+\mu_+} \right)$$

We know the total displacement in plastic zone, then we can calculate the total strain in plastic zone:

$$\varepsilon_r = \frac{u_0}{\mathrm{R}} + \operatorname{sign}\left(\sigma_r - \sigma_\varphi\right) \frac{\sigma_{yd}}{3k_+} \left(2\ln\frac{\varsigma}{r} - \frac{4}{3} + \frac{k_+ \varsigma^3}{2\mu_+ \mathrm{R}^3} + \frac{\left(3k_+ + 4\mu_+\right)\varsigma^3}{3\mu_+ r^3} \right)$$

$$\varepsilon_\phi = \frac{u_0}{\mathrm{R}} + \operatorname{sign}\left(\sigma_r - \sigma_\varphi\right) \frac{\sigma_{yd}}{3k_+} \left(2\ln\frac{\varsigma}{r} + \frac{2}{3} + \frac{k_+ \varsigma^3}{2\mu_+ \mathrm{R}^3} - \frac{\left(3k_+ + 4\mu_+\right)\varsigma^3}{6\mu_+ r^3} \right)$$

Since plasticity does not produce any volume change, the volume variation is due to the elastic strain only, $e_r - e_\phi = \dfrac{1}{2\mu_+}\left(\sigma_r - \sigma_\phi\right) + e_r^p - e_\phi^p$, we obtain the plastic deformation

$$\boldsymbol{e}^p = \operatorname{sign}\left(\sigma_r - \sigma_\phi\right) \cdot \frac{\sigma_{yd}\left(3k_+ + 4\mu_+\right)}{6\mu_+ k_+} \left(\frac{\varsigma^3}{r^3} - 1 \right) \boldsymbol{\alpha}$$

Then the derivative of the plastic deformation

$$\dot{\boldsymbol{e}}^p = \operatorname{sign}\left(\sigma_r - \sigma_\phi\right) \cdot \frac{\sigma_{yd}\left(3k_+ + 4\mu_+\right)}{2\mu_+ k_+} \frac{\varsigma^2 \dot{\varsigma}}{r^3} \boldsymbol{\alpha}$$

We compare the result with the associated flow law, and we obtain the equation for determining $\dot{\lambda}$

$$\dot{\lambda} = \operatorname{sign}\left(\sigma_r - \sigma_\phi\right) \cdot \frac{\sigma_{yd}\left(3k_+ + 4\mu_+\right)}{3\mu_+ k_+} \frac{\varsigma^2 \dot{\varsigma}}{r^3}, \quad \dot{\lambda} \geq 0$$

Notations

$n_{\pm,*}$	Stoichiometric coefficients
$\mathbf{M}$	Chemical potential tensor
μ_*	Chemical potential of the diffusing constituent
$\mathbf{A}$	Chemical affinity tensor
A_{NN}	Normal component of affinity tensor
$\mathscr{M}_{\pm,*}$	Molar masses
k_*	Kinetic constant
R_g	Universal gas constant
c	Molar concentration of the diffusive constituent per unit volume
ω	Reaction rate
V_N	Reaction front velocity of surface element with normal $\boldsymbol{N}$
T	Temperature
t	Time
ρ	Mass density
f_*	Referential chemical energy of the diffusing constituent
c_*	Solubility of the diffusing constituent
γ	Temperature-dependent chemical energy parameter
$f_0^{\pm}$	Chemical energy
$w_{\pm}$	Strain energies of the solid constituents per unit volume
$\boldsymbol{\sigma}$	Stress
$\boldsymbol{\varepsilon}$	Strain
$\boldsymbol{\varepsilon}^{tr}$	Transformation strain
$\mathbf{s}$	Deviatoric stress
$\mathbf{e}$	Deviatoric strain
c_{eq}	Equilibrium concentration of the diffusing constituent
$\mathbf{j}_*$	Gas diffusion flux
D	Diffusion coefficient of the diffusive reactant through the transformed material
α	Mass transfer coefficient
$k_{\pm}$	Bulk modulus
$\mu_{\pm}$	Shear modulus
R	Initial radius of sphere or cylinder
H	Initial thickness of the plate
h	Thickness of the transformed layer
ξ	Relative thickness or degree of the chemical transformation
η	Viscosity coefficient
σ_{yd}	Yield stress
$\dot{\lambda}$	Plastic multiplier

List of figures

List of Tables

Bibliography

[1] M. Abbas, L. Guo, and H. Guo. Evaluation of stress distribution and failure mechanism in lanthanum-titanium-aluminum oxides thermal barrier coatings. *Ceramics International*, 2013.

[2] R. Abeyaratne and J. K. Knowles. *Evolution of Phase Transitions. A Continuum Theory*. Cambridge University Press, Cambridge et al., 2006.

[3] L. Anand and S. Narayan. An elastic-viscoplastic model for lithium. *Journal of the Elecrochemical Society*, 116:A1092–A1095, 2019.

[4] A. Atkinson and R.I. Taylor. The self-diffusion of ni in nio and its relevance to the oxidation of ni. *Journal of Materials Science*, 13:427–432, 1978.

[5] H.V. Atkinson. Evolution of grain structure in nickel oxide scales. *Oxidation of Metals*, 28, 1987.

[6] A. Auge, A. Weddemann, B. Vogel, F. Wittbracht, and A. Hutten. A level set based approach for modeling oxidation processes of ligand stabilized metallic nanoparticles. *APPl. Phys. Lett.*, 96:093111, 2010.

[7] L.Y. Beaulieu, K.W. Eberman, R.L. Turner, L.J. Krause, and J.R. Dahn. Colossal reversible volume changes in lithium alloys. *Electrochem. Solid-State Lett.*, 4:137–140, 2001.

[8] R.M. Bowen. Toward a thermodynamics and mechanics of mixtures. *Arch. Rat. Mech. Anal.*, 24:370–403, 1967.

[9] A.F. Bower and P.R. Guduru. A simple finite element model of diffusion, finite deformation, plasticity and fracture in lithium ion insertion electrode materials. *Modelling and Simulation in Materials Science and Engineering*, 20 (4):045004, 2012.

[10] A.F. Bower, P.R. Guduru, and E. Chason. Analytical solutions for composition and stress in spherical elastic-plastic lithium-ion electrode particles containing a propagating phase boundary. *International Journal of Solids and Structures*, 69–70:328–342, 2015.

[11] A.F. Bower, P.R. Guduru, and V.A. Sethuraman. A finite strain model of stress, diffusion, plastic flow, and electrochemical reactions in a lithium ion half-cell. *Journal of the Mechanics and Physics of Solids*, 59 (4):804–828, 2011.

[12] L. Brassart and Z. Suo. Reactive flow in large-deformation electrodes of lithium-ion batteries. *International Journal of Applied Mechanics*, 4 (3):1250023, 2012.

[13] L. Brassart and Z. Suo. Reactive flow in solids. *Journal of the Mechanics and Physics of Solids*, 61 (1):61–77, 2013.

[14] L. Brassart, K. Zhao, and Z. Suo. Cyclic plasticity and shakedown in high-capacity electrodes of lithium-ion batteries. *International Journal of Solids and Structures*, 50:1120–1129, 2013.

[15] C.C. Buttner and M. Zacharias. Retarded oxidation of Si nanowires. *Applied physics letter*, 89, 2006.

[16] N. Cabrera and N.F. Mott. Theory of the oxidation of metals. *Reports on Progress in Physics*, 12:163, 1949.

[17] C.K. Chan, H. Peng, G. Liu, K. McIllwrath, X.F. Zhang, R.A. Huggins, and Y. Cui. High-performance lithium battery anodes using silicon nanowires. *Nature Nanotechnology*, 3:31–35, 2008.

[18] H. Chen, S.H. Kim, C. Kim, J. Chen, and C. Jang. Corrosion behaviors of four stainless steels with similar chromium content in supercritical carbon dioxide environment at 650°c. *Corrosion Science*, 156:16–31, 2019.

[19] H. Coffin, C. Bonafos, S. Schamm, N. Cherkashin, G. Ben Assayag, A. Claverie, M. Respaud, P. Dimitrakis, and P. Normand. Oxidation of Si nanocrystals fabricated by ultralow-energy ion implantation in thin SiO_2 layers. *Applied Physics*, 99:044302, 2006.

[20] T.H. Courtney. *Mechanical behavior of materials*. McGraw-Hill, New York, 2000.

[21] Z.W. Cui, F. Gao, and J.M. Qu. A finite deformation stress-dependent chemical potential and its applications to lithium ion batteries. *Journal of the Mechanics and Physics of Solids*, 60 (7):1280–1295, 2012.

[22] Z.W. Cui, F. Gao, and J.M. Qu. Interface-reaction controlled diffusion in binary solids with applications to lithium ion batteries. *Journal of the Mechanics and Physics of Solids*, 61 (2):293–310, 2013.

[23] H. Dal and C. Miehe. Computational electro-chemo-mechanics of lithium-ion battery electrodes at finite strains. *Computational Mechanics*, 2:303–325, 2015.

[24] S.G. Danjumma, Y. Abubakar, and S. Suleiman. Nickel oxide (NiO) devices and applications: a review. *International Journal of Engineering Research and Technology*, 8:2278–0181, 2019.

[25] Th. De Donder and P. Van Rysselberghe. *Thermodynamic Theory of Affinity: A Book of Principles*. Stanford University Press, Stanford University, Stanford, 1936.

[26] E. Deal and A.S. Grove. General relationship for the thermal oxidation of silicon. *Applied Physics*, 36:3770–3778, 1965.

[27] S. Deb. 2 - degradable polymers and polymer composites for tissue engineering. *Cellular Response to biomaterials*, pages 28–60, 2009.

[28] C.V. Di Leo, E. Rejovitzky, and L. Anand. Diffusion-deformation theory for amorphous silicon anodes: The role of plastic deformation on electrochemical performance. *Int. Journal of Solids and Structures*, 67–68:283–296, 2015.

[29] B.J. Dimitrijevic, K.E. Aifantis, and K. Hackl. The influence of particle size and spacing on the fragmentation of nanocomposite anodes for li batteries. *Journal of Power Sources*, 206:343–348, 2012.

[30] E.P. EerNisse. Viscous flow of thermal SiO_2. *Applied Physics Letters*, 30:290, 1977.

[31] E.P. EerNisse. Stress in thermal SiO_2 during growth. *Applied Physics Letters*, 35:8, 1979.

[32] B. EMaack and N. Nilius. Morphological and kinetic insights into $Cu_2O - CuO$ oxidation. *Basic Solid State Physics*, 257:1900365, 2019.

[33] A. Ermoline and E. Dreizin. Equations for the cabrera-mott kinetics of oxidation for spherical nanoparticles. *Chemical Physics Letters*, 505:47–50, 2011.

[34] A. Ermoline, M. Schoenitz, and E. Dreizin. Reactions leading to ignition in fully dense nanocomposite Al-oxide systems. *Combustion and Flame*, 158:1076–1083, 2011.

[35] A.G. Evans, D. Rajdev, and D.L. Douglass. The mechanical properties of nickel oxide and their relationship to the morphology of thick oxide scales formed on nickel. *Oxidation of Metals*, 4, 1972.

[36] J. Everaerts, E. Salvati, H. Li, W. Li, and A. Korsunsky. Mechanical properties of thermally grown submicron oxide layers on a nickel-based superalloy. *Corrosion Science*, 165:108388, 2020.

[37] A. B. Freidin. On chemical reaction fronts in nonlinear elastic solids. In D.A. Indeitsev and A. M. Krivtsov, editors, *Proc. of the XXXVII Summer School–Conference Advanced Problems in Mechanics (APM 2009), St. Petersburg (Repino), June 30 – July 5, 2009*, pages 231–237. Institute for Problems in Mechanical Engineering of Russian Academy of Sciences, 2009.

[38] A. B. Freidin. Chemical affinity tensor and stress-assist chemical reactions front propagation in solids. In *Proceedings of the ASME 2013 International Mechanical Engineering Congress and Exposition*, volume 9, page V009T10A102. American Society of Mechanical Engineers, 2013.

[39] A. B. Freidin and L. L. Sharipova. Forbidden strains and stresses in mechanochemistry of chemical reaction fronts. In H. Altenbach, J. Pouget, M. Rousseau, B. Collet, and T. Michelitsch, editors, *Generalized Models and Non-classical Approaches in Complex Materials 1. Advanced Structured Materials*, volume 89, pages 335–348. Springer, Cham, 2018.

[40] A.B. Freidin. On a chemical affinity tensor for chemical reactions in deformable solids. *Mechanics of Solids*, 50(3):260–285, 2015.

[41] A.B. Freidin, I.K. Korolev, S.P. Aleshchebko, and E.N. Vilchevskaya. Chemical affinity tensor and chemical reaction front propagation: Theory and fe-simulations. *International Journal of Fracture*, 202 (2):245–259, 2016.

[42] A.B. Freidin, N.F. Morozov, S.E. Petrenko, and E.N. Vilchevskaya. Chemical reactions in spherically-symmetric problems of mechanochemestry. *Acta Mechanica*, 227 (1):43–56, 2016.

[43] A.B. Freidin and E.N. Vilchevskaya. *Chemical Affinity Tensor in Coupled Problems of Mechanochemistry*. Altenbach H., Ã–chsner A. (eds) Encyclopedia of Continuum Mechanics, Springer, Berlin, Heidelberg, 2020.

[44] A.B. Freidin, E.N. Vilchevskaya, and I.K. Korolev. Stress-assist chemical reactions front propagation in deformable solids. *International Journal of Engineering Science*, 83:57–75, 2014.

[45] H. Galinski, A. Bieberle-Hutter, J. Rupp, and L. Gauckler. Nonlinear oxidation kinetics of nickel cermets. *Acta Materialia*, 59:6239–6245, 2011.

[46] T. Gheno, D. Monceau, and D. Young. Kinetics of breakaway oxidation of $Fe-Cr$ and $Fe-Cr-Ni$ alloys in dry and wet carbon dioxide. *Corrosion Science*, 77:246–256, 2013.

[47] J. Gibbs. *The Collected Works of J.W. Gibbs, Vol. 1: Thermodynamics*. Yale University Press, London, 1948.

[48] M. Grinfeld. *Thermodynamic Methods in the Theory of Heterogeneous Systems*. Longman, Sussex, 1991.

[49] R. Haugsrud. On the high-temperature oxidation of nickel. *Corrosion Science*, 45:211–235, 2003.

[50] R. Hay. Calculation of growth stress in SiO_2 scales formed by oxidation of SiC fibers. *Ceramic Engineering and Science Proceedings*, 2012.

[51] T.W. Heo, K.B. Colas, A.T. Motta, and L.-Q. Chen. A phase-field model for hydride formation in polycrystalline metals: application to δ-hydride in zirconium alloys. *Acta Materialie*, 181:262–277, 2019.

[52] S.H. Hsieh, J.M. Hsieh, W.J. Chen, and C.C. Chuang. Electroless nickel deposition for front side metallization of silicon solar cells. *Materials*, 10:942, 2017.

[53] C.H. Hsueh and A.G. Evans. Oxidation induced stresses and some effects on the behavior of oxide films. *Journal of Applied Physics*, 54:6672, 1983.

[54] C. K. Huang, R. J. Jaccodine, and S. R. Butler. Stress effect on the oxidation of silicon. In V. J. Kapoor and K. T. Hankins, editors, *Silicon Nitride and Silicon Dioxide Thin Insulating Film*, volume 87–10, pages 343–349. The Electrochemical Society, Pennington NJ, 1987.

[55] B. Iwanschitz, L. Holzer, A. Mai, and M. Schutze. Nickel agglomeration in solid oxide fuel cells: The influence of temperature. *Solid State Ionics*, 211:69–73, 2012.

[56] N.S. Jacobson, D.S. Fox, and E.J. Opilab. High temperature oxidation of ceramic matrix composites. *Computers and Chemical Engineering*, 35:1923–1836, 2011.

[57] Z. Jia and T. Li. Stress-modulated driving force for lithiation reaction in hollow nano-anodes. *Journal of Power Sources*, 275:866–876, 2015.

[58] H. Kahn, R. Ballarini, J.J. Bellante, and A.H. Heuer. Fatigue failure in polysilicon not due to simple stress corrosion cracking. *Science*, 298:1215–1218, 2002.

[59] D.B. Kao, J.P. McVitie, W.D. Nix, and K.S. Saraswat. Two dimensional silicon oxidation experiment and theory. *In IEDM Tech. Dig*, pages 388–391, 1985.

[60] D.B. Kao, J.P. McVitie, W.D. Nix, and K.S. Saraswat. Two dimensional thermal oxidation of silicon-i. experiments. *IEEE Trans. Electron Devices*, ED-34:1008–1017, 1987.

[61] D.B. Kao, J.P. McVitie, W.D. Nix, and K.S. Saraswat. Two dimensional thermal oxidation of silicon-ii. modeling stress effect in wet oxides. *IEEE Trans. Electron Devices*, ED-35:25–37, 1988.

[62] R. Karmhag, T. Tesfamichael, E. Wackelgard, G. Nicklasson, and M. Nygren. Oxidation kinetics of nickel particles: comparison between free particles and particles in an oxide matrix. *Solar Energy*, 68:329–333, 2000.

[63] N. Kaur, E. Comini, N. Poli, D. Zappa, and G. Sberveglieri. Nickel oxide nanowires growth by VLS technique for gas sensing application. *Procedia Engineering*, 120:760–763, 2015.

[64] S.T. Kelly and B.M. Clemens. Moving interface hydride formation in multilayered metal thin films. *J. Applied Physics*, 108(1), 2010.

[65] U. Khalilov, G. Pourtois, A.C.T. van Duin, and E.C. Neyts. Self-limiting oxidation in small-diameter Si nanowires. *Chemistry of Materials*, 24:2141–2147, 2012.

[66] E.S. Kikkinides. Design and optimization of hydrogen storage units using advanced solid materials: General mathematical framework and recent developments. *Computers and Chemical Engineering*, 35:1923–1936, 2011.

[67] M. Klinsmann, D. Rosato, M. Kamhal, and R.M. McMeeking. Modeling crack growth during Li extraction and insertion within the second half cycle. *Journal of Power Sources*, 331:32–42, 2016.

[68] M. Klinsmann, D. Rosato, M. Kamhal, and R.M. McMeeking. Modeling crack growth during Li insertion in storage particles using a fracture phase field approach. *Journal of the Mechanics and Physics of Solids*, 92:313–344, 2016.

[69] D. Knoll, T. Grabolla, and E. Bugiel. Influence of mechanical stress on thermal oxidation phenomena of silicon. *Cryst. Res. Technol.*, 22:713–722, 1987.

[70] J.K. Knowles. On the dissipation associated with equilibrium shocks in finite elasticity. *J. Elasticity*, 9:131–158, 1979.

[71] A.G. Knyazeva. Cross effects in solid media with diffusion. *Journal of Applied Mechanics and Technical Physics*, 44:373–384, 2003.

[72] A.G. Knyazeva. Application of irreversible thermodynamics to diffusion in solids with internal surfaces. *Journal of Non-Equilibrium Thermodynamics*, 45(4):401–418, 2020.

[73] E. Kobeda and E.A. Irene. SiO_2 film stress distribution during thermal history on stress-related properties of very thin films of thermally grown silicon dioxide. *Journal of Vacuum Science and Technology*, B 6:574, 1988.

[74] E. Kobeda and E.A. Irene. In situ stress measurements during thermal oxidation of silicon. *Journal of Vacuum Science and Technology*, B 7:163, 1989.

[75] V.P. Kofstad. *High temperature corrosion*. Elsevier Applied Science Publishers Ltd., London – New York, 1988.

[76] C. Krzeminski and X.-L. Han. Understanding of the retarded oxidation effects in silicon nanostructures. *Applied Physics Letters*, 100:26, 2012.

[77] D. Laboureur, G. Glabeke, and J.-B. Gouriet. Validation of cabrera-mott model for low-temperature oxidation of aluminum nanoparticles. *Journal of Nanoparticles Research*, 23, 2021.

[78] E.H. Lee. Elastic-plastic deformation at finite strains. *ASME J. Appl. Mech.*, 36:1–8, 1969.

[79] J. Leszczynski, K. Wojciechowski, and A.L. Malecki. Studies on thermal decomposition and oxidation of $CoSb_3$. *Journal of Thermal Analysis and Calorimetry*, 105, 2011.

[80] V.I. Levitas and H. Attariani. Anisotropic compositional expansion and chemical potential for amorphous lithiated silicon under stress tensor. *Scientific Reports*, 3:1615, 2013.

[81] J. Li, A.K. Dozier, Y. Li, F. Yang, and Y.-T. Cheng. Crack pattern formation in thin film lithium-ion battery electrodes. *J. Electrochem. Soc.*, 158:689–694, 2011.

[82] M.H. Li, X.F. Sun, J.G. Li, Z.Y. Zhang, T. Jin, and Guan H.R. Oxidation behavior of a single-crystal Ni-based superalloy in air: at 800 and 900°c. *Oxidation of Metals*, 59, 2003.

[83] C.-C. Lin and K.S.2 Anseth. Chapter ii.4.3 - the biodegradation of biodegradable polymeric biomaterials. *Biomaterials Science (Third Edition)*, pages 716–728, 2013.

[84] L. Liu, G.-Y. Kim, and A. Chandra. Modeling of thermal stresses and lifetime prediction of planar solid oxide fuel cell under thermal cyclic conditions. *Journal of Power Sources*, 195:2310–2318, 2010.

[85] X. Liu, F. Fan, H. Yang, S. Zhang, J.Y. Huang, and T. Zhu. Self-limiting lithiation in silicon nanowires. *ACS NANO*, 7:1495–1503, 2013.

[86] X. Liu, J. Wang, and S. et al. Huang. In situ atomic-scale imaging of electrochemical lithiation in silicon. *Nature Nanotech*, 7:749–756, 2012.

[87] X. Liu, L. Zhong, S. Huang, S.X. Mao, T. Zhu, and J.Y. Huang. Size-dependent fracture of silicon nanoparticles during lithiation. *ACS NANO*, 6:1522–1531, 2012.

[88] X.H. Liu, L. Zhong, S. Huang, S.X. Mao, T. Zhu, and J.Y. Huang. Size-dependent fracture of silicon nanoparticles during lithiation. *ACS NANO*, 6:1522–1531, 2012.

[89] K. Loeffel and L. Anand. A chemo-thermo-mechanically coupled theory for elastic-viscoplastic deformation, diffusion, and volumetric swelling due to a chemical reaction. *Int. J. Plasticity*, 27:1409–1431, 2011.

[90] K. Loeffel, L. Anand, and Z.M. Gasem. On modeling the oxidation of high-temperature alloys. *Acta Materialia*, 61:399–424, 2013.

[91] L. Luo, J. Wu, J. Luo, J. Huang, and V.P. Dravid. Dynamics of electrochemical lithiation/delithiation of graphene-encapsulated silicon nanoparticles studied by in-situ tem. *Scientific Report*, 4:3863, 2014.

[92] R.B. Marcus and T.T. Sheng. The oxidation of shaped silicon surfaces. *Electrochem.Soc.*, 129(6):1278–1282, 1982.

[93] M.T. McDowell, S.W. Lee, W.D. Nix, and Y. Cui. 25th anniversary article: Understanding the lithiation of silicon and other alloying anodes for lithium-ion batteries. *Advanced Materials*, 25 (36):4966–4984, 2013.

[94] I.A. Menzies and K.N. Strafford. Observations on the mechanical properties of nickel oxide scales. *Journal of Material Science*, 2:358–364, 1967.

[95] A. Mihalyi, R. J. Jaccodine, and T. J. Delph. Stress effects in the oxidation of planar silicon substrates. *Applied physics letter*, 74(14):1981–1983, 1999.

[96] A.V. Morozov, A. B. Freidin, and W.H. Müller. Stability of chemical reaction fronts in the vicinity of a blocking state. *PNRPU Mechanics Bulletin*, 2019(3):58–64, 2019.

[97] A.V. Morozov, A.B. Freidin, V.A. Klinkov, and et al. Experimental and theoretical studies of $Cu-Sn$ intermetallic phase growth during high-temperature storage of eutectic $SnAg$ interconnects. *Journal of Elec Materi*, 49(12):7194–7210, 2020.

[98] C.L. Muhlstein, S.B. Brown, and R.O. Ritchie. High-cycle fatigue and durability of polycrystalline silicon thin films in ambient air. *Sensors and Actuators*, A94:177–188, 2001.

[99] C.L. Muhlstein and R.O. Ritchie. High-cycle fatigue of micron-scale polycrystalline silicon films: fracture mechanics analyses of the role of the silica/silicon interface. *Int. J. Fracture*, 119/120:449–4745, 2003.

[100] A. Mukhopadhyay and B.W. Sheldon. Deformation and stress in electrode materials for Li-ion batteries. *Progress in Materials Science*, 63:58–116, 2014.

[101] M. Nanko. High-temperature oxidation of ceramic matrix composites dispersed with metallic particles. *Science and Technology of Advanced Materials*, 6:129–134, 2005.

[102] M. Nanko, M. Yoshimura, and T. Maruyama. High-temperature oxidation of Y_2O_3 partially-stabilized ZrO_2 composites dispersed with Ni particles. *Materials Transactions*, 44:736–742, 2003.

[103] S. Narayan and L. Anand. A large deformation elastic-viscoplastic model for lithium. *Extreme Mechanics Letters*, 24:21–29, 2018.

[104] M.N. Obrovac and L.J. Krause. Reversible cycling of crystalline silicon powder. *Journal of the Electrochemical Society*, 154:103–108, 2007.

[105] H. Ogihara, M. Fujii, and T. Saji. Hydrogen evolution reaction (HER) over electroless-deposited nickel nanospike arrays. *Royal society of chemistry*, 4:58660–58663, 2014.

[106] V. Palmov. *Vibrations of Elasto-Plastic Bodies*. Springer-Verlag, Berlin Heidelberg, 1998.

[107] B. Panicaud, J.L. Grosseau-Poussard, and J.F. Dinhut. General approach on the growth strain versus viscoplastic relaxation during oxidation of metals. *Computational Material Science*, 42:286–294, 2008.

[108] R. Paulose, R. Mohan, and V. Parihar. Nanostructured nickel oxide and its electrochemical behaviour - a brief review. *Nano-structures and Nano-Objects*, 11:102–111, 2017.

[109] M. Peigney. Cyclic steady states in diffusion-induced plasticity with applications to lithium-ion batteries. *Journal of the Mechanics and Physics of Solids*, 11:530–556, 2018.

[110] R. Peraldi, D. Monceau, and B. Pieraggi. Correlations between frowth kinetics and microstructure for scales formed by high-temperature oxidation of pure nickel. ii. growth kinetics. *Oxidation of Metals*, 58, 2002.

[111] R. Peraldi, D. Monceau, and B. Pieraggi. Correlations between growth kinetics and microstructure for scales formed by high-temperature oxidation of pure nickel. i. morphologies and microstructures. *Oxidation of Metals*, 58, 2002.

[112] S. Perusin, D. Monceau, and E. Andrieu. Investigations on the diffusion of oxygen in nickel at 1000ř*c* by SIMS analysis. *Journal of The Electrochemical Society*, 152:390–397, 2005.

[113] M.H. Pihlatie, H.L. Frandsen, A. Kaiser, and M. Mogensen. Continuum mechanics simulations of NiO/Ni − YSZ composites during reduction and re-oxidation. *Journal of Power Sources*, 195:2677–2690, 2010.

[114] N.B. Pilling. The oxidation of metals at high temperature. *J. Inst. Met.*, 29:529–582, 1923.

[115] M.F. Pillis, E. Goncalves de Araujo, and L.V. Ramanathan. Effect of rare earth oxide additions on oxidation behavior of aisi 304l stainless steel. *Materials Research*, 9:375–379, 2006.

[116] M. Poluektov, A. B. Freidin, and Ł. Figiel. Modelling stress-affected chemical reactions in non-linear viscoelastic solids with application to lithiation reaction in spherical Si particles. *International Journal of Engineering Science*, 128:44–62, 2018.

[117] M. Poluektov, A. B. Freidin, and Ł. Figiel. Micromechanical modelling of mechanochemical processes in heterogeneous materials. *Modelling Simul. Mater. Sci. Eng.*, 27:084005, 2019.

[118] R.-M. Pradeilles-Duval and C. Stolz. Mechanical transformations and discontinuities along a moving surface. *J. Mech. Phys. Solids*, 43:91–121, 1995.

[119] I. Prigogine and R. Defay. *Chemical Thermodynamics*. Longmans, Green, London, 1954.

[120] C.S. Rafferty. Stress effects in silicon oxidation-simulation and experiments. phd dissertation. Technical report, Stanford University, 1989.

[121] V. S. Rao and T. J. R. Hughes. On modelling thermal oxidation of silicon i: Theory. *Int. J. Numer. Meth. Engng.*, 47:341–358, 2000.

[122] V. S. Rao, T. J. R. Hughes, and K. Garikipati. On modelling thermal oxidation of silicon ii: Numerical aspects. *Int. J. Numer. Meth. Engng.*, 47:359–377, 2000.

[123] A.M. Rashidi, F. Mozafari, and A.R. Eivani. Predicition of the thickness loss of nanocrystalline nickel at elevated temperatures. *Solid State Science*, 17:151–155, 2013.

[124] M. Reiner. *Rheology*. Springer-Verlag, Gottingen Heidelberg, 1958.

[125] A. I. Rusanov. Surface thermodynamics revisited. *Surface Science Reports*, 58:111–239, 2005.

[126] A.I. Rusanov. *Thermodynamic foundations of mechanochemistry*. Nauka, St. Petersburg, 2006.

[127] I. Ryu, J.W. Choi, Y. Cui, and W.D. Nix. Size-dependent fracture of Si nanowire battery anodes. *J. Mech. Phys. Solids*, 59:1717–1730, 2011.

[128] J. Salencon. *Handbook of Continuum Mechanics. General Concepts Thermoelasticity*. Springer, Berlin, 2000.

[129] H. Schmidt, B. Jerliu, E. Huger, and J. Stahn. Volume expansion of amorphous silicon electrodes during potentiostatic lithiation of Li-ion batteries. *Electrochemistry Communications*, 115:106738, 2020.

[130] V.A. Sethuraman, V. Srinivasan, A.F. Bower, and P.R. Guduru. In situ measurement of stress-potential couplings in lithiated silicon. *J. Electrochem. Soc. Commun.*, 12:1614–1617, 2010.

[131] M.T. Shim and W.J. Moore. Diffusion of nickel and nickel oxide. *Journal of Chemical Physics*, 26:82, 1957.

[132] G. Smola, R. Gawel, K. Kyziol, M. Miszczak, and A. Grzesik. Influence of nickel on the oxidation resistance at high temperatures of thin chromium coatings. *Oxidation of Metals*, 91:625–640, 2019.

[133] W.O. Soboyejo, P. Mensah, R. Diwan, J. Crowe, and S. Akwaboa. High temperature oxidation interfacial growth kinetics in YSZ thermal barrier coatings of NiCoCrAlY with 0.25% hf. *Material Science and Engineering A*, 528:2223–2230, 2011.

[134] R. Song, M. Murphy, C. Li, K. Ting, C. Soo, and A. Z. Current development of biodegradable polymeric materials for biomedical applications. *Drug Design, Development and Therapy*, 12:3117–3145, 2018.

[135] P. Stahle and W. Reheman. Interface instabilities of growing hydrides. *ECF21, Catania, Italy*, 2016.

[136] Hugh St.C.O'Neill. Free energies of formation of NiO, CoO, Ni_2SiO$_4$, and Co_2SiO$_4$. *American Mineralogist*, 72:280–291, 1987.

[137] P. Sutardja and W.G Oldham. Modeling of stress effects in silicon oxidation. *IEEE Trans. Electron Devices*, 36(11):2415–2421, 1988.

[138] T. Takamura, S. Ohara, M. Uehara, and K. Sekine. A vacuum deposited Si film having a Li extraction capacity over 200 mah/g with a long cycle life. *J. Power Sources*, 129:96–100, 2004.

[139] G. Tammann. Uber anlauffarben von metallen. *Zeitschrift fur anorganische und allemeine Chemie*, 11:78–89, 1920.

[140] G. Tammann and W. Koster. The velocity of reaction of oxygen, hydrogen sulphide, and halogens with metals. *Z. anorg. allg. Chem.*, 123:196, 1922.

[141] J. Toriibio. Role of drawing-induced residual stresses and strains in the hydrogen embrittlement susceptibility of prestressing steels. *Corrosion Science*, 10:3346–3355, 2011.

[142] D. Uxa, B. Jerliu, E. Hüger, L. Dörrer, M. Horisberger, J. Stahn, and H. Schmidt. On the lithiation mechanism of amorphous silicon electrodes in Li-ion batteries. *Journal of Physical Chemistry*, 123:22027–22039, 2019.

[143] E.N. Vilchevskaya and A.B Freidin. On kinetics of chemical reaction fronts in elastic solids. In H. Altenbach and N. Morozov, editors, *Surface Effects in Solid Mechanics*, pages 105–117. Springer–Verlag, Berlin–Heidelberg, 2013.

[144] A.I. Visan, G. Popescu-Pelin, and G. Socol. Degradation behavior of polymers used as coating materials for drug delivery— a basic review. *Ploymers*, 13:1272, 2021.

[145] M.J. Volve and J. Reddy. Cation self-diffusion and semiconductivity in NiO. *Journal of Chemical Physics*, 53:1117, 1970.

[146] C. Wagner. Cbaitrag zur theorie des anlaufvorgangs. *Z. Phys. Chem.*, B41:25–41, 1933.

[147] C. Wagner. Zeitschrift physikalische chemie. *Z. Phys. Chem.*, 32:447, 1936.

[148] C. Wagner. The formation of thin oxide films on metals. *Corrosion Sciense*, 13:23–52, 1973.

[149] F. Xing, N. Ta, J. Zhong, Y. Zhong, and L. Zhang. Kinetic modeling of high-temperature oxidation of pure nickel. *Solid State Ionics*, 341:115018, 2019.

[150] Z. Xu, K. Rosso, and S. Bruemmer. Metal oxidation kinetics and the transition from thin to thick films. *Physical Chemistry Chemical Physics*, 14:14534–14539, 2012.

[151] Z.-L. Xu, S. Cao, K. Abouali, M.A. Garakani, J. Huang, J.-Q. Huang, E.K. Heidari, H. Wang, and J.-K. Ki. Study of lithiation mechanisms of high performance carbon-coated Si anodes by in-situ microscopy. *Energy Storage Materials*, 3:45–54, 2016.

[152] H. Yang, F. Fan, W. Liang, X. Guo, T. Zhu, and S. Zhang. A chemo-mechanical model of lithiation in silicon. *Journal of the Mechanics and Physics of Solids*, 70:349–361, 2014.

[153] J.-Y. Yen and J.-G. Hwu. Enhancement of silicon oxidation rate due to tensile mechanical stress. *Applied physics letter*, 76:1834–1835, 2000.

[154] M.V. Zdorovets and A.L. Kozlovsky. Study of phase transformation in Co/CoCo2O4 nanowires. *Journal of Alloys and Compounds*, 815:152450, 2020.

[155] Z. Zeng, N. Liu, Q. Zeng, S.W. Lee, W.L. Mao, and Y. Cui. In situ measurement of lithiation-induced stress in silicon nanoparticles using micro-raman spectroscopy. *Nano Energy*, 22:105–110, 2016.

[156] X. Zhang, A. Krischok, and C. Linder. A variational framework to model diffusioninduced large plastic deformation and phase field fracture during initial two-phase lithiation of silicon electrodes. *Computer Methods in Applied Mechanics and Engineering*, 312, 2016.

[157] X. Zhang, S.W. Lee, H.W. Lee, Y. Cui, and C. Linder. A reaction-controlled diffusion model for the lithiation of silicon in lithium-ion batteries. *Extreme Mechanics Letters*, 4:61–75, 2015.

[158] Y. Zhang, B. Liu, B. Tu, Y. Dong, and M. Cheng. Understanding of redox behavior of Ni − YSZ cermets. *Solid State Ionics*, 180:1580–1586, 2009.

[159] K. Zhao, M. Pharr, Q. Wan, W.L. Wang, E. Kaxiras, J.J. Vlassak, and Z. Suo. Concurrent reaction and plasticity during initial lithiation of crystalline silicon in lithium-ion batteries. *Journal of The Electrochemical Society*, 159:A238–A243, 2012.

[160] V. Zhdanov and B. Kasemo. Cabrera-mott kinetics of oxidation of metals nanowires. *Applied Physics Letters*, 100:243105, 2012.

ECOLE DOCTORALE

Titre : Couplages chimio-mécaniques dans les solides inélastiques : solutions analytiques et application à l'oxydation

Mots clés : Chimio-mécanique, Solutions analytiques, Oxydation, Viscoélasticité, Plasticité

Résumé : Au cours des dernières décennies, une attention particulière en mécanique des solides a été consacrée à l'étude des matériaux, dont la structure change en raison de transformations chimiques, ce qui induit des couplages forts entre la chimie, la mécanique et la physique. Ces réactions chimiques assistées par les contraintes sont observées dans diverses applications industrielles et médicales. Il est donc nécessaire de prendre en compte en détail l'influence de l'état de contrainte et de déformation sur la transformation chimique pour prédire le comportement des éléments structurels sous des chargements thermomécaniques et chimiques simultanés. Le travail présenté dans cette thése de doctorat s'appuie sur le cadre de la mécanique des milieux continus et sur les couplages chimio-mécaniques appliqués à des géométries particuliéres et des lois de comportement inélastiques afin d'obtenir des solutions analytiques de référence. Dans la première partie de la thèse, à l'aide d'une approche thermodynamique basée sur le concept de tenseur d'affinité chimique, une analyse théorique est menée afin de prendre en compte les effets de la viscosité et de la plasticité sur la propagation du front de réaction chimique pour différentes géométrie (plan, sphère, cylindre), la vitesse de réaction étant définie par la composante normale du tenseur d'affinité chimique. Les expressions analytiques de la relaxation des contraintes en arrière du front de réaction sont développées dans le cas viscoélastique. Par ailleurs, la solution obtenue pour un matériau transformé parfaitement plastique montre que même uniquement en raison de transformations chimiques, sans chargement externe, le matériau peut plastifier. Il est également montré comment les propriétés mécaniques du matériau initial et transforme peuvent avoir un impact sur les évolutions des réactions chimiques. Dans la deuxième partie de la thèse, afin de valider cette approche, des expériences d'oxydation à haute température de fils et de billes de nickel pur sont menées. L'objectif est d'étudier la cinétique d'un tel front aux échelles locales et de comparer les résultats obtenus avec les diverses solutions analytiques. De telles comparaisons montrent ainsi comment les propriétés rhéologiques des matériaux et de la géométrie du solide considérées sont importantes pour prédire la propagation du front de réaction.

Title : Chemo-mechanical couplings in inelastic solids: analytical solutions and application to oxidation

Keywords : Mechanochemistry, Analytical solutions, Oxidation, Viscoelasticity, Plasticity

Abstract : In the last decades, a particular attention in solid mechanics has been devoted to the investigation of materials, whose structure changes due to chemical transformations , which induces strong couplings between chemistry, mechanics and physics. Such stress-assisted chemical reactions are relevant in various industrial and medical applications and in modern technologies like batteries charging/discharging cycles introducing volume changes and cracks in electrodes, oxidation processes in MEMS or metal-based composite materials, thermo- or photo-oxidation of polymers. It is thus necessary to take into account the influence of stress-strain state on chemical transformation in detail for predicting the lifetime and the behavior of structural elements under simultaneous thermomechanical and chemical effects. Such processes can be described using the two-phase reaction model, in which reaction is localized at the sharp interface- reaction front, and the diffusing reactant is transported to the reaction front through the transformed material. The work presented in this PhD thesis is based on a coupled chemo-mechanical continuum theory applied to particular geometries and constitutive relations in order to obtain analytical solutions compared to experiments results. In the first part of the work, using the thermodynamical approach based on the concept of chemical affinity tensor, a theoretical analysis is conducted in order to take into account inelastic effects (viscosity, plasticity) and the geometry of structural elements (plane, spherical and cylindrical) on the chemical front propagation. The reaction rate is defined by the normal component of the chemical affinity tensor, which is equal to the combination of chemical potentials. After defining equilibrium conditions, the influence of inelastic behaviour of the transformed material on the reaction rate is studied in details. Analytical expressions of stress relaxation behind the reaction front are developed in the viscoelastic case. The analytical solution for perfectly plastic transformed material is obtained and shows that even only due to chemical transformations, without any external loading, the material can plastify. The effect of the structure's geometry on the chemical reaction propagation is studied for plane, spherical and cylindrical problems. It is also shown how the mechanical properties of initial and new material can impact chemical reaction evolutions. In the second part of the work, in order to validate this approach, high-temperature oxidation experiments for pure nickel wires and balls are conducted. The objective of such experiments is to study the kinetics of such a front at local scales and to compare the obtained results with analytical solutions. Such comparisons show how the rheological properties of materials and geometry of the considered body are important to predict the reaction front propagation. By combining these experiments with the analytical solutions, values for the diffusion coefficient and the chemical reaction constants are obtained.

Institut Polytechnique de Paris
91120 Palaiseau, France